UNIVERSIDAD AUTÓNOMA DE NUEVO LEÓN
FACULTAD DE INGENIERÍA MECÁNICA Y ELÉCTRICA

TESIS

"THIN FILMS OF Cu, In and Sb CHALCOGENIDES AS PHOTOVOLTAIC ABSORBERS"

POR

M. C. RAÚL ERNESTO ORNELAS ACOSTA

COMO REQUISITO PARCIAL PARA OBTENER EL GRADO DE DOCTOR EN INGENIERÍA DE MATERIALES

JULIO, 2015

UNIVERSIDAD AUTÓNOMA DE NUEVO LEÓN
FACULTAD DE INGENIERÍA MECÁNICA Y ELÉCTRICA
DIVISIÓN DE ESTUDIOS DE POSGRADO

TESIS

"THIN FILMS OF Cu, In and Sb CHALCOGENIDES AS PHOTOVOLTAIC ABSORBERS"

POR
M. C. RAÚL ERNESTO ORNELAS ACOSTA

COMO REQUISITO PARCIAL PARA OBTENER EL GRADO DE DOCTOR EN INGENIERÍA DE MATERIALES

JULIO, 2015

UNIVERSIDAD AUTÓNOMA DE NUEVOLEÓN
FACULTAD DE INGENIERÍAMECÁNICA Y ELÉCTRICA
DIVISIÓN DE ESTUDIOS DE POSGRADO

Los miembros del comité de tesis aprobado por la **Facultad de Ingeniería Mecánica y Eléctrica,** recomendamos que la tesis **"Thin films of Cu, In and Sb chalcogenides as photovoltaic absorbers"** realizada por el M. C. Raúl Ernesto Ornelas Acosta, sea aceptada para su defensa como opción al grado de Doctor en Ingeniería de Materiales.

El comité de tesis

_____

Dra. Bindu Krishnan

Asesor

_____   _____

Dr. Sadasivan Shaji   Dr. David Avellaneda Avellaneda

Revisor   Revisor

_____   _____

Dr. Manuel García Méndez   Dr. Eduardo Martínez Guerra

Revisor   Revisor

_____

Dr. Simón Martínez Martínez

Subdirector de Estudios de Posgrado

Ciudad Universitaria, San Nicolás de los Garza, N.L., Julio de 2015

For the loves of my life

Grisel and Diego

ACKNOWLEDGMENTS

To my mother-in-law Silvia.

To my entire research group: Grisel, Isabel, Linda, Jorge, Daniel, Dorian, José, Eleazar, Agustín.

To my friends, classmates and co-workers.

To my wife Grisel and my son Diego, the light of my days and the loves of my life.

LIST OF RELATED PUBLICATIONS AND CONFERENCES

Journal Papers

- B. Krishnan, S. Shaji, **R. Ernesto Ornelas** (2015). Progress in development of copper antimony sulfide thin films as an alternative material for solar energy harvesting. *Journal of Materials Science: Materials in Electronics*, 26 (7) 4770-4781. doi: 10.1007/s10854-015-3092-2.

- **Ornelas-Acosta R.E.**, Shaji S., Avellaneda D., Castillo G.A., Das Roy T.K., Krishnan B. (2015). Thin films of copper antimony sulfide: A photovoltaic absorber material. *Materials Research Bulletin*, 61, 215-225, ISSN 0025-5408, doi: http://dx.doi.org/10.1016/j.materresbull.2014.10.027

- **Ornelas-Acosta, R. E.**, Avellaneda, D., Shaji, S., Castillo, G. A., Das Roy, T. K., & Krishnan, B. (2014). $CuSbS_2$ thin films by heating Sb_2S_3/Cu layers for PV applications. *Journal of Materials Science: Materials in Electronics*, 25 (10) 4356-4362. doi: 10.1007/s10854-014-2173-y.

- **Ornelas-Acosta, R. E.**, Shaji, S., Avellaneda, D., Castillo, G. A., Das Roy, T. K., & Krishnan, B. (2013). Indium selenide thin films by laser irradiation of In/Se layered structure. *Surface Review and Letters*, 20(06), 1350058. doi:10.1142/S0218625X13500583

- **Ornelas, R. E.**, Avellaneda, D., Shaji, S., Castillo, G. A., Roy, T. K. D., & Krishnan, B. (2012). In_6Se_7 thin films by heating thermally evaporated indium and chemical bath deposited selenium multilayers. *Applied Surface Science*, 258(15), 5753-5758. doi:http://dx.doi.org/10.1016/j.apsusc.2012.02.084

- **<u>Ornelas A, R. E</u>**., Shaji, S., Arato, O., Avellaneda, D., Castillo, A., Das Roy, T. K., & Krishnan, B. (2011). Copper Indium Diselenide thin films using a hybrid method of chemical bath deposition and thermal evaporation. *MRS Online Proceedings Library*, 1324, 121-127. doi:10.1557/opl.2011.1254.

Conference Talks

- "CuSbS2 thin films for photovoltaic applications". *International Materials Research Congress*. Cancun, Mexico, August 2013.

- "In6Se7 thin films formed by laser irradiation of In/Se multilayer*". International Materials Research Congress*. Cancun, Mexico, August 2012.

- "Copper Indium Diselenide Thin Films Using a Hybrid Method of Chemical Bath Deposition and Thermal Evaporation". *MRS Spring Meeting*. San Francisco, CA, USA, April 2011.

- "Preparation and characterization of indium selenide thin films for photovoltaic applications*". International Congress of Industrial Chemistry*. Monterrey, N.L., México, April 2011.

Conference Posters

- "Solar cells using CuSbS2 thin films as absorber material". *MRS Spring Meeting*. San Francisco, CA, USA, April 2014.

- "CuSbS2 thin films for photovoltaic applications*". International Symposium on Renewable Energy and Sustainability*. Temixco, Mexico, March 2013.

- CuInSe2 thin films PV structures through selenization process using solution grown selenium". *International Materials Research Congress*. Cancun, Mexico, August 2012.

TABLE OF CONTENTS

SYNOPSIS

Many different photovoltaic technologies are being developed for large-scale solar energy conversion such as crystalline silicon solar cells, thin film solar cells based on a-Si:H, CIGS and CdTe. As the demand for photovoltaics rapidly increases, there is a pressing need for the identification of new visible light absorbing materials for thin-film solar cells. Nowadays there are a wide range of earth-abundant absorber materials that have been studied around the world by different research groups.

The current thin film photovoltaic market is dominated by technologies based on the use of CdTe and CIGS, these solar cells have been made with laboratory efficiencies up to 19.6% and 20.8% respectively. However, the scarcity and high cost of In, Ga and Te can limit in the long-term the production in large scale of photovoltaic devices. On the other hand, quaternary CZTSSe which contain abundant and inexpensive elements like Cu, Zn, Sn, S and Se has been a potential candidate for PV technology having solar cell efficiency up to 12.6%, however, there are still some challenges that must be accomplished for this material. Therefore, it is evident the need to find the alternative inexpensive and earth abundant materials for thin film solar cells. One of these alternatives is copper antimony sulfide($CuSbS_2$) which contains abundant and non-toxic elements which has a direct optical band gap of 1.5 eV, the optimum value for an absorber material in solar cells, suggesting this material as one among the new photovoltaic materials.

This thesis work focuses on the preparation and characterization of In_6Se_7, $CuSbS_2$ and $CuSb(S_{1-x}Se_x)_2$ thin films for their application as absorber material in photovoltaic structures using two stage process by the combination of chemical bath deposition and thermal evaporation.

First chapter is structured in six topics which covers a general overview of thin film solar cells. Begins with the knowledge of what is a semiconductor and what are its properties in order to understand the main role of this kind of material into a photovoltaic device. After knowing the semiconductor principles, it looks into the application as p-n junction solar cells and their limitations on energy conversion. Further, it describes the main reason to use thin films for solar cells instead of silicon technology. A brief review of the thin film solar cell technologies and the current status and the research issues are described.

Second chapter presents different deposition techniques for thin film technology. It describes the characterization tools for thin film materials, which contain the main techniques that characterize crystal structure, composition, morphology, optical and electrical properties of the solar cell materials as well as the devices.

Third chapter describes the main research issues leading to the search of novel earth abundant materials for photovoltaic applications. Starts with current research problems for the existing PV technology. An outlook and current status of copper antimony sulfide ($CuSbS_2$) and copper antimony sulfo-selenide ($CuSb(Se_x,S_{1-x})_2$), two of the earth abundant absorber materials for solar cells are present. The chapter includes the preparation and characterization of indium selenide thin films synthesized by laser annealing.

Fourth chapter provides details of the experimental formation of $CuSbS_2$ and $CuSb(S_{1-x}Se_x)_2$ thin films by heating glass/Sb_2S_3/Cu and glass/Sb_2S_3/Se/Cu layers. Also, the fabrication of photovoltaic devices using $CuSbS_2$ and $CuSb(S_{1-x}Se_x)_2$ thin films as absorber materials incorporated onglass/SnO_2:F/(n)CdS/(p)CuSbS$_2$, glass/SnO_2:F/(n)CdS/(i)Sb$_2$S$_3$/(p)CuSbS$_2$ and glass/SnO_2:F/(n)CdS/(i)Sb$_2$S$_3$/(p)CuSb(S$_{1-x}$Se$_x$)$_2$structuresis present. The thin films formed at different heating conditions were characterized using X-ray diffraction (XRD), X-ray photoelectron spectroscopy (XPS), scanning electron

microscopy (SEM), atomic force microscopy (AFM), UV-Vis spectrophotometry and electrical measurements.

Fifth chapter gives a complete discussion of the results obtained in the characterization of structural, morphological, optical and electrical properties of $CuSbS_2$ and $CuSb(Se_x,S_{1-x})_2$ thin films deposited using hybrid technique of chemical bath deposition and thermal evaporation as well as the results obtained for the photovoltaic devices fabricated using the chalcostibite thin films. The absorption coefficient of the $CuSbS_2$ thin films is $\sim 10^5$ cm^{-1}, a direct band gap of 1.55 eV and conductivity values in range of 10^{-2}-10^{-5} ($\Omega \cdot$cm)$^{-1}$. The best photovoltaic device performance is using a p-i-n structure of glass/SnO$_2$:F/(n)CdS/(i)Sb$_2$S$_3$/(p)CuSbS$_2$ having a photovoltaic parameters of J_{sc} = 7.54 mA/cm^2, V_{oc} = 405 mV, FF = 32% and efficiency $\sim$1.0%.

Sixth chapter gives the final conclusions of the entire thesis.

HYPOTHESIS

$CuSbS_2$ and $CuSb(S_{1-x}Se_x)_2$ thin films of suitable optoelectronic properties are formed by heating glass/Sb_2S_3/Cu and glass/Sb_2S_3/Se/Cu layers deposited by chemical bath deposition and thermal evaporation, for their applications in PV structures.

The performance of photovoltaic devices of glass/SnO_2:F/(*n*)CdS/(*p*)CuSbS_2, glass/SnO_2:F/(*n*)CdS/(*i*)Sb_2S_3/(*p*)CuSbS_2 and glass/SnO_2:F/(*n*)CdS/(*i*)Sb_2S_3/(*p*)CuSb(S_{1-x}Se_x)_2, using $CuSbS_2$ and $CuSb(S_{1-x}Se_x)_2$ thin films as absorber materials and CdS window layer depends on thickness, annealing temperature, annealing time and presence of an intrinsic layer.

GENERAL OBJECTIVE

Preparation and characterization of In and Cu-Sb chalcogenides thin films by heating stacked layers deposited by chemical bath deposition and thermal evaporation for solar cell applications.

SPECIFIC OBJECTIVES

- Preparation and characterization of indium selenide (In_6Se_7) thin films heating the stacked layers glass/In/Se by laser annealing.
- Preparation of $CuSbS_2$ and $CuSb(S_{1-x}Se_x)_2$ thin films by heating glass/Sb_2S_3/Cu and glass/Sb_2S_3/Se/Cu layers.
- Study the effect of annealing at different temperatures of $CuSbS_2$ and $CuSb(S_{1-x}Se_x)_2$ thin films.
- Study the effect of annealing of $CuSbS_2$ and $CuSb(S_{1-x}Se_x)_2$ thin films on structural, morphological, optical and electrical properties.
- Study the effect of different thickness of Sb_2S_3, Se and Cu layers on $CuSbS_2$ and $CuSb(S_{1-x}Se_x)_2$ thin films.
- Study the effect of different thickness of $CuSbS_2$ and $CuSb(S_{1-x}Se_x)_2$ thin films on structural, morphological, optical and electrical properties.
- Analyze the structural properties of the $CuSbS_2$ and $CuSb(S_{1-x}Se_x)_2$ thin films.
- Analyze the elemental composition and depth profiling of $CuSbS_2$ and $CuSb(S_{1-x}Se_x)_2$ thin films.
- Analyze the optical properties of $CuSbS_2$ and $CuSb(S_{1-x}Se_x)_2$ thin films.
- Analyze the electrical properties of $CuSbS_2$ and $CuSb(S_{1-x}Se_x)_2$ thin films.
- Preparation of photovoltaic devices using p-n junction of glass/SnO_2:F/(n)CdS/(p)$CuSbS_2$/C-Ag.

- Preparation of photovoltaic devices using p-i-n junction of glass/SnO_2:F/(n)CdS/(i)Sb_2S_3/(p)$CuSbS_2$/C-Ag and glass/SnO_2:F/(n)CdS/(i)Sb_2S_3/(p)$CuSb(S_{1-x}Se_x)_2$ /C-Ag.
- Study the effect of thickness and post-annealing of CdS layer on photovoltaic device performance.
- Study the effect of intrinsic layer on p-i-n junction on photovoltaic device

1
Thin Film Photovoltaics

The mankind has been experimented and developed one essential need to live, called "*energy*" for the last many decades. This energy is produced mainly from oil, coal and gas, calling them "fossil fuels". Eventually the use of this type of fuels has been detrimental for the environment. The production and use of this energy has been increased every year. One solution to maintain the same production rate of environmentally friendly energy is to use the sources of renewable energy, such as solar, wind and geothermal. Among these, considering the full potential and availability, photovoltaic devices that use solar energy to make electricity is the most promising.

In 1839 Edmond Becquerel discovered the photovoltaic effect. He found that certain materials would produce small amounts of electric current when they are exposed to light (Becquerel, 1839). All photovoltaic devices are made of p-n junction semiconductors. These devices are known as solar cells.

This chapter is structured in six topics which covers a general overview of thin film solar cells. The chapter begins with the knowledge of what is a semiconductor and what are its properties in order to understand the main role of this kind of material into a photovoltaic device. After knowing the semiconductor principles, it looks into the application as p-n junction solar cells and their limitations on energy conversion. Further, it describes the main reason to use thin film for solar cells instead of silicon technology. There will be a brief review of the thin film solar cell technologies and the current status and the research issues.

1.1 FUNDAMENTALS OF PHOTOVOLTAICS

Photovoltaic (PV) is the direct conversion of radiation into electricity. Photovoltaic systems contain cells that convert sunlight into electricity. Inside each cell there are layers of semiconducting materials. Conventionally, photovoltaic devices use inorganic semiconductors. The semiconductor of interest allows the formation of charge-carrier separating junction. The junction can be either a homojunction or heterojunction to collect the excess carriers when exposed to light. In the case of thin film solar cells, a p-n heterojunction is the most used. In a p-n junction photovoltaic cell, a photon of light produces an electron-hole pair if the energy of the photon is at least equal to the band gap of the material constituting the p-n junction. The electrons and holes first diffuse toward the respective edge of the depletion region, and then drift across the junction due to the built-in potential and are collected at the electrodes. The performance of photovoltaic devices is related to the properties of the materials by which they are made (i.e. semiconducting materials).

1.1.1 Semiconductors

A semiconductor is a material for which the valence band is almost totally occupied, having electrical resistivity in the range of $10^{-2} - 10^{9} \Omega \cdot cm$ and whose energy band gap for electronic excitations lies between $0 - 3$ eV (Yu and Cardona, 1996).

1.1.1.1 Absorption of photons

For solar cells, the generation of electrons and holes by the absorption of photons is the most important process. The absorption of a photon of energy $h\nu$ depends on absorption coefficient of material. The transitions involved in this process are shown in Figure 1.1.
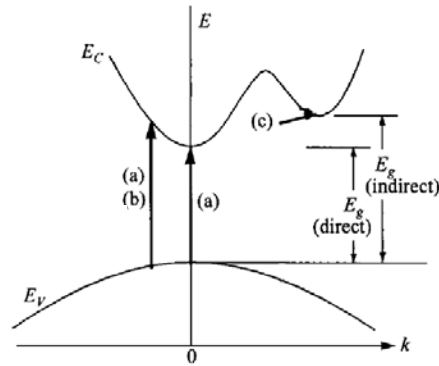
Figure 1.1 Transitions involved in the absorption of photons (a) allowed and (b) forbidden direct transition; (c) indirect transition

The allowed direct transition occurs when the momentum k of the electron does not change, this implies that the top of the valence band and the bottom of the conduction band are in the same value of $k = 0$. The forbidden direct transition occurs at values of $k \neq 0$. For indirect transitions, the transition from the top of the valence band to the bottom of the conduction band is not possible only by the absorption of a photon. It needs an extra momentum from a lattice vibration or phonon(Sze and Ng, 2006).

1.1.2 *p-n* junction

When a p-type and n-type semiconductors are brought into contact, a p-n junction is formed. Since there is a concentration difference of holes and electrons between two semiconductors, holes from p-type region diffuse into n-type region and the electrons from n-type region diffuse into p-type region. Due to the diffusion, the number of majority carriers is reduced on both sides of the p-n junction resulting to form a negative space charge on the p-side and a positive space charge on the n-side (Figure 1.2). As a result, an electrical field is built up across the junction. The transition region between the n-type and p-type semiconductors is called *space charge region* or *depletion zone*.
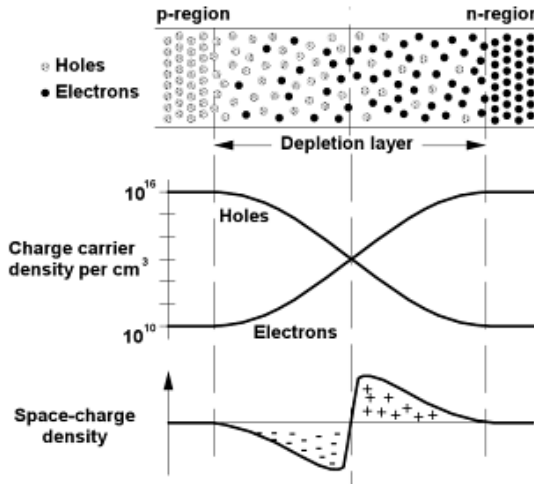
Figure 1.2 Creation of a depletion layer in the p-n junction

When a zero bias voltage is applied, the junction is in thermal equilibrium. The valence and conduction band must bend since the relative position of the Fermi level to the valence and conduction band is different for the p-type and n-type semiconductor. This band bending produces a potential barrier denoted by V_{bi} (built in voltage) (Figure 1.3).
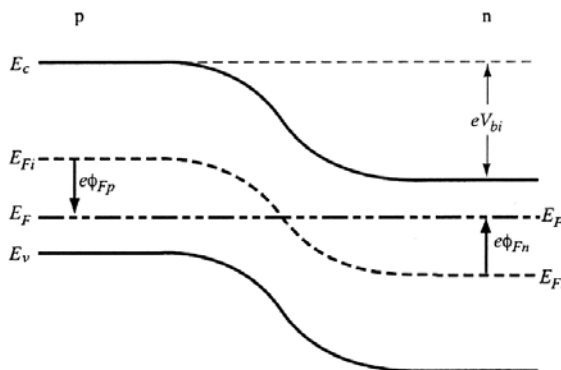
Figure 1.3 Energy band diagram of a p-n junction in thermal equilibrium

Then, the built in potential barrier is calculated by:

$$V_{bi} = \frac{k_B T}{e} \ln\left(\frac{N_a N_d}{n_i^2}\right) \tag{1.1}$$

Where N_a and N_d are net concentrations on p-type and n-type semiconductors respectively.

1.1.3 *p-n* junction under illumination

Previously, it was assumed that there is no light falling on the p-n junction, but solar cells works under illumination of solar radiation.

1.1.3.1 *Photovoltaic effect*

When a semiconductor is illuminated by light (photons) having energy greater than its band gap energy, the light is absorbed in the semiconductor and electron-hole pairs are generated. If such a photon is absorbed within the depletion layer, the internal electrical field directly separates the electron-hole pairs. The electron moves towards the n-side and the hole moves to the p-side. If during light absorption, electron-hole pairs are created outside the depletion zone within the p-side or n-side (i.e. outside of the electrical field), they may also reach the space charge region by diffusion due to thermal movements. The minority carriers (i.e. electrons within p-side and holes in the n-side) are collected by the electrical field of the space charge region and are transferred to the opposite side to be collected by electrical contacts and pass through an external circuit to create an electric current. Minority electrons from p-side will come to the n-side leaving behind a positively charge (hole) and minority holes from n-side to p-side leaving behind a negatively charge (electron). In this way, there is a net increase in the positive charges at p-side and a net increase in the negative charges at n-side. This build up of positive and negative charges causes a potential difference to appear across the p-n junction due to illumination, generating a photovoltage. This process is called *photovoltaic effect* and is important for understanding performance of solar cells (Figure 1.4) (Solanki, 2009). The potential barrier of the depletion layer, in contrast, reflects the majority carriers. Not all the minority carriers that are generated outside the depletion zone will cross the junction, they will travel an average distance L_n or L_p before they recombine, these distances are known as diffusion length of electrons and holes respectively. The minority carriers generated further away

from the depletion zone will recombine before reaching the space charge region edge and doesn't contribute to the photovoltage.
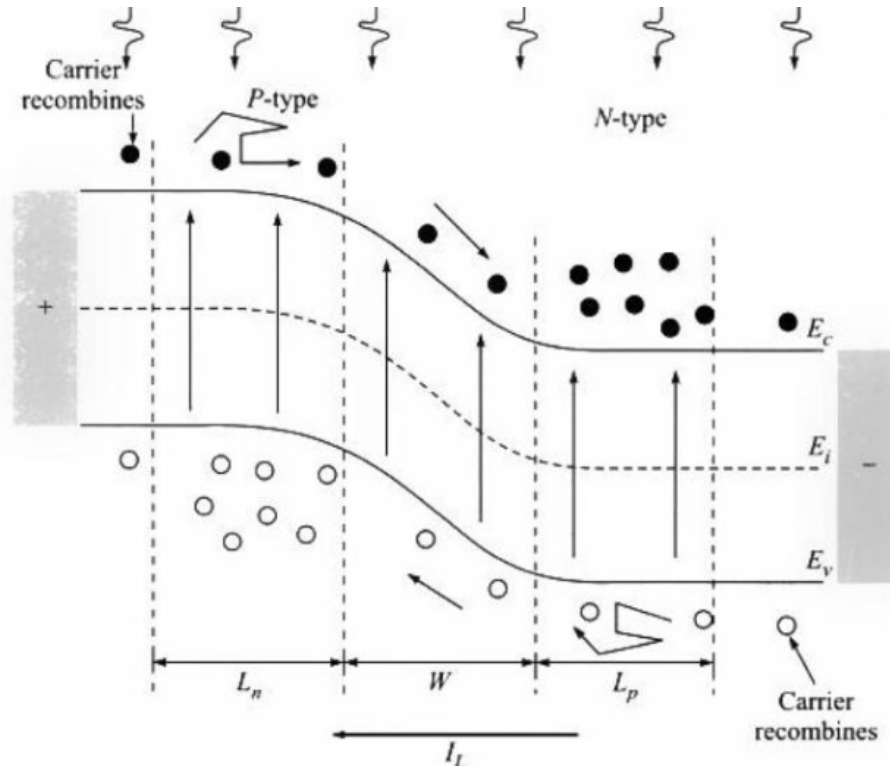
Figure 1.4 Photovoltaic effect

1.1.3.2 I-V Solar cell characteristics under dark

When we have a p-n junction, the behavior of the device is similar to a diode. In reverse bias, the current flowing from n-side to p-side is negative. The negative drift current or generation current in this mode is independent of the bias and is represented by $-I_{drift}$ = $-I_0$ (Figure 1.5). I_0 is called reverse saturation current which is a measure of the recombination in a device. A diode with larger recombination will have a large I_0, and can be calculated by:

$$I_0 = eA \left(\frac{D_n}{L_n} n_{p0} + \frac{D_p}{L_p} p_{n0} \right) \tag{1.2}$$

Where A is the cross sectional area, D_n-D_p are diffusion coefficients of electrons and holes, respectively, L_n-L_p are diffusion length of electrons and holes, respectively, n_{p0}-p_{n0} are minority electrons at p-side and holes at n-side, respectively. In forward bias, the diffusion current increases exponentially with bias and the diffusion current can be written as $I_0[exp(qV/k_BT)]$, where V is the applied bias. The total current is written as:

$$I = I_0 \left[\exp\left(\frac{eV}{K_B T} \right) - 1 \right] \tag{1.3}$$
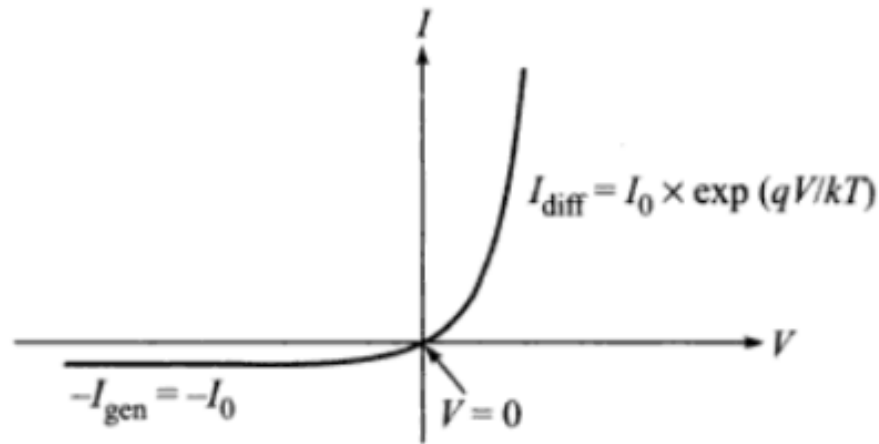
Figure 1.5Ideal I-V curve of a p-n junction diode under dark

In practice is notorious that real p-n junction behavior is different than ideal behavior. For real diodes the equation becomes:

$$I = I_0 \left[\exp\left(\frac{eV}{n K_B T} \right) - 1 \right] \tag{1.4}$$

where n is the ideality factor, being value of 1 the recombination current in the quasi-neutral regions and value of 2 the recombination in the depletion region. Figure 1.6 shows the comparison between ideal I-V diode curve versus real I-V diode curve, where thermal generation, recombination and resistive losses contribute to deviation of the ideality.
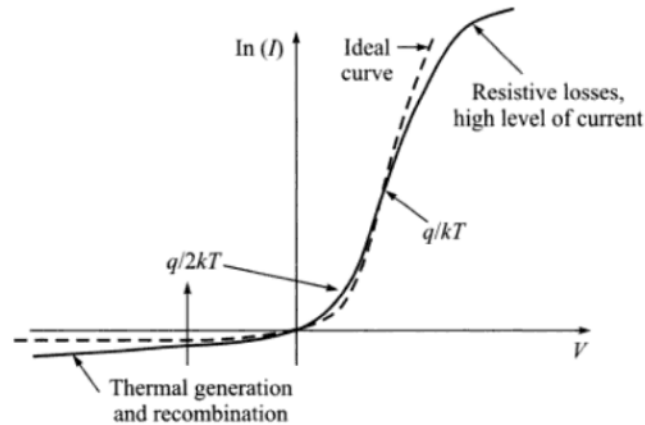
Figure 1.6 Real I-V p-n junction diode curve (solid line) vs ideal diode (dotted line)

1.1.3.3 I-V characteristics of solar cell under Illumination

When a solar cell is illuminated, there will be a large drift current due to minority electrons and holes caused by light, this is known as light generated current (I_L). The overall effect of solar cell illumination is to shift the I-V curve of the diode under dark downwards in the current-voltage axis as shown in Figure 1.7.
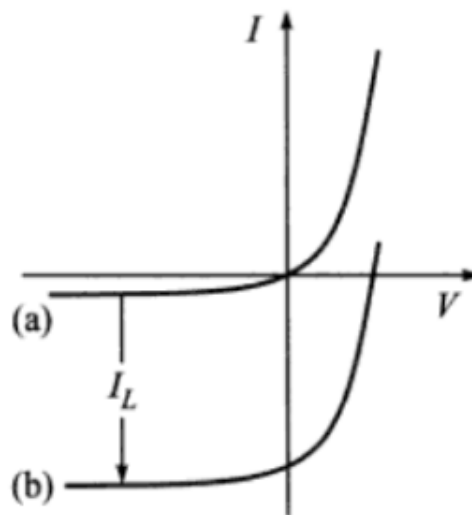
Figure 1.7 I-V curves of p-n junction on solar cell (a) under dark and (b) under illumination

Therefore, the current through the p-n junction under illumination is given by

$$I = I_0 \left[\exp\left(\frac{eV}{K_B T}\right) - 1 \right] - I_L \tag{1.5}$$

Solar cells are characterized with four parameters: short circuit current I_{sc}, open circuit voltage V_{oc}, fill factor *FF* and efficiency η. These parameters are shown in Figure 1.8.
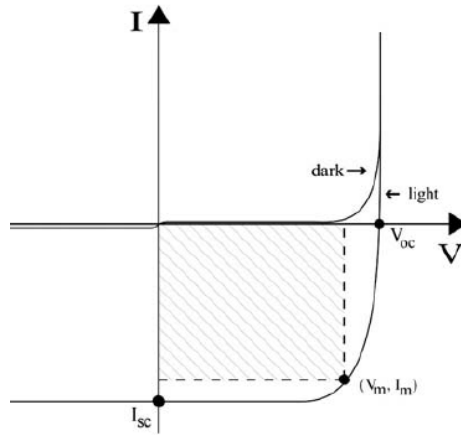
Figure 1.8 I-V characteristics of a solar cell under illumination

The *short circuit current* I_{sc} is the maximum current that flows in a solar cell when its terminals are short circuited, which imply a zero voltage across the contacts. This means, from eq. (1.5), $I_{sc} = -I_L$. If we divide the short circuit current by area, we obtain current density (J_{sc}) in terms of mA/cm^2.

The *open circuit voltage* V_{oc} is the maximum voltage generated across the contacts when the external circuit is in open condition ($I = 0$). The expression for open circuit voltage is:

$$V_{oc} = \frac{k_B T}{e} \ln\left(\frac{I_L}{I_0} + 1\right) \approx \frac{k_B T}{e} \ln\left(\frac{I_L}{I_0}\right), \text{if} I_L \gg I_0 \tag{1.6}$$

The built-in potential V_{bi} across a solar cell is usually described as an upper limit to the V_{oc} of the cell under illumination (Fonash, 2010).

The *fill factor FF* is the ratio of maximum power $P_m = V_m \times I_m$ that can be extracted from a solar cell to the ideal power $P_0 = V_{oc} \times I_{sc}$, given by

$$FF = \frac{V_m I_m}{V_{oc} I_{sc}} \tag{1.7}$$

The *efficiency* η is defined as the ratio of the power output (P_m) to power input (P_{in} = 100 mW/cm^2) according to standard AM 1.5, and can be written as:

$$\eta = \frac{V_m I_m}{P_{in}} = \frac{V_{oc} I_{sc} FF}{P_{in}} \tag{1.8}$$

The current through the p-n junction under illumination according to eq. (1.5) do not taking into account the parasitic series and shunt resistances typically associated with real solar cells. An electrical circuit representing these parasitic resistances is shown in Figure 1.9.
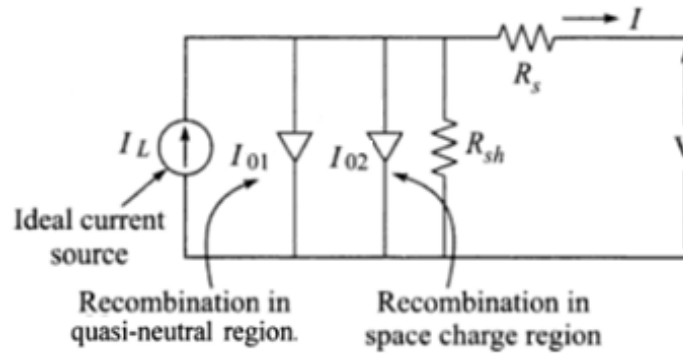
Figure 1.9 Equivalent circuit of a p-n junction solar cell

The ohmic losses in the cell occur due to the series and shunt resistances denoted by R_s and R_{sh}, respectively. The R_s is the resistance in the path of current flow and R_{sh} is the leakage path of the current. The I-V equation for the equivalent circuit is given by:

$$I = I_L - I_{01}\left\{\exp\left[\frac{e(V+IR_S)}{K_B T}\right] - 1\right\} - I_{02}\left\{\exp\left[\frac{e(V+IR_S)}{2K_B T}\right] - 1\right\} - \frac{V+IR_S}{R_{sh}} \tag{1.9}$$

where I_{01} and I_{02} are the saturation current when the recombination current in the quasi-neutral regions (I_{01}) and the recombination is in the depletion region (I_{02}).

The I-V equation for a simple solar cell model is given by (Luque and Hegedus, 2011):

$$I = I_L - I_{01}\left\{\exp\left[\frac{e(V+IR_S)}{nK_BT}\right] - 1\right\} - \frac{V+IR_S}{R_{sh}} \tag{1.10}$$

where *n* is the ideality factor, being value of 1 the recombination current in the quasi-neutral regions and value of 2 the recombination in the depletion region.

The effect of these parasitic resistances is shown in Figure 1.10 and affects directly the fill factor of solar cells changing the squareness of the curves. From Figure 1.10a, the series resistance is the sum of all the components that are related in the path of the current, this includes the p-type and n-type materials, semiconductor-metal contact resistance and resistance of metal contact. As the series resistance increases, voltage drop occurs within the cell and the I-V curve start to deviate. For very high value of R_s it gets nearly straight line with reduced I_{sc} remaining V_{oc}, as in open circuit no current flows and voltage drop in the cell is zero. For that, it is desirable to have value of series resistance as low as possible ($R_s \sim 0$). From Figure 1.10b, the shunt resistance is the leakage across the p-n junction, it means that crystal defects or precipitates of impurities are present in the junction region. Very low values of R_{sh} affects the V_{oc} but not I_{sc}, as in short circuited path, it provides the lowest resistance, hence the current flow through the short circuited path rather than leakage path. For that it is desirable to have value of shunt resistance as high as possible ($R_{sh} \sim \infty$)(Solanki, 2009).
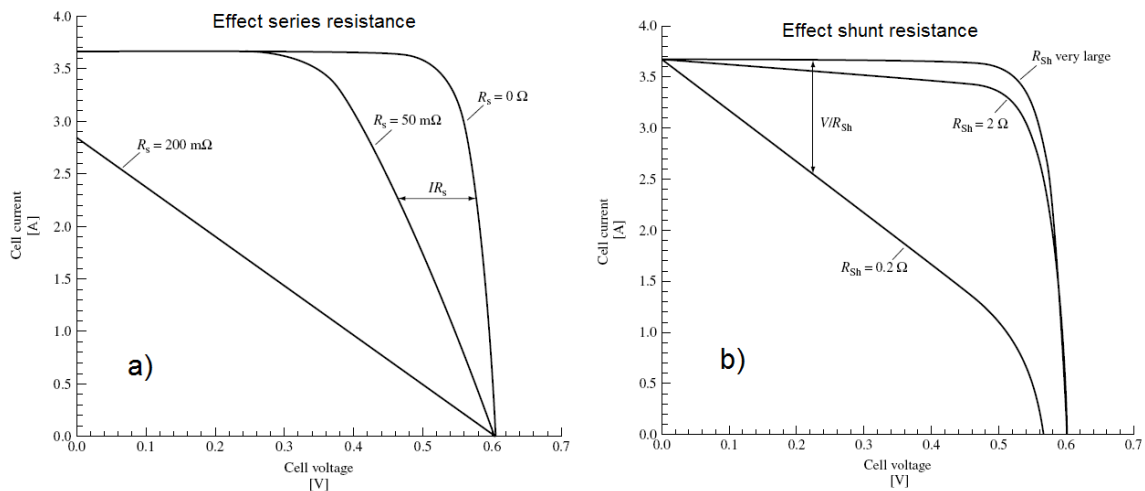
Figure 1.10 Effect of (a) series resistance and (b) shunt resistance on the I-V curve

1.1.4 Thin film solar cell technologies: A brief review

A thin film is a material created ab initio by the random nucleation and growth processes of individually condensing / reacting atomic / ionic / molecular species on a substrate. The structural, chemical, metallurgical and physical properties of such material are strongly dependent on a large number of deposition parameters and thickness. Thin film thickness varies from a few nanometers to tens of micrometers and thus is best defined in terms of the birth processes rather than by thickness.

There are some features that thin film processes have been shown to be of interest for solar cell technology (Chopra et al., 2004), such as:

1. A variety of physical, chemical, electrochemical and hybrid techniques are available for depositing thin films of the same material.

2. Microstructure of the films can be varied from amorphous/nanocrystalline to highly oriented and/or epitaxial growth, depending on the technique, deposition parameters and substrate.

3. Can be obtained semiconducting materials doping and alloying, having different optoelectronic properties.

4. Different types of electronic junctions, single and tandem junction are possible.

5. Composition, band gap and other optoelectronic properties can be graded in desired manner.

6. Surfaces and interfaces can be modified to provide an interlayer diffusion barrier and surface electric field.

7. Surfaces can be modified to achieve desired optical characteristics.

8. Thin film processes are in general eco-friendly and green processes

In present day there are a wide range of photovoltaic solar cell technologies using different types of materials and methods of fabrication. These technologies are classified into three generations depending on the material used (Gangopadhyay et al., 2013):

1. *First generation*: Photovoltaic systems based on crystalline silicon (c-Si), single crystalline silicon (sc-Si), ribbon silicon and multicrystalline silicon (mc-Si).

2. *Second generation*: Photovoltaic systems based on thin film technology using amorphous (a-Si) and micromorph silicon (a-Si/µc-Si), cadmium telluride (CdTe), copper indium diselenide (CIS) and copper indium gallium diselenide (CIGS) and related compounds.

3. *Third generation*: Photovoltaic systems based on concentrating (CPV) and organic solar cells for which their novel concepts are under development.

Thin film photovoltaic technology arises primarily due to the use of less material reducing costs of solar cells comparing to non-thin film technology. Figure 1.11 shown the timeline of research on PV solar cells by technology over the years according their respective classification (NREL, 2014).
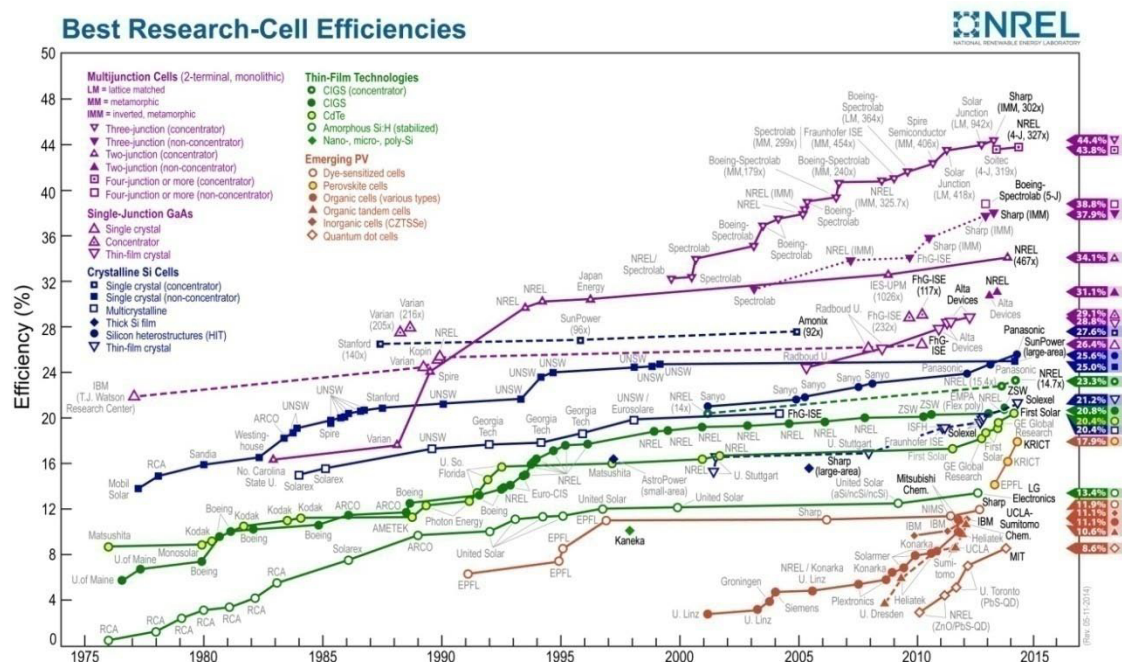
Figure 1.11 Best research cell efficiencies by PV technology(NREL, 2014)

.

1.1.5 Current status and research issues

The thin film solar cells consist of several layers of different materials classified as substrate, TCO (Transparent Conductive Oxide), window layer, absorber layer and metal contact layer. Each of the component materials has different physical and chemical properties and each affects the overall performance of the device. The major thin film photovoltaic technologies are based on amorphous silicon, CdTe and CIGS materials.

1.1.5.1 *Amorphous silicon (a-Si) based solar cells*

Amorphous silicon is one of the first thin film technologies developed using a p-i-n structure and having a conversion efficiency of 2.4% (Carlson and Wronski, 1976). The randomness in the atomic structure has an important effect on electronic properties and possesses a direct band gap of 1.7 eV which makes the use of less material than crystalline silicon.Efficiency of a-Si decreases when it is exposed to sunlight due to the Staebler-Wronski effect (Staebler and Wronski, 1977). In order to improve efficiency it has been developed tandem a-Si and nano-crystalline or micro-crystalline silicon (nc-Si or µc-Si) junctions, also called "micromorph". Using a double junction a-Si/nc-Si a thin film solar cell has been fabricated obtaining a V_{oc}, J_{sc}, FF and efficiency of 1.365 V, 12.93 mA/cm^2, 69.4% and 12.3% respectively (Green et al., 2014), as well a minimodule using this configuration was fabricated with an aperture area of 14.23 cm^2 and efficiency of 11.7% (Yoshimi M, 2003). Triple junction has improved the efficiency using a configuration of a-Si/nc-Si/nc-Si obtaining a V_{oc}, J_{sc}, FF and efficiency of 1.963 V, 9.52 mA/cm^2, 71.9% and 13.4% respectively (Ahn SW, 2012), being the a-Si solar cell champion so far. Current research is focused on improving thin film quality and reducing the Staebler-Wronski effect by improved fabrication techniques.

.

1.1.5.2 *Cadmium telluride based solar cells (CdTe/CdS)*

CdTe solar cells are one of the most dominant thin film photovoltaic technology in the world market. CdTe is a direct band gap material with 1.45 eV and high optical absorption coefficient. The CdTe solar cells are made of p-n heterojunction using a p-type material (CdTe) and n-type material (CdS). CdTe/CdS can be grown in superstrate and substrate configuration, obtaining best results using superstrate configuration. Different deposition techniques such as sputtering (Gupta and Compaan, 2003), electrodeposition(Miyake et al., 2004), closed-space sublimation (CSS)(Wu et al., 2001) and spray pyrolysis (Krishna and Dutta, 2004)were used. The CdTe/CdS solar cells showed poor photovoltaic properties, hence it required a heat treatment under $CdCl_2$ atmosphere, helping in the grain growth and improves electronic properties of CdTe thin film and thus high efficiencies were obtained(Paulson and Dutta, 2000). At high annealing temperatures, formation of CdS_xTe_{1-x} due to interdiffusion of CdS into CdTe at interface was observed(Mathew et al., 2012). The diffusion of sulfur atoms decreased the thickness of CdS causing pinholes leading to shorting paths across the junction. This has been a serious problem that restricts the application of thinner CdS to minimize the optical absorption losses. Other issue to be resolved is the formation of an efficient and stable ohmic contact on CdTe layer. CdTe/CdS solar cells in superstrate configuration have achieved efficiencies up to 19.6% (V_{oc}=857 mV, J_{sc}=28.6 mA/cm^2, FF=0.8) using close-spaced sublimation technique in glass substrate (Green et al., 2014). Different types of substrate were used for this solar cell achieving efficiencies of 14% for those fabricated on flexible glass substrate (Kranz et al., 2013). Many companies are commercializing CdTe solar modules such as Advance Solar Power, Antec Solar, Calyxo, GE Energy and First Solar, being the latter which possesses best solar module with efficiency up to 16.1% (Green et al., 2014). Recently both solar cell and module have achieved world record efficiencies of 20.4% and 17.0% respectively obtained by First Solar (Solar, Solar). Current research is focused on higher cell efficiencies by increasing

crystal quality, minority lifetime and improving doping control. The possibility of materials reuse and recycling in order to mitigate toxicity and materials scarcity are also investigated((DOE), 2014a).

1.1.5.3 Copper indium gallium diselenide based solar cells (CIGS/CdS)

Cu(In,Ga)Se$_2$ has received recently a large amount of attention due to the fact that has high absorption coefficient and a direct optical band gap which can be varied from 1.1 eV (CIS) to 1.7 eV (CGS), substituting Ga atoms for In atoms. CIGS solar cells can be grown using superstrate and substrate configuration. In this case, substrate configuration gives the highest efficiency. Various deposition techniques have been used to grow CIGS thin films, such as vacuum evaporation(Lundberg et al., 2003), flash evaporation(Ahmed et al., 1998), electrodeposition(Zhang et al., 2003) and spray pyrolysis (Shirakata et al., 1999). Among these, there are some techniques for depositing CIGS for highest efficiency solar cells. Co-evaporation process involves simultaneous evaporation of the elements from multiple sources in single or sequential processes during the deposition. The highest efficiencies are achieved using the so called "three stage process" in which start with deposition of (In,Ga)$_x$Se$_y$ precursor (first stage) followed by the co-deposition of Cu and Se (second stage) and finally the subsequent deposition of In, Ga and Se (third stage). Using this method, itwas achieved an efficiency of 19.9% with a device structure of glass/Mo/CIGS/CdS/ZnO/Ni-Al obtaining photovoltaic parameters of V$_{oc}$, J$_{sc}$ and FF of 690 mV, 35.5 mA/cm^2 and 81.2% respectively(Repins et al., 2008). The world record efficiency for CIGS thin film solar cells with device structure glass/Mo/CIGS/CdS/i-ZnO/ZnO:Al/Ni-Al has been reported, obtaining an efficiency of 20.8% (Jackson et al., 2011). Selenization of precursor materials is a sequential process which is favorable for large area film deposition with good control of the composition and the film thickness. The process consists of the deposition of metallic precursors (Cu-In-Ga) by evaporation, sputtering or electrodeposition followed by a thermal annealing in a controlled reactive or inert

atmosphere of H_2Se or Se vapors. Showa Shell (Japan) use the sputtering technique for precursor deposition and has achieved best efficiency of 13.5% for CIGS module (Green et al., 2014). One of the research directions to improve quality of CIGS solar cells is to seek a suitable replacement for CdS layer due to its low band gap prevents many high energy photons reaching the CIGS absorber layer((DOE), 2014b).

The main thin film photovoltaic technologies have been demonstrated that possess great advantages to fabricate high efficiency solar cells. However, the scarcity and high cost of some elements such as In, Ga and Te limit the large scale production of photovoltaic devices. In this context, it is essential to find alternative inexpensive and earth abundant materials for the fabrication of solar cell devices. Recently in Mexico, there are several groups working to develop high efficiency solar cells with earth abundant materials and low cost techniques. Such materials that are used for fabrication of solar cells are binary, ternary and quaternary compounds based on Ag, Cu, Sb, S, Se, Al, Sn, Zn elements. Primarily, in our research group we are focusing our efforts to fabricate Sb_2S_3, SnS, $AgSb(S,Se)_2$, $CuSbS_2$ based solar cells pursuing the best solar energy efficiency conversion.

1.2 REFERENCES

(DOE), U. S. D. O. E. 2014a. *Sunshot Initiative - Photovoltaics CdTe* [Online]. Available: http://energy.gov/eere/sunshot/cadmium-telluride.

(DOE), U. S. D. O. E. 2014b. *Sunshot Initiative - Photovoltaics CIGS* [Online]. Available: http://energy.gov/eere/sunshot/copper-indium-gallium-diselenide.

AHMED, E., TOMLINSON, R. D., PILKINGTON, R. D., HILL, A. E., AHMED, W., ALI, N. & HASSAN, I. U. 1998. Significance of substrate temperature on

the properties of flash evaporated $CuIn_{0.75}Ga_{0.25}Se_2$ thin films. *Thin Solid Films,* 335**,** 54-58.

AHN SW, L. S., LEE HM. 2012. Toward commercialization of triple-junction thin-film silicon solar panel with >12% efficiency. *27th European Photovoltaic Solar Energy Conference.* Frankfurt.

BECQUEREL, A. E. 1839. Recherches sur les effets de la radiation chimique de la lumiere solaire au moyen des courants electriques. *Comptes Rendus de L´Academie des Sciences,* 9**,** 145-149.

CARLSON, D. E. & WRONSKI, C. R. 1976. Amorphous silicon solar cell. *Applied Physics Letters,* 28**,** 671-673.

CHOPRA, K. L., PAULSON, P. D. & DUTTA, V. 2004. Thin-film solar cells: an overview. *Progress in Photovoltaics: Research and Applications,* 12**,** 69-92.

FONASH, S. 2010. *Solar Cell Device Physics*, Elsevier Science.

GANGOPADHYAY, U., JANA, S. & DAS, S. 2013. State of Art of Solar Photovoltaic Technology. *Conference Papers in Energy,* 2013**,** 9.

GREEN, M. A., EMERY, K., HISHIKAWA, Y., WARTA, W. & DUNLOP, E. D. 2014. Solar cell efficiency tables (version 43). *Progress in Photovoltaics: Research and Applications,* 22**,** 1-9.

GUPTA, A. & COMPAAN, A. D. 2003. 14% CdS/CdTe Thin Film Cells with ZnO:Al TCO. *MRS Online Proceedings Library,* 763**,** 161-166.

JACKSON, P., HARISKOS, D., LOTTER, E., PAETEL, S., WUERZ, R., MENNER, R., WISCHMANN, W. & POWALLA, M. 2011. New world record efficiency for $Cu(In,Ga)Se_2$ thin-film solar cells beyond 20%. *Progress in Photovoltaics: Research and Applications,* 19**,** 894-897.

KRANZ, L., BUECHELER, S. & TIWARI, A. N. 2013. Technological status of CdTe photovoltaics. *Solar Energy Materials and Solar Cells,* 119**,** 278-280.

KRISHNA, K. V. & DUTTA, V. 2004. Effect of in situCdCl$_2$ treatment on spray deposited CdTe∕CdS heterostructure. *Journal of Applied Physics,* 96**,** 3962-3971.

LUNDBERG, O., BODEGÅRD, M., MALMSTRÖM, J. & STOLT, L. 2003. Influence of the Cu(In,Ga)Se$_2$ thickness and Ga grading on solar cell performance. *Progress in Photovoltaics: Research and Applications,* 11**,** 77-88.

LUQUE, A. & HEGEDUS, S. 2011. *Handbook of Photovoltaic Science and Engineering*, Wiley.

MATHEW, X., CRUZ, J. S., CORONADO, D. R., MILLÁN, A. R., SEGURA, G. C., MORALES, E. R., MARTÍNEZ, O. S., GARCIA, C. C. & LANDA, E. P. 2012. CdS thin film post-annealing and Te–S interdiffusion in a CdTe/CdS solar cell. *Solar Energy,* 86**,** 1023-1028.

MIYAKE, M., MURASE, K., HIRATO, T. & AWAKURA, Y. 2004. Hall effect measurements on CdTe layers electrodeposited from acidic aqueous electrolyte. *Journal of Electroanalytical Chemistry,* 562**,** 247-253.

NREL 2014. Research Cell Efficiency Records.

PAULSON, P. D. & DUTTA, V. 2000. Study of in situ CdCl$_2$ treatment on CSS deposited CdTe films and CdS/CdTe solar cells. *Thin Solid Films,* 370**,** 299-306.

REPINS, I., CONTRERAS, M. A., EGAAS, B., DEHART, C., SCHARF, J., PERKINS, C. L., TO, B. & NOUFI, R. 2008. 19.9%-efficient ZnO/CdS/CuInGaSe$_2$solar cell with 81·2% fill factor. *Progress in Photovoltaics: Research and Applications,* 16**,** 235-239.

SHIRAKATA, S., KANNAKA, Y., HASEGAWA, H., KARIYA, T. & ISOMURA, S. 1999. Properties of Cu(In,Ga)Se$_2$ Thin Films Prepared by Chemical Spray Pyrolysis. *Japanese Journal of Applied Physics,* 38**,** 4997-5002.

SOLANKI, C. S. 2009. *Solar Photovoltaics: Fundamentals Technologies And Applications*, Prentice-Hall Of India Pvt. Limited.

SOLAR, F. http://investor.firstsolar.com/releasedetail.cfm?ReleaseID=828273[Online].

SOLAR, F. http://investor.firstsolar.com/releasedetail.cfm?ReleaseID=833971[Online].

STAEBLER, D. L. & WRONSKI, C. R. 1977. Reversible conductivity changes in discharge-produced amorphous Si. *Applied Physics Letters,* 31**,** 292-294.

SZE, S. M. & NG, K. K. 2006. *Physics of Semiconductor Devices*, Wiley.

WU, X., KEANE, J. C., DEHART, C., ALBIN, D. S., DUDA, A., GESSERT, T. A., ASHER, S., LEVI, D. H. & SCHELDON, P. 16.5% efficient CdS/CdTe polycrystalline thin film solar cell. Proc. of the 17th European Photovoltaic Solar Energy Conference, 2001 Munich, Germany. 995-999.

YOSHIMI M, S. T., SAWADA T, SUEZAKI T, MEGURO T, MATSUDA T, SANTO K, WADANO K, ICHIKAWA M, NAKAJIMA A, YAMAMOTO K. 2003. High efficiency thin film silicon hybrid solar cell module on $1m^2$-class large area substrate. *Conf. Record, 3rd World Conference on Photovoltaic Energy Conversion.* Osaka.

YU, P. Y. & CARDONA, M. 1996. *Fundamentals of Semiconductors: Physics and Materials Properties*, Springer.

ZHANG, L., JIANG, F. D. & FENG, J. Y. 2003. Formation of $CuInSe_2$ and Cu(In,Ga)Se2 films by electrodeposition and vacuum annealing treatment. *Solar Energy Materials and Solar Cells,* 80**,** 483-490.

2
Thin Films: Deposition and Characterization techniques

This chapter gives a brief overview on the different deposition techniques for thin film technology. The main focus is on the techniques used in the present research work for the fabrication of thin films and photovoltaic devices namely thermal evaporation (TE) and chemical bath deposition (CBD). Among the various characterization tools for thin film materials, the main techniques that characterize crystal structure, composition, morphology and optical and electrical properties of the solar cell materials as well as the devices are described.

2.1 DEPOSITION TECHNIQUES

In chapter 1, "thin film", was defined, now it is being explained how this thin film is deposited on a substrate. The entire process of the thin films formation, exhibits some characteristics such as (Wasa et al., 2004):

1. The formation of thin films independent of deposition technique starts with a random nucleation process followed by nucleation and growth stages.
2. The nucleation and growth stages are dependent on growth temperature, rate and substrate chemistry.
3. The nucleation stage can be modified by external agencies, such as electron or ion bombardment.

The basic properties of the thin film such as composition, crystal phase, orientation, thickness and microstructure are controlled by the deposition method and deposition conditions. Thin films have unique properties compared with that of bulk materials, resulting from the growth process and possess size

effects, including quantum size effects characterized by the thickness, crystalline orientation and multilayer aspects.

The thin film deposition process involves three main steps (Wasa and Hayakawa, 1992):

1. Production of the appropriate atomic, molecular or ionic species.
2. Transport of these species to the substrate through a medium.
3. Condensation on the substrate, either directly or via chemical and/or electrochemical reaction to form a solid deposit.

The growth process consisting of a statistical process of nucleation, surface-diffusion controlled growth of the three dimensional nuclei and formation of a network structure and its subsequent filling to give a continuous film (Wasa et al., 2004). The initial nucleation and growth stages can be described as *island type*, called Volmer-Weber type (Figure 2.1a), *layer type*, called Frank-van der Merwe type (Figure 2.1b) and *mixed type*, called Stranski-Krastanov type.
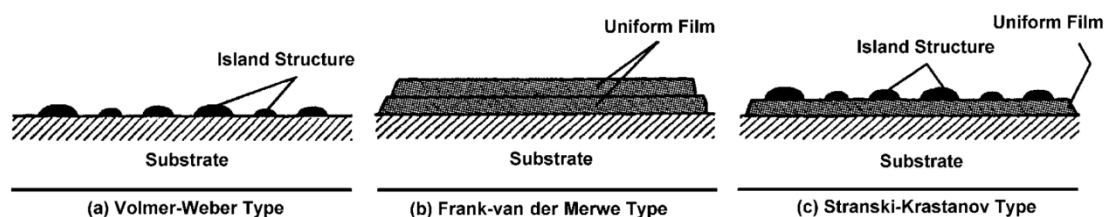
Figure 2.1 Types of thin film growth processes

The thin film deposition techniques can be classified in two principal processes, *physical* and *chemical* processes. Physical process is related to the techniques which depend on the evaporation of the material from a source and is divided into two main categories: evaporation and sputtering, meanwhile, the chemical process depend on physical properties and is divided into gas phase and liquid phase. The complete classification is included in Figure 2.2.

The deposition techniques used in this thesis work are thermal evaporation and chemical bath deposition and these methods are described in detail.
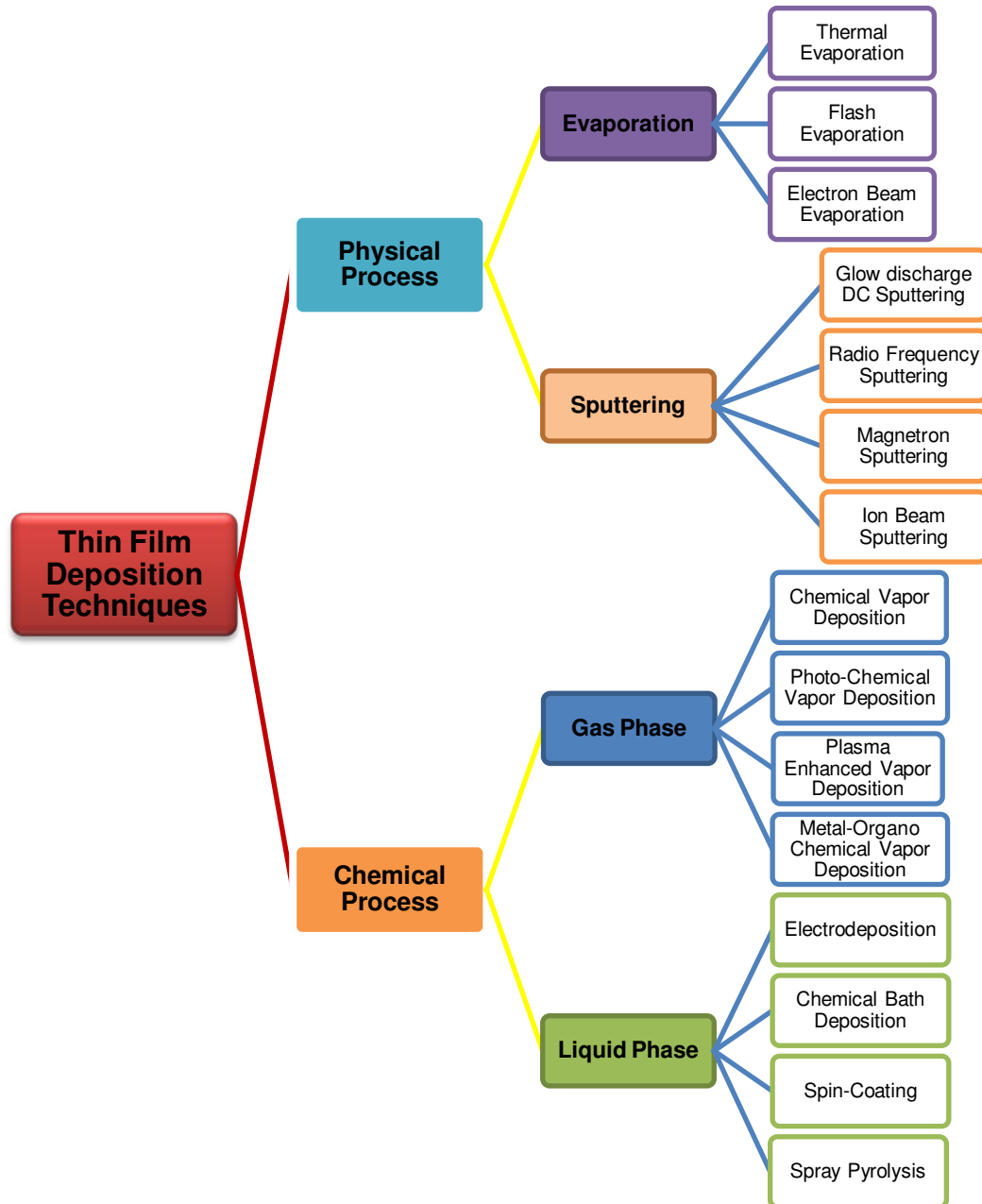
Figure 2.2 Thin film deposition techniques

2.1.1 Thermal evaporation (TE)

Thermal evaporation is one of the most common thin film deposition techniques. Basically consists of three stages: (i) A vapor is generated by boiling or subliming a source material, (ii) the vapor is transported from the source to

the substrate, and (iii) the vapor is condensed to a solid film on the substrate(Seshan, 2001).

This technique has some advantages:

1. Small impurity concentrations.
2. Boiling point temperature decreases in vacuum conditions.
3. Thickness can be easily controlled.
4. Deposition on different types of substrates is possible.

Two types of thermal evaporation processes are shown in Figure 2.3. Resistive heating is most commonly used. The source materials are evaporated by a resistively heated filament or boat, generally made of refractory metals such as tungsten (W), molybdenum (Mo) or tantalum (Ta). Crucibles of quartz, graphite, alumina or boron-nitride are used with indirect heating. Refractory metals are evaporated by electron beam deposition since simple resistive heating cannot evaporate high melting point materials.
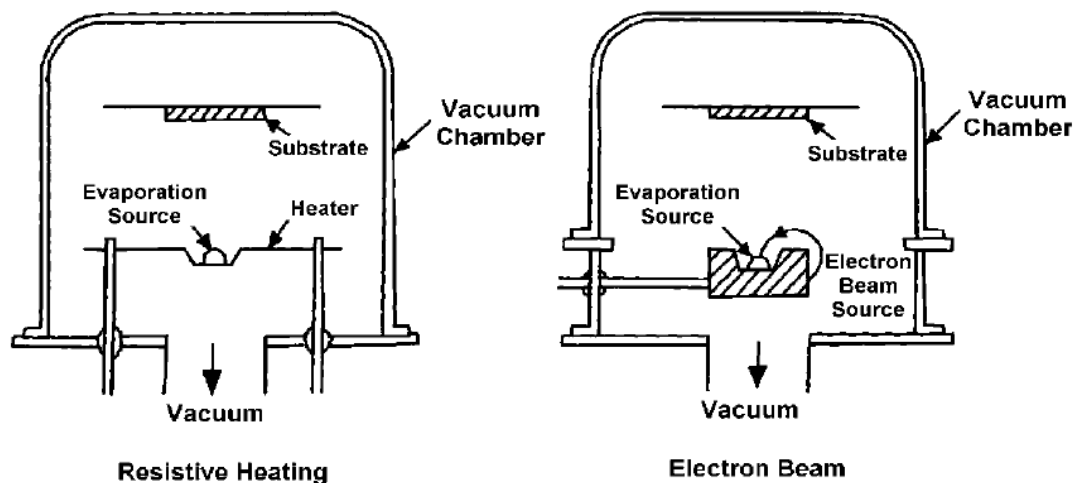
Figure 2.3 Thermal evaporation processes, resistive heater and electron beam

2.1.2 Chemical bath deposition (CBD)

Chemical deposition is the deposition of films on a solid substrate from a reaction occurring in a solution (Figure 2.4). Can be carried out in both acidic and alkaline solutions, most reactions have been carried out in alkaline

solutions. Chemical deposition can be used to deposit any compound that satisfies four basic requirements (Hodes, 2002):

1. The compound can be made by simple precipitation, although not exclusively, refers to the formation of a stoichiometric compound formed by ionic reaction.
2. The compound should be relatively insoluble in the solution used.
3. The compound should be chemically stable in solution.
4. If the reaction proceeds via free anion, this anion should be relatively slowly generated to prevent sudden precipitation.

The mechanisms of chemical deposition processes can be divided into two different processes (Hodes, 2002):

1. Formation of the required compound by ionic reactions involving free anions.
2. Decomposition of metal complexes.

These two categories can be further divided in two:

a) Formation of isolated single molecules that cluster.
b) Form a crystal or particle and mediation of a solid phase, usually the metal hydroxide.

The chemical deposition technique for the preparation of thin films has recently been shown to be an attractive technique due to its simplicity, low cost and low temperature, and it has been successfully used for depositing binary Sb_2S_3(Nair, 1998), CdS (Gonzalez et al., 2011), ZnS (Qi et al., 2008), SnS (Garcia-Angelmo et al., 2014), ternary $CuInSe_2$(Pathan and Lokhande, 2005), $CuSbS_2$(Ezugwu et al., 2010) and quaternary Cu_2ZnSnS_4(Shinde et al., 2012) metal chalcogenide thin films.

Figure 2.4 Chemical bath deposition

2.2 THIN FILM CHARACTERIZATION TECHNIQUES

It is indispensable to measure thin film properties for the study of thin film materials for photovoltaic applications. The thin films and devices fabricated in this research work were characterized for their crystal structure, morphology, surface and depth profile of chemical composition, optical and electrical properties. Several methods are available for the evaluation of thin film properties. Detailed explanation of the characterization techniques used in this work is given below.

2.2.1 X-Ray Diffraction (XRD)

When an X-ray strikes an atom, it will be weakly scattered in all directions. If it encounters a periodic array of atoms, the waves scattered by each atom will reinforce in certain directions and cancel in others. Geometrically, a crystal made of lattice planes the scattering from a given family of planes will only be strong if the X-rays reflected by each plane arrive at the detector in phase. This leads to a relationship between the X-ray wavelength, λ, the spacing between lattice planes, d, and the angle of incidence, θ, known as Bragg's law (Kaufmann, 2003):

$$n\lambda = 2d\sin\theta \tag{2.1}$$

where n is an integer number, called reflection order.

The X-ray diffraction technique is suited to resolve crystalline structures, also could reveal information on sample microstructure. The crystallite size from X-ray diffraction data can be evaluated using the Scherrer equation:

$$D = \frac{0.9\lambda}{\beta\cos\theta} \tag{2.2}$$

where β is the width of the Bragg reflections (which could be FWHM-Full Width Half Maximum (rad), or the integral breadth-total area/peak height (deg)) and D is the crystallite size. If the width increases, the crystallite size decreases.

The width of Bragg reflections is also affected by microstructural features other than size broadening, like crystallite shape, shape distribution and any distortion of the crystal structure like microstrain, dislocations, twin planes and stacking faults (Birkholz, 2006). Microstrains play a prominent role in the distortion of crystal lattice. The strain fields causes that the position and broadening of the peak reflections changes. The way to calculate this microstrains is using the Williamson-Hall plot (Williamson and Hall, 1953), which also introduce crystallite size as well, and is given by:

$$\beta\cos\theta = \frac{0.9\lambda}{D} + 2\varepsilon\sin\theta \tag{2.3}$$

where ε is the strain of the lattice.

The equation (2.3) shows that the plot $\beta\cos\theta$ versus $\sin\theta$ should give a straight line that allows for the crystallite size (D) and strain (ε) to be determined from the intercept and slope respectively.

In the case of thin films, X-ray diffraction measurements using conventional scanning methods generally produce a weak signal from the film and an intense signal from the substrate. One of the ways to avoid intense signal from the substrate and get stronger signal from the film itself is to perform a scan with a

fixed grazing angle of incidence (few degrees or even less), known as GIXRD. In order to know the penetration depth of the x-rays in the film related with the incidence angle, we perform a calculation using the relation:

$$\tau_{1/e} = \frac{\sin \alpha}{\mu} \tag{2.4}$$

where α is the incidence angle and μ is the attenuation coefficient.

For this work the XRD study in standard mode (θ-2θ)was performed by a Bruker D8 Advance diffractometer using Cu Kα_1 radiation (λ = 1.54056 Å). The study in grazing incidence angle was performed by a Rigaku D-Max 2000 diffractometer using Cu Kα_1 radiation.

2.2.2 X-ray Photoelectron Spectroscopy (XPS)

X-ray photoelectron spectroscopy (XPS) uses X-ray of a characteristic energy to excite electrons from orbitals in atoms (photoemission process). The photoelectrons emitted from the material are collected as a function of their kinetic energy, and the number of photoelectrons collected in a defined time interval is plotted versus kinetic energy. Peaks appears in the spectrum at discrete energies due to emission of electrons from states of specific binding energies in the material. The position of the peaks identifies the chemical elements in the material. Peak areas are proportional to the number of orbitals in the analysis volume and are used to quantify the elemental composition. The positions and shapes of the peaks in an XPS spectrum can also be analyzed in detail to determine the chemical state of the constituent elements in the material, including oxidation state, partial charge and hybridization.

Thin films can be analyzed to determine film thickness. Typical method of analysis involves measuring composition as a function of sputter depth into the sample (depth profiling). The method requires the use of an Ar$^+$ ion etching process to sputter away successive layers of the sample, for that reason is destructive.

An XPS survey spectrum covers all of the energy levels that can be excited by the X-ray energy being used. The orbitals p, d and f split into two peaks. This is due to coupling between the electron spin (s) and orbital angular momentum (l) for these orbitals. The s orbitals ($l=0$) do not split because they have no orbital angular momentum. The nomenclature used in XPS to designate the spin-orbit splitting uses principal quantum number, orbital designation (s, p, d, f) and $|l\pm s|$ (s is the spin of the electron being 1/2). If we have a $3p_{3/2}$ peak, it designates electrons from p orbital (l=1) of the n=3 level with a total angular momentum (j) of either $|1+1/2|$ (spin-up in an upwardly aligned p orbital) or $|1-1/2|$ (spin-down in a downwardly aligned p orbital). The separation of the spin-orbit splitting depends on the magnitude of the coupling between electron spins and orbital angular momentum. For a given element, the separation of the spin-orbit coupling decreases with increasing principal quantum number (4p levels are split more than 5p levels) and with increasing angular momentum quantum number (4p levels are split more than 4f levels). The spin-orbit split levels have different relative occupancies (peak area ratios), in proportion to the respective degeneracies of the levels. Thus, p 1:2, d 2:3 and f 3:4 corresponding to 2-4, 4-6 and 6-8 electrons, respectively (Moulder et al., 1992).

The chemical state is an important information obtained from high resolution XPS spectra. The chemical state of an atom depends on the type of bond it forms. The core electrons are contained spatially on shells within the outer valence shells. The work needed to remove the inner core electrons is affected proportionally by changes in the potentials on the valence shell. In atoms that acquire a partial negative valence charge, the core levels will shift to lower binding energies because less work is needed. The core levels in atoms that become more positively charged will shift to higher binding energies.

For this work the XPS study of survey and high resolution spectra and depth profiling was performed using a Thermo Scientific K-Alpha XPS instrument with monochromatized Al Kα radiation (hν=1486.68 eV). Binding energies (B.E) of all the peaks were corrected using C 1s energy at 284.6 eV corresponding to adventitious carbon in addition to the charge compensation by the flood gun

associated with the spectrometer. The peaks were de-convoluted using Shirley type background calculation and peak fitting using Gaussian-Lorentzian sum function.

2.2.3 Atomic Force Microscopy (AFM)

Atomic force microscopy (AFM) is an imaging technique that can produce topographic images of a surface with atomic resolution in all three dimensions. AFM is composed of a probe in the shape of cantilever with a small tip, a laser, photodiode and a piezoelectric element (Rau et al., 2011).

The laser beam is focused onto the back of the end of cantilever and from there is reflected to the photodiode, this allows detecting the bending of the cantilever accurately. When the tip scan the sample surface, the force of interaction between the tip and sample leads to changes in the static bending of the cantilever (tip in contact) or in the resonance frequency of the cantilever oscillation (tip is at small distance from the surface). The first operating mode is called *contact mode* and the second is called *noncontact mode*. The forces interacting between the tip and the sample include the Van der Waals force, chemical binding force, electrostatic and magnetic forces.

1. *Contact mode*: Is performed when at the distance between the tip and the sample surface, attractive forces are replaced by repulsive forces originating repulsion between ion cores and electron cloud of atoms at the tip and the sample. When the tip-surface distance decreases will result in a normal deflection of the cantilever, originated by the repulsive force acting. Some applications of this mode is the characterization of surface morphology, grain size, shape and its distribution (Al-Jassim et al., 2001), grain orientation (Sadewasser et al., 2002) and surface defects.

2. *Noncontact mode*: The cantilever oscillates close to its resonance frequency using a piezoelectric element. The oscillation is monitored by the photodiode when it receives the laser signal. When the tip is close to the surface, forces between tip and surface become relevant.

In this work morphology and topography of the thin films surface was studied using Atomic Force Microscope (Model Solver Pro from NT-MDT).

2.2.4 Scanning Electron Microscopy (SEM) with EDX

SEM is one of the most widely used equipment in materials research and is applied most frequently for imaging of thin film solar cells. The SEM analysis provides information relating to topographical features, morphology, phase distribution, compositional differences, crystal structure, crystal orientation and the presence and location of electrical defects. Also is capable of determining elemental composition of micro-volumes with the addition of an X-ray spectrometer and phase identification through analysis of electron diffraction patterns. The strength of the SEM lies in its inherent versatility due to the multiple signals generated, simple image formation process, wide magnification range and excellent depth of field (Kaufmann, 2003).

Electrons used for imaging in SEM are secondary electrons and backscattering electrons. *Secondary electrons* (SE) are those electrons with <50 eV energy, are due to inelastic interaction and are influenced more by surface properties than by atomic number. The depth from which secondary electrons escape the specimen is generally between 5 and 50 nm due to their low energy. Secondary electrons provides for high resolution image of the specimen surface. The intensity is a function of the surface orientation with respect to the beam and the SE detector and thus produces an image of the specimen morphology.

Backscattering electrons (BSE) are electrons from the incident probe that have elastic interactions with the sample, change trajectory and escape from the sample. This majority of electrons emitted from the specimen at high beam voltage and their average energy is much higher than that of the secondary electrons. The depth from which backscattered electrons escape from the specimen is dependent upon the beam energy and the specimen composition. The intensity of the BSE signal is a function of the average atomic number (Z) of

the specimen, with heavier elements (higher *Z*) producing more BSE and the phases appear brighter than lower *Z* phases.

The *energy dispersive X-ray spectrometry* (EDX) is a technique for measuring the intensity of X-ray emission as a function of the energy of the X-ray photons. When an electron impinges on a specimen strikes an electron in inner shells of the specific atom and transfers its energy to eject the electron outside the specimen. The vacancy leave behind is occupied by an outer shell electron and the excess of energy is emitted in the form of characteristic X-ray. Recording all X-rays emitted the chemical composition of specimen can be analyzed.

Electron beam induced current (EBIC) can be studied using charge collection in SEM with the specimen as detector. Has been used to determine carrier lifetime, diffusion length, defect energy levels, surface recombination velocities and to locate p-n junctions and recombination sites (Leamy, 1982).

In this work we used the imaging technique using secondary and backscattered electrons. Morphology was studied using Scanning Electron Microscope (SEM) (Model FEI Nova NanoSEM 200) and elemental analysis was obtained using Energy Dispersive X-Ray Analyzer (EDX) associated with the SEM.

2.2.5 Optical properties

The optical characterization is performed using the technique UV-Vis absorption spectroscopy and is the measurement of the attenuation of a beam of light after it passes through a sample or after reflection from a sample surface. This include a variety of absorption, transmittance and reflectance in the ultraviolet (UV), visible and near-infrared (NIR) spectral regions.

The use of UV-Vis spectroscopy in materials can be divided into two categories: (1) quantitative measurements in gas, liquid or solid phase, which is often necessary to measure the absorbance or reflectivity at a single wavelength and serves as a diagnostic tool for the preparation of materials; (2) characterization of the optical and electronic properties of a material, which is a

qualitative application that requires recording at least a portion of the UV-Vis spectrum for characterization of the optical or electronic properties of materials.

Experimental measurements are made in terms of percentage transmittance *T*:

$$T = (I/I_0) \times 100\% \tag{2.5}$$

where *I* is the intensity of light after it passes through the sample and I_O is the initial incident light intensity.

The absorption of light by an optical medium with thickness *t*, is quantified by its absorption coefficient, α, which can be obtained using the Beer's law:

$$I = I_0 \exp(-\alpha t) \tag{2.6}$$

Commonly, transmittance and reflectance spectra were recorded, combining these experimental measurements it is possible to calculate the absorption coefficient, given by:

$$\alpha = \frac{1}{t} \ln \left[\frac{(1-R)^2}{T} \right] \tag{2.7}$$

Using the optical absorption coefficient, the band gap can be determined by the Tauc plot (Fox, 2010):

$$(\alpha h v)^n = A(h v - E_g) \tag{2.8}$$

where E_g is the optical band gap and *n* = 2, 1/2, 2/3 respectively for direct allowed, indirect allowed and direct forbidden transitions, *h* is the Planck's constant, v is the frequency and *A* is a constant. The optical band gap is an important parameter for solar cells, especially for the absorber material, and it can be considered as the minimum energy necessary to promote an electron from the valence band to the conduction band. The maximum theoretical efficiency for a p-n junction as a function of band gap was calculated by Shockley-Queisser, resulting in an optical band gap of 1.5 eV being the value at which a solar cell achieved its maximum efficiency (Shockley and Queisser, 1961).

In this work, optical transmittance and reflectance spectra were recorded by a UV-Vis spectrometer (model Shimadzu UV-1800) in the 300-1100 nm wavelength range and the optical band gap was calculated using the Tauc plot.

2.2.6 Electrical Characterization

2.2.6.1 D.C. Conductivity

A material's conductivity, σ, it is the ability to conduct electrical current, and can be calculated as follows:

$$\sigma = \frac{1}{\rho} \tag{2.9}$$

where ρ is the resistivity of the material. For thin films, the resistivity can be obtained by measuring the resistance and physical dimensions of the electrodes painted over the thin film by the two-point probe technique. The resistance R is given by Ohm's law:

$$R = \frac{V}{I} \tag{2.10}$$

where V is the applied voltage and I is the current. The two-point resistivity of the material is calculated by:

$$\rho = \frac{Rwt}{l} \tag{2.11}$$

where ρ is the resistivity in $\Omega{\cdot}cm$, R is the measured resistance in Ω, w is the width of the electrodes, l is the distance between two electrodes and t is the thickness of the thin film.

2.2.6.2 Photoconductivity

When radiation of sufficient energy is absorbed in a semiconductor material, resulting an increase of electrical conductivity, this phenomenon is called photoconductivity (Bube, 1960). In most photoconductors, the contribution of the

minority carriers to the current can be neglected, so, the conductivity can be expressed in terms of majority carriers.

In this work, the materials were characterized using the two probe technique. The contacts were made using conductive carbon paint (SPI® supplies): two planar electrodes of 2 mm in length separated by 5 mm. Dark conductivity and photoconductivity were measured using a picoammeter/voltage source (Model Keithley 6487) and a tungsten halogen lamp set up.

2.2.6.3 Hall effect

The Hall effect determines the concentration and type (*n* or *p*) of charge carriers in semiconductors. The method is used in conjunction with a conductivity measurement to also determine the mobility of the charge carriers. Figure 2.5 shows the set up where an electric field is applied along the *x*-axis and a magnetic field is applied perpendicular along the *z*-axis. The force of a particle of charge q moving in a magnetic field *B* at velocity *v*,is given by the Lorentz force (Neamen, 2011):

$$F = qv_x \times B_z \qquad (2.12)$$

The electrons and holes flowing in the semiconductor along x-axis will experience the Lorentz force due to magnetic field. The electrons and holes deflects to the front side in (-*y*)-direction. For p-type semiconductor there will be a buildup of positive charge and for n-type there will be a buildup of negative charges. This charge creates an electric field in *y*-direction. This electric field is called the Hall field, which produces a voltage across the semiconductor from the Hall voltage is obtained. We can write

$$V_H = +E_H W \qquad (2.13)$$

E_H is assumed positive in (+*y*)-direction. In a *p*-type semiconductor (*p>>n*) the Hall voltage will be positive, and in a *n*-type semiconductor (*n>>p*) the Hall voltage will be negative. For that reason, the Hall voltage is used to determine the conductivity type.

To determine the carrier concentration in a semiconductor, it can be calculated using the relation:

$$n = - \frac{I_x B_z}{e d V_H} \qquad (2.14)$$

for electrons, and

$$p = \frac{I_x B_z}{e d V_H} \qquad (2.15)$$

for holes.

The electron mobility for a n-type semiconductor is calculated by:

$$\mu_n = \frac{I_x L}{e n V_x W d} \qquad (2.16)$$

The hole mobility for a p-type semiconductor is calculated by:

$$\mu_p = \frac{I_x L}{e p V_x W d} \qquad (2.17)$$
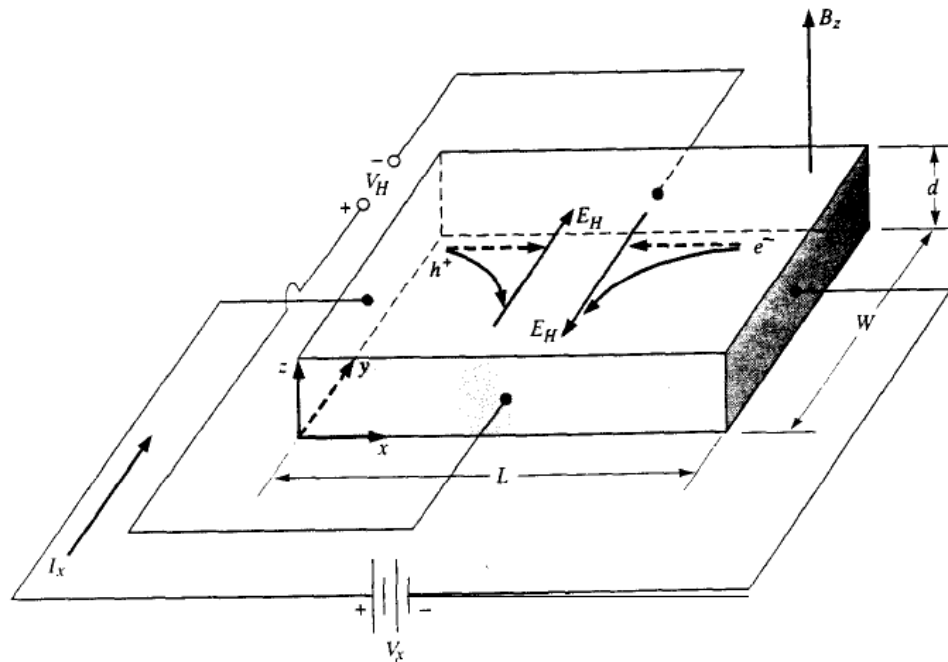
Figure 2.5 Set up to measure Hall effect

2.2.6.4 Current-Voltage characteristics

The electrical characterization of photovoltaic devices is performed measuring current-voltage parameters, plotting these values on a graph, the intersections on *x*-axis and *y*-axis gives the open circuit voltage (V_{oc}) and short circuit density (J_{sc}) respectively. Figure 2.6 shows a typical setup for measurement of the illuminated current-voltage curve using solar simulator under an AM1.5 spectrum. The voltage and current are usually measured during the voltage sweep, generally using the two point technique, in which two planar electrodes are connected in the bottom and top of the device.
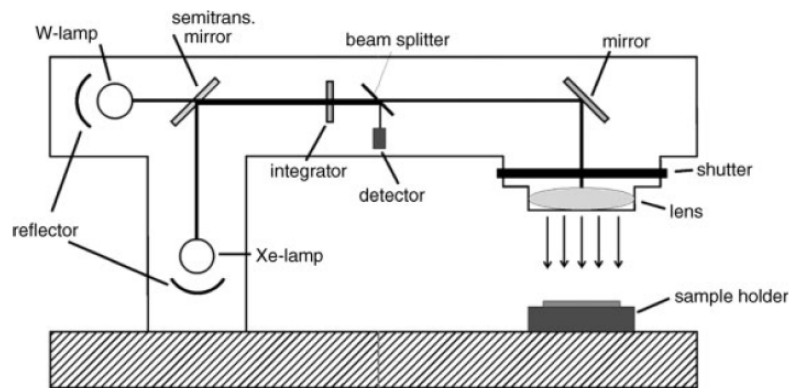
Figure 2.6 Schematic of solar simulator

The parameters obtained plotting the current-voltage curve are useful to calculate the fill factor (FF) and efficiency (η) of the device (eq. 1.24 and 1.25).

In this work, the J-V characteristics of the PV structures under dark and illumination conditions were measured using carbon/silver contacts. Illumination was performed by solar simulator (Oriel) under an AM1.5 radiation of intensity 100 mW/cm^2.

2.3 REFERENCES

AL-JASSIM, M. M., YAN, Y., MOUTINHO, H. R., ROMERO, M. J., DHERE, R. D. & JONES, K. M. 2001. TEM, AFM, and cathodoluminescence characterization of CdTe thin films. *Thin Solid Films,* 387**,** 246-250.

BIRKHOLZ, M. 2006. *Thin Film Analysis by X-Ray Scattering,* Weinheim, Wiley-VCH.

BUBE, R. H. 1960. *Photoconductivity of solids*, Wiley.

EZUGWU, S. C., EZEMA, F. I. & ASOGWA, P. U. 2010. Synthesis and characterization of ternary $CuSbS_2$ thin films: Effect of deposition time. *Chalcogenide Letters,* 7**,** 341-348.

FOX, M. 2010. *Optical Properties of Solids*, OUP Oxford.

GARCIA-ANGELMO, A. R., NAIR, M. T. S. & NAIR, P. K. 2014. Evolution of crystalline structure in SnS thin films prepared by chemical deposition. *Solid State Sciences,* 30**,** 26-35.

GONZALEZ, G., KRISHNAN, B., AVELLANEDA, D., CASTILLO, G. A., DAS ROY, T. K. & SHAJI, S. 2011. Modification of optical and electrical properties of chemical bath deposited CdS using plasma treatments. *Thin Solid Films,* 519**,** 7587-7591.

HODES, G. 2002. *Chemical Solution Deposition Of Semiconductor Films*, Taylor & Francis.

KAUFMANN, E. N. 2003. *Characterization of materials*, Wiley-Interscience.

LEAMY, H. J. 1982. Charge collection scanning electron microscopy. *Journal of Applied Physics,* 53**,** R51-R80.

MOULDER, J. F., STICKLE, W. F., SOBOL, P. E. & BOMBEN, K. D. 1992. *Handbook of X-ray Photoelectron Spectroscopy,* Eden Prairie, Minnesota, Perkin-Elmer Corporation.

NAIR, M. T. S. 1998. Chemically Deposited Sb2S3 and Sb_2S_3-CuS Thin Films. *Journal of The Electrochemical Society,* 145**,** 2113.

NEAMEN, D. 2011. *Semiconductor Physics And Devices*, McGraw-Hill Education.

PATHAN, H. M. & LOKHANDE, C. D. 2005. Chemical deposition and characterization of copper indium diselenide (CISe) thin films. *Applied Surface Science,* 245**,** 328-334.

QI, L., MAO, G. & AO, J. 2008. Chemical bath-deposited ZnS thin films: Preparation and characterization. *Applied Surface Science,* 254**,** 5711-5714.

RAU, U., ABOU-RAS, D. & KIRCHARTZ, T. 2011. *Advanced Characterization Techniques for Thin Film Solar Cells*, Wiley.

SADEWASSER, S., GLATZEL, T., RUSU, M., JÄGER-WALDAU, A. & LUX-STEINER, M. C. 2002. High-resolution work function imaging of single grains of semiconductor surfaces. *Applied Physics Letters,* 80**,** 2979-2981.

SESHAN, K. 2001. *Handbook of Thin Film Deposition Processes and Techniques*, Elsevier Science.

SHINDE, N. M., LOKHANDE, C. D., KIM, J. H. & MOON, J. H. 2012. Low cost and large area novel chemical synthesis of Cu_2ZnSnS_4 (CZTS) thin films. *Journal of Photochemistry and Photobiology A: Chemistry,* 235**,** 14-20.

SHOCKLEY, W. & QUEISSER, H. J. 1961. Detailed Balance Limit of Efficiency of p-n Junction Solar Cells. *Journal of Applied Physics,* 32**,** 510-519.

WASA, K. & HAYAKAWA, S. 1992. *Handbook of Sputter Deposition Technology: Principles, Technology, and Applications*, Noyes Publications.

WASA, K., KITABATAKE, M. & ADACHI, H. 2004. *Thin Film Materials Technology: Sputtering of Compound Materials*, Elsevier Science.

WILLIAMSON, G. K. & HALL, W. H. 1953. X-ray line broadening from filed aluminium and wolfram. *Acta Metallurgica,* 1**,** 22-31.

3
Cu-Sb and In chalcogenides: Novel materials for solar cell applications

This chapter focuses on the main research issues leading to the search of novel earth abundant materials for photovoltaic applications. The chapter begins with current research problems for the existing PV technology. To continue an overview and current status of copper antimony sulfide ($CuSbS_2$) and copper antimony sulfo-selenide ($CuSb(Se_x,S_{1-x})_2$), two of the earth abundant absorber materials for solar cells are presented. Further, the chapter includes the preparation and characterization of indium selenide thin films synthesized by laser annealing. This part seems quite different from the main topic of this thesis, but helps to understand the rapid process of annealing via laser and the scope of this method for synthesizing optoelectronic materials.

3.1 INTRODUCTION

As mentioned in chapter 1, the current thin film photovoltaic market is dominated by technologies based on CdTe and CIGS absorbers, having laboratory efficiencies achieved up to 20.4% (Solar) and 20.8% (Jackson et al., 2011) respectively. However, the scarcity, toxicity and high cost of some elements such as In, Te, Ga can limit the large scale production of photovoltaic devices.

Figure 3.1 shows the relative abundance and prices of some elements indicating a large abundance and low price for elements such as S, Cu, Zn, Sn and Sb compared to Ga, In and Te, which means that the combination to use these kind of elements to form absorber materials is of high feasibility for low cost and non-toxic photovoltaic devices.
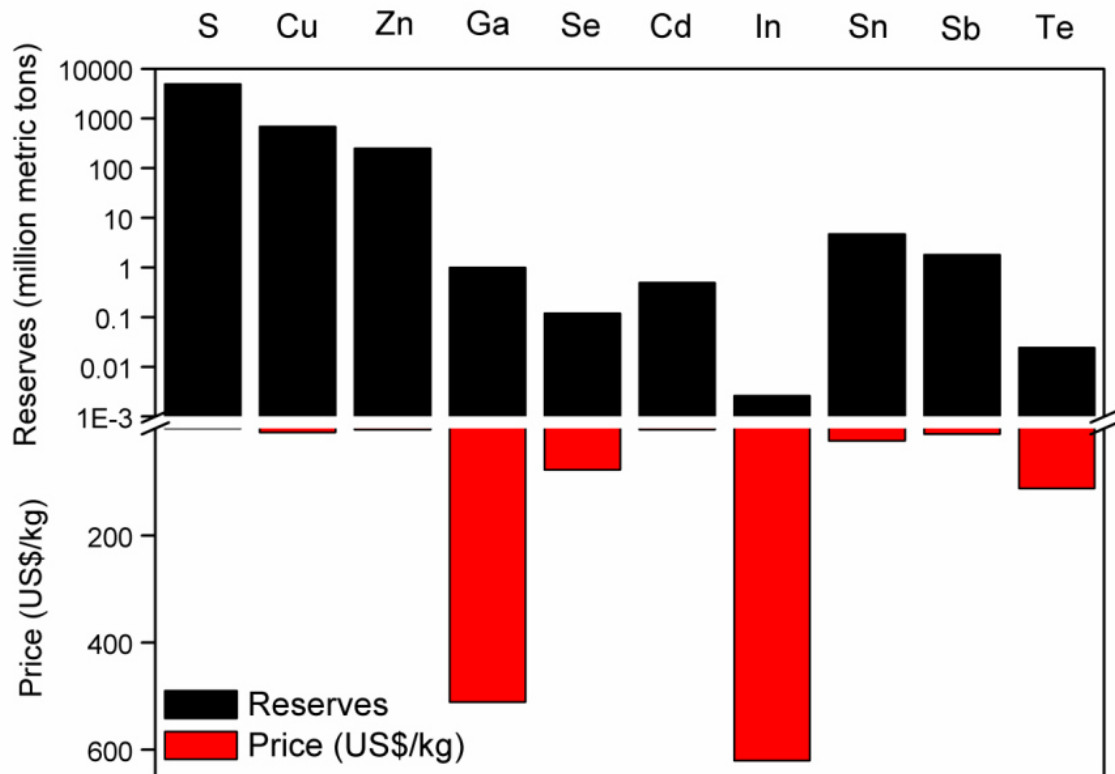
Figure 3.1Comparison on elemental abundance (reserves) and price of S, Cu, Zn, Ga, Se, Cd, In, Sn, Sb and Te (USGS, 2014)

Hence low-toxicity and earth abundant absorbers materials for thin film photovoltaics are intensively explored recently to reduce the cost of solar cells. Among these earth abundant materials, currently the copper zinc tin sulfo-selenide (CZTSSe) absorber thin film is the most promising in terms of device efficiency, achieving up to 12.6% for laboratory solar cell (Wang et al., 2013).

Another alternative absorber material for harvesting solar energy is chalcostibite $CuSbS_2$, which is proposed as a promising absorber material due to its direct optical band gap of 1.38~1.69 eV (Zhou et al., 2009, Rodríguez-Lazcano et al., 2005, Dufton et al., 2012), high optical absorption coefficient ($>10^4$ cm^{-1}) and the spectroscopic limited maximum efficiency (SLME) was calculated by Yu et al. having a value of 23% for this absorber material (Yu et al., 2013).

3.2 COPPER ANTIMONY SULFIDE (CuSbS$_2$) AND ITS ALLOY COPPER ANTIMONY SULFO-SELENIDE (CuSb(Se$_x$,S$_{1-x}$)$_2$)

CuSbS$_2$ is a less explored ternary chalcogenide in which the constituent metallic elements Cu and Sb are relatively abundant on the earth's crust and non-toxic as mentioned earlier. This material is proposed as promising absorber material for solar cells due to its direct optical band gap 1.38~1.69 eV (Zhou et al., 2009, Rodríguez-Lazcano et al., 2005, Dufton et al., 2012) and high optical absorption coefficient ($>10^4$ cm^{-1}).Figure 3.2 shows the calculated spectroscopic limited maximum efficiencies (SLME) for various materials of band gap (E$_g$ = 0.5-2.5 eV range) (Yu et al., 2013). From the figure, having a value of 23% for this absorber material, the SLME for CuSbS$_2$ is close to CuInSe$_2$ which is a well known thin film material achieving efficiency up to 20.8% when is combined with Ga in order to form Cu(In,Ga)Se$_2$(Jackson et al., 2011).
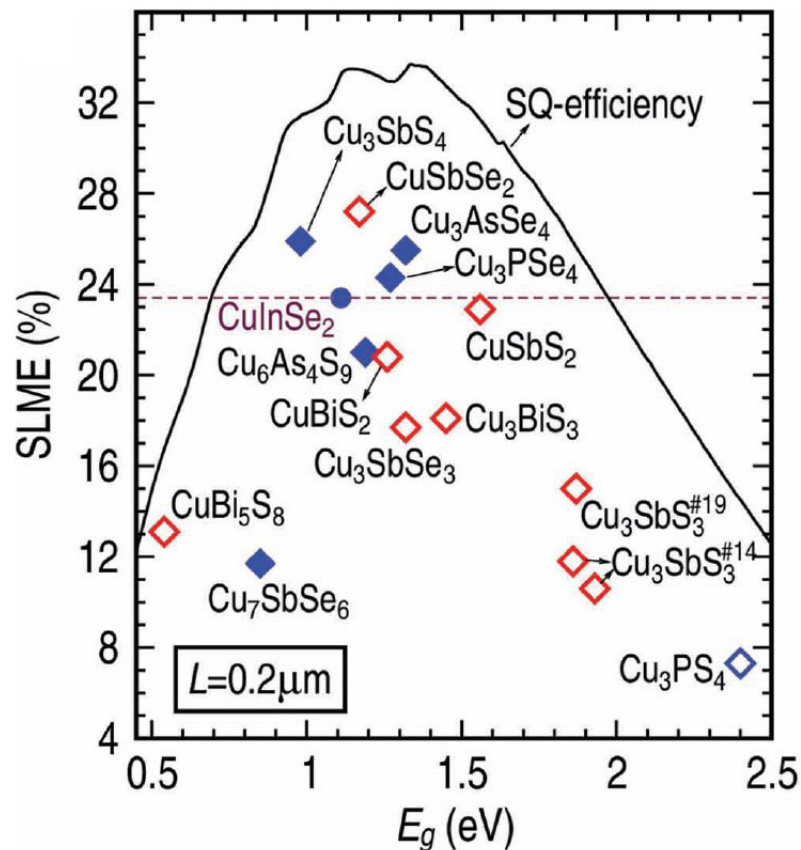
Figure 3.2 Calculated Spectroscopic Limited Maximum Efficiency (SLME) at a film thickness of 0.2 μm for group Cu-V-VI materials (Yu et al., 2013)

3.2.1 Crystal structure

$CuSbS_2$ crystallize in orthorhombic layered structure (Pnma; space group 62) (Figure 3.3), with a unit cells containing total 16 atoms with 4 Cu, 4 Sb and 8 S atoms. The calculated lattice parameters are a = 6.045 Å, b = 3.807 Å and c = 14.545 Å (Kumar and Persson, 2013). The layered structure could have some advantages, one of them is the structural stability and other one is in forming the interface structures comparing with other structural forms (Nguyen et al., 2013).
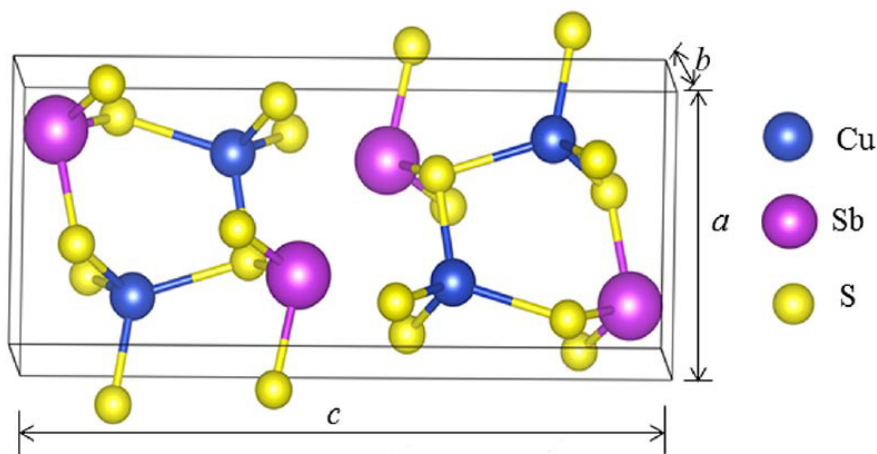
Figure 3.3 Crystal structure of $CuSbS_2$ (Reproduced with kind permission from Springer)

Several deposition techniques have been used to prepare $CuSbS_2$ thin films, which are described as follows.

3.2.2 Physical process

3.2.2.1 Thermal evaporation

$CuSbS_2$ powder made from an ingot prepared using high purity Cu, Sb and S (Rabhi et al., 2008) wasthermal evaporated to form $CuSbS_2$ thin films. The thin films were annealed at temperature of 130 °C – 200 °C in vacuum for 2 h to form samples of thickness 135-280 nm. Their XRD results showed amorphous phase below 200 °C; at 200 °C showed polycrystalline structure with the presence of Sb_2S_3 as a secondary phase. Isolated particle growths at the

surface corresponding to a Cu rich phase for anneal below 200 °C and Sb rich phase for anneal at 200 °C. The optical band gap was calculated as 1.3 eV. The electrical measurements showed low resistivity for samples formed below 200 °C ($10^{-2}\Omega\cdot$cm) and high resistivity for samples annealed at 200 °C ($2\ \Omega\cdot$cm).

Further, instead of vacuum annealing, the substrate temperature (T_s) was varied from 100 °C to 200 °C (Rabhi et al., 2009) decreasing thickness of the film by increasing substrate temperature, from 290 nm to 190 nm. At $T_s<$ 170 °C the thin film was amorphous and the film was smooth and no isolated particles were observed at the surface. At $T_s>$ 170 °C the thin films crystallized in orthorhombic $CuSbS_2$. EDX analysis revealed at $T_s>$ 170 °C there were sulfur poor layers due to the evaporation of sulfur at high substrate temperature decreasing the film thickness. The optical band gap and resistivity varied with substrate temperature (25 °C – 200 °C) obtaining values of 1.89 - 0.91 eV and 0.03 – 0.96 $\Omega\cdot$cm, respectively.

Sulfurization of sequentially evaporated Sb and Cu in a stacked layers in a tubular furnace in the presence of excess sulfur (0.1 g) was reported (Colombara et al., 2011). The anneal temperature was in the range of 200 °C - 400 °C for 30 min. For films annealed at 200 °C and 250 °C Cu reacts with sulfur to form CuS. Annealing at 300 °C, CuS and Sb still remained and a part of Sb reacted with sulfur to form Sb_2S_3. At 350 °C - 400 °C, interdiffusion of the elements lead to the formation of chalcostibite $CuSbS_2$. The optical band gap was calculated as 1.5 eV and when the samples were dipped in 5% KCN solution for 60 s or more, the magnitude of photoresponse was high. Also, $CuSbS_2$ thin films were p-type semiconductor.

3.2.2.2 Reactive sintering

One method for the preparation of $CuSbS_2$ in bulk were performed mixing CuS and Sb_2S_3 powders in a conventional ball milling, sintering this powders at

different temperatures from 350 °C to 500 °C for 2 h (Wubet and Kuo, 2014). The electrical properties of the pellets showed that increasing sintering temperature from 350 °C to 400 °C the carrier concentration, mobility and conductivity increases, meanwhile for higher temperatures the electrical properties decay. The best electrical parameters were obtained sintering at 400 °C with conductivity and mobility values of 15 $(\Omega \cdot cm)^{-1}$ and 20 cm^2/Vs, respectively.

3.2.3 Chemical process

3.2.3.1 *Electrodeposition and sulfurization*

Colombara et al., deposited thin films of $CuSbS_2$ by electrodeposition of Sb-Cu alloy using $SbCl_3$ and $CuSO_4$(Colombara et al., 2011). The films were annealed in a tubular furnace in the presence of excess sulfur (0.1 g) at temperature in the range 200 °C - 400 °C for 30 min. For films annealed at 200 °C - 250 °C CuS phase was observed and for those annealed at 300 °C appears CuS, Sb, Sb_2S_3 and $CuSbS_2$ phases. At 350 °C - 400 °C, only chalcostibite $CuSbS_2$ was present. Below 350 °C the electroplated films showed a characteristic surface covered by idiomorphic crystals that were identified as CuS. Above 350 °C the samples showed a compact film with grain size close to 1 µm. The optical band gap was calculated as 1.5 eV and the samples were dipped in KCN solution as reported earlier increasing the photoresponse. Also, $CuSbS_2$ thin films showed p-type conductivity.

Wilman Septina et al. used a stacked metal layers deposited by electrodeposition of copper and antimony. The first condition was sulfurized stacked layers at 450 °C for 30 min and a second condition was annealed the stacked layers at 510 °C for 60 min in Ar atmosphere and sulfurized at 450 °C for 30 min to obtain $CuSbS_2$ thin films (Septina et al., 2014). Using the first condition they obtained $CuSbS_2$ and Sb_2S_3 as a secondary phase, and an

unidentified peak at 44.5° and the morphology showed the formation of densely packed microsized grains and some pinholes between grains. Using the second condition, only the $CuSbS_2$ phase was obtained along with the unidentified peak at 44.5° and they had a dense morphology and relatively large and homogenous grain sizes without pinholes. They fabricated photovoltaic devices using substrate configuration of Glass/Mo/$CuSbS_2$/CdS/ZnO:Al, depositing $CuSbS_2$ by electrodeposition and immerse in KCN solution (10%) for 2 min in order to clean surface, CdS layer was obtained by the chemical bath deposition, whereas ZnO:Al by RF magnetron sputtering. Using the first condition, the photovoltaic parameters were J_{sc} = 10.27 mA/cm^2, V_{oc} = 370 mV, FF = 33% and η = 1.24%. For the second condition, the photovoltaic parameters were J_{sc} = 14.73 mA/cm^2, V_{oc} = 490 mV, FF = 44% and η = 3.13%. The presence of an unidentified peak observed in XRD shows the incomplete formation of ternary $CuSbS_2$and the lack of information about the contact area of the solar cell suggests and questions about the high short current density and efficiency obtained.

3.2.3.2 Chemical bath deposition (CBD)

$CuSbS_2$ thin films were prepared by annealing of stacked layers deposited by CBD of Sb_2S_3 and CuS (Rodríguez-Lazcano et al., 2001). The annealing temperature was in the range 350 °C – 400 °C for 30 min and 1h under nitrogen atmosphere. The chalcostibite structured $CuSbS_2$ thin film was of 500 nm in thickness and was formed at 350 °C and 400 °C. The optical band gap was calculated as 1.52 eV and the conductivity values were in the range of 10^{-4}-$10^{-3}(\Omega \cdot cm)^{-1}$. Also, they fabricated photovoltaic device using superstrate p-i-n configuration of glass/SnO_2:F/(n)CdS:In/(i)Sb_2S_3/(p)$CuSbS_2$. The n-type layer CdS was deposited by CBD having a thickness of 60 nm, then an In layer of 8 nm was thermally evaporated, after that, the layers were annealed at 250 °C in air, then Sb_2S_3 of 100 nm was deposited by CBD and after was annealed at 300 °C for 1 h in nitrogen, finally the stacked Sb_2S_3-CuS was deposited by CBD having a thickness of 500 nm and after annealed at 350 °C to form the complete

p-i-n structure (Rodríguez-Lazcano et al., 2005). The photovoltaic parameters of J_{sc} and V_{oc} were 0.2 mA/cm^2 and 345 mV respectively.

A one step CBD using SbCl$_3$, acetone, Na$_2$S$_2$O$_3$ and CuCl$_2$ at room temperature for 1 h, 1.5 h, 3 h and 3.5 h was performed to deposit CuSbS$_2$ thin films (Ezugwu et al., 2010). The thickness was dependent on deposition time, varying from 600 nm to 850 nm when deposition time increased. The XRD results revealed a poor crystallinity of the films. The optical band gap varied from 1.3 eV to 2.3 eV with deposition time. Due to poor crystallinity the thin films were not suitable for application in PV device.

3.2.3.3 Spray Pyrolysis

CuSbS$_2$ thin films were deposited by spray pyrolysis using as precursors CuCl$_2$·2H$_2$O, antimony (III) acetate and thiourea in aqueous solution. During the spraying the carrier gas was Ar, the distance between nozzle and heater was fixed at 27 cm. The substrate temperature was 240 °C and antimony precursor weight ratio was varied from 2.57 to 6.86 (Manolache et al., 2007). Orthorhombic CuSbS$_2$ having a crystallite size of 49-88 nm was formed. Increasing antimony amount, the films transformed from grain aggregates with fiber texture in films with porous morphology. They attempted to fabricate a 3D cell using a configuration of TCO/dense TiO$_2$ (anatase)/nanoporous TiO$_2$ (anatase)/CuSbS$_2$ (absorber)/Au, could not obtain results in the photovoltaic performance under illumination.

CuSbS$_2$ thin films were deposited on FTO conductive glass by spray pyrolysis using CuCl$_2$·2H$_2$O, antimony (III) acetate and thiourea as precursors, small addition of HCl for insuring solubility of antimony acetate. Two polymeric additives, sodium maleate-methyl metacrylate (hydrophilic polymer- HFL) and sodium maleate-vinyl acetate (hydrophobic polymer- HFB) were used for completing the complexion effect of thiourea (Popovici and Duta, 2012). The

substrate temperature was fixed at 240 °C, the carrier gas air and the spraying height (25 cm). A variation of copper and antimony precursors was performed, and selected two samples to vary the polymeric additives. In all selected samples, formation of $CuSbS_2$, Cu_3SbS_4 and $Cu_3SbS_3$was present. The crystallite size was in the range of 140-210 nm. The roughness measured by AFM showed a RMS for samples without additive of 193 nm, RMS of sample with HFL and HFB additives of 138 nm and 152 nm. The use of polymeric additives resulted in a densification of the films to decrease grain size. The use of polymeric additives promoted the formation of Cu_3SbS_4 and Cu_3SbS_3 phases without any binary secondary phases, leading to understand that the use of polymeric additives are not good way to improve the structure and properties of single $CuSbS_2$.

3.2.3.4 Spin Coating

Bo Yang et al. used spin coating for deposition of $CuSbS_2$ thin films. Cu and S powders as well as Sb and S were dissolved in anhydrous hydrazine to produce Cu-S and Sb-S solutions at room temperature (this process is called "hydrazine process"). They prepared a Cu-Sb-S solution mixing Cu-S and Sb-S solutions followed by stirring before spin-coating. The Cu-Sb-S was spin coated onto FTO substrate and was annealed at 250 °C for 3 min to eliminate excess of hydrazine and sulfur. XRD peaks of Sb_2S_3 and $CuSbS_2$ phases and poor quality of the film with voids (cracks and pinholes) and small grain size (100 nm) were present. After that, the thin film was annealed at 350 °C for 10 min to promote grain growth, obtaining completely $CuSbS_2$ orthorhombic structure and the morphology showed compact film with large grains (1 µm) (Yang et al., 2014). They measured the high resolution core level spectra using XPS, and they obtained the binding energies for Cu $2p_{3/2}$, Cu $2p_{1/2}$, Sb $4d_{5/2}$, Sb $4d_{3/2}$, S $2p_{3/2}$ and S $2p_{1/2}$ in values of 932.6 eV, 952.3 eV, 33.0 eV, 34.2 eV, 161.4 eV and 162.6 eV respectively. The optical band gap was calculated from transmittance spectra having a value of 1.4 eV. The resistivity, mobility and

carrier concentration were measured using the Hall effect and the values were 4.8 x $10^2 \Omega \cdot$cm, 49 cm^2/Vs and 2.66 x 10^{18} cm^{-3} respectively. Also, they fabricated a photovoltaic device using a substrate configuration of FTO/CuSbS$_2$/CdS/ZnO/ZnO:Al/Au, where CdS was deposited by CBD, ZnO and ZnO:Al by magnetron sputtering and Au electrodes by thermal evaporation. The photovoltaic parameters obtained were J$_{sc}$ = 3.65 mA/cm^2, V$_{oc}$ = 440 mV, FF = 31% and η = 0.5%. Additional analysis using density functional theory (DFT) calculations, they reported the defect physics of CuSbS$_2$ with extremely low concentration of recombination center defects. It was established that CuSbS$_2$ is a p-type semiconductor due to dominant Cu vacancy (V$_{Cu}$) which is a shallow acceptor that can be ionized easily and generate free hole carriers at room temperature and has the lowest energy formation. This research group provided detailed theoretical information of CuSbS$_2$ to understand the behavior of this material in order to find alternatives that improve the performance of the solar devices using CuSbS$_2$ as absorber material.

3.2.3.5 *Chemical bath deposition and thermal evaporation*

Previous research works used a single deposition technique for the formation of CuSbS$_2$ thin films, some of them annealing in sulfur atmosphere to complete the entire process. The combination of two different deposition techniques such as thermal evaporation and chemical bath deposition is an option to obtain good quality thin films with great properties (Hurtado et al., 2014, Hibberd et al., 2009).

In our laboratory in a pioneer work by Garza et al., it was prepared CuSbS$_2$ thin films by annealing stacked layers of Sb$_2$S$_3$ (300 nm) and Cu (variation of Cu thickness of 10, 20, 30, 40 and 50 nm) deposited by CBD and thermal evaporation respectively. The thin films were annealed at 300 °C and 380 °C in vacuum for 1h and 2 h (Garza et al., 2011). Orthorhombic CuSbS$_2$ was formed along with Cu$_2$S as a secondary phase. The morphology showed a uniform surface with spherical particles of 200 nm. The calculated optical band gap was

~1.5 eV. From the Hall measurement data, conductivity, carrier concentration and mobility values were in the range of 60-0.5 $(\Omega \cdot cm)^{-1}$, 10^{18}-10^{20} cm^{-3}, 10^{-1}-10^{-3} cm^2/Vs, respectively. No photovoltaic device was fabricated using these $CuSbS_2$ thin films. This work was focused to synthesize $CuSbS_2$ thin films by varying Cu thickness for chemically deposited Sb_2S_3 of given thickness.

3.2.4 Copper Antimony Sulfo-Selenide ($CuSb(Se_x,S_{1-x})_2$)

Most of the reports on chalcostibite thin films are focused on the preparation of ternary $CuSbS_2$. Sulfide and sulfoselenide based compounds offers a wide range of properties that are suitable to use in materials for solar cells. Alloying this compound with Se in solid solution leads to form a quaternary $CuSb(Se_x,S_{1-x})_2$. As the Se content increases, the band gap of the compound can be shifted from 1.5 eV for $CuSbS_2$ to 1.2 eV for $CuSbSe_2$(Colombara et al., 2011). The kesterite alloys $Cu_2ZnSn(S_{1-x}Se_x)_4$ have the same behavior of changing its band gap from 1.5 eV at x=0 (sulfide) to 0.96 eV at x=1 (pure selenide). Also alloying with high Se concentration the kesterites have shown higher efficiency than those with low Se content because the former can be converted more easily to n-type at the surface of the p-type absorber, facilitating the electron-hole separation of photogenerated carriers (Chen et al., 2011), thus the highest solar cell efficiency of 12.6% achieved for CZTSSe alloys with high Se concentration (Wang et al., 2013). So far, there is no report on the preparation of $CuSb(Se_x,S_{1-x})_2$, except Maiello et al. obtained a different phase, $Cu_3Sb(S_{1-x},Se_x)_3$ by chalcogenisation of Cu-Sb metallic precursors deposited by DC magnetron sputtering, obtaining an optical band gap of 1.38 eV for an atomic ratio of x=0.49 (Maiello et al., 2013). The implementation of this material into photovoltaic devices showed a low photovoltaic performance.

From this background of Cu-Sb sulfide and sulfo-selenide based compounds, it was found the lack of some issues such $CuSbS_2$ material with good optical

and electrical properties, formation of $CuSb(Se_x,S_{1-x})_2$ thin films and photovoltaic devices with good performance.

Motivated by these results, the present research work is focused in the process to obtain $CuSbS_2$ thin films using a combination of deposition methods of CBD and thermal evaporation which are relatively low cost and less toxic methods. Besides, such $CuSbS_2$ the thin films were incorporated to photovoltaic devices using a superstrate configuration of CdS as window layer, C/Ag as electrodes. Also,$CuSb(Se_x,S_{1-x})_2$ thin films will be prepared using CBD and thermal evaporation. Photovoltaic devices will be fabricated using $CuSb(Se_x,S_{1-x})_2$ as absorber material. Details of this process are explained in chapter 4.

3.3 INDIUM SELENIDE (In_6Se_7)

Indium selenide (In_6Se_7) belongs to III-VI class of compound semiconductors which exists in different stoichiometry such as InSe, In_2Se_3, In_4Se_3, In_9Se_{11}, In_5Se_7 and In_6Se_7. Among these, In_6Se_7 was reported as one of the most stable phases (Okamoto, 2004). In_6Se_7 thin films have been found promising to potential application in photovoltaic devices (Gordillo and Calderón, 2003) and other optoelectronic devices (Hirohata et al., 2006). Several techniques have been used for the preparation of indium selenide thin films such as thermal evaporation (El-Kabnay et al., 2008), spray pyrolysis (Bouzouita et al., 2002), metal-organic chemical vapor deposition (MOCVD) (Afzaal et al., 2005), pulse laser deposition (PLD) (Hrdlicka et al., 2007), sol-gel (Mutlu et al., 2007), electrodeposition (Gopal et al., 2004), chemical bath deposition (CBD) (Asabe et al., 2008) and hybrid methods combining CBD of Se and thermal evaporation of In were used for the synthesis of In_2Se_3(Bindu et al., 2002) and In_6Se_7(Ornelas et al., 2012). Most of these techniques involve a thermal treatment of the precursor materials in a conventional furnace, which produce a slow annealing process. In order to reduce the time of annealing which contribute to reduce

energy cost, one alternative is the use of rapid annealing process via continuous wave laser irradiation.

Laser processing has been extensively used in the optoelectronic device industry due to the technological applications of photo-induced modifications of structure and morphology of various important semiconductor thin film materials (Sreekumar et al., 2008, Shaji et al., 2010). Laser annealing processes have been found promising to improve performance of display and photovoltaic devices (Mastio et al., 2000, Wang et al., 2005). The mechanism by which continuous wave laser annealing takes place has been clearly identified as transient local heating of the sample, incident radiation is absorbed and converted to lattice heat(Cullis, 1985), in this case the sample is transiently heated by the beam to a temperature below the melting point and annealing takes place in the solid phase. Laser irradiation on materials offers a localized high temperature with excellent annealing selectivity to the under layers or substrate for a rapid process and a precise control of the heating time and zone (Kim et al., 2013).

3.3.1 Experimental procedure

Indium layer was deposited by thermal evaporation of 99.999% pure indium wire on well cleaned microscopic glass substrates loaded in a high vacuum system (TE12P, Intercovamex) at pressure of 10^{-5} Torr. The layer thickness was in situ measured using a quartz crystal thickness monitor installed in the evaporation system. Indium layer of 20 and 30 nm in thickness were deposited. Indium coated samples were dipped in an aqueous solution containing 10 ml of sodium selenosulphate (0.1 M), 1.0 ml acetic acid (25%) and 70 ml distilled water during 5 minutes for the deposition of selenium. Three coatings of selenium were done, drying the thin film using warm air after each dip. The layered structures of Glass/In/Se thin films were irradiated at selenium coated side by a 532 nm continuous laser (DPSS MGL W-532) of power 7 W at room temperature for 3, 4 and 5 minutes. To produce samples of sufficient quantity for

analysis, the laser beam was expanded using a concave lens and the samples were fixed at a distance of 17.8 cm from the lens so that the irradiated sample region was 0.8 cm in radius. The power density for the expanded beam was 3.5 W/cm^2. The as prepared films were labeled as IS20 and IS30 for 20 nm and 30 nm of indium thickness. The irradiated thin films were labeled as IS20-3, IS20-4, IS20-5 for samples of 20 nm of indium and IS30-3, IS30-4, IS30-5 for samples of 30 nm of indium, irradiated at 3, 4 and 5 minutes respectively.

These thin films were characterized using X-ray diffraction (XRD), scanning electron microscope (SEM), X-ray photoelectron spectroscopy (XPS),optical and electrical properties. The photoconductivity of the thin films was detected using a solar simulator.

3.3.2 Characterization

Figure 3.4shows the XRD patterns recorded for triply dipped selenium coated indium of 30 nm thickness (IS30-3, IS30-4, IS30-5) irradiated for 3, 4 and 5 minutes respectively. From the figure, in IS30-3 a dominant peak corresponding to (101) plane of metallic indium (PDF#05-0642) is present. In sample IS30-4 the intensity of metallic indium peak decreases with the evolution of two feeble peaks of monoclinic In_6Se_7 (PDF#25-0385) labeled as (-212) and (-304) in the Figure 3.4. In sample IS30-5, the intensity of indium peak is reduced to less than 30% as that of 3 min irradiated sample, while the In_6Se_7 peaks indexed by (-212), (-304) and (-206) became more distinct.   This indicates the formation of crystalline indium selenide as the laser time increases. These results demonstrates the rapid process of diffusion and reaction of selenium into indium at short times of annealing, providing a good alternative to produce crystalline thin films.
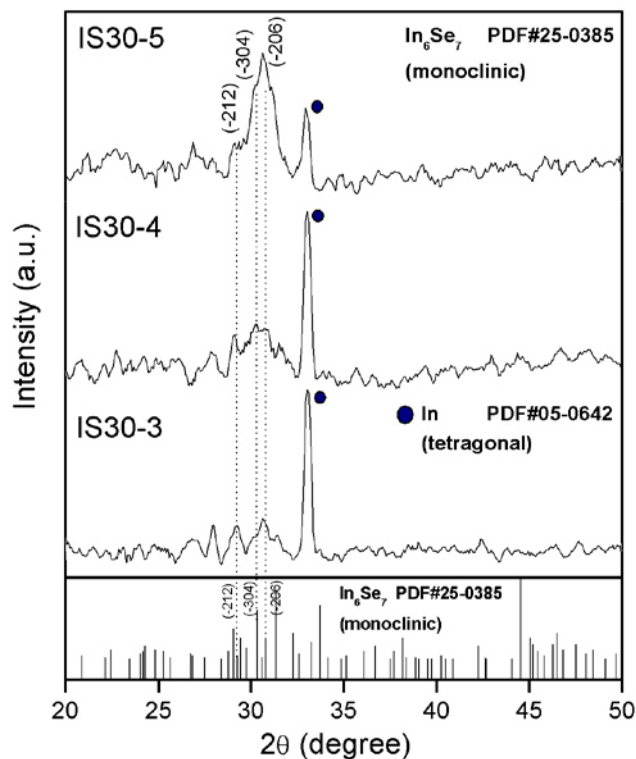
Figure 3.4 XRD patterns for 30 nm indium layer coated with three dip selenium and irradiated using 532 nm laser of power density 3.5 W/cm^2 (IS30-3, IS30-a, IS30-5) at 3, 4 and 5 min respectively. Standard pattern corresponding to monoclinic In$_6$Se$_7$ is given. (Reproduced with kind permission from World Scientific)

The morphological features of the as prepared and the irradiated thin films are illustrated in scanning electron micrographs as given in Figure 3.5. The as-deposited In/Se thin film IS20 showed elongated grains of average size 300 nm uniformly distributed on the surface (Figure 3.5a). In the case of sample IS30, grains were longer of average size 500 nm as observed in Figure 3.5d. These elongated grains were that of selenium layer. For the laser irradiated thin films, donut shaped grains having concave centers were seen as given in the figure. This type of feature was reported for In$_6$Se$_7$ thin films produced by thermal annealing of In/Se thin films (Ornelas et al., 2012). Also, by comparing with the XRD results, this donut shaped morphology could be due to the formation of In$_6$Se$_7$ after the irradiation. Moreover, in the present case, laser irradiation resulted in a distinct growth of spherical particles filling the concave centers, giving 'flower like' morphology for the thin films. These spherical particles of size in a scale of 50-100 nm appears, as shown in Figure 3.5 (b), (c), (e) and (f) were

associated to dewetting phenomenon in which the film break-up into droplets during the melting process induced by laser irradiation(Henley et al., 2007). Also, the grains were connected by well-defined channels as observed in Figure 3.5 (b), (c), (e) and (f). For further analyses, we selected IS30-5 sample, being the best among all, consisting of distinct XRD peaks of In_6Se_7.
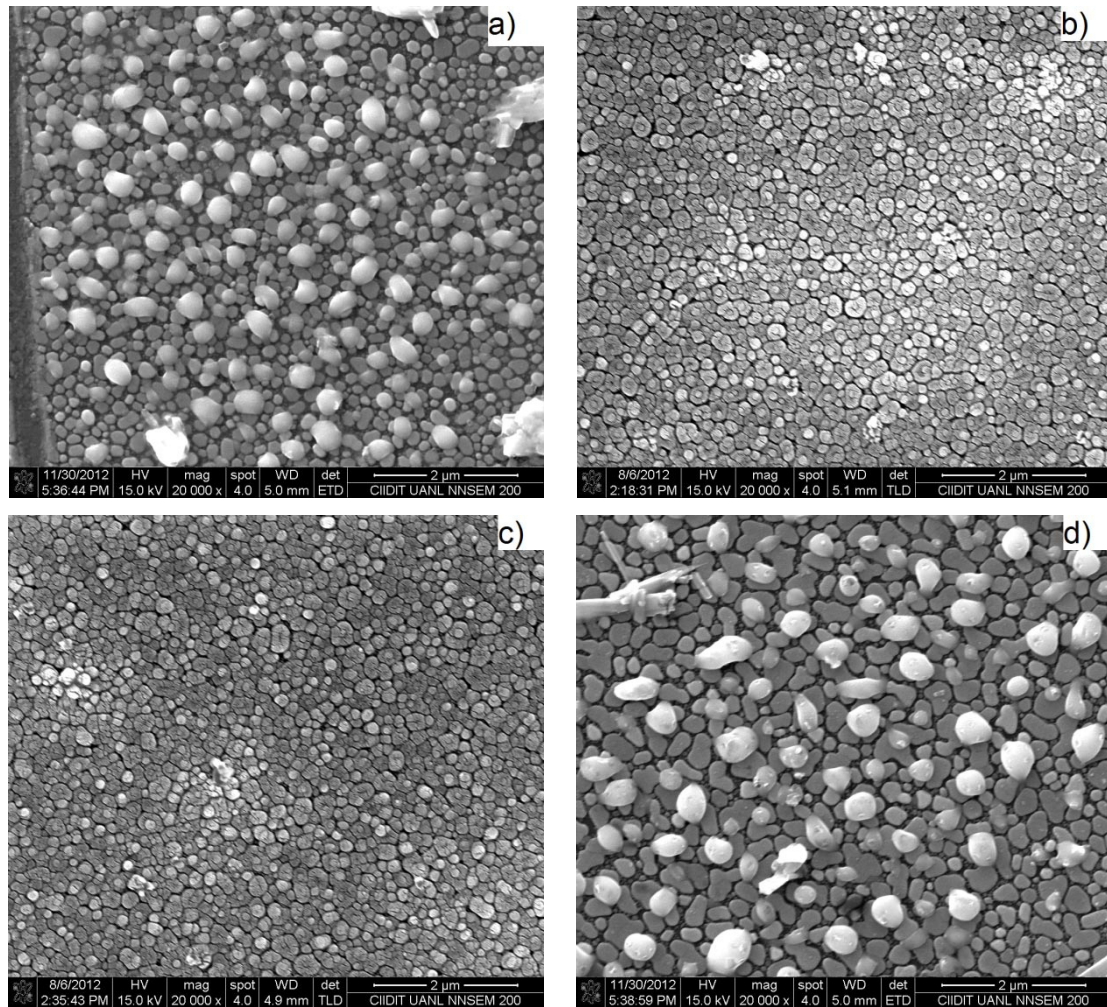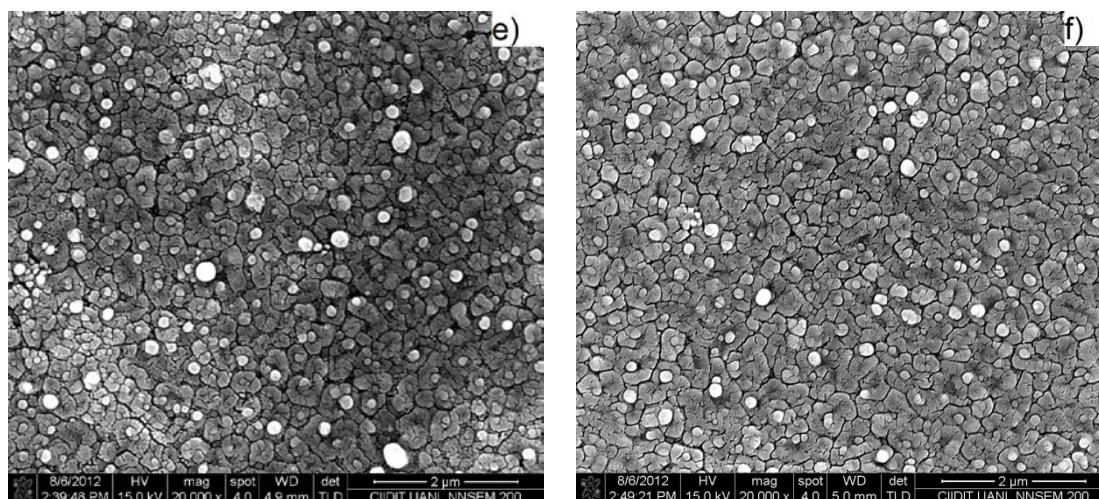
Figure 3.5 SEM for as prepared and irradiated thin films using 532 nm laser of power density 3.5 W/cm^2 (a) IS20 as prepared sample, (b) IS20-3 and (c) IS20-5; samples 20 nm of indium thickness irradiated during 3 and 5 min, respectively, (d) IS30 as prepared sample, (e) IS30-3 and (f) IS30-5; samples 30 nm of indium thickness irradiated during 3 and 5 min, respectively. (Reproduced with kind permission from World Scientific)

Compositional analysis of IS30-5 was done using XPS. A typical survey spectrum recorded from the surface of the thin film is shown in Figure 3.6a, which indicates the presence of In, Se, O and C. For the detailed analysis, a narrow scan was done for all these elements, after one cycle of etching using Ar$^+$ ions generated at 1 keV for 30 seconds. Figure 3.6bshows the In 3d core level spectrum where the binding energy (BE) values for In $3d_{5/2}$ and In $3d_{3/2}$ are 444.3 eV and 451.9 eV respectively with a doublet splitting of 7.6 eV. The BE values showed a chemical shift from corresponding elemental state of In (443.9 eV and 451.4 eV)(Moulder et al., 1992) , implying a compound formation. Figure 3(c) shows the Se $3d_{5/2}$ and Se $3d_{3/2}$ core level peaks located at 53.6 eV and 54.4 eV and doublet splitting of 0.8 eV. In the elemental state, Se 3d B.E values are at 55.6 eV and 56.4 eV(Moulder et al., 1992). The BE values of Se in the present sample showed a chemical shift of 2.0 eV. These results indicated that due to laser irradiation, In and Se reacted to form indium selenide. Even though the BE values obtained were close to those reported for In_2Se_3 (443.8 eV and 451.3 eV) 9(Afzaal et al., 2005), we assigned the values for In_6Se_7, in agreement with our XRD results.
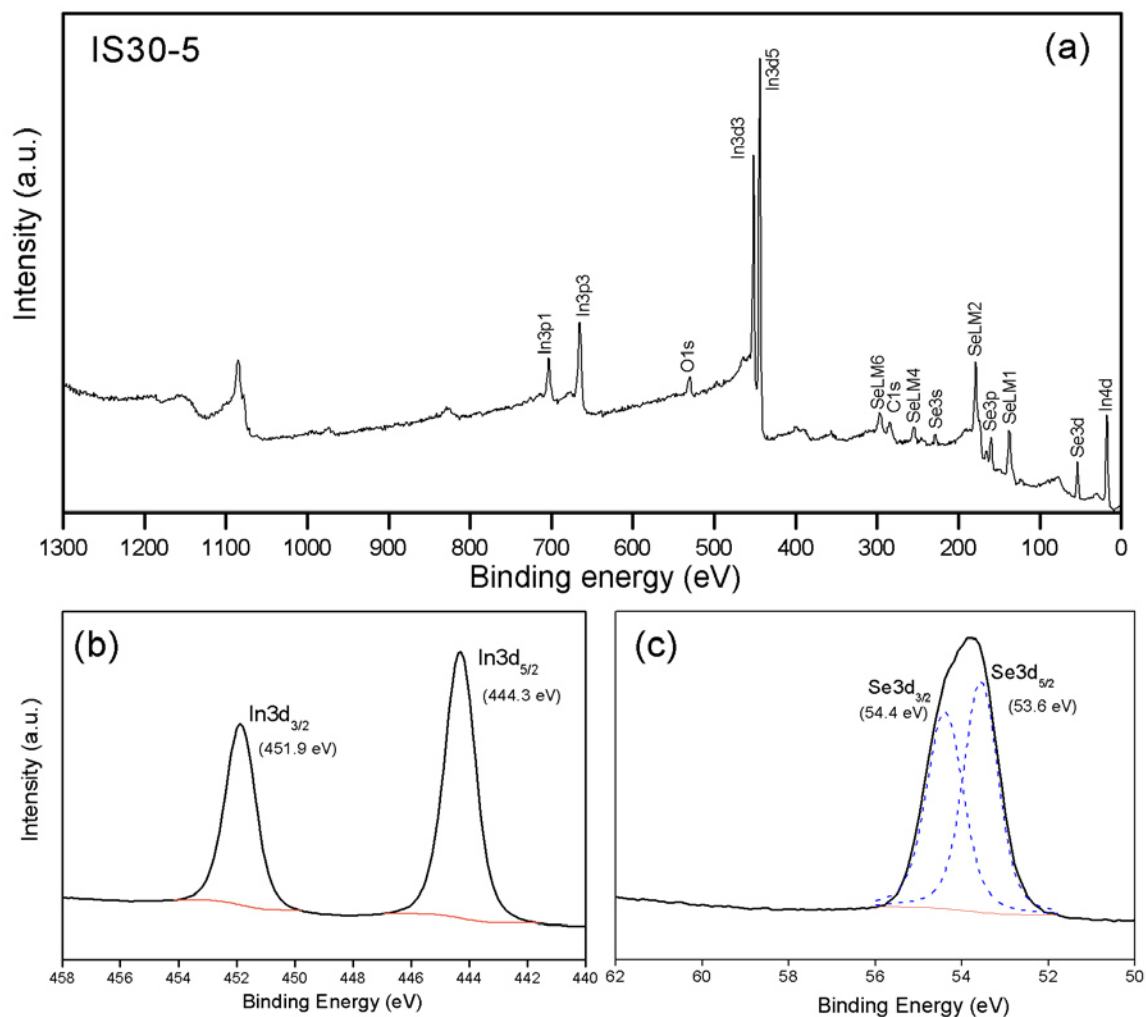
Figure 3.6 (a) XPS survey spectra, (b) high-resolution spectra of In3d core level, (c) high-resolution spectra of Se3d core level of IS30-5 sample (Reproduced with kind permission from World Scientific)

The depth profile analysis of the samples is shown in the XPS profile montage given in Figure 3.7a, where In 3d, Se 3d and Si 2p core levels are present. Si 2p levels were from the glass substrate. Presence of In 3d and Se 3d peaks throughout the depth from the surface to the substrate showed the interlayer diffusion and reaction of In and Se to form indium selenide due to the laser irradiation. Further, close to substrate, the B.E values of In 3d doublets coincided with that of metallic indium, which supported the XRD results. We did not find any oxygen except at the surface due to contamination in air. The depth profile of relative composition for the sample was given in Figure 3.7b. From the

figure, we observed that the relative compositions of indium and selenium were uniform throughout the thin film thickness as marked in the figure.
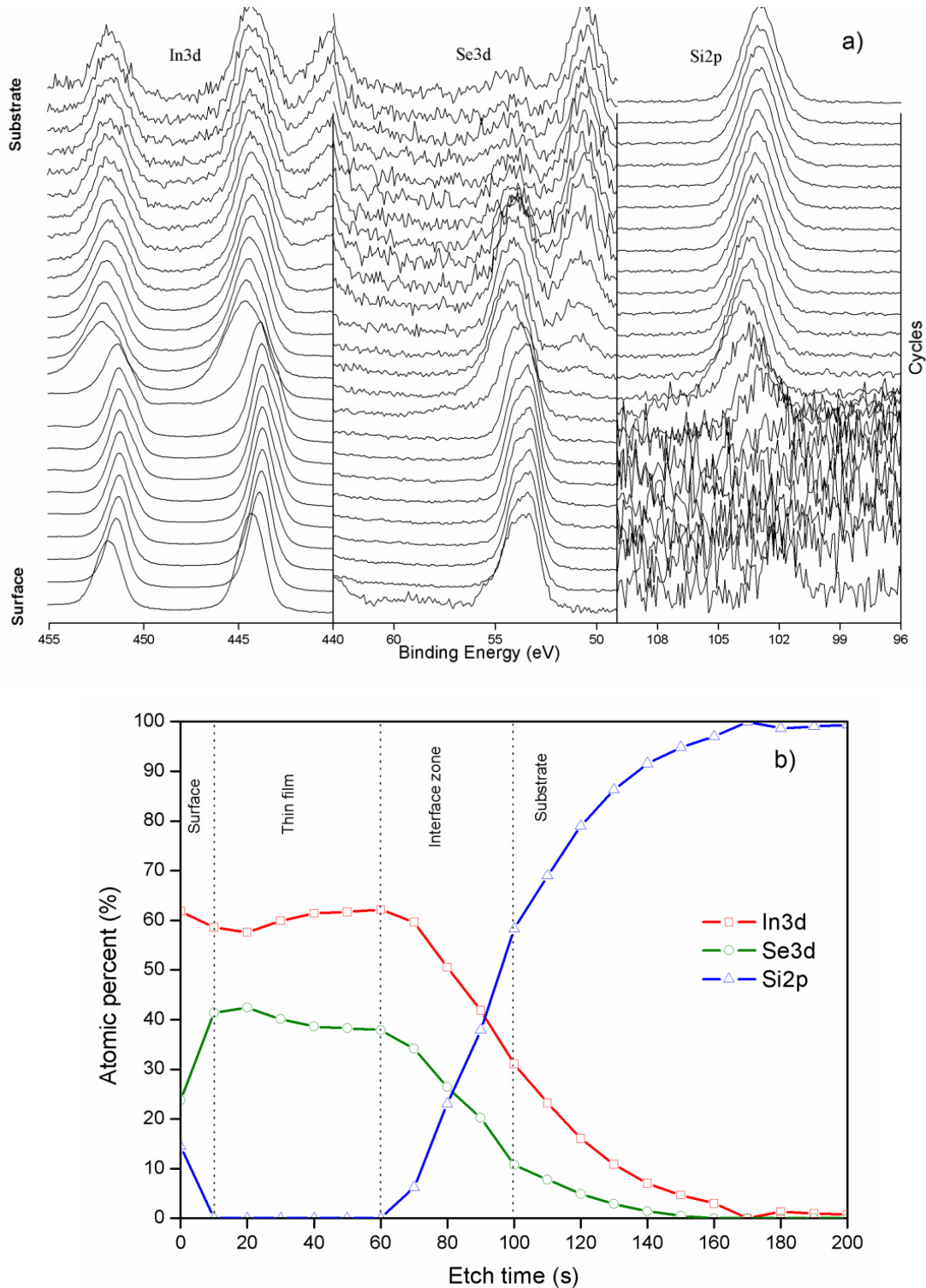
Figure 3.7 (a) XPS profile montage, (b) depth profile for compositional analysis of irradiated IS30-5 thin film. (Reproduced with kind permission from World Scientific)

Figure 3.8a and b show the optical transmittance (%T) and reflectance (%R) spectrum of indium selenide thin film (IS30-5) in the wavelength range of 300-1100 nm. In the non-absorbing region an average of 55% transmittance and 45% reflectance were observed. From this spectrum, it was evaluated absorption coefficient for the indium selenide thin film using eq. 2.7.Figure 3.8c shows the calculated absorption spectra (α vs hν) of the indium selenide laser annealed thin films. The band gap value of the thin film was determined using eq. 2.8. Figure 3.8d illustrates the plot of $(\alpha h\nu)^n$ vs hν (Tauc plot) for the sample IS30-5 giving good linear fit for n=2. This imply that the fundamental optical absorption in In_6Se_7 thin films was dominated by direct allowed transition, with an onset of absorption resulting in a α value of 10^5 cm^{-1}. From the curve, the value of band gap was estimated by extrapolating the linear region of the respective plot to α=0, as shown in the figure. The E_g value was 2.2 eV. In general, the optical band gap of various phases of indium selenide was reported in the range of 1.1-2.4 eV depending on the stoichiometry and the preparation technique (Mutlu et al., 2007, Asabe et al. 2008,Bindu et al., 2002).
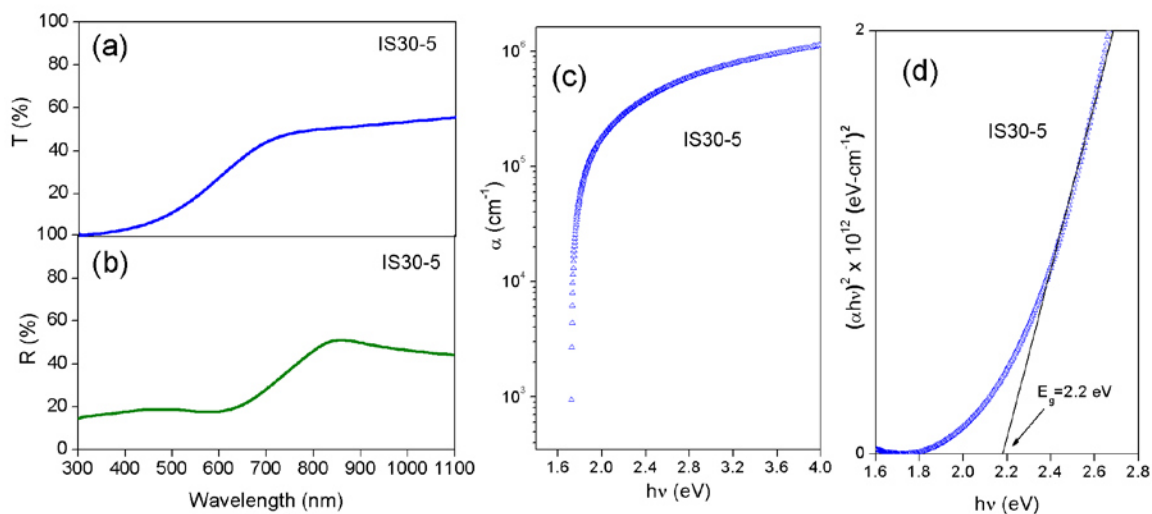
Figure 3.8 (a) Transmittance (*T*) spectra, (b) reflectance (*R*) spectra, (c) absorption spectra, (d) evaluation of band gap for IS30-5 sample. (Reproduced with kind permission from World Scientific)

Dark conductivity and photoconductivity of the indium selenide thin films formed by laser irradiation were determined from dark current and photocurrent

response measurements at room temperature, by applying a D.C. bias. Figure 3.9 shows the measurements results for the IS30-5 sample using a solar simulator of intensity 100 mW/cm^2. In this experiment a bias of 0.5 V was applied across a pair of planar silver paint electrodes, the current through the sample was measured in an interval of 20 s, first in the dark (I_o) followed by illumination of the sample (I) and then after switching off the light source. The value of dark conductivity was evaluated as approximately ~3 ($\Omega \cdot cm$)$^{-1}$. The sample was photoconductive as seen from the figure. The photosensitivity, defined as (I-I_o)/I_o, was determined as 0.02. Besides, the thin film shows persistent photoconductivity (PPC) which is a phenomenon present in semiconductors and is the occurrence of photoconductivity that persists for a very long period of time after the termination of the photoexcitation (Narayanan et al., 2001).This phenomenon present in our thin films might be due to the presence of defects or traps which are metastable between a shallow and deep energy states induced by laser irradiation as reported previously(Kuriyama et al., 2009).
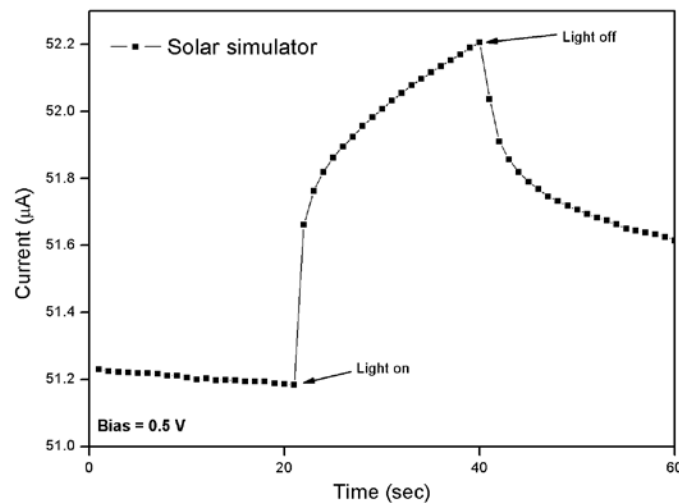
Figure 3.9 Photoresponse curve for IS30-5 sample. (Reproduced with kind permission from World Scientific)

Thus our results revealed the formation of indium selenide thin films due to laser irradiation of In/Se through Se layer side. Energy corresponding to 532 nm laser is 2.4 eV, higher than the band gap energy of selenium (1.8 eV)(Bindu et

al., 2006). During irradiation, part of the incident laser radiation was reflected, while the remaining part was absorbed throughout the selenium layer in accordance with the Beer-Lambert law. The absorbed optical energy was converted to thermal energy. The temperature rise due to laser irradiation depends not only on the laser parameters but also on the material parameters and can be calculated using the relation (Lax, 1977):

$$T = \frac{I_0 R \sqrt{\pi}}{2k} \qquad (3.1)$$

where I_0 is the absorbed power density (3.5 W/cm^2), R is the laser spot radius (0.8 cm) and k is the thermal conductivity of selenium thin film (0.005 Wcm^{-1}K^{-1}). Some important considerations to keep in mind in the use of eq. (3.1) are (Römer and Meijer, 1995):

a) The temperature represents a temperature increase relative to the initial temperature of the irradiated body.

b) The thermal conductivity varies with temperature and hence with the position in the material, here this parameter is assumed to be constant.

c) The surface absorptivity of the laser radiation is assumed to be constant.

Assuming the previous conditions and considering a linear case, we roughly estimate the maximum temperature produced at the center of the irradiated spot using the eq. (3.1) as ~223°C. Even at 100°C, formation of indium selenide due to reaction between selenium and indium by conventional furnace annealing was reported(Bindu et al., 2002). Thus, the thermal energy generated in the precursor layers due to absorption of laser energy resulted in the formation of indium selenide thin films.

The results obtained by the use of a rapid annealing process via laser leads to understand an alternative method for synthesizing optoelectronic materials, especially materials for solar cell applications.

In the next chapters we will focus in detail on experimental procedure, analysis and discussion of ternary CuSbS$_2$ and their alloys with selenium.

3.4 REFERENCES

AFZAAL, M., CROUCH, D. & O'BRIEN, P. 2005. Metal-organic chemical vapor deposition of indium selenide films using a single-source precursor. *Materials Science and Engineering: B,* 116**,** 391-394.

ASABE, M. R., CHATE, P. A., DELEKAR, S. D., GARADKAR, K. M., MULLA, I. S. & HANKARE, P. P. 2008. Synthesis, characterization of chemically deposited indium selenide thin films at room temperature. *Journal of Physics and Chemistry of Solids,* 69**,** 249-254.

BINDU, K., NAIR, M. T. S. & NAIR, P. K. 2006. Chemically Deposited Se Thin Films and Their Use as a Planar Source of Selenium for the Formation of Metal Selenide Layers. *Journal of the Electrochemical Society,* 153**,** C526-C534.

BINDU, K., SUDHA KARTHA, C., VIJAYAKUMAR, K. P., ABE, T. & KASHIWABA, Y. 2002. Structural, optical and electrical properties of In_2Se_3 thin films formed by annealing chemically deposited Se and vacuum evaporated In stack layers. *Applied Surface Science,* 191**,** 138-147.

BOUZOUITA, H., BOUGUILA, N., DUCHEMIN, S., FIECHTER, S. & DHOUIB, A. 2002. Preparation and characterization of In_2Se_3 thin films. *Renewable Energy,* 25**,** 131-138.

COLOMBARA, D., PETER, L. M., ROGERS, K. D., PAINTER, J. D. & RONCALLO, S. 2011. Formation of $CuSbS_2$ and $CuSbSe_2$ thin films via chalcogenisation of Sb–Cu metal precursors. *Thin Solid Films,* 519**,** 7438-7443.

CULLIS, A. G. 1985. Transient annealing of semiconductors by laser, electron beam and radiant heating techniques. *Reports on Progress in Physics,* 48**,** 1155.

CHEN, S., WALSH, A., YANG, J.-H., GONG, X. G., SUN, L., YANG, P.-X., CHU, J.-H. & WEI, S.-H. 2011. Compositional dependence of structural and electronic properties of $Cu_2ZnSn(S,Se)_4$ alloys for thin film solar cells. *Physical Review B,* 83.

DUFTON, J. T., WALSH, A., PANCHMATIA, P. M., PETER, L. M., COLOMBARA, D. & ISLAM, M. S. 2012. Structural and electronic properties of $CuSbS_2$ and $CuBiS_2$: potential absorber materials for thin-film solar cells. *Phys Chem Chem Phys,* 14**,** 7229-33.

EL-KABNAY, N., SHAABAN, E. R., AFIFY, N. & ABOU-SEHLY, A. M. 2008. Optical and physical properties of different composition of In_xSe_{1-x} thin films. *Physica B: Condensed Matter,* 403**,** 31-36.

EZUGWU, S. C., EZEMA, F. I. & ASOGWA, P. U. 2010. Synthesis and characterization of ternary $CuSbS_2$ thin films: Effect of deposition time. *Chalcogenide Letters,* 7**,** 341-348.

GARZA, C., SHAJI, S., ARATO, A., PEREZ TIJERINA, E., ALAN CASTILLO, G., DAS ROY, T. K. & KRISHNAN, B. 2011. p-Type CuSbS2 thin films by thermal diffusion of copper into Sb_2S_3. *Solar Energy Materials and Solar Cells,* 95**,** 2001-2005.

GOPAL, S., VISWANATHAN, C., THAMILSELVAN, M., PREMNAZEER, K., NARAYANDASS, S. K. & MANGALARAJ, D. 2004. Conduction studies on electrodeposited indium selenide thin films. *Ionics,* 10**,** 300-303.

GORDILLO, G. & CALDERÓN, C. 2003. CIS thin film solar cells with evaporated InSe buffer layers. *Solar Energy Materials and Solar Cells,* 77**,** 163-173.

HENLEY, S. J., CAREY, J. D. & SILVA, S. R. P. 2007. Metal nanoparticle production by pulsed laser nanostructuring of thin metal films. *Applied Surface Science,* 253**,** 8080-8085.

HIBBERD, C. J., GANCHEV, M., KAELIN, M., DANN, S. E., BILGER, G., UPADHYAYA, H. U. & TIWARI, A. N. 2009. Structural properties of $Cu(In,Ga)Se_2$ thin films prepared from chemically processed precursor layers. *Thin Solid Films,* 517**,** 2235-2239.

HIROHATA, A., MOODERA, J. S. & BERERA, G. P. 2006. Structural and electrical properties of InSe polycrystalline films and diode fabrication. *Thin Solid Films,* 510**,** 247-250.

HRDLICKA, M., PRIKRYL, J., PAVLISTA, M., BENES, L., VLCEK, M. & FRUMAR, M. 2007. Optical parameters of In–Se and In–Se–Te thin amorphous films prepared by pulsed laser deposition. *Journal of Physics and Chemistry of Solids,* 68**,** 846-849.

HURTADO, M., CRUZ, S. D., BECERRA, R. A., CALDERÓN, C., BARTOLO-PÉREZ, P. & GORDILLO, G. 2014. XPS analysis and structural characterization of CZTS thin films prepared using solution and vacuum based deposition techniques. *Photovoltaic Specialist Conference (PVSC), 2014 IEEE 40th***,** 0368 - 0372.

JACKSON, P., HARISKOS, D., LOTTER, E., PAETEL, S., WUERZ, R., MENNER, R., WISCHMANN, W. & POWALLA, M. 2011. New world record efficiency for $Cu(In,Ga)Se_2$ thin-film solar cells beyond 20%. *Progress in Photovoltaics: Research and Applications,* 19**,** 894-897.

KIM, N.-H., PARK, C. I. & PARK, J. 2013. A pilot investigation on laser annealing for thin-film solar cells: Crystallinity and optical properties of laser-annealed CdTe thin films by using an 808-nm diode laser. *Journal of the Korean Physical Society,* 62**,** 502-507.

KUMAR, M. & PERSSON, C. 2013. $CuSbS_2$ and $CuBiS_2$ as potential absorber materials for thin-film solar cells. *Journal of Renewable and Sustainable Energy,* 5**,** 031616.

KURIYAMA, K., MATSUMOTO, K., SUZUKI, Y., KUSHIDA, K. & XU, Q. 2009. Persistent photoconductivity and thermally stimulated current related to electron-irradiation induced defects in single crystal ZnO bulk. *Solid State Communications,* 149**,** 1347-1350.

LAX, M. 1977. Temperature rise induced by a laser beam. *Journal of Applied Physics,* 48**,** 3919-3924.

MAIELLO, P., ZOPPI, G., MILES, R. W., PEARSALL, N. & FORBES, I. 2013. Chalcogenisation of Cu–Sb metallic precursors into $Cu_3Sb(Se_xS_{1-x})_3$. *Solar Energy Materials and Solar Cells,* 113**,** 186-194.

MANOLACHE, S., DUTA, A., ISAC, L., NANU, M., GOOSSENS, A. & SCHOONMAN, J. 2007. The influence of the precursor concentration on

CuSbS$_2$ thin films deposited from aqueous solutions. *Thin Solid Films,* 515**,** 5957-5960.

MASTIO, E. A., CRANTON, W. M. & THOMAS, C. B. 2000. Pulsed laser annealing for high-efficiency thin film electroluminescent devices. *Journal of Applied Physics,* 88**,** 1606-1611.

MOULDER, J. F., STICKLE, W. F., SOBOL, P. E. & BOMBEN, K. D. 1992. *Handbook of X-ray Photoelectron Spectroscopy,* Eden Prairie, Minnesota, Perkin-Elmer Corporation.

MUTLU, I. H., ZARBALIYEV, M. Z. & ASLAN, F. 2007. Indium selenide thin film preparation by sol–gel technique. *Journal of Sol-Gel Science and Technology,* 43**,** 223-226.

NARAYANAN, K. L., RAJARAMAN, R., VALSAKUMAR, M. C., VIJAYAKUMAR, K. P. & NAIR, K. G. M. 2001. Irradiation-induced persistent photoconductivity in CdS films prepared by chemical bath deposition. *Optical Materials,* 17**,** 355-358.

NGUYEN, M. C., CHOI, J.-H., ZHAO, X., WANG, C.-Z., ZHANG, Z. & HO, K.-M. 2013. New Layered Structures of Cuprous Chalcogenides as Thin Film Solar Cell Materials: Cu$_2$Te and Cu$_2$Se. *Physical Review Letters,* 111.

OKAMOTO, H. 2004. In-Se (indium-selenium). *Journal of Phase Equilibria and Diffusion,* 25**,** 201-201.

ORNELAS, R. E., AVELLANEDA, D., SHAJI, S., CASTILLO, G. A., ROY, T. K. D. & KRISHNAN, B. 2012. In$_6$Se$_7$ thin films by heating thermally evaporated indium and chemical bath deposited selenium multilayers. *Applied Surface Science,* 258**,** 5753-5758.

POPOVICI, I. & DUTA, A. 2012. Tailoring the Composition and Properties of Sprayed CuSbS2 Thin Films by Using Polymeric Additives. *International Journal of Photoenergy,* 2012**,** 6.

RABHI, A., KANZARI, M. & REZIG, B. 2008. Growth and vacuum post-annealing effect on the properties of the new absorber CuSbS$_2$ thin films. *Materials Letters,* 62**,** 3576-3578.

RABHI, A., KANZARI, M. & REZIG, B. 2009. Optical and structural properties of $CuSbS_2$ thin films grown by thermal evaporation method. *Thin Solid Films,* 517**,** 2477-2480.

RODRÍGUEZ-LAZCANO, Y., NAIR, M. T. S. & NAIR, P. K. 2005. Photovoltaic p-i-n Structure of Sb_2S_3 and $CuSbS_2$ Absorber Films Obtained via Chemical Bath Deposition. *Journal of The Electrochemical Society,* 152**,** G635.

RODRÍGUEZ-LAZCANO, Y., NAIR, M. T. S. & NAIR, P. K. 2001. $CuSbS_2$ thin film formed through annealing chemically deposited Sb_2S_3–CuS thin films. *Journal of Crystal Growth,* 223**,** 399-406.

RÖMER, G. R. B. E. & MEIJER, J. 1995. Metal surface temperature induced by moving laser beams. *Optical and Quantum Electronics,* 27**,** 1397-1406.

SEPTINA, W., IKEDA, S., IGA, Y., HARADA, T. & MATSUMURA, M. 2014. Thin film solar cell based on CuSbS2 absorber fabricated from an electrochemically deposited metal stack. *Thin Solid Films,* 550**,** 700-704.

SHAJI, S., ARATO, A., BRIEN, J. J. O., LIU, J., CASTILLO, G. A., PALMA, M. I. M., ROY, T. K. D. & KRISHNAN, B. 2010. Chemically deposited Sb2S3 thin films for optical recording. *Journal of Physics D: Applied Physics,* 43**,** 075404.

SOLAR,   F. *http://investor.firstsolar.com/releasedetail.cfm?ReleaseID=828273*[Online].

SREEKUMAR, R., JAYAKRISHNAN, R., SUDHA KARTHA, C., VIJAYAKUMAR, K. P., KHAN, S. A. & AVASTHI, D. K. 2008. Enhancement of band gap and photoconductivity in gamma indium selenide due to swift heavy ion irradiation. *Journal of Applied Physics,* 103**,** 023709.

USGS 2014. U.S. Geological Survey: Mineral commodity summaries.

WANG, W., WINKLER, M. T., GUNAWAN, O., GOKMEN, T., TODOROV, T. K., ZHU, Y. & MITZI, D. B. 2013. Device Characteristics of CZTSSe Thin-Film Solar Cells with 12.6% Efficiency. *Advanced Energy Materials***,** n/a-n/a.

WANG, X., LI, S. S., HUANG, C. H., RAWAL, S., HOWARD, J. M., CRACIUN, V., ANDERSON, T. J. & CRISALLE, O. D. 2005. Investigation of pulsed non-melt laser annealing on the film properties and performance of Cu(In,Ga)Se$_2$ solar cells. *Solar Energy Materials and Solar Cells,* 88**,** 65-73.

WUBET, W. & KUO, D.-H. 2014. Process limitation for p-type CuSbS^2 semiconductor with high electrical mobility of 20cm^{2}V^{-1}s^{-1}. *Materials Research Bulletin,* 53**,** 290-294.

YANG, B., WANG, L., HAN, J., ZHOU, Y., SONG, H., CHEN, S., ZHONG, J., LV, L., NIU, D. & TANG, J. 2014. CuSbS^2 as a Promising Earth-Abundant Photovoltaic Absorber Material: A Combined Theoretical and Experimental Study. *Chemistry of Materials.*

YU, L., KOKENYESI, R. S., KESZLER, D. A. & ZUNGER, A. 2013. Inverse Design of High Absorption Thin-Film Photovoltaic Materials. *Advanced Energy Materials,* 3**,** 43-48.

ZHOU, J., BIAN, G.-Q., ZHU, Q.-Y., ZHANG, Y., LI, C.-Y. & DAI, J. 2009. Solvothermal crystal growth of CuSbQ$_2$ (Q=S, Se) and the correlation between macroscopic morphology and microscopic structure. *Journal of Solid State Chemistry,* 182**,** 259-264.

4

Preparation of CuSbS$_2$ and CuSb(Se$_x$,S$_{1-x}$)$_2$ thin films

This chapter provides details of the experimental process to produce CuSbS$_2$ and CuSb(Se$_x$,S$_{1-x}$)$_2$ thin films using a hybrid method of chemical bath deposition and thermal evaporation. Also, the procedure to fabricate photovoltaic devices using CuSbS$_2$ and CuSb(Se$_x$,S$_{1-x}$)$_2$ thin films as absorber materials is explained.

4.1 PREPARATION OF CuSbS$_2$THIN FILMS

Copper antimony sulfide (CuSbS$_2$) thin films were prepared bya two-stage process which involved the heating of layered structures of Sb$_2$S$_3$/Cudeposited sequentially on glass substrates by chemical bath deposition and thermal evaporation(Garza et al., 2011) (Figure 4.1).Previously, this type of two-stage was used for depositing CuInSe$_2$(Bindu et al., 2003), In$_2$Se$_3$(Bindu et al., 2002b)and Cu$_2$ZnSnS$_4$(Hurtado et al., 2014) thin films.
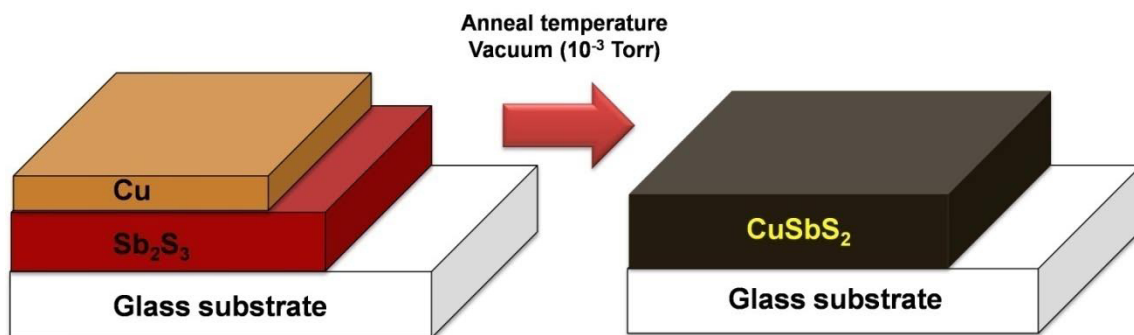
Figure 4.1Stack layers of Glass/Sb$_2$S$_3$/Cu to produce after heating CuSbS$_2$

The entire process is described below.

(i)   Chemical bath deposition of Sb₂S₃

First, the glass substrates were cleaned using chromic acid solution. The solution was prepared in a 100 ml beaker by dissolving 6 grams of potassium dichromate in 15 ml of deionized water and then slowly adding concentrated sulfuric acid to produce a total volume of 100 ml. The substrates were dipped in the acid and then, were cleaned with distilled water and dried with hot air. For the deposition of antimony sulfide thin film,a 100 ml bath containing 650 mg of $SbCl_3$ dissolved in 2.5 ml of acetone, 25 ml of $Na_2S_2O_3$ (1 M) and 72.5 ml of deionized water (previously heated at 40°C) were prepared and the cleaned substrates were arranged horizontally in a petri dish. The solution was stirred well and the solution was poured into the petri. The bath was kept at 40°C for 1 h. After 1 h deposition, the thin films formed were of thickness ~200 nm. Three, four and five consecutive depositions (consecutive dipping in freshly prepared baths) of Sb_2S_3 were done giving 600 nm, 800 nm and 1000 nm in thickness respectively.

(ii)   Thermal evaporation

.Copper thin film was deposited by thermal evaporation of 99.999% pure copper wire on Sb_2S_3 coated glass substrates loaded in a high vacuum system (TE12P, Intercovamex) operated at a pressure of 10^{-5} Torr. The copper film thickness was measured in situ using a quartz crystal thickness monitor installed in the evaporation system. Copper layer of thickness 50 nm was deposited on all Sb_2S_3 coated glass samples and copper layer of thicknesses 10 nm and 30 nm were deposited onto samples having 1000 nm in thickness of Sb_2S_3.

(iii)   Heating process

The heating process is the step in which all the precursor layers will undergo an interlayer diffusion and reaction to form the desired compound.

Glass/Sb_2S_3/Cu thin films of 600 nm and 50 nm of Sb_2S_3 and Cu respectively, were annealed at 350°C, 375°C and 400°C in low vacuum (10^{-3} Torr) for 1 h in a vacuum furnace (T-M Vacuum Products model No. V/IG-803-14). A second type of heating, a step by step heating at 350 °C, 375 °C and 400 °C was applied being analyzed the thin films after each step, i.e., the thin films formed at 350 °C were subjected to a post-heat treatment at 375°C (labeled C650T1,2) and then at 400 °C at same conditions (labeled C650T1,2,3). For thin films of 800 nm and 1000 nm of Sb_2S_3 and 10, 30 and 50 nm were annealed at 350 °C in low vacuum for 1 h. Annealing time was varied as 1 - 4 h for samples of 1000 nm of Sb_2S_3 and 50 nm of Cu stack layer. The sample labels and their corresponding process conditions are shown in Table 4.1.

Table 4.1Labels of Glass/Sb_2S_3/Cu samples

Sample	Sb_2S_3 thickness (nm)	Cu thickness (nm)	Anneal temperature	Time of annealing
C650T1	600	50	350 °C	1 h
C650T2			375 °C	
C650T3			400 °C	
C650T1,2			350 °C + 375 °C	
C650T1,2,3			350 °C + 375 °C + 400 °C	
C850T1	800	50	350 °C	
C1010T1	1000	10	350 °C	
C1030T1		30		
C1050T1-1		50		
C1050T1-2				2h
C1050T1-3				3 h
C1050T1-4				4 h

4.2 SELENIZATION OF CuSbS_2 BY A DIPPING PROCESS

CuSb$(Se_x,S_{1-x})_2$ thin films were prepared by heating layered structures of Sb$_2$S$_3$/Se/Cu deposited on glass substrates as shown in Figure 4.2. This configuration was selected due to previous observations that the use of stack Sb$_2$S$_3$/Cu/Se leads to the reaction of Se with Cu to form Cu$_2$Se and the multilayers after heat treatment did not react to form quaternary CuSb$(Se_x,S_{1-x})_2$. For that reason, it was selected the selenization process after chemical deposition of Sb$_2$S$_3$ followed by the deposition of evaporated Cu layer. The diffusion and reaction of the precursors are achieved after the heat treatment. The selenization of thin films was the process in which selenium atoms were incorporated into the stack layers by deposition of Se thin film by CBD and subsequent diffusion after heat treatment (Ornelas et al., 2012), by reaction forming a binary phase (González et al., 2014) and by diffusion controlled reaction of evaporated metallic precursors with selenium (Martín and Guillén, 2011, Dwyer et al., 2010).
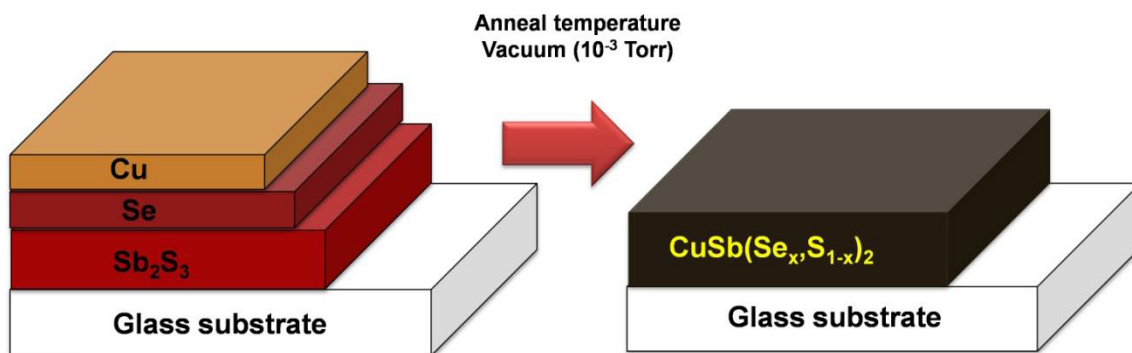
Figure 4.2Stack layers of Glass/Sb$_2$S$_3$/Se/Cu to produce after heating CuSb$(Se_x,S_{1-x})_2$

(i)   *Chemical bath deposition*

First, the glass substrates were cleaned using chromic acid solution using the same conditions as mentioned in section 4.1. Then, antimony sulfide thin films were chemically deposited on glass substrates from a bath containing 650 mg of SbCl$_3$ dissolved in 2.5 ml of acetone, 25 ml of Na$_2$S$_2$O$_3$ (1 M) and 72.5 ml of

deionized water (previous heated at 40°C) as mentioned earlier. The solution was stirred well and the substrates were arranged horizontally in a petri dish and the solution was poured into it. The conditions of bath were 1 h at 40°C. Five depositions (consecutive dipping in freshly prepared baths) of Sb_2S_3 were done giving 1000 nm in thickness. Then a selenium layer was deposited over Sb_2S_3 coated glass substrates, which were dipped in an aqueous solution containing 10 ml of Na_2SeSO_3 (0.1 M),1.5 ml acetic acid (25%) and 70 ml of deionized water at room temperature. One and three depositions of Se were made for 20 minutes (consecutive dipping in freshly prepared baths) drying the sample after each dipped in hot air flux. The Na_2SeSO_3 (0.1 M) precursor solution was prepared by dissolving 0.78 grams of selenium powder (99.999 % purity) and 4.5 grams of Na_2SO_3 in 100 ml of deionized water at 90 °C for 3 h with stirring. After that, the heating was off and the solution was left stirred at room temperature for 3 h (Bindu et al., 2002a).

(ii)   Thermal evaporation

For the preparation of $CuSb(Se_x,S_{1-x})_2$,copper thin films were evaporated onto Sb_2S_3/Se coated glass substrates deposited by thermal evaporation of 99.999% pure copper wire loaded in a high vacuum system at a pressure of 10^{-5} Torr. The copper film thickness was measured in situ using a quartz crystal thickness monitor installed in the evaporation system. Copper layer of thickness 10, 30 and 50 nm were deposited in Sb_2S_3/Se coated glass samples.

(iii)   Heating process

Glass/Sb_2S_3/Se/Cu thin films were annealed at 350°C in low vacuum (10^{-3} Torr) for 1 h in a vacuum furnace. The samples and the conditions are shown in Table 4.2.

Table 4.2 Labels of Glass/Sb$_2$S$_3$/Se/Cu samples

Sample	Sb$_2$S$_3$ thickness (nm)	Se thickness (nm)	Cu thickness (nm)	Anneal temperature
C1110T1			10	
C1130T1		100	30	
C1150T1	1000		50	350 °C
C1310T1			10	
C1330T1		300	30	
C1350T1			50	

The CuSbS$_2$ and CuSb(Se$_x$,S$_{1-x}$)$_2$ thin films formed at different conditions of thickness, anneal temperature and time were characterized using various techniques. X-ray diffraction (XRD) study was carried out for determined crystal structure in standard mode (θ-2θ) by a Bruker D8 Advance diffractometer using Cu Kα_1 radiation (λ = 1.54056 Å). The study in grazing incidence angle was performed by a Rigaku D-Max 2000 diffractometer using Cu Kα_1 radiation. X-ray photoelectron spectroscopy (XPS) was performed for oxidation states analysis and depth profile of composition for selected samples by a Thermo Scientific K-Alpha XPS instrument with monochromatized Al Kα radiation (hν=1486.68 eV). Scanning electron microscope (Model FEI Nova NanoSEM 200) was used for morphology and cross-sectional images of representative sample. Atomic force microscope (Model Solver Pro NT-MDT) was used to analyze topography of the surface of representative samples. Optical properties were measured by a UV-Vis spectrometer (Model Shimadzu UV-1800) in the 300-1100 nm wavelength range using optical transmittance and reflectance spectra for calculation of absorption coefficient and optical band gap. Electrical measurements were carried out for photoconductivity measurements painting contacts as electrodes using conductive carbon paint (SPI® supplies) using a picoammeter/voltage source (model Keithley 6487) and a tungsten halogen lamp set up. The Hall

effect measurements were performed by an Ecopia HMS 3000 Hall measurement system.

4.3 FABRICATION OF SOLAR CELL DEVICES

Superstrate p-n junction configuration

Photovoltaic structures were fabricated on commercially available SnO_2:F coated glass (TEC-15 Pilkington) using $CuSbS_2$ as absorber material and CdS as window layer using a superstrate configuration of glass/SnO_2:F/CdS/Sb_2S_3/Cu as shown in Figure 4.3.
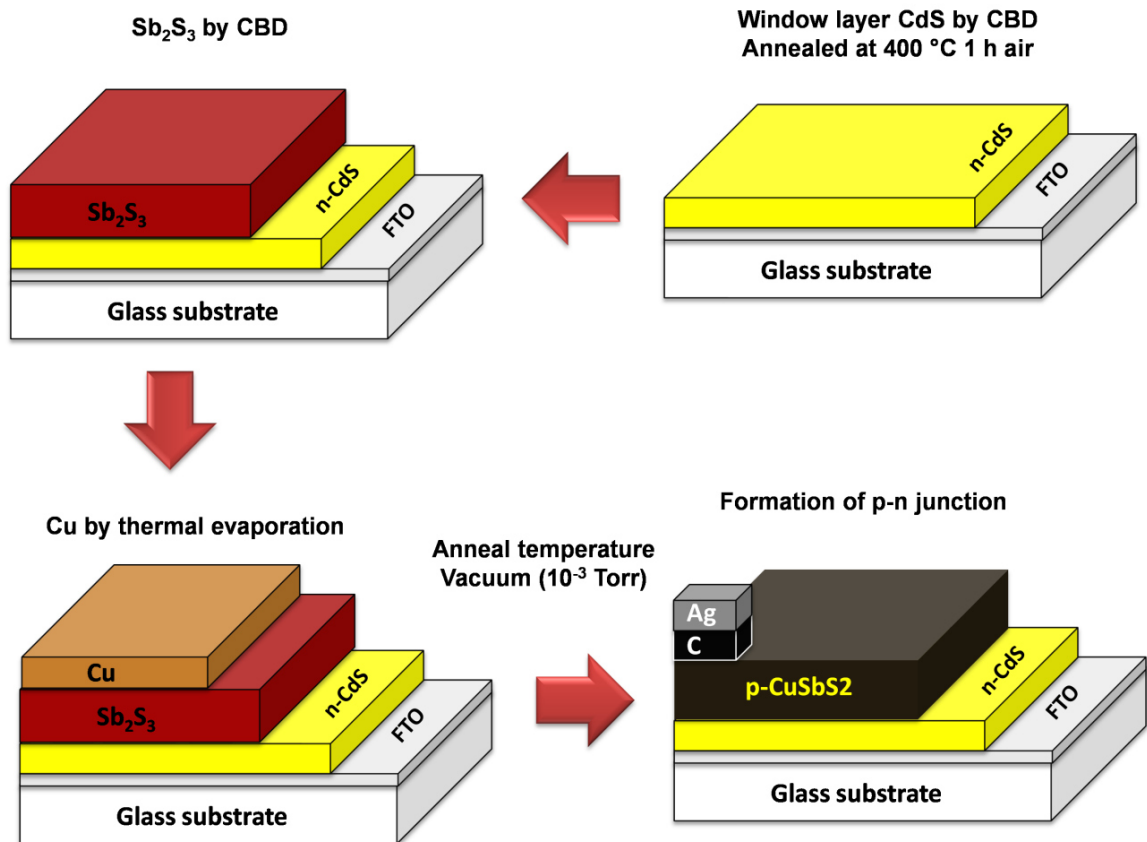
Figure 4.3 Fabrication of superstrate p-n configuration of glass/SnO_2:F/(*n*)CdS/(*p*)CuSbS$_2$/C/Ag

Window layer (CdS) by chemical bath deposition

CdS thin films were deposited from a chemical bath containing 10 ml of $CdCl_2$ (0.1 M), 5 ml of Triethanolamine (50%), 10 ml of NH_4OH (15 M), 10 ml of thiourea (1 M) and 65 ml of deionized water at 70 °C(Gonzalez et al., 2011). The time of deposition for CdS films was 45 minutes. CdS thin films were prepared at two different conditions for the photovoltaic device: (i) as prepared and (ii) CdS thin film was pre-annealed at 400°C for 1 h in air before the deposition of the absorber precursor materials. The pre-annealing of CdS layer in air is beneficial for improve photovoltaic device parameters due to the grain hardening effect which in turn could prevent further diffusion of the absorber layer during heating to form the devices(Mathew et al., 2012).

Absorber layer (Sb_2S_3/Cu) by CBD and thermal evaporation

CdS coated TCO samples were dipped in Sb_2S_3 bath, three, four and five consecutive depositions, one hour dipping in each bath to achieve nearly 600, 800 and 1000 nm, respectively, as specified in section 4.1. Then, Cu thin films of 50 nm in thickness were thermally evaporated to glass/SnO_2:F/CdS/Sb_2S_3 stacked layers.

Heating process of stack layers

The layered precursor samples of glass/SnO_2:F/CdS/Sb_2S_3/Cu were heated at 350 °C, 375 °C and 400 °C for 1 h in low vacuum (10^{-3} torr) to form PV structures of glass/SnO_2:F/(n)CdS/(p)$CuSbS_2$. To study the evolution of the PV effect with temperature, the precursor samples were first heated to 350°C then 375°C and finally at 400°C, evaluating the PV parameters after each thermal treatment for the samples of 650 nm in thickness of $CuSbS_2$ thin film. The photovoltaic devices were labeled as shown in Table 4.3.

Characterization of photovoltaic devices

To measure current-voltage characteristics, the ohmic contacts were made using silver and carbon colloidal suspensions, first carbon contact on which silver was painted. The contact area was 3-4 mm^2. The solar cell was measured using a solar simulator of 100 mW/cm^2 at room temperature.

Table 4.3 Labels of photovoltaic devices of Glass/SnO$_2$:F/(n)CdS/(p)CuSbS$_2$/C/Ag

Solar cell	CdStime of deposition	Sb$_2$S$_3$ thickness (nm)	Se thickness (nm)	Cu thickness (nm)	Anneal temperature
SC1	45 min as prepared	600	None Se thin film was deposited	50	350 °C
SC2					375 °C
SC3					400 °C
SCPT1					350+375 °C
SCPT2					350+375+400 °C
SC4		800			350 °C
SC5	45 min annealed at 400 °C 1 h in air	600			350 °C
SC6					375 °C
SC7					400 °C
SC8		800			350 °C
SC9		1000			350 °C-1 h
SC10					350 °C-2 h
SC11					350 °C-3 h
SC12					350 °C-4 h

Superstrate p-i-n configuration

In many semiconductor materials especially direct band gap semiconductors, most of the electron-hole pairs are created very near the surface. If a thin intrinsic (undoped) layer is placed between n and p regions, this will result in enhancing the built-in electric field and the carrier collection (Luque and

Hegedus, 2011). The presence of an intrinsic layer essentially stretches out the electrostatic field region and hence allows more photogenerated carriers to be brought to the collection region. With p-i-n structure, the drift field enhances minority carrier collection, which will improve the efficiency in the device. The application of this p-i-n structure is preferable in devices using materials with short minority carrier diffusion lengths.

Photovoltaic structures using $CuSbS_2$ as absorber material and a superstrate p-i-n configuration of glass/SnO_2:F/CdS/i-Sb_2S_3/Sb_2S_3/Cu is shown in Figure 4.4.
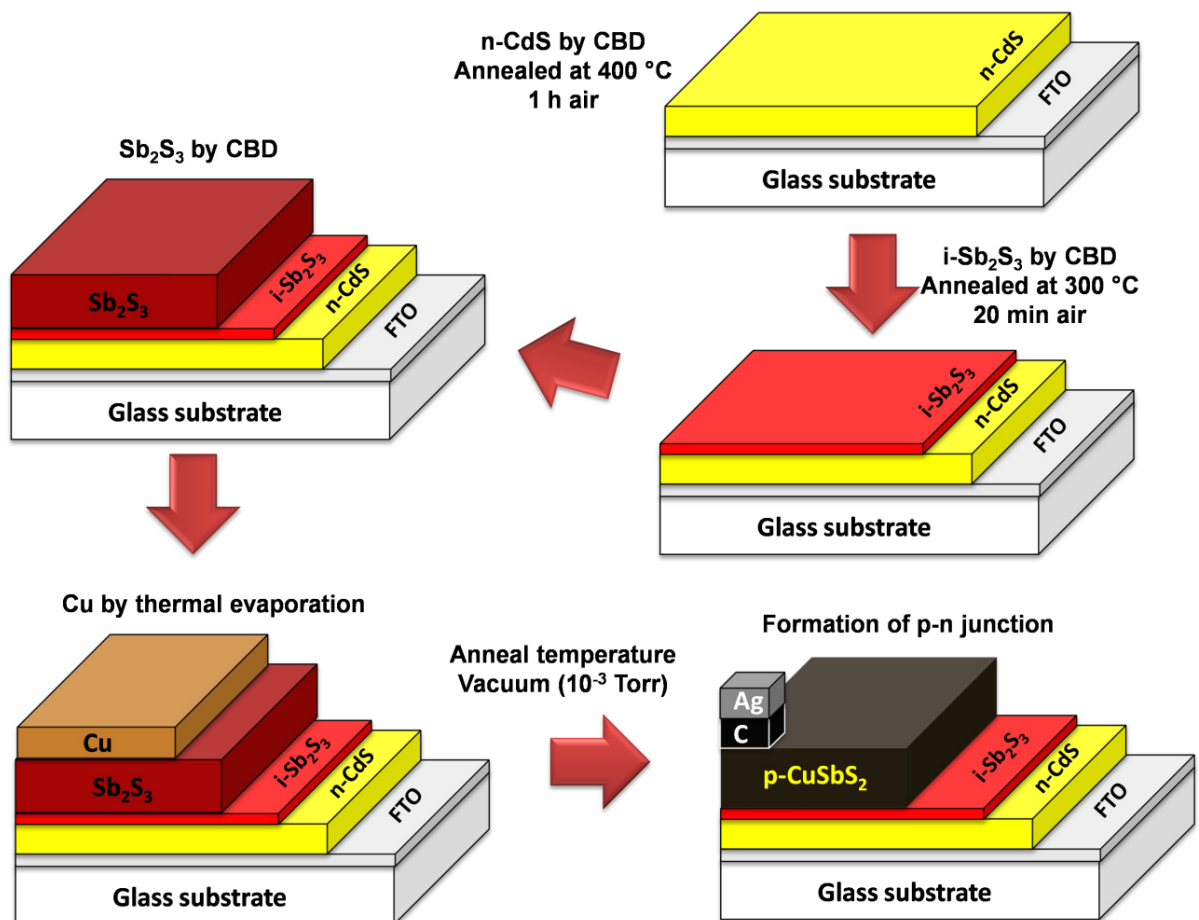
Figure 4.4 Superstrate p-i-n configuration of glass/SnO_2:F/(*n*)CdS/(*i*)Sb_2S_3/(*p*)$CuSbS_2$/C/Ag

Window layer (CdS) by chemical bath deposition

CdS thin films were deposited as mentioned earlier. The time of deposition for CdS films was 20 minutes and 45 min. The CdS thin films were pre-annealed at 400°C for 1 h in air before the deposition of the intrinsic layer.

Intrinsic layer (Sb_2S_3) by chemical bath deposition

CdS coated TCO samples were dipped in Sb_2S_3 bath giving one deposition of 15, 30 and 60 minutes for each bath achieving a thickness of 50, 100 and 200 nm respectively. The layered precursors of glass/SnO_2:F/CdS/Sb_2S_3 were annealed at 300 °C for 20 minutes in air in order to form Sb_2S_3 intrinsic layer.

(Sb_2S_3/Cu) by CBD and thermal evaporation

Sb_2S_3 layer is deposited by CBD giving five consecutive depositions, one hour dipping in each bath to achieve nearly 1000 nm, the deposition process is the same as specified in section 4.1. Then, Cu thin films of 50 nm in thickness were thermally evaporated to glass/SnO_2:F/(n)CdS/(i)Sb_2S_3/Sb_2S_3 stacked layers.

Heating process of stack layers

The layered precursor samples of glass/SnO_2:F/CdS/Sb_2S_3/Sb_2S_3/Cu were heated at 350 °C for 1 h in low vacuum (10^{-3} torr) to form PV structures of glass/SnO_2:F/(n)CdS/(i)Sb_2S_3/(p)CuSbS$_2$. Also, PV devices were prepared using $CuSb(Se_x,S_{1-x})_2$ as absorber material. The process of selenization is the same as specified in section 4.2. The photovoltaic devices labels are shown in Table 4.4.

Characterization of photovoltaic devices

To measure current-voltage characteristics, ohmic contacts were made using silver and carbon colloidal suspensions, first carbon contact on which silver was painted. The contact area was 3-4 mm^2. The solar cell was measured using a solar simulator of 100 mW/cm^2 at room temperature.

Table 4.4 Labels of photovoltaic devices of Glass/SnO$_2$:F/(n)CdS/(i)Sb$_2$S$_3$/(p)CuSbS$_2$/C/Ag

Solar cell	CdS time of deposition	i-Sb$_2$S$_3$ thickness (nm)	Sb$_2$S$_3$ thickness (nm)	Se thickness (nm)	Cu thickness (nm)	Anneal temperature
SC13	20 min	50	1000	None Se thin film were deposited	50	350 °C
SC14		100				
SC15		200				
SC16		100		300 (3 dips/ 20 min each)		
SC17	45 min	50		None Se thin film were deposited		
SC18		100				
SC19		200				
SC20		100		300 (3 dips/ 20 min each)		

In this chapter the experimental procedure for the preparation of CuSbS$_2$ and CuSb(Se$_x$,S$_{1-x}$)$_2$ thin films as well as the photovoltaic devices are explained in detail using these materials.

In the next chapter the results of all the characterizations performed for the thin films and photovoltaic devices will be discussed.

4.4 REFERENCES

BINDU, K., KARTHA, C. S., VIJAYAKUMAR, K. P., ABE, T. & KASHIWABA, Y. 2003. CuInSe$_2$ thin film preparation through a new selenisation process using chemical bath deposited selenium. *Solar Energy Materials and Solar Cells,* 79**,** 67-79.

BINDU, K., LAKSHMI, M., BINI, S., KARTHA, C. S., VIJAYAKUMAR, K. P., ABE, T. & KASHIWABA, Y. 2002a. Amorphous selenium thin films prepared using chemical bath deposition: optimization of the deposition process and characterization. *Semiconductor Science and Technology,* 17**,** 270.

BINDU, K., SUDHA KARTHA, C., VIJAYAKUMAR, K. P., ABE, T. & KASHIWABA, Y. 2002b. Structural, optical and electrical properties of In_2Se_3 thin films formed by annealing chemically deposited Se and vacuum evaporated In stack layers. *Applied Surface Science,* 191**,** 138-147.

DWYER, D., REPINS, I., EFSTATHIADIS, H. & HALDAR, P. 2010. Selenization of co-sputtered CuInAl precursor films. *Solar Energy Materials and Solar Cells,* 94**,** 598-605.

GARZA, C., SHAJI, S., ARATO, A., PEREZ TIJERINA, E., ALAN CASTILLO, G., DAS ROY, T. K. & KRISHNAN, B. 2011. p-Type CuSbS2 thin films by thermal diffusion of copper into Sb_2S_3. *Solar Energy Materials and Solar Cells,* 95**,** 2001-2005.

GONZALEZ, G., KRISHNAN, B., AVELLANEDA, D., CASTILLO, G. A., DAS ROY, T. K. & SHAJI, S. 2011. Modification of optical and electrical properties of chemical bath deposited CdS using plasma treatments. *Thin Solid Films,* 519**,** 7587-7591.

GONZÁLEZ, J. O., SHAJI, S., AVELLANEDA, D., CASTILLO, G. A., DAS ROY, T. K. & KRISHNAN, B. 2014. Photovoltaic structures using $AgSb(S_x Se_{1-x})_2$ thin films as absorber. *Applied Physics A,* 116**,** 2095-2105.

HURTADO, M., CRUZ, S. D., BECERRA, R. A., CALDERÓN, C., BARTOLO-PÉREZ, P. & GORDILLO, G. 2014. XPS analysis and structural characterization of CZTS thin films prepared using solution and vacuum based deposition techniques. *Photovoltaic Specialist Conference (PVSC), 2014 IEEE 40th***,** 0368 - 0372.

LUQUE, A. & HEGEDUS, S. 2011. *Handbook of Photovoltaic Science and Engineering*, Wiley.

MARTÍN, S. & GUILLÉN, C. 2011. Study of the chalcopyrite Cu(In,Al)Se$_2$ crystalline growth by selenization of different evaporated precursors ratios. *Journal of Crystal Growth,* 336**,** 82-88.

MATHEW, X., CRUZ, J. S., CORONADO, D. R., MILLÁN, A. R., SEGURA, G. C., MORALES, E. R., MARTINEZ, O. S., GARCIA, C. C. & LANDA, E. P. 2012. CdS thin film post-annealing and Te-S interdiffusion in a CdTe/CdS solar cell. *Solar Energy,* 86**,** 1023-1028.

ORNELAS, R. E., AVELLANEDA, D., SHAJI, S., CASTILLO, G. A., DAS ROY, T. K. & KRISHNAN, B. 2012. In$_6$Se$_7$ thin films by heating thermally evaporated indium and chemical bath deposited selenium multilayers. *Applied Surface Science,* 258**,** 5753-5758.

5
Results and Discussion

This chapter gives a complete discussion on the results obtained in the characterization of structural, morphological, optical and electrical properties of $CuSbS_2$ and $CuSb(Se_x,S_{1-x})_2$ thin films deposited using an hybrid technique of chemical bath deposition and thermal evaporation as described in the previous chapter. Also, the results obtained for the photovoltaic devices fabricated using the chalcostibite thin films are discussed.

5.1 CuSbS$_2$ THIN FILMS

The formation of $CuSbS_2$ thin films is proposed by the diffusion of Cu and reaction with the Sb_2S_3 layer. The formation mechanism of chemical deposited Sb_2S_3 is suggested as an ion by ion condensation mechanism, in which the dissociation of the soluble antimony thiosulphate formed by the reaction of $SbCl_3$ and $Na_2S_2O_3$ releases Sb^{+3} ions:

$$Sb_2(S_2O_3)_3 \leftrightarrow \mathbf{2Sb^{+3}} + 3S_2O_3^{-2} \qquad [1]$$

and the hydrolysis of thiosulphate releases S^{-2} ions:

$$S_2O_3^{-2} + H_2O \leftrightarrow SO^{-4} + \mathbf{S^{-2}} + 2H^+ \qquad [2]$$
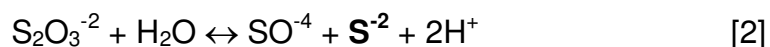
The Sb^{+3} and S^{-2} ions produced by the reactions [1] and [2] in the bath condense at the substrate to form Sb_2S_3 thin film (Nair, 1998). During the annealing, Cu diffuses into Sb_2S_3 lattice and reacts to form the compound $CuSbS_2$. The final thickness for $CuSbS_2$ thin films were 650 nm, 850 nm and 1050 nm.

5.1.1 Structure (XRD)

Structural characteristics of the thin films formed at different conditions were analyzed from the XRD patterns.

(a) Variation of annealing temperature

Figure 5.1 shows the diffraction patterns of the as deposited multilayers glass/Sb_2S_3/Cu and that of annealed ones at 350 °C, 375 °C, 400 °C (C650T1, C650T2, C650T3 respectively). For the as-deposited thin film glass/Sb_2S_3/Cu, a single peak is present at $2\theta=43.38°$ which matched the standard pattern of cubic copper (PDF#04-0836), as expected due to reflection from the copper layer. No diffraction peaks of Sb_2S_3 were observed indicating that the Sb_2S_3 layer was amorphous. This result is common for as-prepared Sb_2S_3 thin films deposited by chemical bath deposition (Calixto-Rodriguez et al., 2010). After heated at 350 °C, 375 °C and 400 °C the thin films show strong peaks of orthorhombic chalcostibite $CuSbS_2$ (PDF#44-1417) as marked by the planes (200), (210), (400), (111), (410), (301), (220), (320), (501), (221), (321), (002), (521), (212) and (402). We assigned the peaks located at $2\theta= 13.8°$, 27.81° and 46.19° for that monoclinic Cu_2S (PDF#83-1462) (Kırmızıgül et al., 2012), as an impurity phase in all the three annealed thin films denoted by solid squares. Average crystallite size of polycrystalline $CuSbS_2$ thin films was evaluated using line broadening analysis of the diffraction patterns given in Figure 5.1. The line broadening can occur due to small grain size as well as due to microstrains associated with the thin films. The width of Bragg reflections realized to be affected by microstructural features other than size broadening, like crystallite shape, shape distribution and any distortion of the crystal structure like microstrain, dislocations, twin planes and stacking faults (Birkholz, 2006). Microstrains play a prominent role in the distortion of crystal lattice. The strain fields causes that the position and broadening of the peak reflections changes. The way to calculate this microstrain is using the Williamson-Hall plot

(Williamson and Hall, 1953), which also introduce crystallite size as well, and is given by:

$$\boldsymbol{\beta \cos \theta = \frac{0.9\lambda}{D} + 2\varepsilon \sin \theta} \tag{5.1}$$

whereε is the strain of the lattice.

The size and the strain effects can be separated where $\beta \cos\theta$ vs. $\sin\theta$ are plotted, β being the full width at half maximum (FWHM) of the diffraction peak located at 2θ. This plot can be fitted to a straight line. The inverse of the intercept of the line on $\beta\cos\theta$ axis gives the ratio of the crystalline grain diameter (D) to wavelength (1.54056 Å) from which the value of D can be extracted. From the slope of the line, the microstrain (ε) is evaluated.

The Williamson-Hall plots for the annealed $CuSbS_2$ thin films at 350 °C, 375 °C and 400 °C were drawn by assigning Lorentzian shape for the prominent diffraction peaks due to (200), (301), (501), (212) and (220) reflections as given in Figure 5.2. Crystallite size computed for the $CuSbS_2$ thin films was approximately 35 nm for thin film annealed at 350 °C (Figure 5.2a) and 32 nm for those annealed at 375 °C and 400 °C (Figure 5.2b,c) and microstrain valuesof 4×10^{-3}, 2×10^{-3} and 0.98×10^{-3}, respectively, decreasing lattice strain can be due to the reduction of defects as the annealing temperature increased (Chandramohan et al., 2011).In crystals there are two types of strains (Tu et al., 1992): *Uniform strain* which causes the unit cell to expand/contract leading to a change in the lattice parameters which in turn shifts the diffraction peaks and *Non-uniform strain* which leads to peak broadening arising from the point defects such as vacancies or site-disorder, plastic deformation and poor crystallinity. There are intrinsic and extrinsic stresses in thin films. Intrinsic stress come from defects in the film. The origin of extrinsic stress comes from the adhesion of the film to substrate. Stress can be produced in a thin film due to differential thermal expansion between the film and substrate, due to lattice misfit with its substrate or due to chemical reaction with its substrate. Also, it was suggested that in thin film grain growth and the removal of grain boundaries will produce stress in the film. This explains the decrease of microstrain in our

thin films. As the crystallite size decrease with anneal temperature leads to increase in grain boundaries giving as result the reduction of the microstrain in the film.
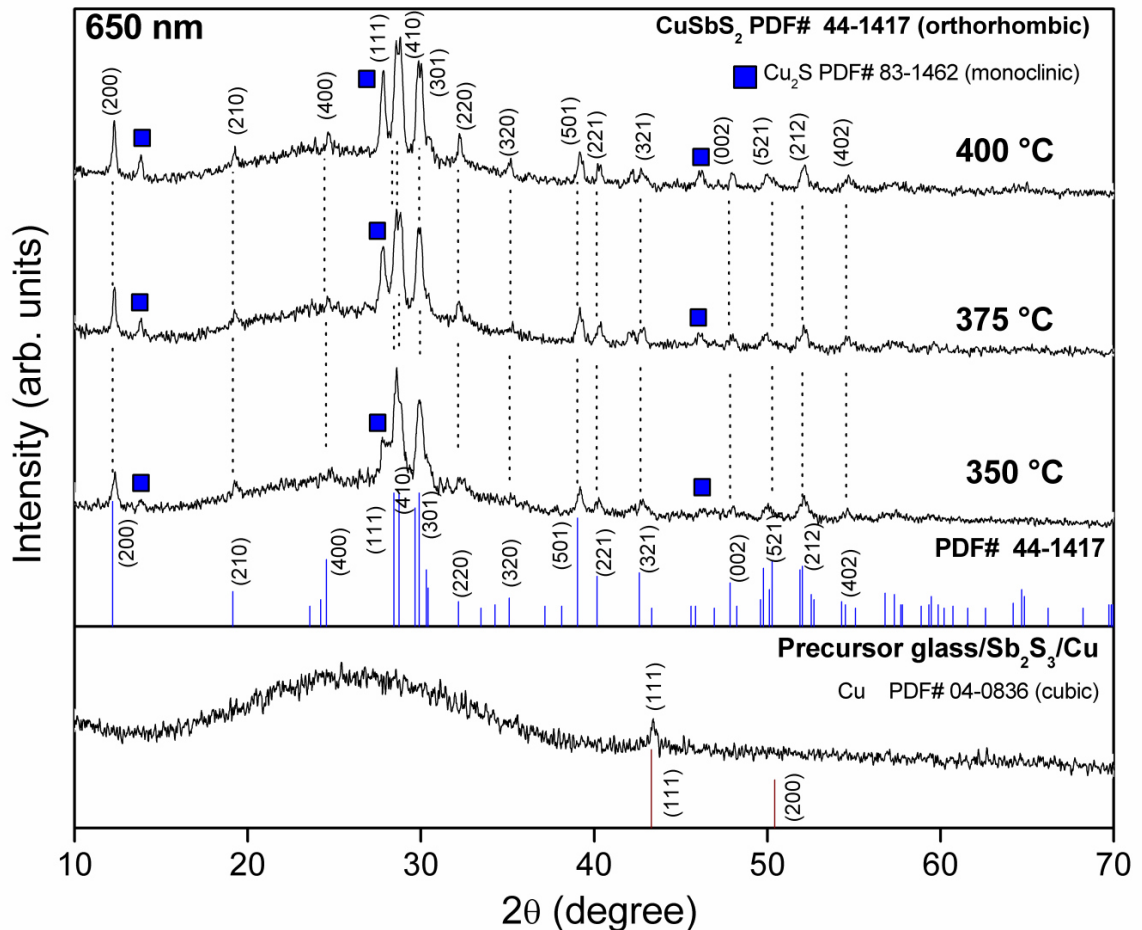
Figure 5.1 XRD patterns for as-deposited glass/Sb₂S₃/Cu and multilayers glass/Sb₂S₃/Cu annealed at 350 °C, 375 °C and 400 °C (C650T1, C650T2, C650T3) for 1h (Reproduced with kind permission from Springer)
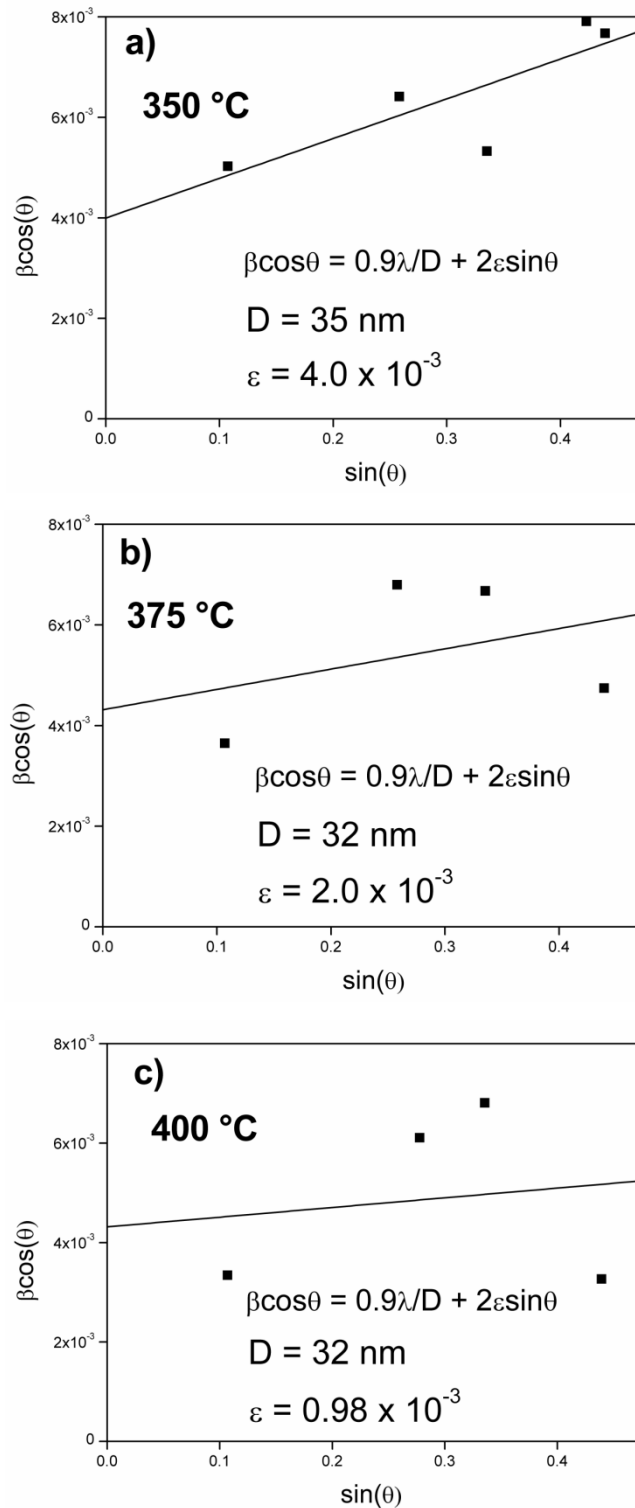
Figure 5.2 Average crystallite sizes and microstrain of the multilayers glass/Sb_2S_3/Cu annealed at 350 °C, 375 °C and 400 °C (C650T1, C650T2, C650T3) for 1h
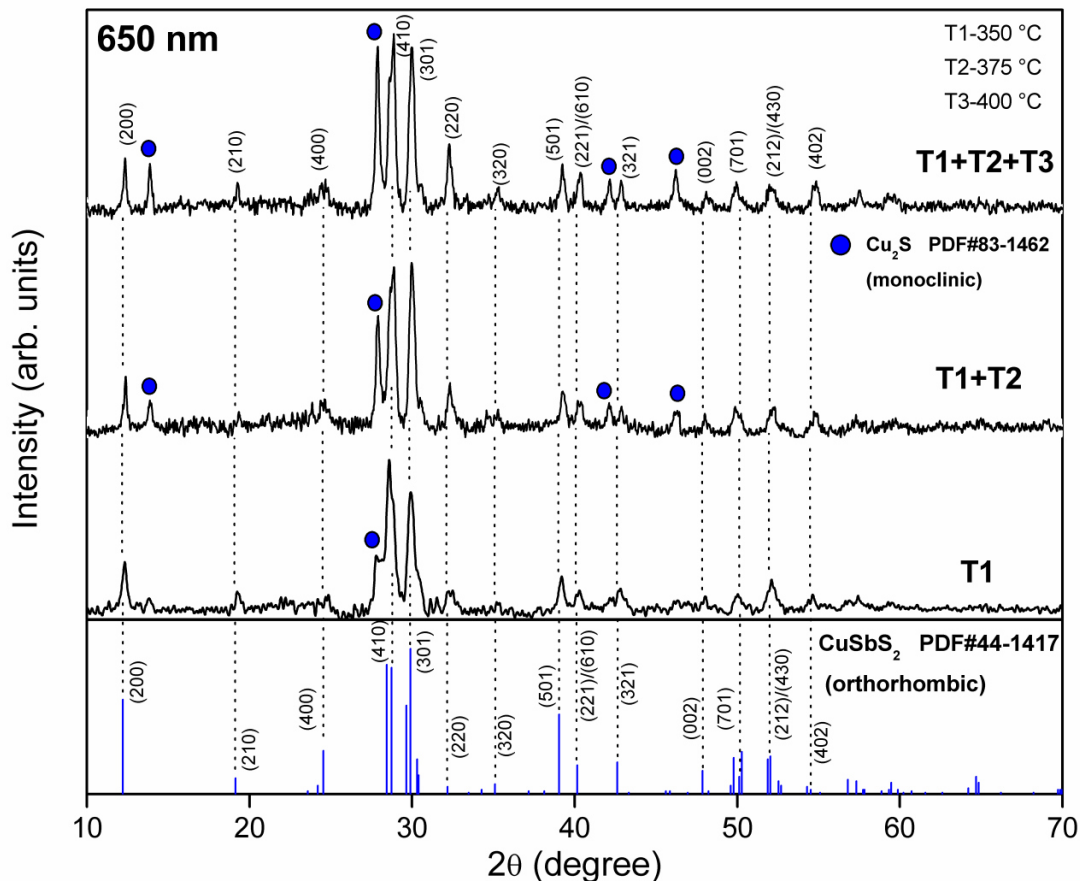
Figure 5.3 XRD patterns for glass/Sb₂S₃/Cu annealed at 350 °C (C650T1) and step by step annealed at 375 °C (C650T1,2) and 400 °C (C650T1,2,3) for 1h

Figure 5.3 illustrates the diffraction patterns for the thin films formed by the step by step heating at 350 °C, 375 °C and 400 °C, showing structural evolution of the $CuSbS_2$ thin films due to heating. All these thin films exhibit reflections due to the presence of orthorhombic $CuSbS_2$, as the primary phase and that of Cu_2S as a secondary phase increasing their peak intensity with temperature as indicated in the figure. The Williamson-Hall plots for the step by step annealed $CuSbS_2$ thin films were drawn by assigning Lorentzian shape for the prominent diffraction peaks due to (200), (301), (501) and (220) reflections as given in the Figure 5.4. Crystallite size computed for all the $CuSbS_2$ thin films formed at 350 °C, 350 °C + 375 °C and 350 °C + 375 °C + 400 °C was 35nm and micro-strain values of 4×10^{-3}, 3.5×10^{-3} and 2.7×10^{-3}, respectively, decreasing microstrain due to reduction of defects by increasing the anneal temperature and the

increase of grain boundaries which imply the reduction in stress in similar way obtained for the samples annealed in single steps of heat treatment.

a)

350 °C

$\beta\cos\theta = 0.9\lambda/D + 2\varepsilon\sin\theta$

D = 35 nm

$\varepsilon = 4.0 \times 10^{-3}$

b)

350 °C + 375 °C

$\beta\cos\theta = 0.9\lambda/D + 2\varepsilon\sin\theta$

D = 35 nm

$\varepsilon = 3.5 \times 10^{-3}$

c)

350 °C + 375 °C + 400 °C

$\beta\cos\theta = 0.9\lambda/D + 2\varepsilon\sin\theta$

D = 35 nm

$\varepsilon = 2.7 \times 10^{-3}$
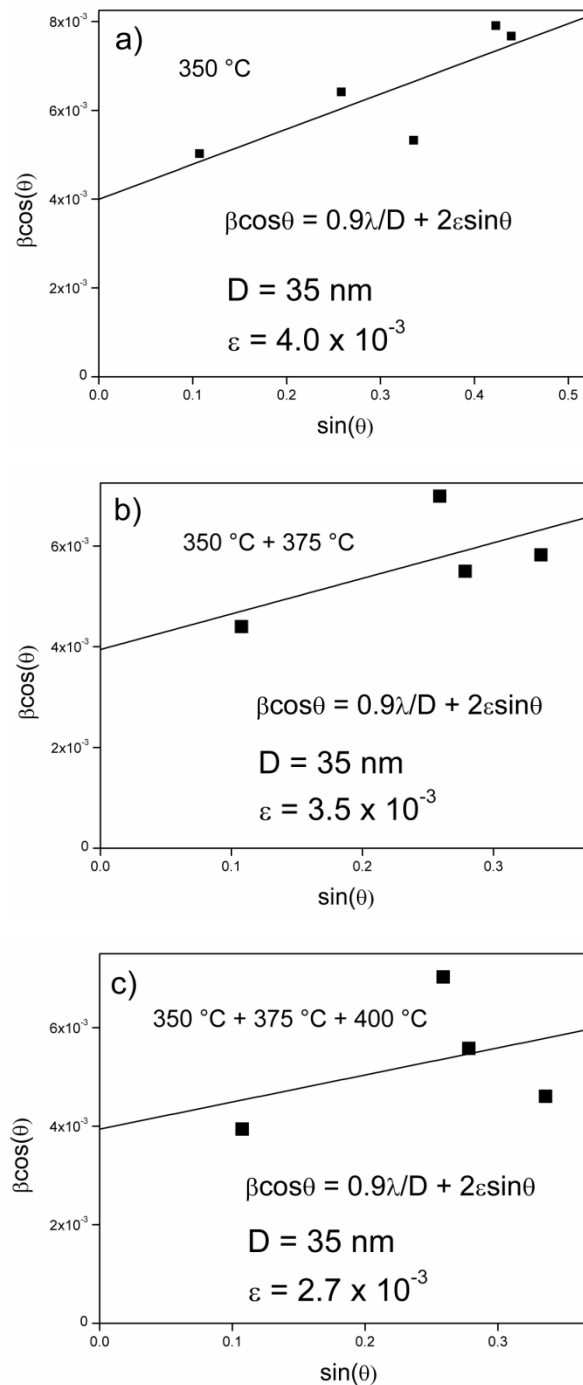
Figure 5.4 Average crystallite sizes and microstrain of the multilayers glass/Sb_2S_3/Cu annealed at 350 °C (C650T1) and step by step annealed at 375 °C (C650T1,2) and 400 °C (C650T1,2,3) for 1h
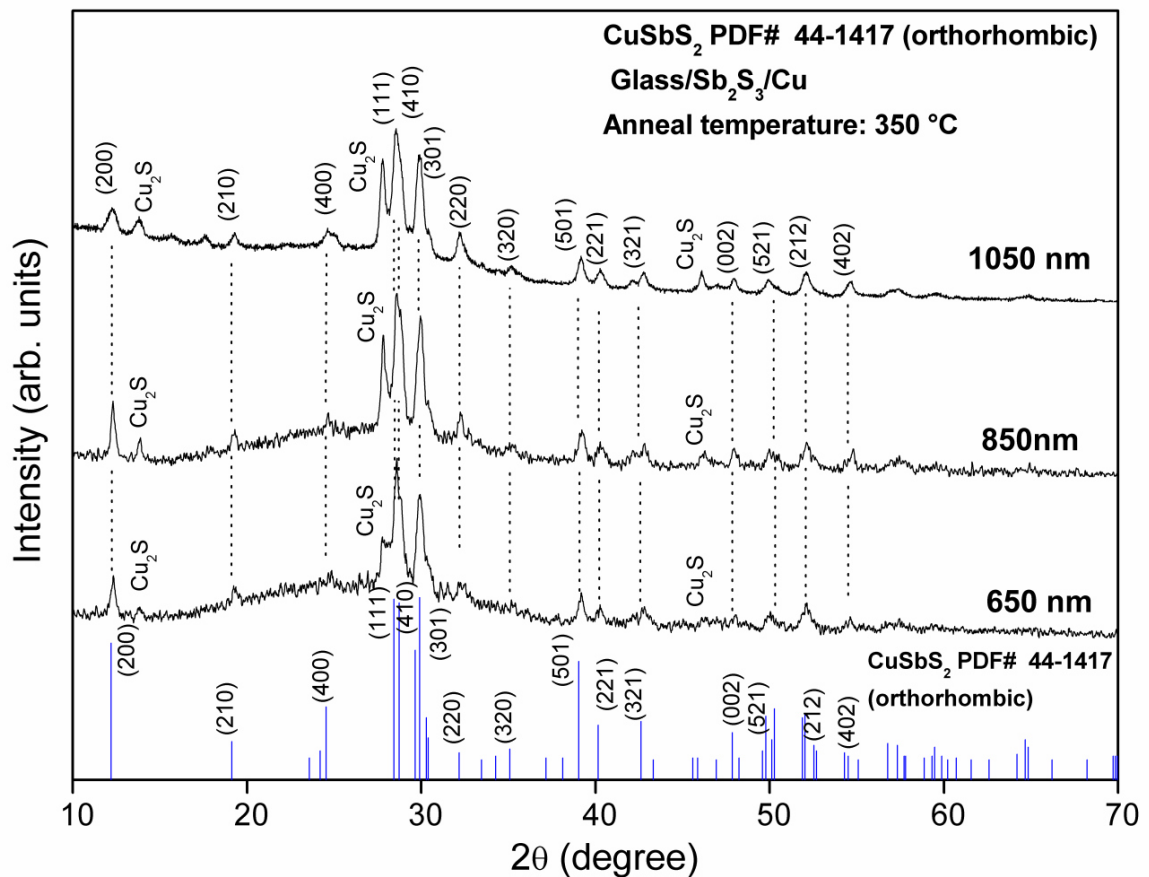
Figure 5.5 XRD patterns for multilayers glass/Sb₂S₃/Cu of 650 nm, 850 nm and 1050 nm in thickness annealed at 350 °C for 1h

(b) Variation of Sb_2S_3 thickness

Further analysis were done on samples formed by annealing Sb_2S_3/Cu at 350 °C, varying Sb_2S_3layer thickness for a fixed Cu layer thickness of 50 nm. Figure 5.5illustrates the diffraction patterns performed in (θ-2θ) mode for the thin films having 600 nm, 800 nm and 1000 nm (three, four and five depositions of Sb_2S_3respectively). All these thin films exhibit reflections due to the presence of orthorhombic $CuSbS_2$, as the primary phase marked by the planes (200), (210), (400), (111), (410), (301), (220), (320), (501), (221), (321), (002), (521), (212) and (402) along with monoclinic Cu_2S (PDF#83-1462) as indicated in the figure.
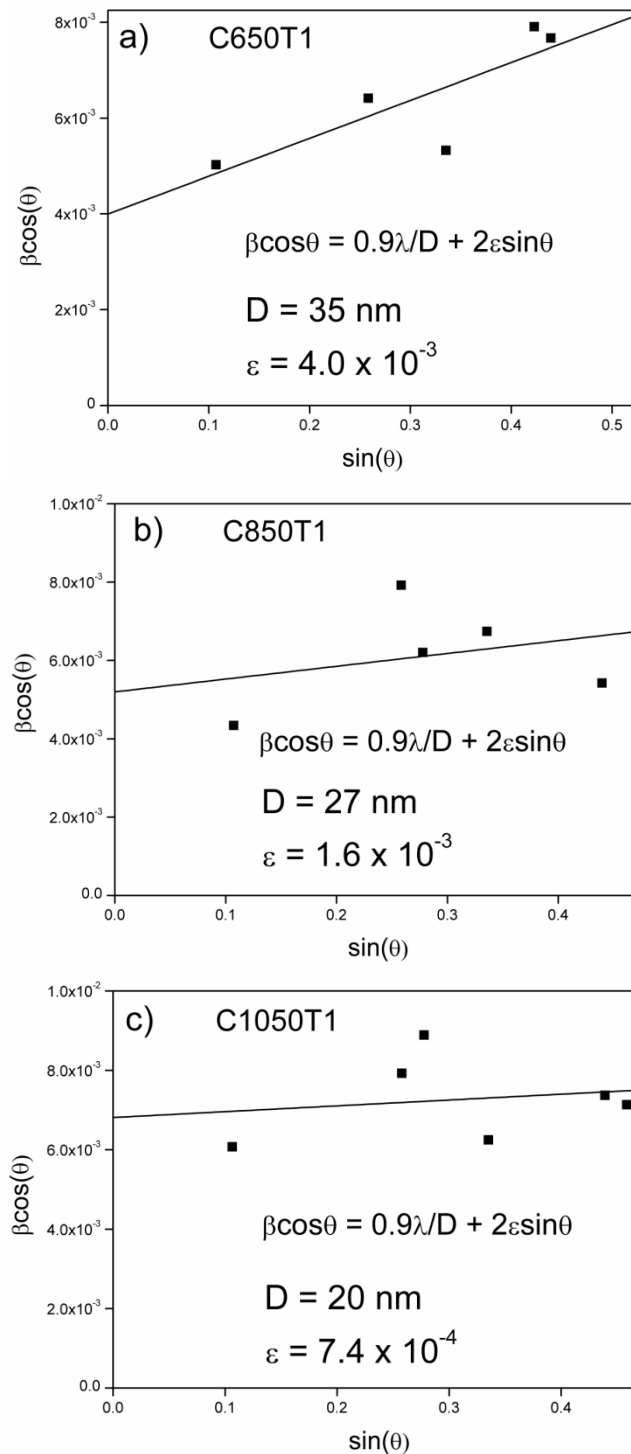
Figure 5.6 Average crystallite sizes and microstrain of the multilayers glass/Sb$_2$S$_3$/Cu of 650 nm, 850 nm and 1050 nm in thickness annealed at 350 °C for 1h

The average crystallite size and lattice strain were evaluated by Williamson-Hall plots for the three annealed CuSbS$_2$ thin films using the diffraction peaks

(200), (301), (501), (212) and (220) as shown in Figure 5.6. Crystallite size computed for all the $CuSbS_2$ thin films formed at thickness of 650, 850 and 1050 nm was approximately 35, 27 and 20 nm and microstrain values of 4 x 10^{-3}, 1.6 x 10^{-3} and 7.4 x 10^{-4}, respectively. The decrease of grain size can be attributed to the formation of new smaller grains on larger grains due to increase of thickness (Lalitha et al., 2004) and the decrease of microstrain is due to the improved of crystallinity of the films by increasing the thickness (Öztas and Bedir, 2008).

(c) Variation of Cu thickness

The sample of five deposition of Sb_2S_3 (1000 nm) was selected on which different Cu thicknesses of 10, 30 and 50 nm were deposited, annealing the samples at 350 °C in low vacuum (Figure 5.7).

Sb₂S₃: five deposition

Cu thickness: 10, 30 and 50 nm
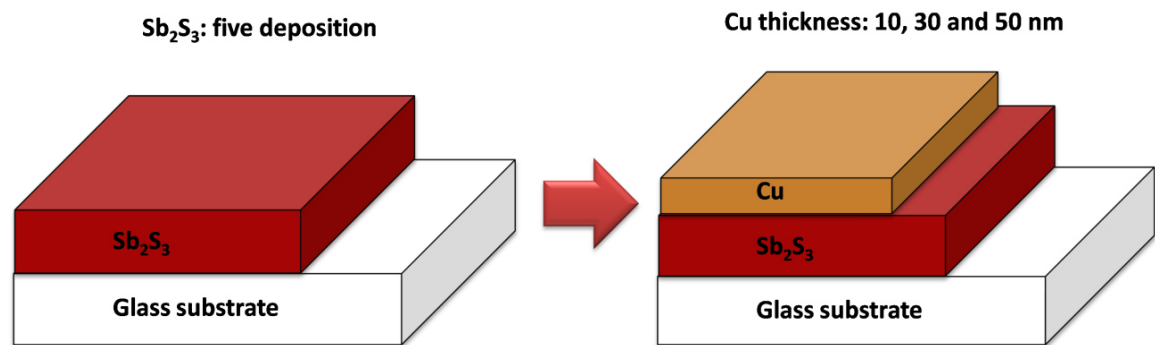
Figure 5.7 Schematic diagram of five depositions of Sb_2S_3 and Cu thickness variation of 10, 30 and 50 nm samples

Figure 5.8shows diffraction patterns recorded in the grazing incidence angle at 0.3° for the thin films formed by heating Sb_2S_3/Cu precursor samples annealed at 350 °C, 1000 nm Sb_2S_3in thickness and Cu of 10, 30 and 50 nm. Thin film formed for 10 nm Cu shows strong peaks of Sb_2S_3 (PDF#42-1393) and peaks of $CuSbS_2$. As Cu thickness increases to 30 nm Sb_2S_3 peaks decreases, evolving peaks due to $CuSbS_2$. For thin film with 50 nm of Cu, a complete formation of $CuSbS_2$marked by the planes (200), (210), (400), (111), (301),

(501), (321), (521) and(212)without any traces of secondary phases was achieved, having a final thickness of around 1050 nm.
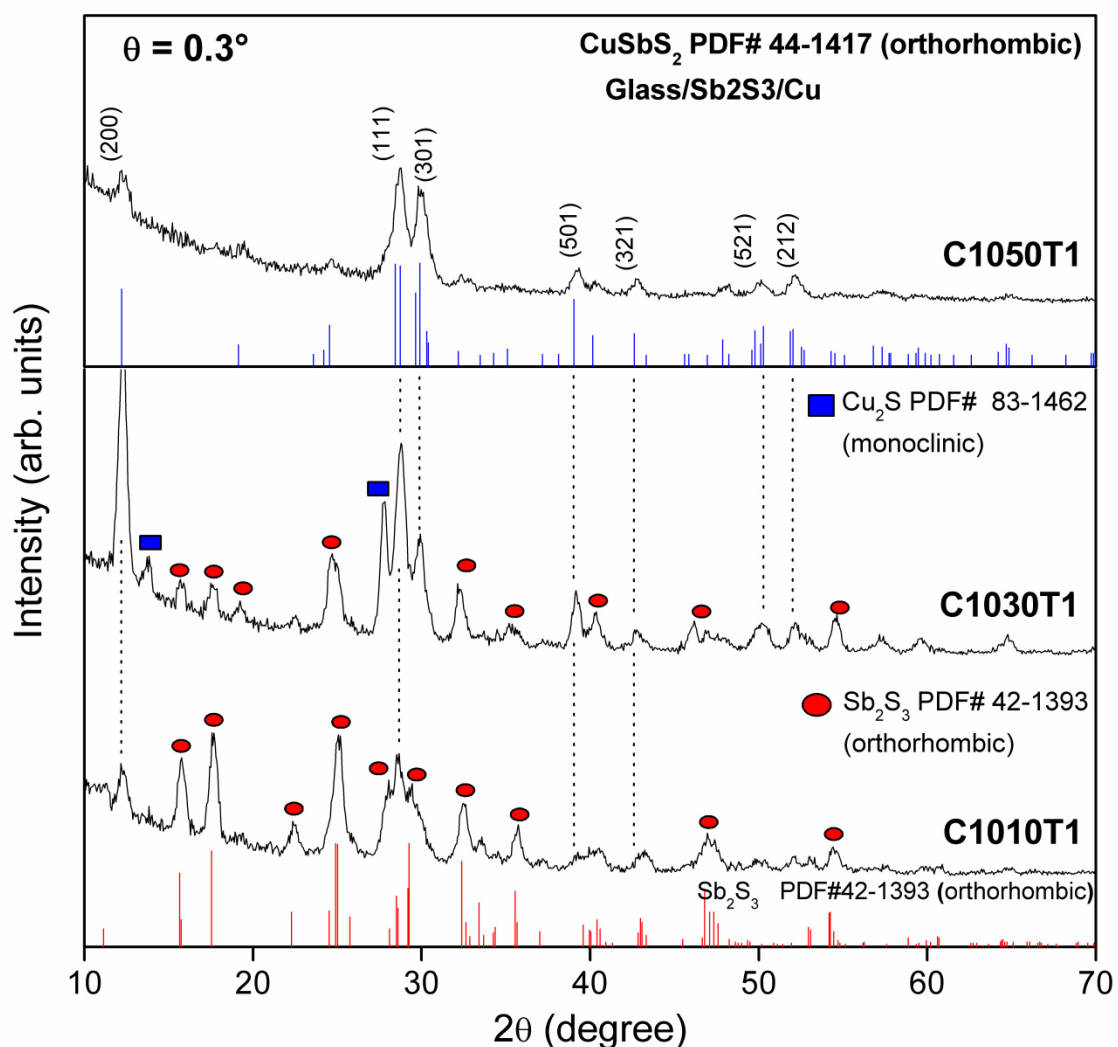
Figure 5.8 GIXRD patterns at θ=0.3° for glass/Sb₂S₃/Cu of 1000 nm Sb₂S₃ and variation of Cu thickness in 10 nm, 30 nm and 50 nm, annealed at 350 °C for 1h (Reproduced with kind permission from Springer)

Based on the last results obtained, the diffraction patterns for the thin film of glass/Sb₂S₃(*5 depositions*)/Cu (*50 nm*) annealed at 350 °C (1050 nm final thickness) at grazing incidence angles of 0.3°, 1.5° and 3.0° are shown in Figure 5.9.From the figure, as the angle of incidence increases CuSbS₂ peaks intensity increases due to enhanced penetration depth of the X-rays and the presence of Cu₂S start to appear at incidence angle of 1.5°. The penetration depth of the X-

rays in the sample is related with the incidence angle. We make a calculation using the equation:

$$\tau_{1/e} = \frac{\sin \alpha}{\mu} \tag{5.2}$$

where α is the incidence angle and μ is the attenuation coefficient.

Our calculations showed a penetration depth of 60 nm, 300 nm and 600 nm for samples at 0.3°, 1.5° and 3.0° of incidence angles respectively. This demonstrates the formation of single $CuSbS_2$ phase near the surface and mixed phases of $CuSbS_2$ and Cu_2S in the depth.
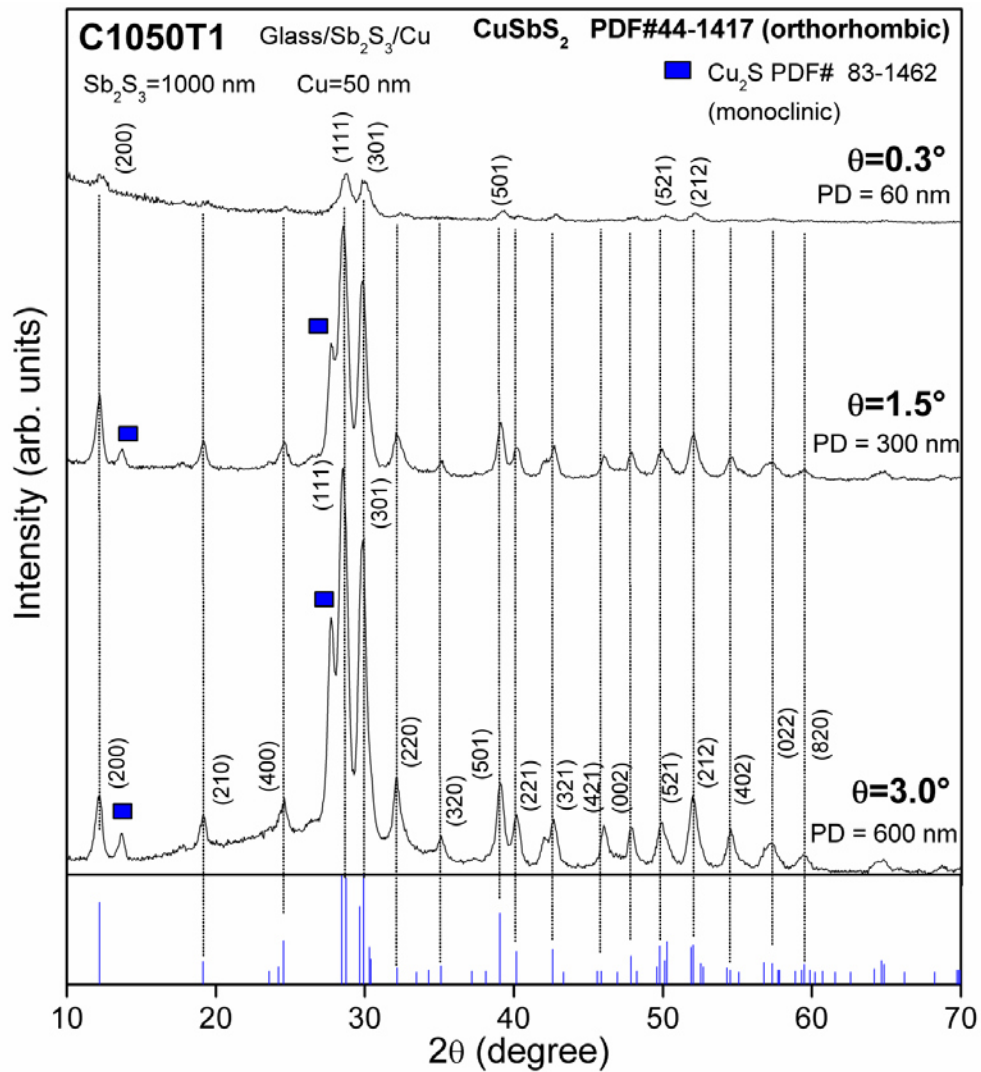
Figure 5.9 GIXRD patterns at θ=0.3°, 1.5° and 3.0° for glass/Sb₂S₃/Cu of 1050 nm annealed at 350 °C for 1h

Now, based on the previous results, samples formed at 350 °C by varying annealing time 1, 2, 3 and 4 h were analyzed.

We selected annealing times above 1 hour to assure a complete diffusion and reaction between all precursors to form the chalcostibite phase with good crystallinity.
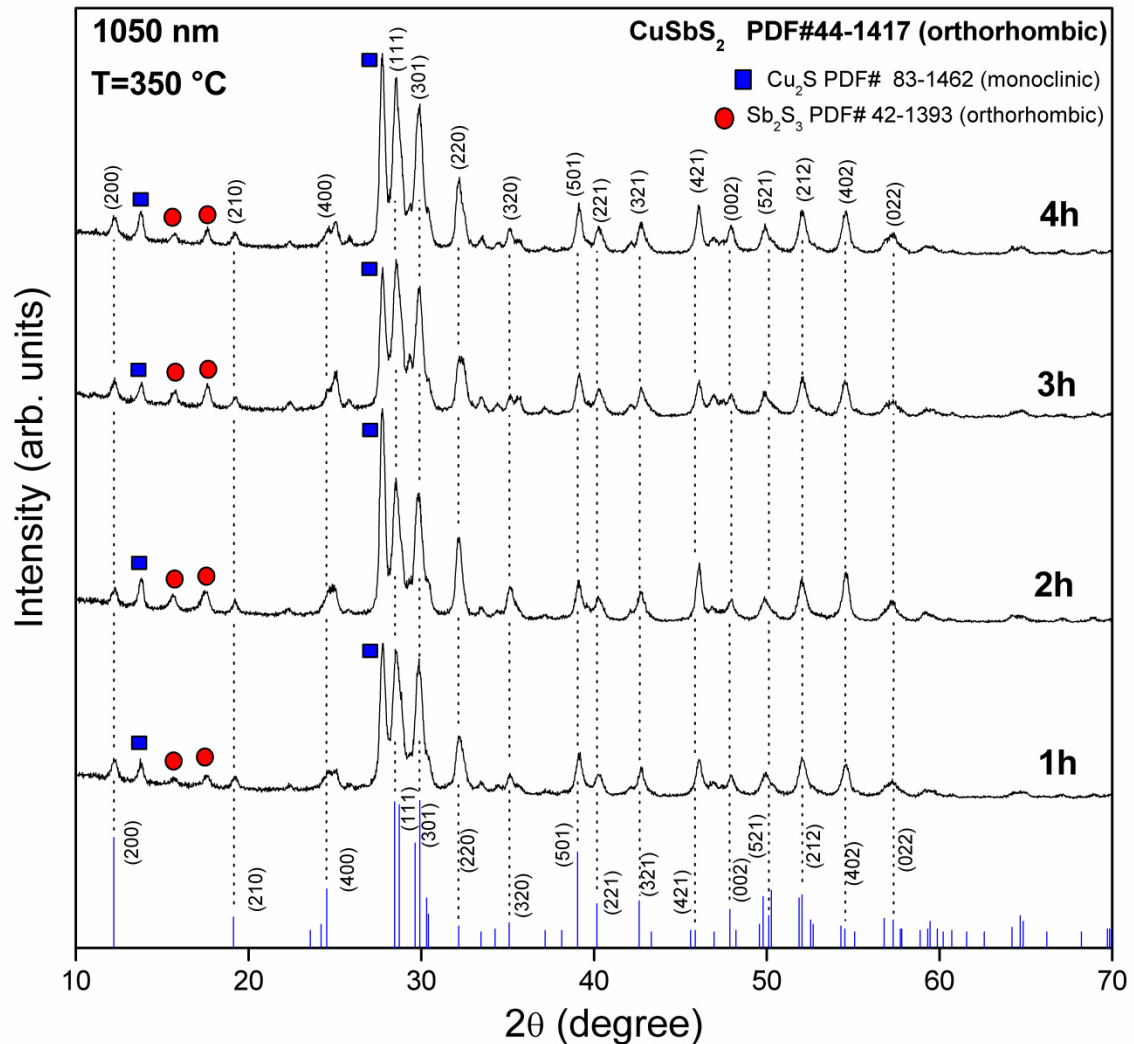
Figure 5.10 XRD patterns for multilayers glass/Sb_2S_3/Cu of 1050 nm in thickness annealed at 350 °C during 1, 2, 3 and 4 h

Figure 5.10shows the diffraction patterns of glass/Sb_2S_3/Cu annealed at 350 °C during 1, 2, 3 and 4 h. All these thin films exhibit reflections due to the presence of orthorhombic $CuSbS_2$, as the primary phase, increasing the peak intensity as annealing time increased. In all the samples, monoclinic Cu_2S as a

secondary phase and orthorhombic Sb_2S_3 as an unreacted precursor as indicated in the figure.
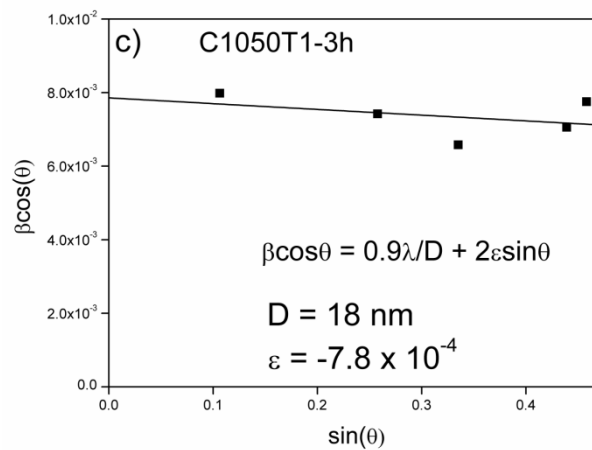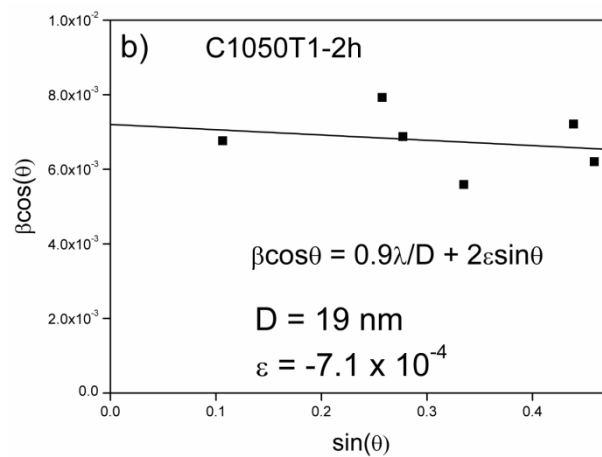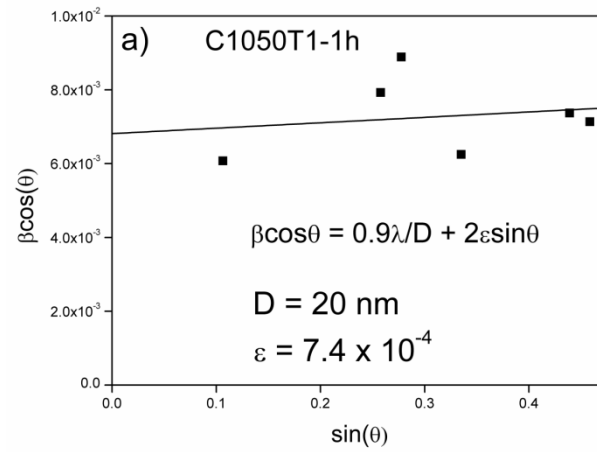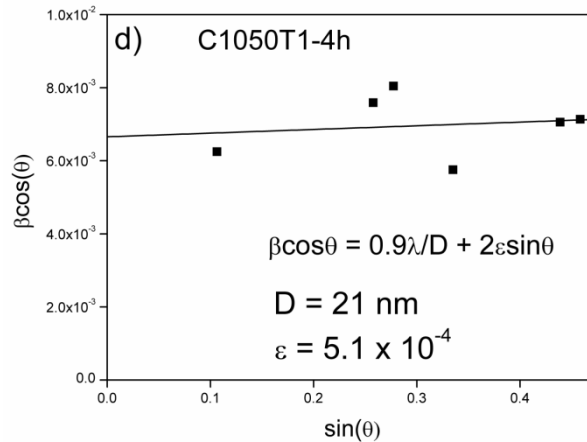
Figure 5.11 Average crystallite sizes and microstrain of the multilayers of glass/Sb$_2$S$_3$/Cu of 1050 nm in thickness annealed at 350 °C during 1, 2, 3 and 4 h

The average crystallite size and lattice strain were evaluated by Williamson-Hall plots for the four annealed CuSbS$_2$ thin films by the peak profile analysis of (200), (301), (220), (501) and (212) planes as shown in Figure 5.11. Crystallite size computed for all the CuSbS$_2$ thin films annealed at 1, 2, 3 and 4 h was approximately 20, 19, 18 and 21 nm and microstrain values of 7.4 x 10^{-4}, -7.1 x 10^{-4}, -7.8 x 10^{-4} and 5.1 x 10^{-4}, respectively.

5.1.2 Morphology (AFM, SEM)

The morphology of selected samples (at different annealing temperatures and different thicknesses) was analyzed by atomic force microscopy (AFM) in height mode using semicontact mode. Also, phase contrast images as well as the RMS values to measure the surface roughness are presented.

Morphological features of glass/Sb$_2$S$_3$/Cu thin films of 650 nm in thickness annealed at 350 °C, 375 °C and 400 °C are illustrated by 1 µm × 1 µm atomic force micrographs (AFM)in Figure 5.12, marked as a, c and e corresponding to height mode in 3D, respectively. These images revealed spherical grains of diameter in ranges of 40-100 nm (Figure 5.12a), 30-60 nm (Figure 5.12c) and 20-50 nm (Figure 5.12e) respectively. The phase contrast images of the respective topographies are illustrated in Figure 5.12b, d and f. In

all the images, we observed densely packed grains with well-defined grain boundaries. The RMS roughness analysis measured from 3D images showed that as the annealing temperature increased from 350 °C to 400 °C, the roughness decreased from 12.9 to 9.2 nm.
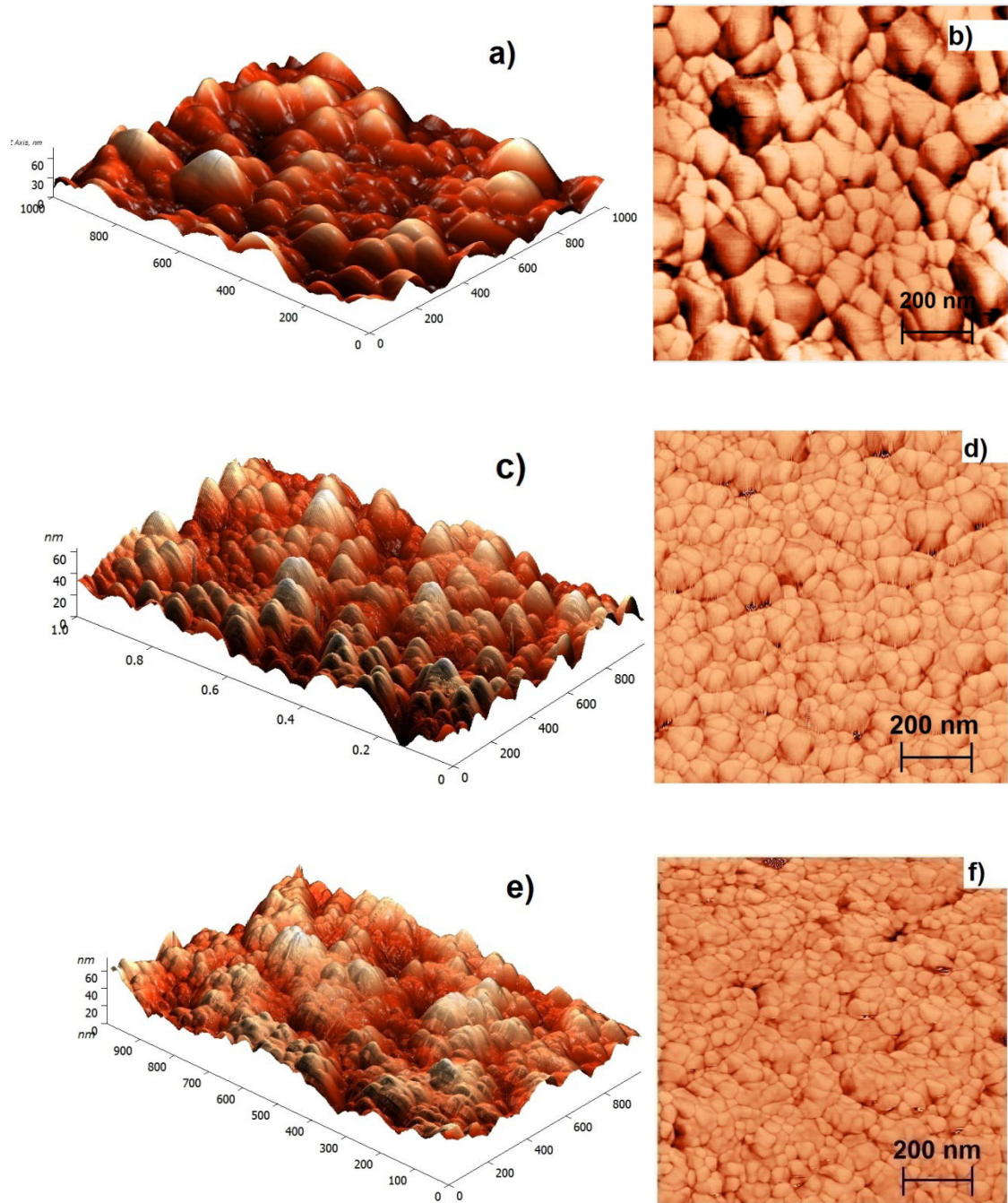
Figure 5.12 Atomic force micrographs for glass/Sb$_2$S$_3$/Cu thin films annealed for 1h at (a) 350 °C (C650T1), (c) 375 °C (C650T2) and (e) 400 °C (C650T3) in height mode 3D, (b) 350 °C, (d) 375 °C and (f) 400 °C corresponding phase contrast images

Figure 5.13 shows morphological features of glass/Sb_2S_3/Cu thin films annealed at 350 °C 1h of 650 nm, 850 nm and 1050 nm in thickness illustrated by 1 µm × 1 µm atomic force micrographs (AFM), marked as a, c and e corresponding to height mode in 3D, respectively. The images revealed spherical grains of diameter in ranges of 40-100 nm (Figure 5.13a), 30-80 nm (Figure 5.13c) and 50-100 nm (Figure 5.13e) respectively. The phase contrast images of the respective topographies are illustrated in Figure 5.13b, d and f. In these images, we can observe densely packed grains with well-defined grain boundaries. The RMS roughness analysis measured from 3D images showed that as the thickness of the samples increases the roughness decreases from 12.9 to 9.5 nm.
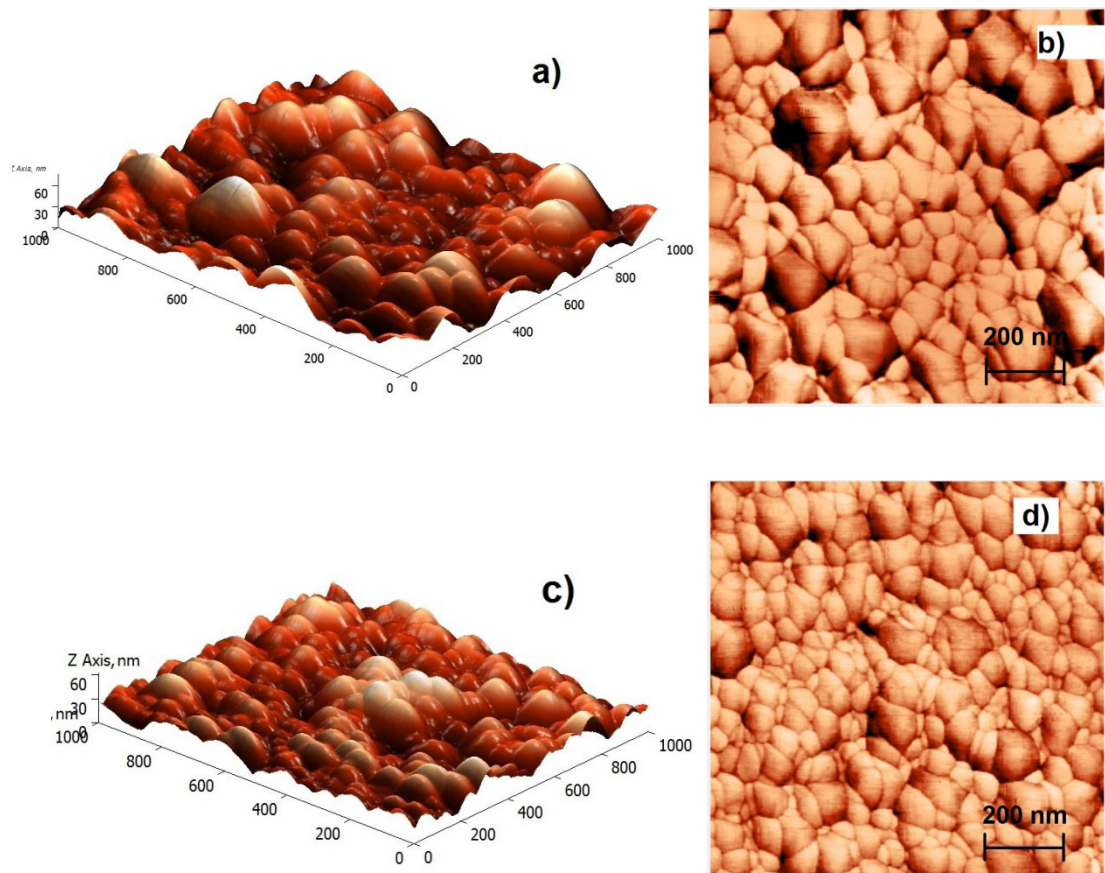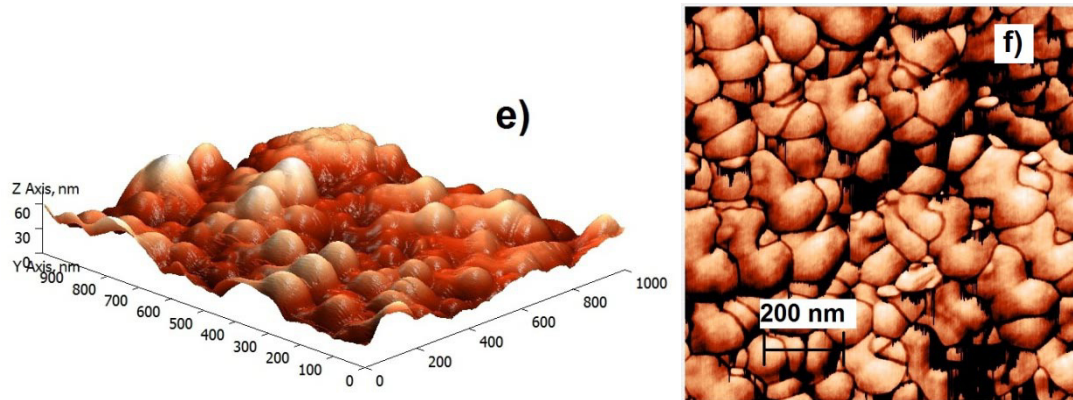
Figure 5.13 Atomic force micrographs for glass/Sb$_2$S$_3$/Cu thin films annealed at 350 °C for 1h of thickness (a) 650 nm (C650T1), (c) 850 nm (C850T1) and (e) 1050 nm (C1050T1) in semi-contact mode 3D, (b) 650 nm, (d) 850 nm and (f) 1050 nm corresponding phase contrast images

According to the results obtained by AFM, we selected some samples to characterize its morphology by scanning electron microscopy.

Figure 5.14 shows SEM micrographs of glass/Sb$_2$S$_3$/Cu of 650 nm in thickness formed by the step by step heating at 350 °C(Figure 5.14a),375 °C (Figure 5.14b) and400 °C(Figure 5.14c) during 1h. Figure 5.14a show a densely and compact surface having small particles distributed over the entire surface of around 50 nm in size. After the step heating at 375 °C (Figure 5.14b) the concentration of the small particles increases over the surface increasing their size up to 100 nm. After the final step heating at 400 °C (Figure 5.14c) the grain boundaries were well defined at the surface increasing the concentration and the size of the small particles, having values in the range of 100-150 nm. The SEM characterization of these three samples revealed the formation of crack and pinhole free thin film after simple annealing and step by step annealing at temperatures from 350 °C to 400 °C.

Figure 5.15 show the cross-sectional SEM image for glass/Sb$_2$S$_3$/Cu thin film of three deposition of Sb$_2$S$_3$ and 50 nm of Cu annealed at 350 °C. The image showed a compact and uniform thin film having a thickness of 650 nm for the sample.
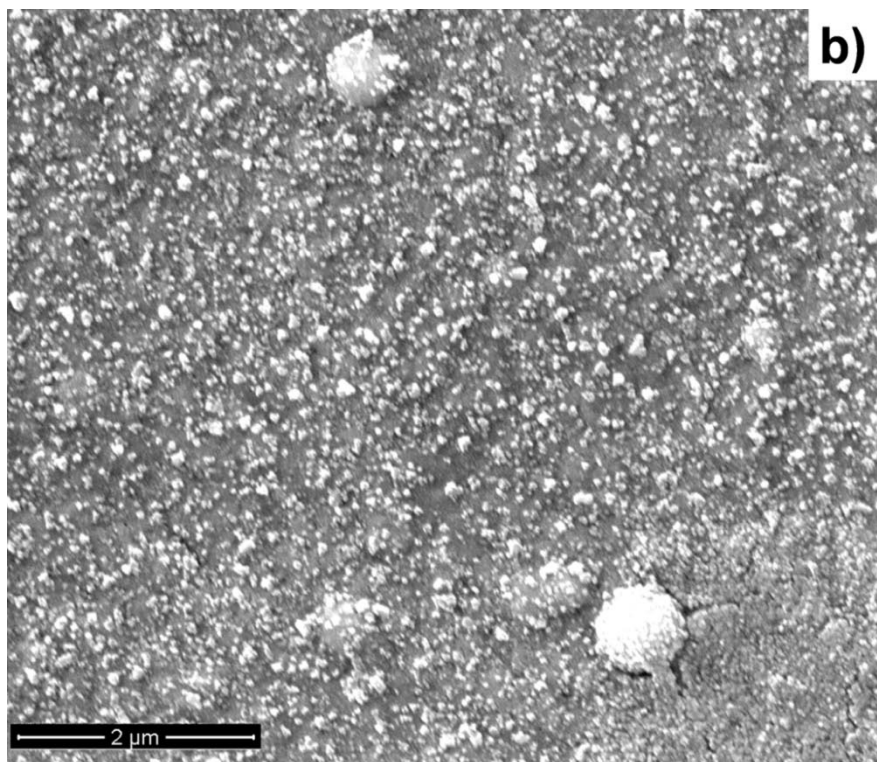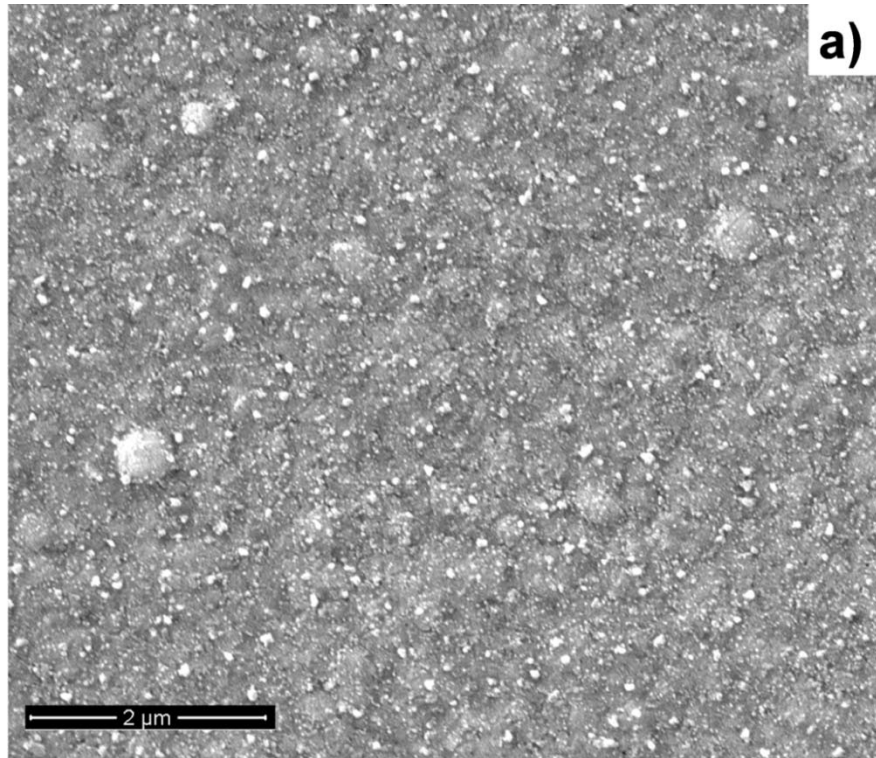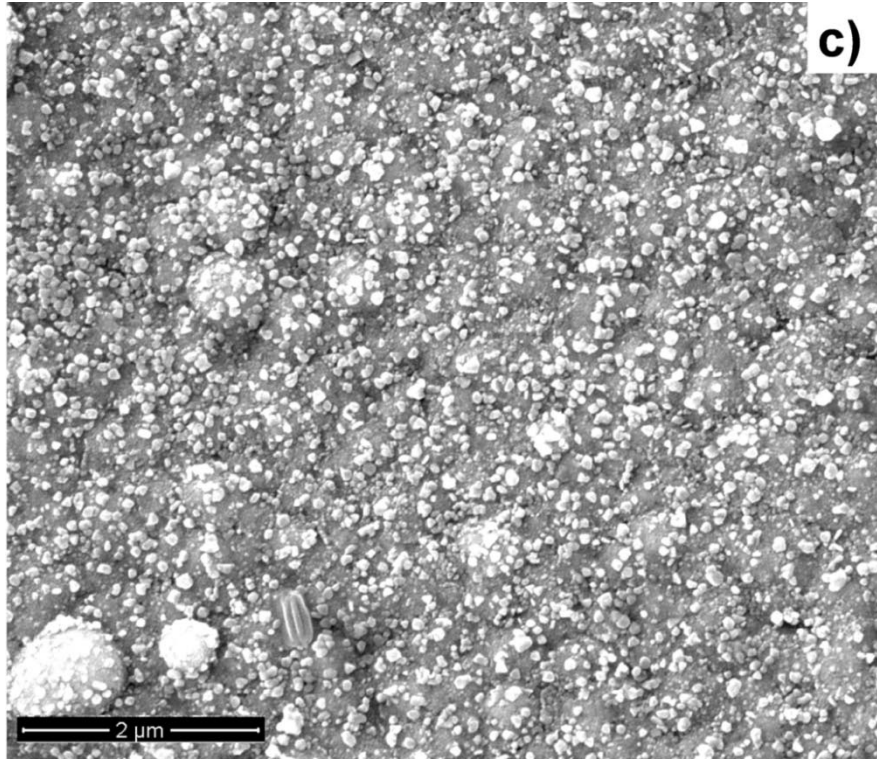
Figure 5.14 SEM micrographs for glass/Sb$_2$S$_3$/Cu thin films of 650 nm in thickness (a) annealed at 350 °C (C650T1) and step by step annealed at (b) 375 °C (C650T1,2) and (c) 400 °C (C650T1,2,3) for 1h
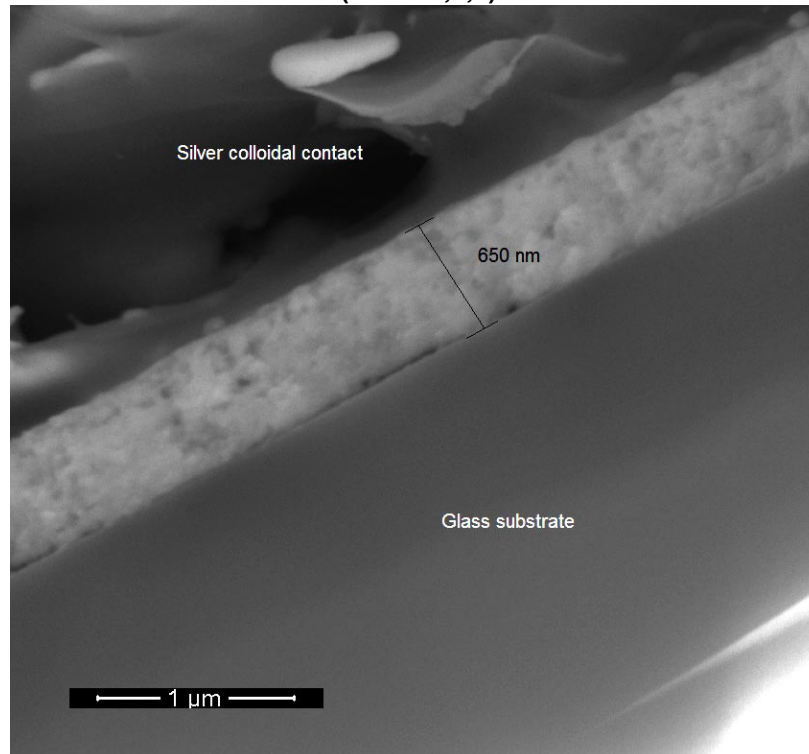
Figure 5.15 Cross-sectional SEM image for glass/Sb$_2$S$_3$/Cu thin film of 650 nm annealed at 350 °C for 1h (Reproduced with kind permission from Elsevier)

Figure 5.16 shows SEM micrographs of precursor glass/Sb_2S_3 (Figure 5.16a), glass/Sb_2S_3/Cu (Figure 5.16b) as prepared and glass/Sb_2S_3/Cu of 1050 nm in thickness annealed at 350 °C during 1h (Figure 5.16c), 2h (Figure 5.16d) 3h (Figure 5.16e) and 4h (Figure 5.16f). The precursor of glass/Sb_2S_3 shows a compact surface with well-defined channels in the entire surface and the formation of pinholes over the surface (Figure 5.16a). For the multilayer glass/Sb_2S_3/Cu as prepared (Figure 5.16b) a well-defined copper spherical particles of 50 nm in diameter covering the surface are shown with the absence of pinholes. After 1h heating (Figure 5.16c) a large concentration of small particles of different sizes (50-100 nm) and shapes are distributed homogeneously over a dense and compact surface with some pinholes. These particles became smaller at large annealing times (Figure 5.16d and e) interconnected each other like a chain until they disappear and combined with the surface (Figure 5.16f) giving a compact surface with remarkable pinholes into it.
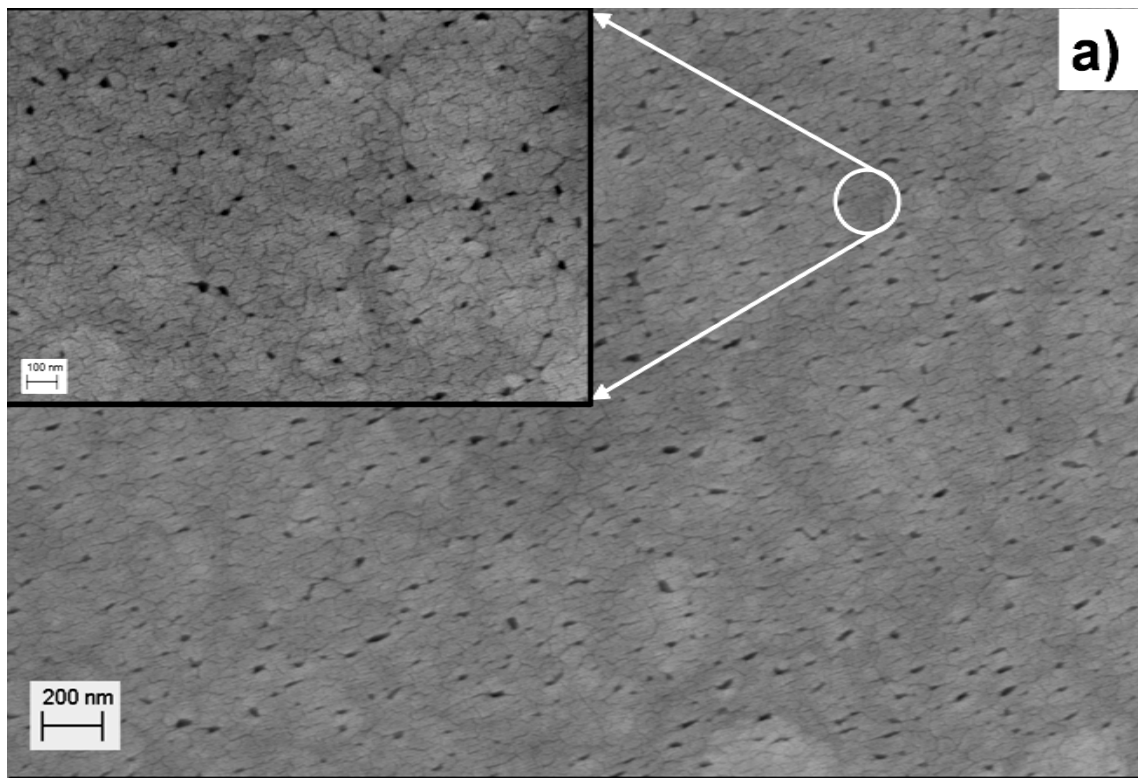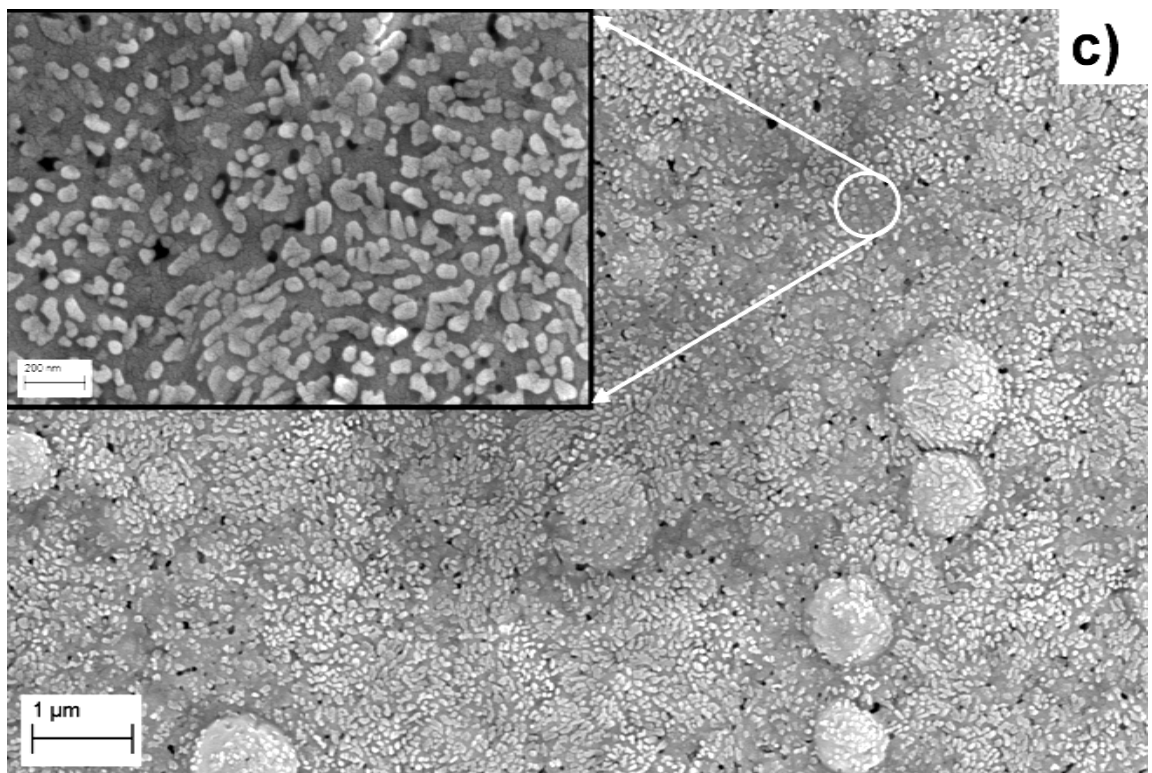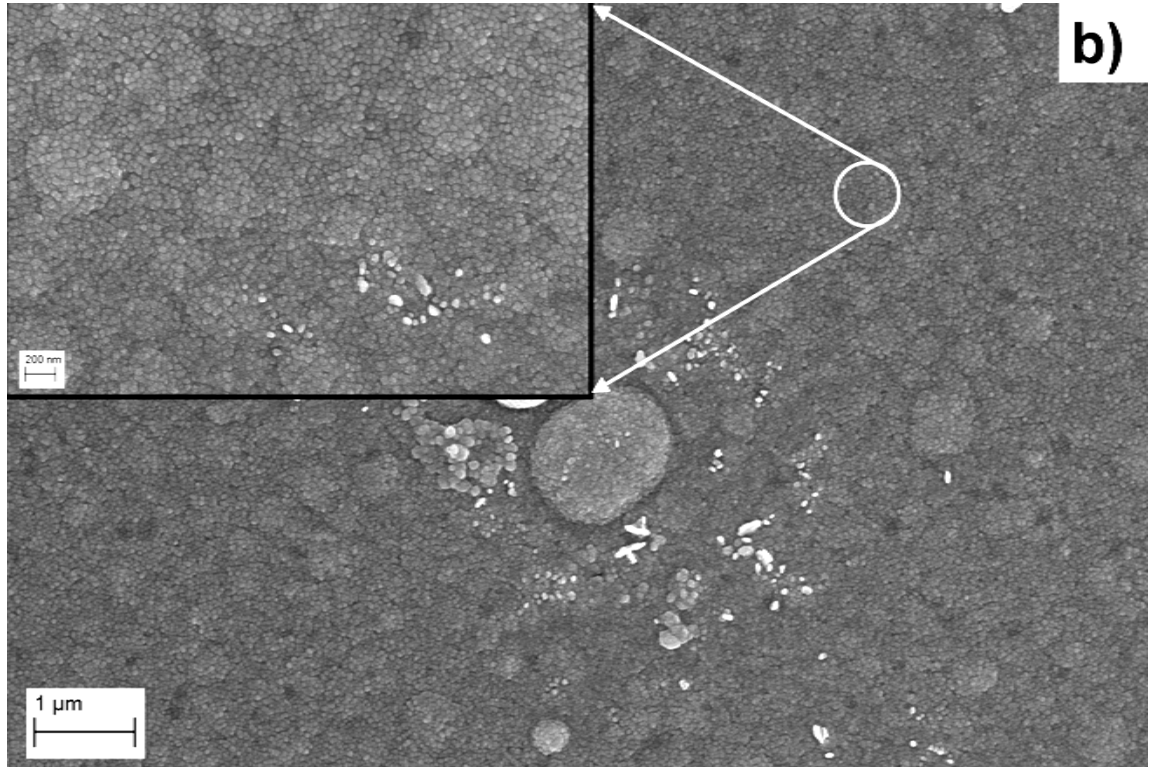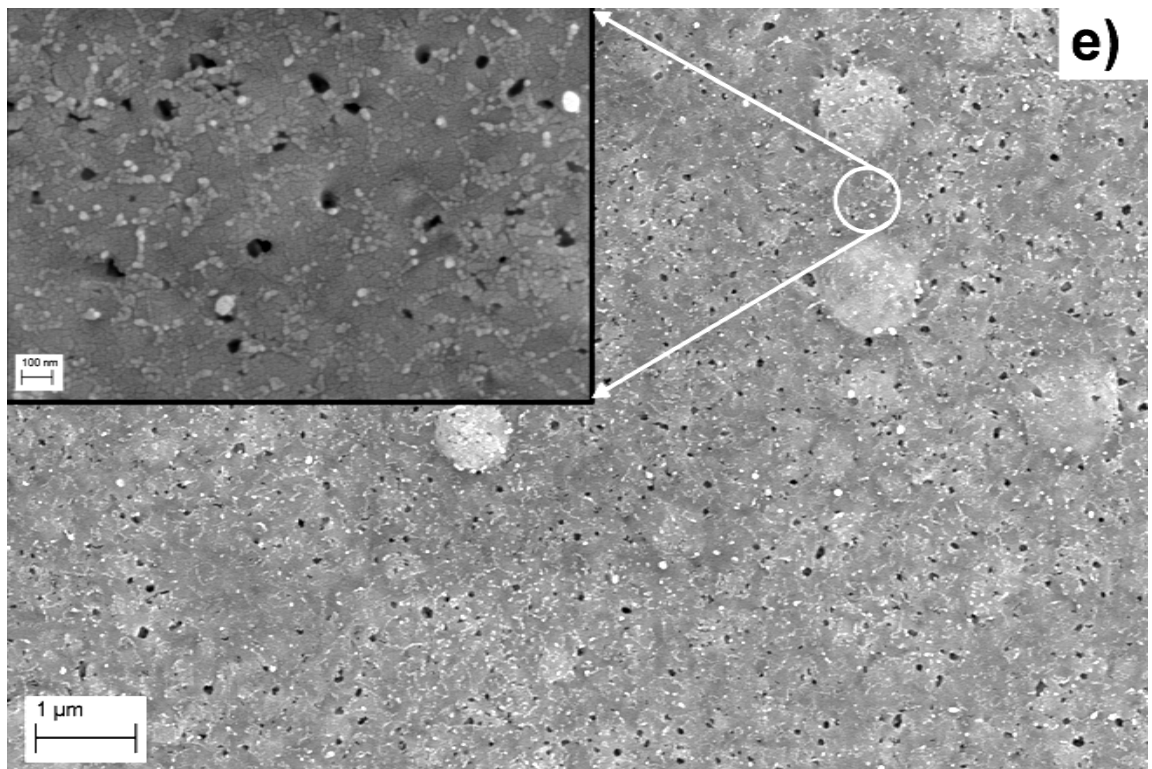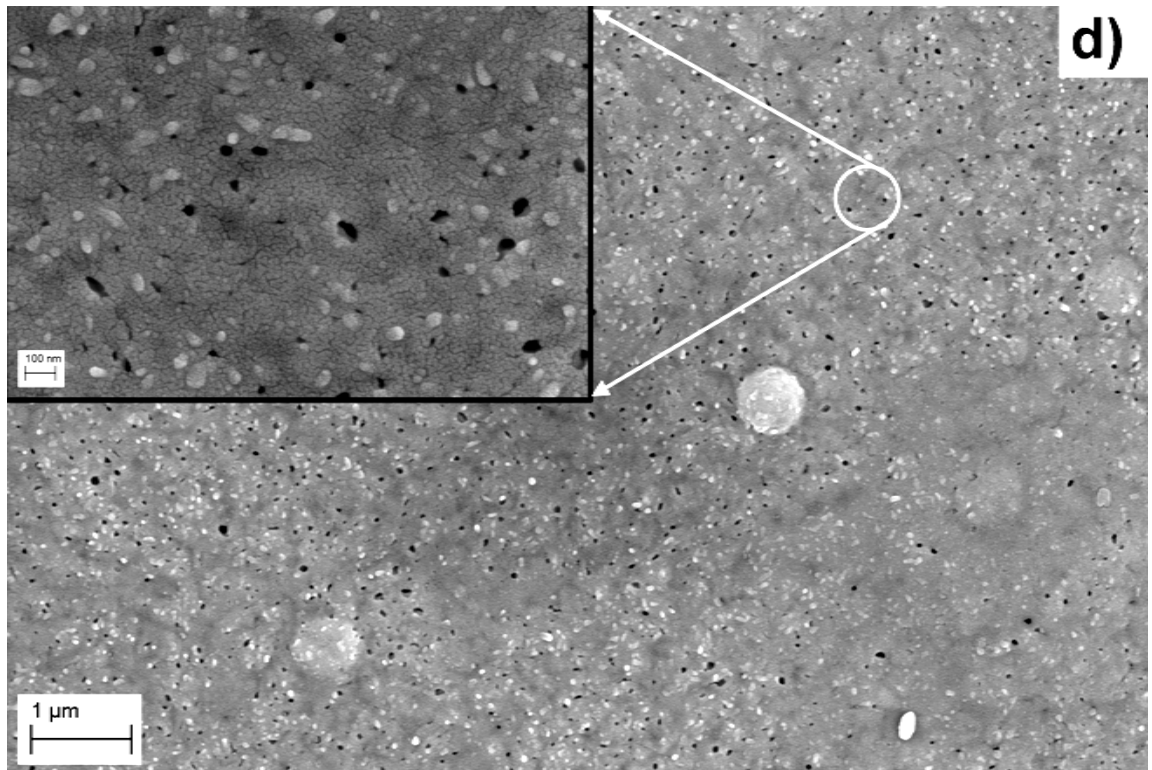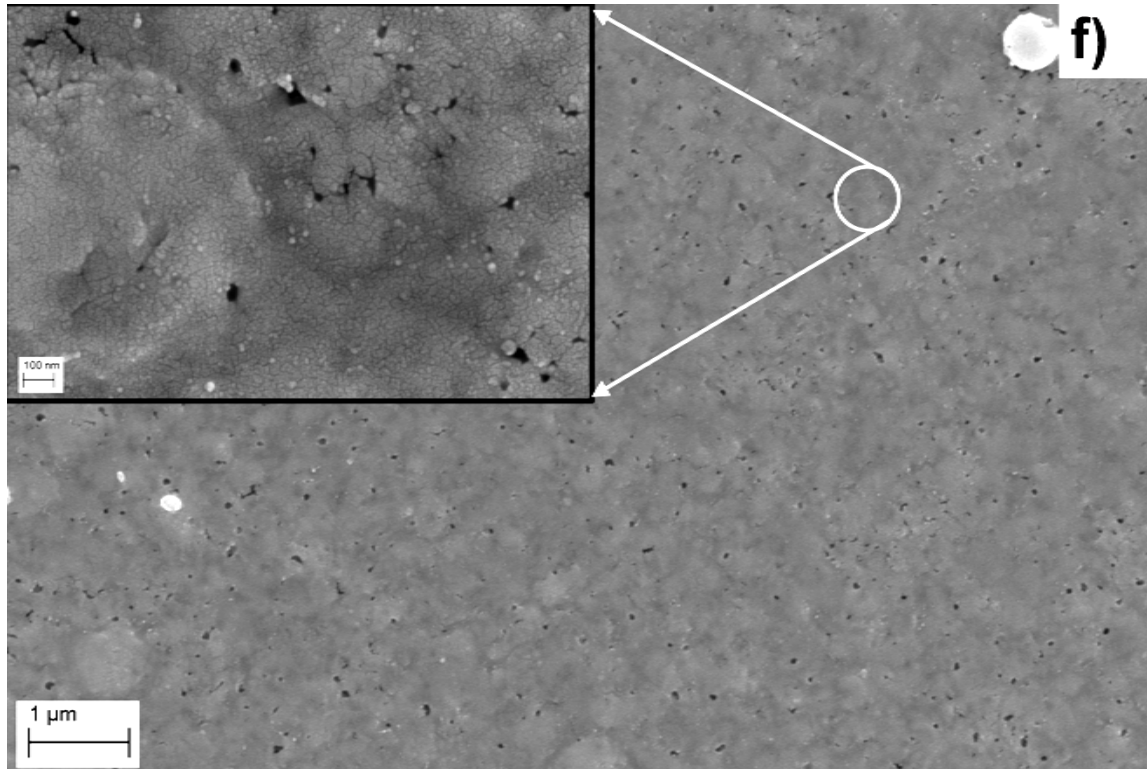
Figure 5.16 SEM micrographs for precursor (a) glass/Sb$_2$S$_3$, (b) glass/Sb$_2$S$_3$/Cu as prepared and glass/Sb$_2$S$_3$/Cu thin films of 1050 nm in thickness annealed at 350 °C for (c) 1h, (d) 2h, (e) 3h and (f) 4h (Reproduced with kind permission from Springer)

5.1.3 Composition (XPS)

The elemental composition and the oxidation states of each element present in the compounds formed by the two stage process deposition using CBD and sequentially thermal evaporation was analyzed by X-ray photoelectron spectroscopy, in order to confirm the results obtained in the structural characterization by XRD. For the complete analysis, only some samples were selected, such as the precursors of glass/Sb$_2$S$_3$ and glass/Sb$_2$S$_3$/Cu and the thin films of glass/Sb$_2$S$_3$/Cu of 650 nm and 1050 nm in thickness annealed at 350 °C for 1h in low vacuum. Analysis of high resolution spectra and depth profile were performed.
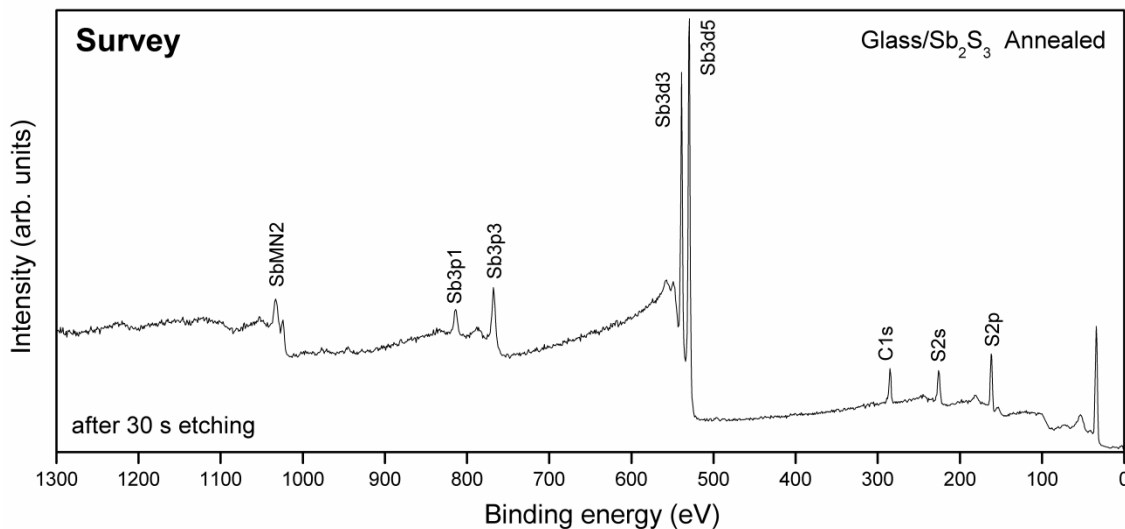
Figure 5.17 Survey spectrum of glass/Sb$_2$S$_3$ precursor thin film annealed at 350 °C after 30 s Ar$^+$ ion etching

For the precursor glass/Sb$_2$S$_3$ annealed at 350 °C, a typical survey spectrum recorded from the surface of the thin film after 30 s Ar$^+$ ions etching is shown in Figure 5.17, which indicates the presence of Sb, S and C. The presence of carbon is due to the carbon adventitious present for the environmental exposure of the sample, reason for which is needed to etch the surface for more time to clean and reduce the amount of carbon in the surface. For the detailed analysis, a narrow scan was done for Sb and S, after one cycle of etching using Ar$^+$ ions generated at 3 keV for 30 seconds. From the Figure 5.18a and b, the Sb3d$_{5/2}$, Sb3d$_{3/2}$, S2p$_{3/2}$ and S2p$_{1/2}$ peaks at 529.50 eV, 538.84 eV, 161.4 eV and 162.56 eV respectively corresponding to Sb^{3+} and S^{2-} in Sb$_2$S$_3$ with a peak splitting of 9.34 eV and 1.16 eV for Sb and S core level peaks respectively (Naumkin et al., 2000).

For the precursor glass/Sb$_2$S$_3$/Cu as prepared, a typical survey spectrum recorded from the surface of the thin film without etching is shown in Figure 5.19, which indicates the presence of Cu, Si, C and O. The presence of carbon is due to the adventitious carbon, the oxygen is due to the oxidized surface for the environmental exposure and meanwhile the presence of silicon is attributed to the small pieces of corning glass left on the surface by the process of cutting in the preparation of the sample. There was no presence of sulfur and antimony

in this surface analysis (without etching), due to the fact that X-ray penetration is less than 10 nm and Sb_2S_3 layer was no reached.

Core Level Peak	Binding energy (eV)	FWHM	Area ratio	Compound
■ $Sb3d_{5/2}$	529.50	1.20	1.00	Sb_2S_3
□ $Sb3d_{3/2}$	538.84	1.20	0.66	Sb_2S_3

Core Level Peak	Binding energy (eV)	FWHM	Area ratio	Compound
■ $S2p_{3/2}$	161.40	1.00	1.00	Sb_2S_3
□ $S2p_{1/2}$	162.56	1.00	0.50	Sb_2S_3
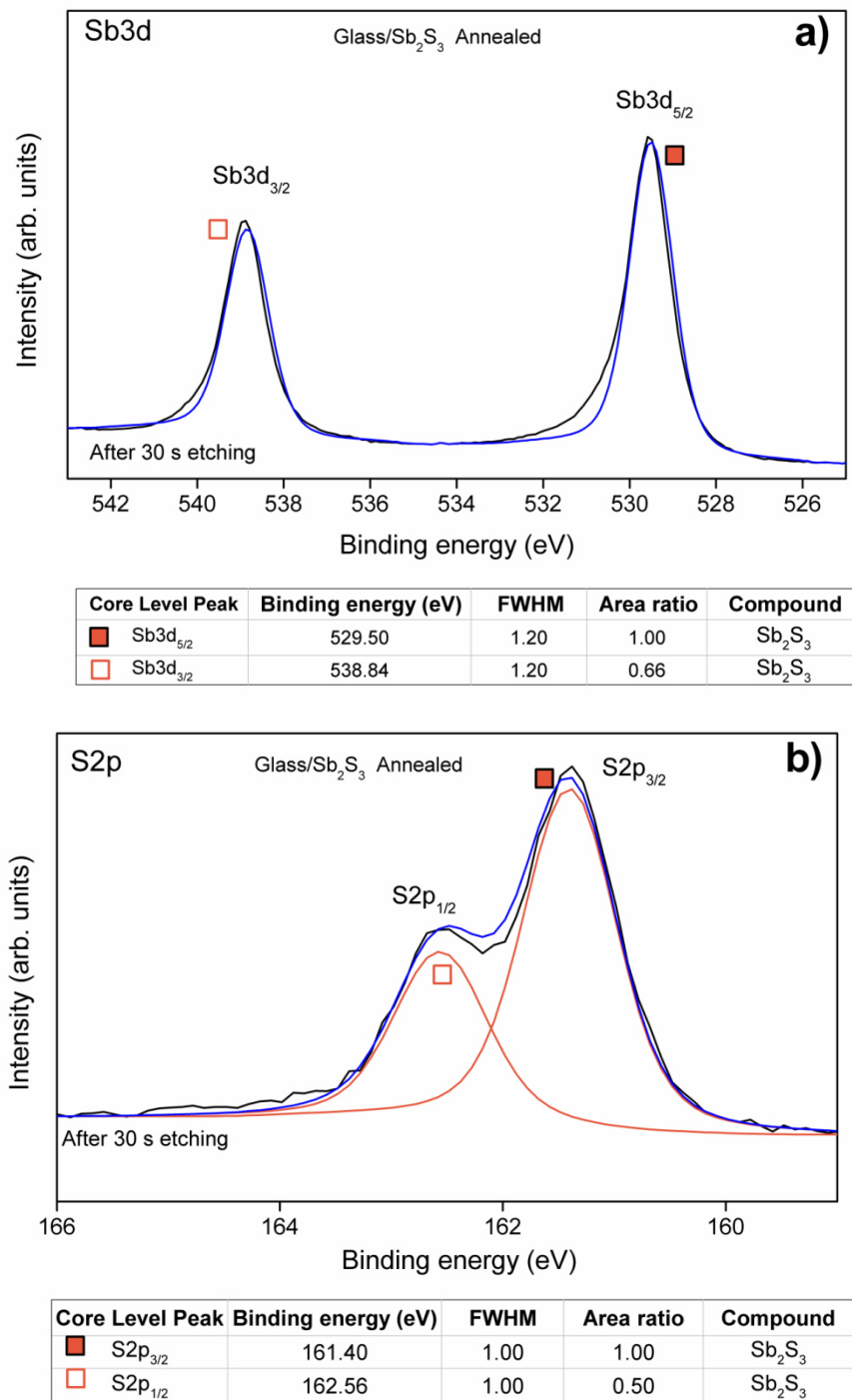
Figure 5.18 High-resolution spectra of (a) Sb3d core level and (b) S2p core level of precursor glass/Sb_2S_3 annealed at 350 °C after 30 s Ar$^+$ ions etching
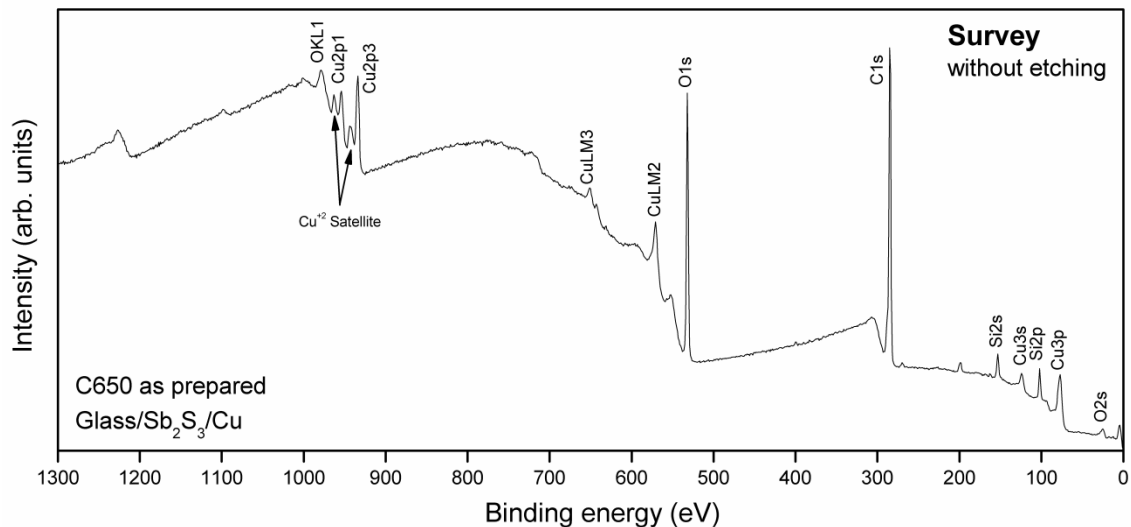
Figure 5.19 Survey spectrum of glass/Sb₂S₃/Cu precursor thin film as prepared without etching

For the precursor glass/Sb₂S₃/Cu as prepared, the analysis of the survey spectrum and high resolution core levels spectra after 540 s Ar⁺ ions etching generated at 3 keV are shown in Figure 5.20 and Figure 5.21 respectively. From the survey spectrum can be observed the presence of Cu, Sb and S without contaminant elements such as carbon and oxygen, which were removed from the surface due to the 180 s etching. From Figure 5.21a, the $Cu2p_{3/2}$ and $Cu2p_{1/2}$ peaks at 932.60 eV and 952.40 eV corresponding to the elemental state of Cu, which indicates that in the as prepared thin film, copper do not react with Sb₂S₃ layer. Figure 5.21b shows the formation of two doublets, indicating the formation of two different compounds. The dominated $Sb3d_{5/2}$ and $Sb3d_{3/2}$ peaks at 529.60 eV and 538.94 eV correspond to Sb^{3+} in Sb₂S₃(Naumkin et al., 2000). The lower intensity $Sb3d_{5/2}$ and $Sb3d_{3/2}$ peaks at 528.50 eV and 537.84 eV correspond to elemental state of Sb. The reduction of Sb^{3+} into Sb° is originated from the preferential sputtering of sulfur. When an ion beam for cleaning or profiling is used it can change the composition of a material through effects such as "*preferential sputtering*" and sputter reduction. In a material with multiple elements, elements may sputter at different rates and hence change the stoichiometry and the chemical environment of the analyzed surface. In preferential sputtering, the sputtering of light elements is preferred in

comparison with heavier elements. Preferential sputtering is extremely material dependent and depends upon ion type, energy, angle of incidence and temperature (Henrich and Cox, 1996).
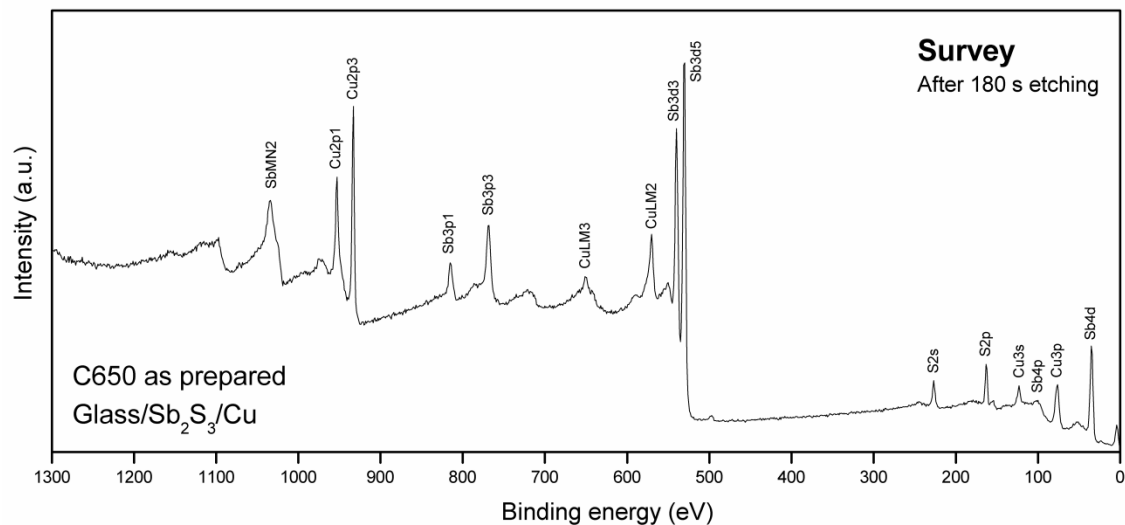
Figure 5.20 Survey spectrum of glass/Sb$_2$S$_3$/Cu precursor thin film as prepared after 180 s Ar$^+$ ions etching
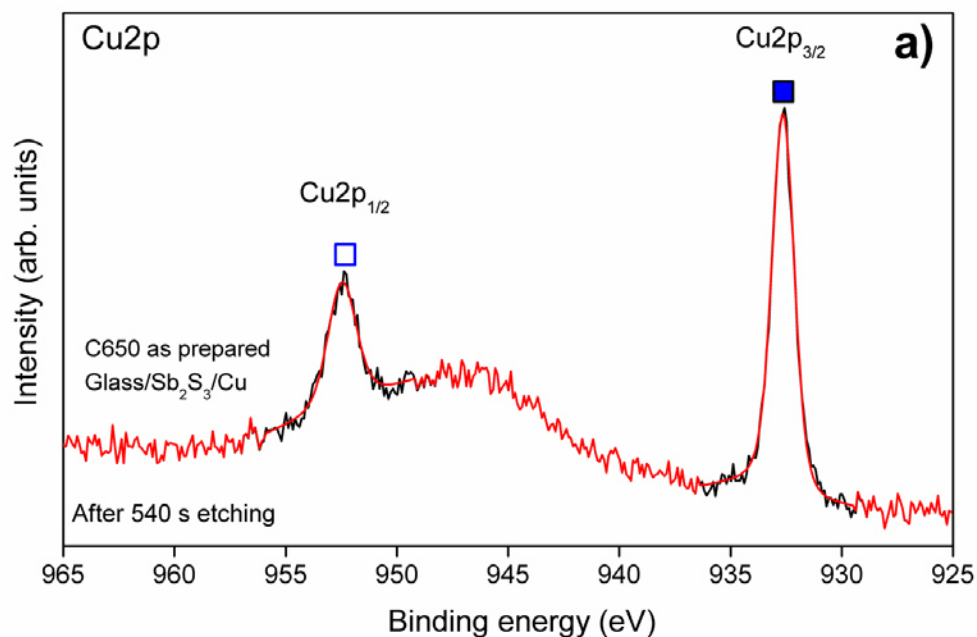
Core Level Peak	Binding energy (eV)	FWHM	Area ratio	Compound
■ Cu2p$_{3/2}$	932.60	1.15	1.00	Cu
□ Cu2p$_{1/2}$	952.40	1.15	0.50	Cu

Core Level Peak	Binding energy (eV)	FWHM	Area ratio	Compound
■ Sb3d$_{5/2}$	528.50	1.40	1.00	Sb
□ Sb3d$_{3/2}$	537.84	1.40	0.66	Sb
● Sb3d$_{5/2}$	529.60	1.40	1.00	Sb$_2$S$_3$
○ Sb3d$_{3/2}$	538.94	1.40	0.65	Sb$_2$S$_3$

Core Level Peak	Binding energy (eV)	FWHM	Area ratio	Compound
■ S2p$_{3/2}$	161.35	1.00	1.00	Sb$_2$S$_3$
□ S2p$_{1/2}$	162.51	1.00	0.50	Sb$_2$S$_3$
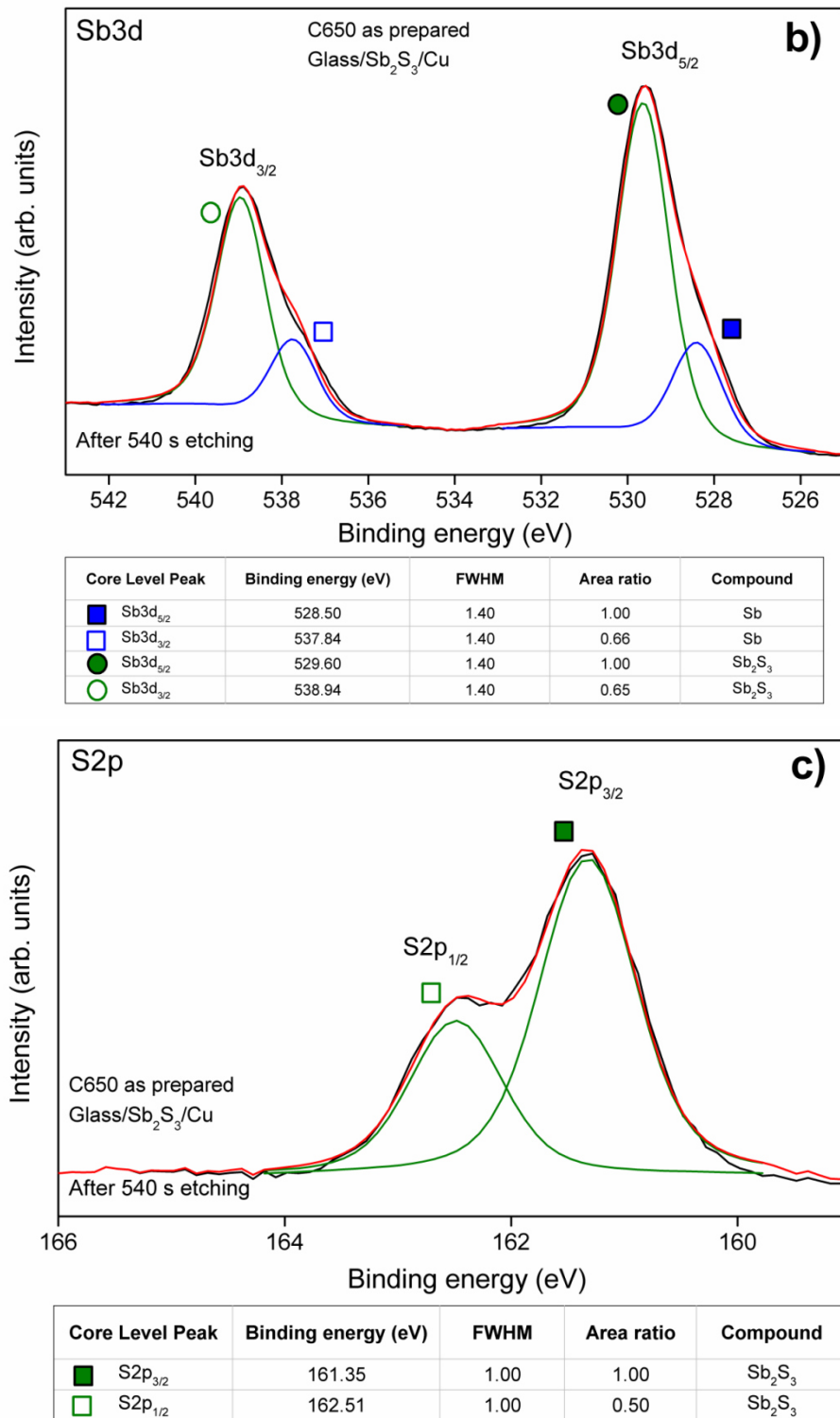
Figure 5.21 High-resolution spectra of (a) Cu2p (b) Sb3d and (c) S2p core levels of precursor glass/Sb$_2$S$_3$/Cu as prepared after 540 s Ar$^+$ ions etching

Figure 5.21c the S2p$_{3/2}$ and S2p$_{1/2}$ peaks located at 161.35 eV and 162.51 eV corresponds to S^{2-} in Sb$_2$S$_3$. After an etching of the as prepared thin film it was confirmed the oxidation states of the precursor layer, having a diffusion of copper into Sb$_2$S$_3$ layer without any reaction between two layers.

To demonstrate the diffusion of copper in the as prepared thin film, a depth profile analysis was performed as shown in the XPS profile montage given in Figure 5.22a, where Cu2p, Sb3d and S2p core levels were detected through the entire thickness until they disappear, showing the O1s core level, which indicate that substrate has been reached, and the relative composition for the elements are shown in Figure 5.22b. According to the as prepared stacked layers in Figure 5.22b a decrease on atomic percentage of Cu followed by an increase of relative composition of Sb$_2$S$_3$ is observed. The diffusion of copper through the Sb$_2$S$_3$ layer is evident, and it was demonstrated that both layer do not react at this condition as shown in the high resolution spectra.

For the thin film of glass/Sb$_2$S$_3$/Cu of 650 nm in thickness annealed at 350 °C (C650T1) the analysis of the survey spectrum and high resolution core levels spectra after 150 s Ar$^+$ ions etching generated at 3 keV are shown in Figure 5.23and Figure 5.24respectively. From the survey spectrum (Figure 5.23), the presence of copper, antimony and sulfur without contaminant elements such as carbon and oxygen which were removed by the Ar$^+$ ion etching are observed.

Figure 5.24a, b and c shows high resolution experimental spectra (black dotted curve) and theoretical spectra (red solid curve) for Cu2p, Sb3d and S2p core levels along with the deconvoluted ones (color curves). From the top graph in Figure 5.24a, the Cu2p$_{3/2}$ and Cu2p$_{1/2}$ core levels peaks constituted two distinct peaks as marked. The two Cu2p doublet peak energies showed distinct chemical shifts indicating the formation of two different compounds of copper. The lower intensity peaks at 932.2 eV and 952.0 eV matched with the formation of Cu$_2$S (Mielczarski and Minni, 1984). The dominated peak values of Cu2p doublets at 932.9 eV and 952.7 eV with a peak splitting of 19.8 eV are in good agreement with Cu^{+1} as expected for CuSbS$_2$ compound (Yang et al., 2014).
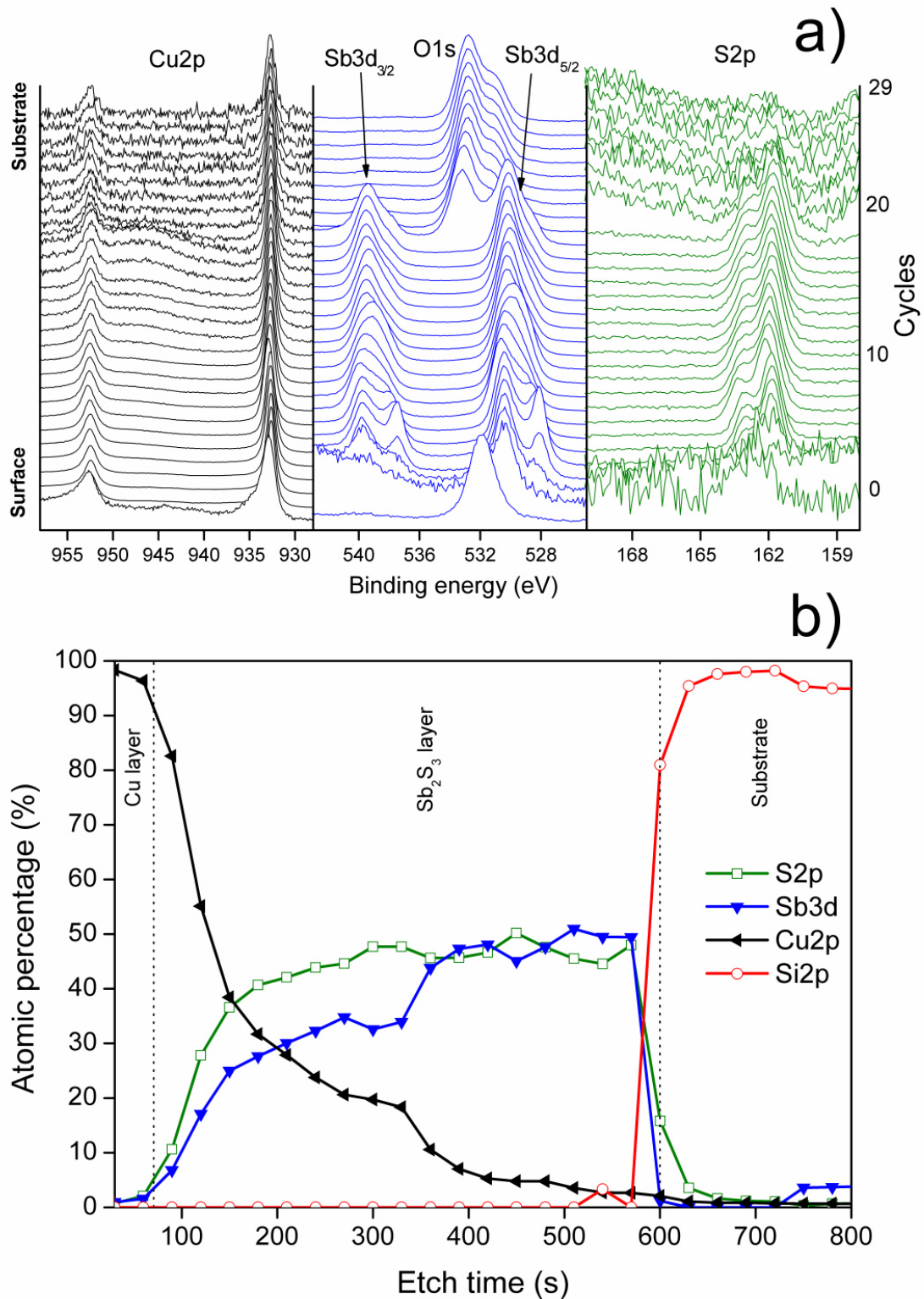
Figure 5.22 Depth profile for glass/Sb$_2$S$_3$/Cu precursor thin film as prepared (a) for core levels montage of Cu2p, O1s, Sb3d and S2p and (b) for compositional analysis

It was compared the Cu2p peak broadening of C650T1 thin film with pure evaporated Cu, having a less broader evaporated Cu peak than C650T1 peak, indicating that the latter is a convolution of two peaks.

Figure 5.24b shows high resolution spectra for $Sb3d_{5/2}$ and $Sb3d_{3/2}$ core levels and the deconvoluted ones. The peaks observed at 528.5 eV and 537.84 eV corresponding to the elemental state that was reduced due to the preferential sputtering of sulfur as was explained before. The peaks at 529.5 eV and 538.84 eV corresponding to Sb^{3+} in Sb_2S_3(Han et al., 2009), were originated from the unreacted precursor layer. More intense peak of $Sb3d_{5/2}$ and $Sb3d_{3/2}$ core levels at 530.6 eV and 539.94 eV did not match with the values for ternary compounds such as Cu_3SbS_3(Jiasong et al., 2010)or Cu_3SbS_4(van Embden and Tachibana, 2012), implying the formation of a new compound.

Also, from high resolution core level spectra for S2p doublets givenFigure 5.24c, the deconvoluted peaks located at 161.1 and 162.26 eV coincide with that for the reported B.E values for Cu_2S (Bhide et al., 1981). The peaks located at 161.5 eV and 162.66 eV matched with the formation of S^{2-} in Sb_2S_3 (Han et al., 2009). Moreover those peaks at 162.0 eV and 163.16 eV did not match with any other compound. Combining our results of the B.E values of Cu2p, Sb3d and S2p core levels and of the phases detected in our XRD results, it was assigned the values for the formation of $CuSbS_2$. The XPS analysis confirmed the formation of $CuSbS_2$ having the normal valence states for each element in the compound as $Cu^{1+}Sb^{3+}S_2^{2-}$ which is in good agreement with the reported (Yang, 2014).
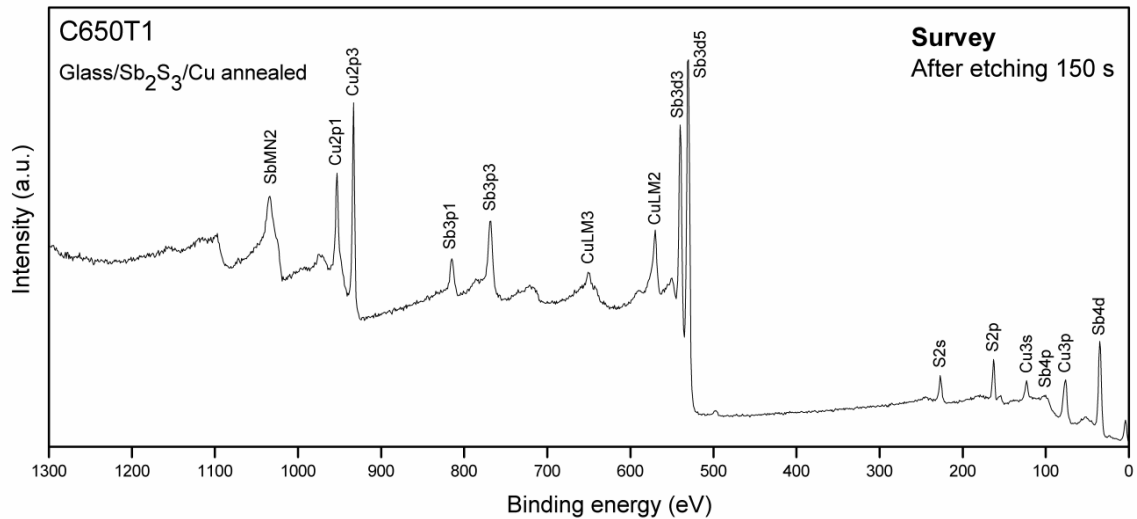
Figure 5.23 Survey spectrum of glass/Sb_2S_3/Cu thin film of 650 nm annealed at 350 °C for 1h (C650T1) after 150 s Ar^+ ions etching
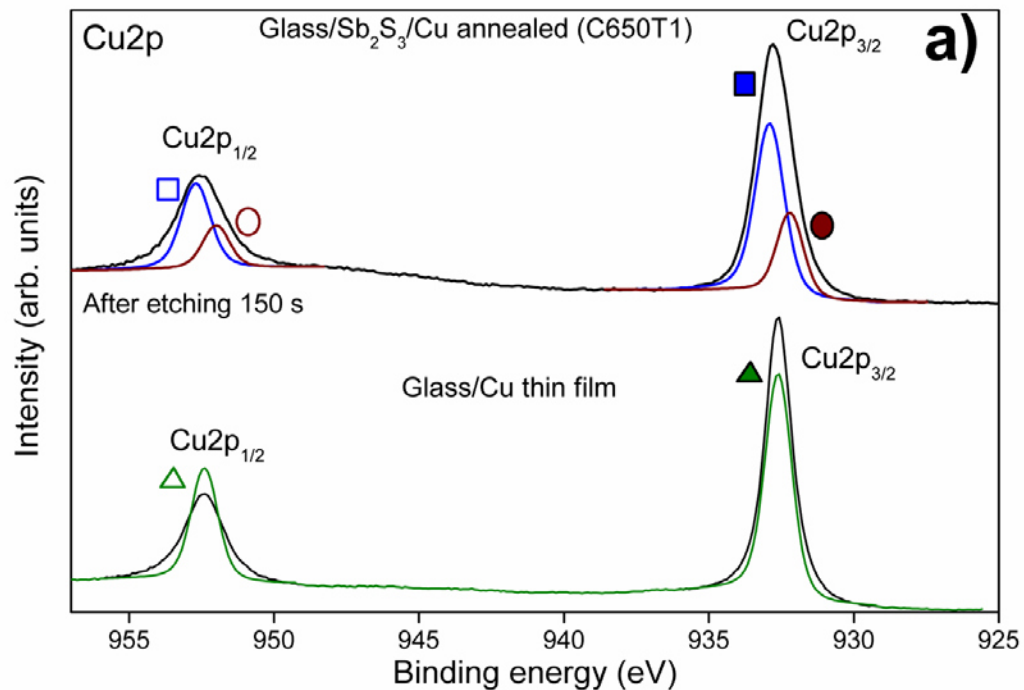
Core Level Peak	Binding energy (eV)	FWHM	Area ratio	Compound
▲ $Cu2p_{3/2}$	932.60	1.10	1.00	Cu
△ $Cu2p_{1/2}$	952.40	1.10	0.50	Cu
■ $Cu2p_{3/2}$	932.90	1.20	1.00	$CuSbS_2$
□ $Cu2p_{1/2}$	952.70	1.20	0.50	$CuSbS_2$
● $Cu2p_{3/2}$	932.20	1.10	1.00	Cu_2S
○ $Cu2p_{1/2}$	952.00	1.10	0.50	Cu_2S

Core Level Peak	Binding energy (eV)	FWHM	Area ratio	Compound
■ $Sb3d_{5/2}$	530.60	1.40	1.00	$CuSbS_2$
□ $Sb3d_{3/2}$	539.94	1.40	0.66	$CuSbS_2$
● $Sb3d_{5/2}$	529.50	1.30	1.00	Sb_2S_3
○ $Sb3d_{3/2}$	538.84	1.30	0.66	Sb_2S_3
▲ $Sb3d_{5/2}$	528.50	1.20	1.00	Sb
△ $Sb3d_{3/2}$	537.84	1.20	0.65	Sb

Core Level Peak	Binding energy (eV)	FWHM	Area ratio	Compound
■ $S2p_{3/2}$	162.00	0.80	1.00	$CuSbS_2$
□ $S2p_{1/2}$	163.16	0.80	0.50	$CuSbS_2$
● $S2p_{3/2}$	161.50	0.70	1.00	Sb_2S_3
○ $S2p_{1/2}$	162.66	0.70	0.50	Sb_2S_3
▲ $S2p_{3/2}$	161.10	0.60	1.00	Cu_2S
△ $S2p_{1/2}$	162.26	0.60	0.50	Cu_2S

Figure 5.24 High-resolution spectra of (a) Cu2p for C650T1 and evaporated Cu thin film, (b) Sb3d and (c) S2p core levels of 650 nm thin film annealed at 350 °C for 1 h (C650T1) after 150 s Ar⁺ ions etching (Reproduced with kind permission from Elsevier)

The atomic composition obtained after 150 s etching for C650T1 sample was 28.27% of Cu, 24.31 % of Sb and 47.42 % of S, having a Cu rich and a sulfur deficiency sample. The atomic percentages for each phase in the sample were 42.35% of $CuSbS_2$, 29.56% of Cu_2S and 28.09% of Sb_2S_3.

In Figure 5.25a the depth profile analysis of the thin films of 650 nm in thickness after annealed at 350 °C is shown in the XPS profile montage where Cu2p, Sb3d and S2p core levels were detected throughout the depth of the thin film until they disappear and O1s and Si2p core levels raised when the substrate has been reached. After annealing, is observed a complete diffusion of Cu into Sb_2S_3 throughout the depth of the film as marked in Figure 5.25b. This diffusion is performed by the movement of the Cu atoms through the Sb_2S_3 layer activated by the annealing of the thin film, reacting with Sb_2S_3 to form $CuSbS_2$. The transport process of the Cu atoms in the diffusion could be via point defects of the thin film such as vacancies, anti-sites, grain boundaries and dislocations.
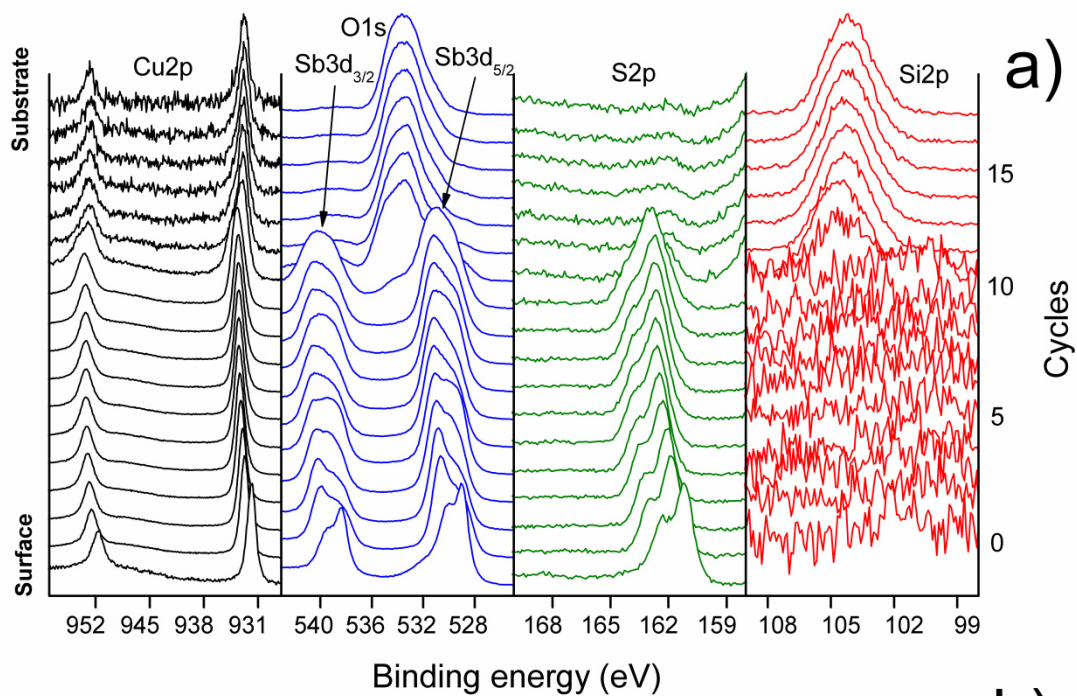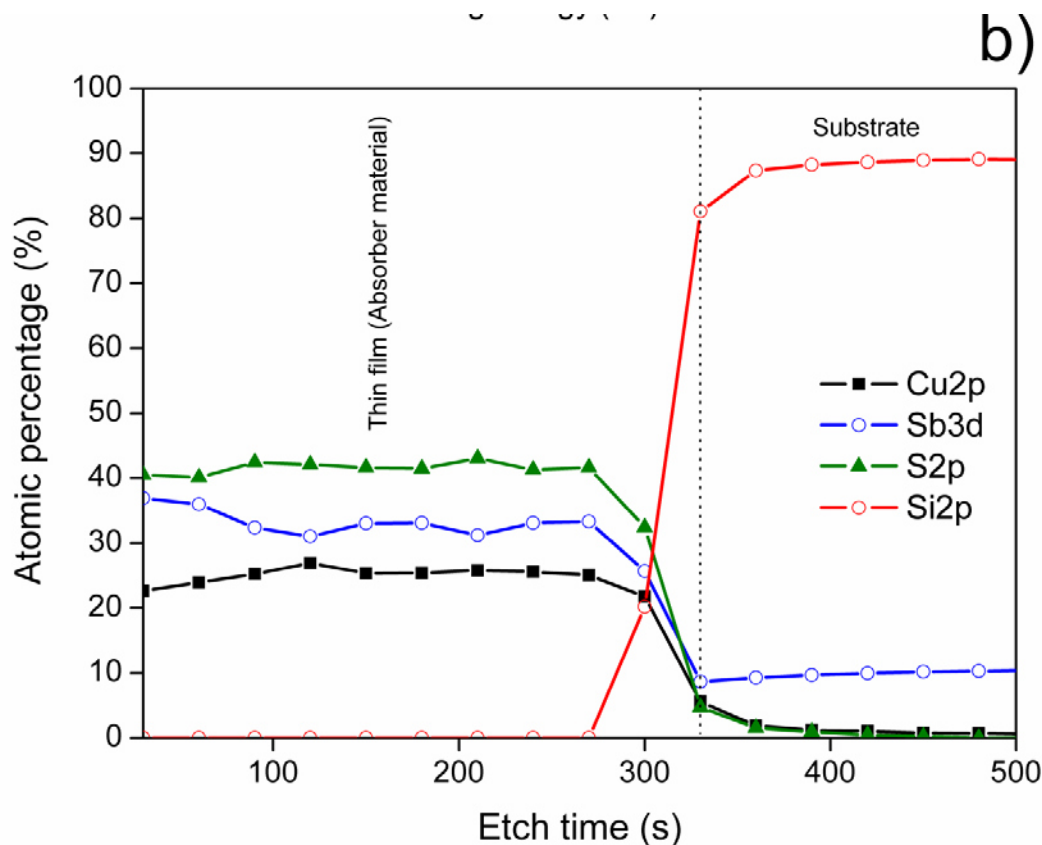
Figure 5.25 Depth profile for glass/Sb$_2$S$_3$/Cu of 650 nm annealed at 350 °C (a) for core levels montage of Cu 2p, O 1s, Sb 3d, S 2p and Si 2p and (b) for compositional analysis (Reproduced with kind permission from Elsevier)

The compositions of copper, antimony and sulfur were uniform (1:1.2:1.6) being sulfur deficiency and antimony rich sample according to the CuSbS$_2$ stoichiometry (1:1:2). This sulfur deficiency might be due to the loss of sulfur in annealing process. This might to explain the formation of Cu$_2$S phase, due there is a preferable reaction between Cu and sulfur vapor to produce Cu$_x$S compounds (Septina et al., 2014).

Figure 5.26 shows Cu2p, Sb3d and S2p core levels for glass/Sb$_2$S$_3$/Cu thin film of 1050 nm annealed at 350 °C 1h after by 2keV Ar$^+$ ion etching of 30 s and 300 s corresponding to a penetration depth of approximately 60 nm and 600 nm respectively, considering a sputter rate of 2 nm/sec. From Figure 5.26a after 30 s (60 nm depth) ion etching, the doublet Cu2p$_{3/2}$ and Cu2p$_{1/2}$ core levels constituted one peak at 932.8 eV and 952.6 eV with a peak splitting of 19.8 eV

are in good agreement with Cu^{1+} as expected for $CuSbS_2$ compo und(Yang et al., 2014). After 300 s (600 nm depth) ion etching, the doublet $Cu2p_{3/2}$ and $Cu2p_{1/2}$ core levels constituted two different peaks corresponding to Cu_2S (932.2 eV and 952.0 eV) and $CuSbS_2$ (932.8 eV and 952.6 eV). From Figure 5.26b after 30 s (60 nm depth) ion etching, the doublet $Sb3d_{5/2}$ and $Sb3d_{3/2}$ core levels constituted three peaks at 528.5 eV and 537.84 eV corresponding to the elemental state may be due to sputter reduced antimony (Moulder et al., 1992), 529.5 eV and 538.84 eV corresponding to Sb^{3+} in Sb_2S_3(Han et al., 2009) and 530.6 eV and 539.94 eV corresponding to Sb^{3+} in $CuSbS_2$. After 300 s (600 nm depth) ion etching, the doublet $Sb3d_{5/2}$ and $Sb3d_{3/2}$ core levels constituted three peaks as observed for C650T1 sample, the peaks observed at 528.5 eV and 537.84 eV corresponding to the elemental state, 529.5 eV and 538.84 eV corresponding to Sb^{3+} in Sb_2S_3(Han et al., 2009), originated from the unreacted precursor layer and 530.6 eV and 539.94 eV for $CuSbS_2$. In Figure 5.26c, the doublet $S2p_{3/2}$ and $S2p_{1/2}$ core levels after 30 s and 300 s ion etching was evaluated observed peaks at 162.0 eV and 163.16 eV corresponding to $CuSbS_2$ (30 s and 300 s), 161.5 eV and 162.66 eV for Sb_2S_3 (30 s and 300 s) and 161.1 eV and 162.26 eV for Cu_2S (300 s). All results are in good agreement with XRD results obtained for this sample, demonstrating the formation of $CuSbS_2$ as single phase near surface (60 nm of depth) and a combination of mixed phases ($CuSbS_2$, Cu_2S and Sb_2S_3) for larger penetration depths.

The atomic composition obtained after 30 s etching for C1050T1 sample was 23.33% of Cu, 25.51 % of Sb and 51.16 % of S. The atomic percentage for the $CuSbS_2$ in the surface confirmed at 100% the formation of pure $CuSbS_2$ which is in good agreement with the results obtained by XRD. For sample after 300 s etching the atomic composition was 22.8% of Cu, 28.45 % of Sb and 48.75 % of S, being Cu deficiency and antimony rich sample. The atomic percentages for each phase in the sample at penetration depth of 600 nm were 38.57% of $CuSbS_2$, 31.41% of $Sb_2S_3$and 30.02% of Cu_2S.
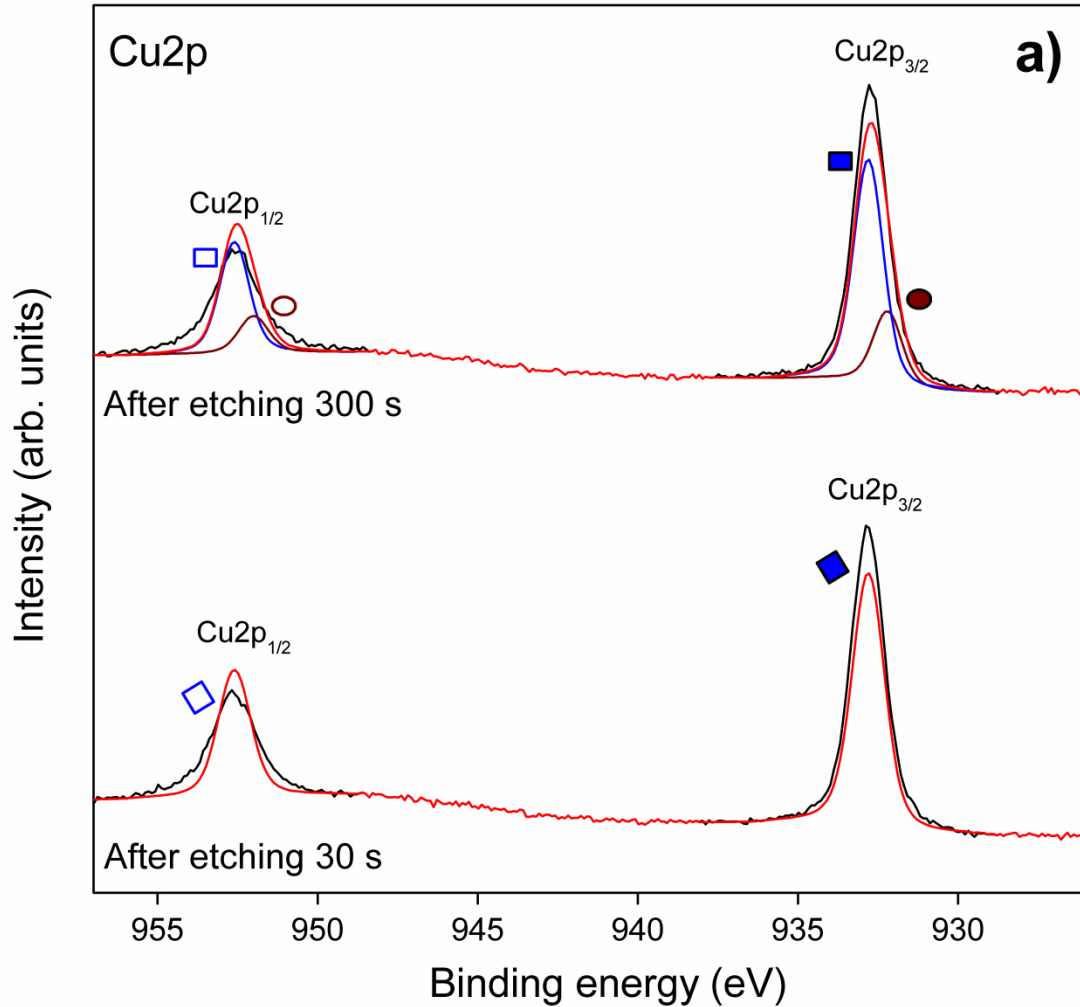
Core Level Peak		Binding energy (eV)	FWHM	Area ratio	Compound
■	$Cu2p_{3/2}$	932.80	1.10	1.00	$CuSbS_2$
□	$Cu2p_{1/2}$	952.60	1.10	0.50	$CuSbS_2$
●	$Cu2p_{3/2}$	932.20	1.10	1.00	Cu_2S
○	$Cu2p_{1/2}$	952.00	1.10	0.50	Cu_2S
◆	$Cu2p_{3/2}$	932.80	1.20	1.00	$CuSbS_2$
◇	$Cu2p_{1/2}$	952.60	1.20	0.50	$CuSbS_2$
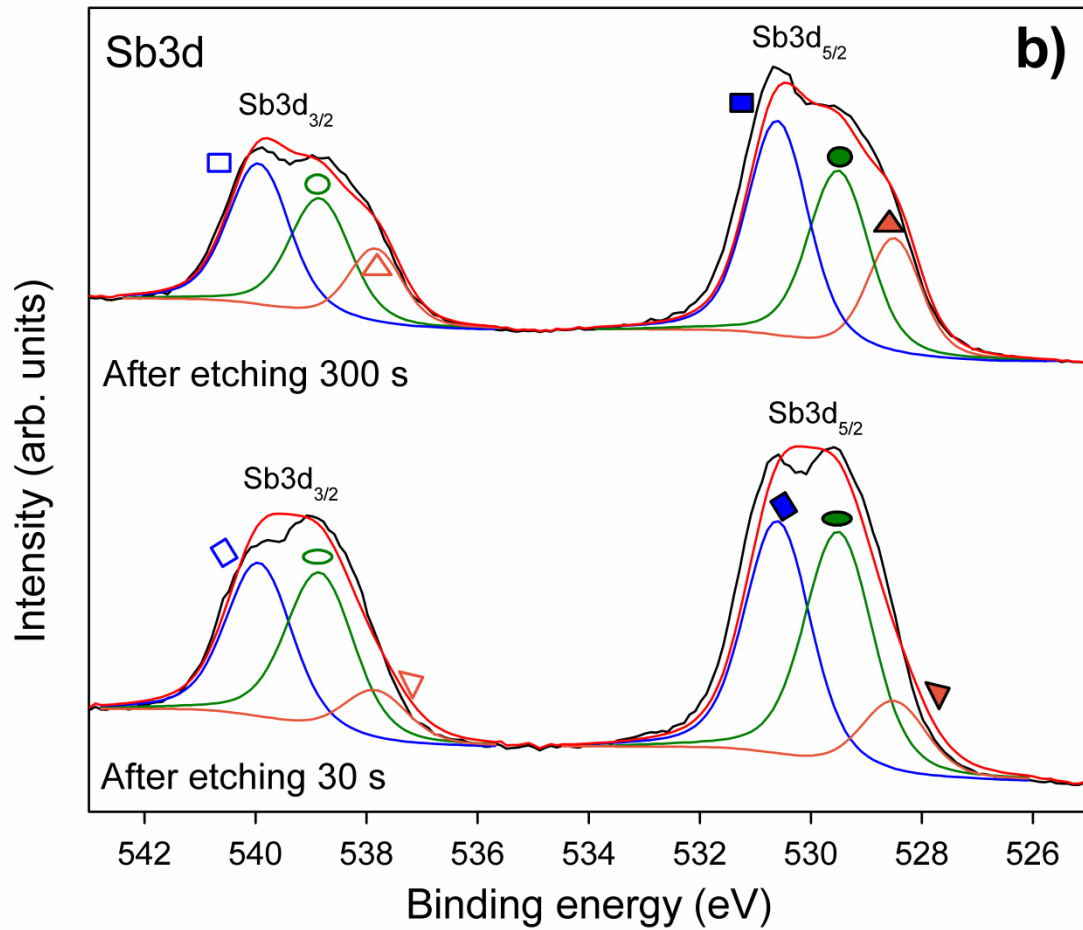
Core Level Peak	Binding energy (eV)	FWHM	Area ratio	Compound
■ Sb3d$_{5/2}$	530.60	1.30	1.00	CuSbS$_2$
□ Sb3d$_{3/2}$	539.94	1.30	0.66	CuSbS$_2$
● Sb3d$_{5/2}$	529.50	1.30	1.00	Sb$_2$S$_3$
○ Sb3d$_{3/2}$	538.84	1.30	0.66	Sb$_2$S$_3$
▲ Sb3d$_{5/2}$	528.50	1.15	1.00	Sb
△ Sb3d$_{3/2}$	537.84	1.15	0.65	Sb
◆ Sb3d$_{5/2}$	530.60	1.40	1.00	CuSbS$_2$
◇ Sb3d$_{3/2}$	539.94	1.40	0.66	CuSbS$_2$
⬬ Sb3d$_{5/2}$	529.50	1.45	1.00	Sb$_2$S$_3$
⬭ Sb3d$_{3/2}$	538.84	1.45	0.67	Sb$_2$S$_3$
▼ Sb3d$_{5/2}$	528.50	1.40	1.00	Sb
▽ Sb3d$_{3/2}$	537.84	1.40	0.67	Sb
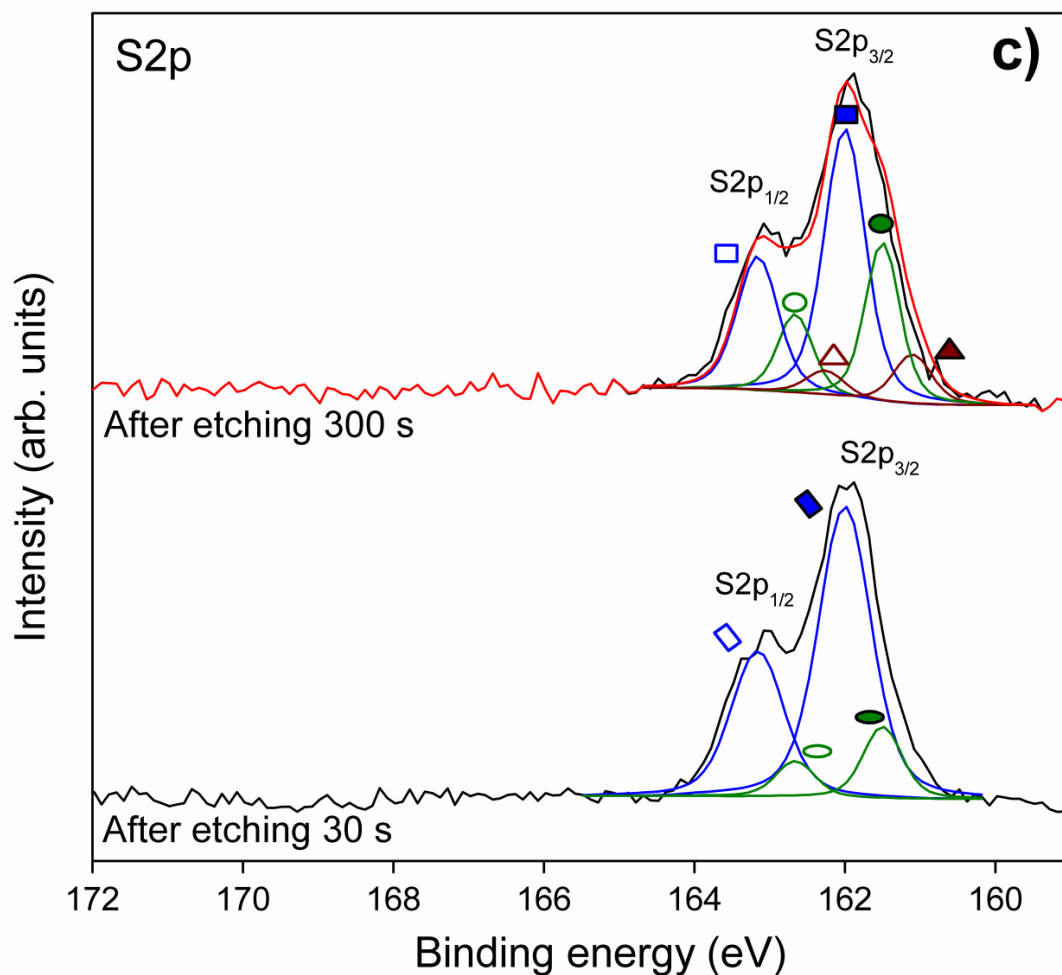
Core Level Peak		Binding energy (eV)	FWHM	Area ratio	Compound
■ (blue filled)	S2p$_{3/2}$	162.00	0.65	1.00	CuSbS$_2$
□ (blue open)	S2p$_{1/2}$	163.16	0.65	0.50	CuSbS$_2$
● (green filled)	S2p$_{3/2}$	161.50	0.55	1.00	Sb$_2$S$_3$
○ (green open)	S2p$_{1/2}$	162.66	0.55	0.50	Sb$_2$S$_3$
▲ (dark red filled)	S2p$_{3/2}$	161.10	0.60	1.00	Cu$_2$S
△ (dark red open)	S2p$_{1/2}$	162.26	0.60	0.49	Cu$_2$S
◆ (blue filled)	S2p$_{3/2}$	162.00	0.83	1.00	CuSbS$_2$
◇ (blue open)	S2p$_{1/2}$	163.16	0.83	0.50	CuSbS$_2$
⬭ (green filled)	S2p$_{3/2}$	161.50	0.61	1.00	Sb$_2$S$_3$
⬭ (green open)	S2p$_{1/2}$	162.66	0.61	0.50	Sb$_2$S$_3$

Figure 5.26 High-resolution spectra of (a) Cu2p, (b) Sb3d and (c) S2p core levels of 1050 nm annealed at 350 °C thin film after 30 s and 300 s Ar^{+} ions etching

5.1.4 Optical properties (UV-Vis)

The optical transmittance (%T) and reflectance (%R) spectra of $CuSbS_2$ thin films of 650 nm, 850 nm and 1050 nm in thickness, annealed at 350 °C for 1h (C650T1, C850T1 and C1050T1, respectively) and $CuSbS_2$ thin films of 1050 nm annealed at 350 °C for 1h, 2h, 3h and 4h are shown in Figure 5.27a and Figure 5.28a respectively. In the region above 900 nm an average 20% transmittance and 30% reflectance are observed. Nearly 50% of absorption in the region of 900-1100 nm is attributed to the presence of Cu_2S compound, confirmed by XRD and XPS, this compound has a band gap of around 1.2-1.3 eV (Klimov et al., 1995) which lies into this region and aid to reduce the transmittance and reflectance of the $CuSbS_2$ compound. In the absorbing region, α can be calculated using the equation (2.7):

$$\alpha = \frac{1}{t}\ln\left[\frac{(1-R)^2}{T}\right]$$

Figure 5.27b and Figure 5.28b show absorption coefficient of the thin films of 650 nm, 850 nm and 1050 nm in thickness, annealed at 350 °C for 1h (C650T1, C850T1 and C1050T1) and $CuSbS_2$ thin films of 1050 nm annealed at 350 °C for 1h, 2h, 3h and 4h, respectively, having values between 10^4-10^5 cm^{-1}, which are in good agreement with those values reported (Yu et al., 2013). The optical band gap value of the thin film was determined using equation (2.8):

$$(\alpha h\nu)^n = A(h\nu - E_g)$$

Figure 5.27c and Figure 5.28c illustrate the plot of $(\alpha h\nu)^2$ vs hν (Tauc plot) for the thin films giving good linear fit for n=2. This implies that the fundamental optical absorption in $CuSbS_2$ thin films was dominated by direct allowed transition. From the curve, the value of band gap was estimated by extrapolating the linear region of the respective plot to α=0, as shown in the figure. The E_g value was around 1.55 eV for all the samples, this value is in consistent with the earlier reports on optical properties of $CuSbS_2$(Garza et al., 2011). Recently, employing a first-principles approach within the density functional theory (DFT), a direct band gap of 1.5-1.7 eV was estimated for this compound. These results

were in agreement with the theoretical approach (Kumar and Persson, 2013, Dufton et al., 2012).
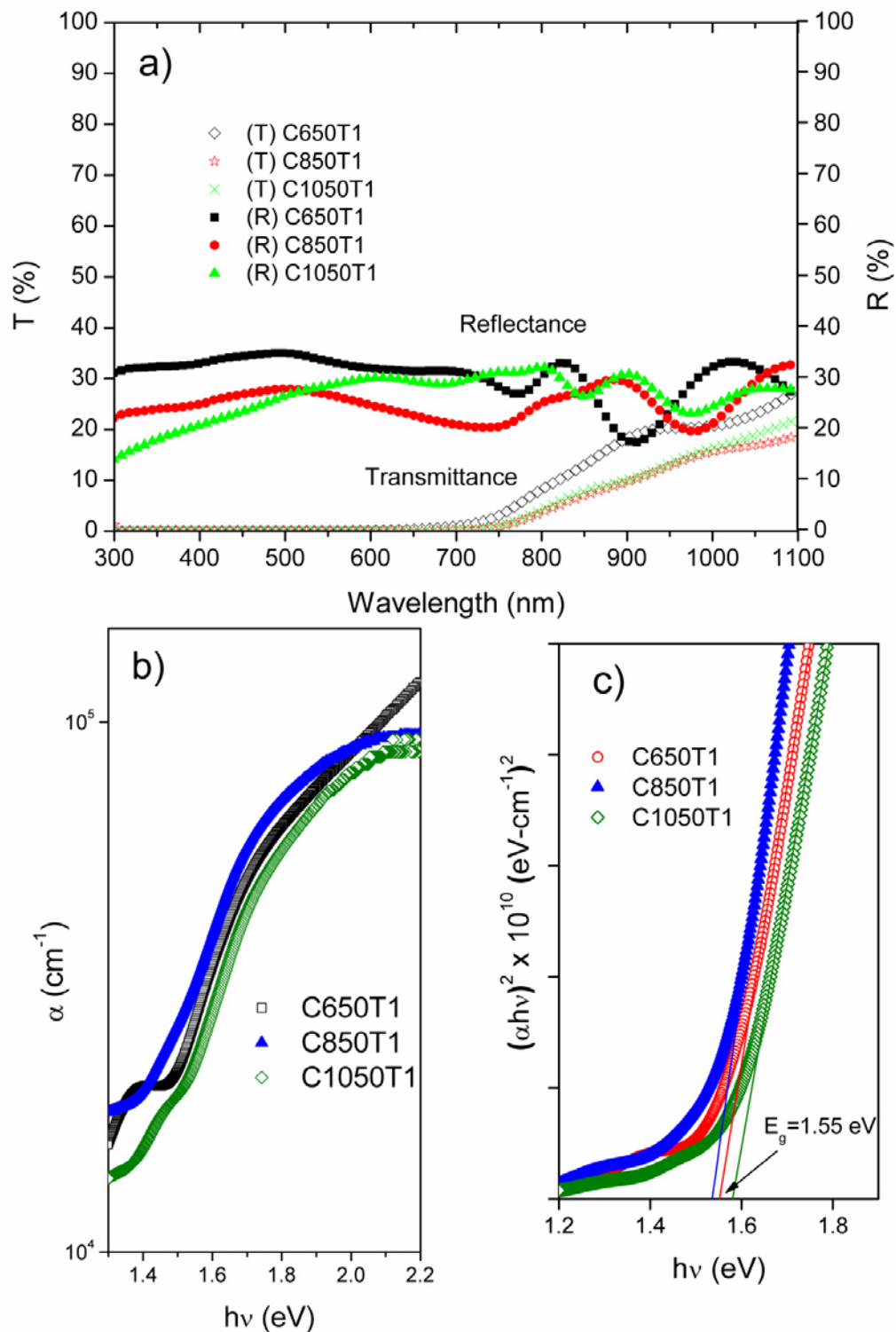
Figure 5.27 (a) Transmittance (T) and Reflectance (R) spectra, (b) absorption coefficient and (c) evaluation of optical band gap for glass/Sb2S3/Cu of 650 nm, 850 nm and 1050 nm annealed at 350 °C (C650T1, C850T1 and C1050T1, respectively)
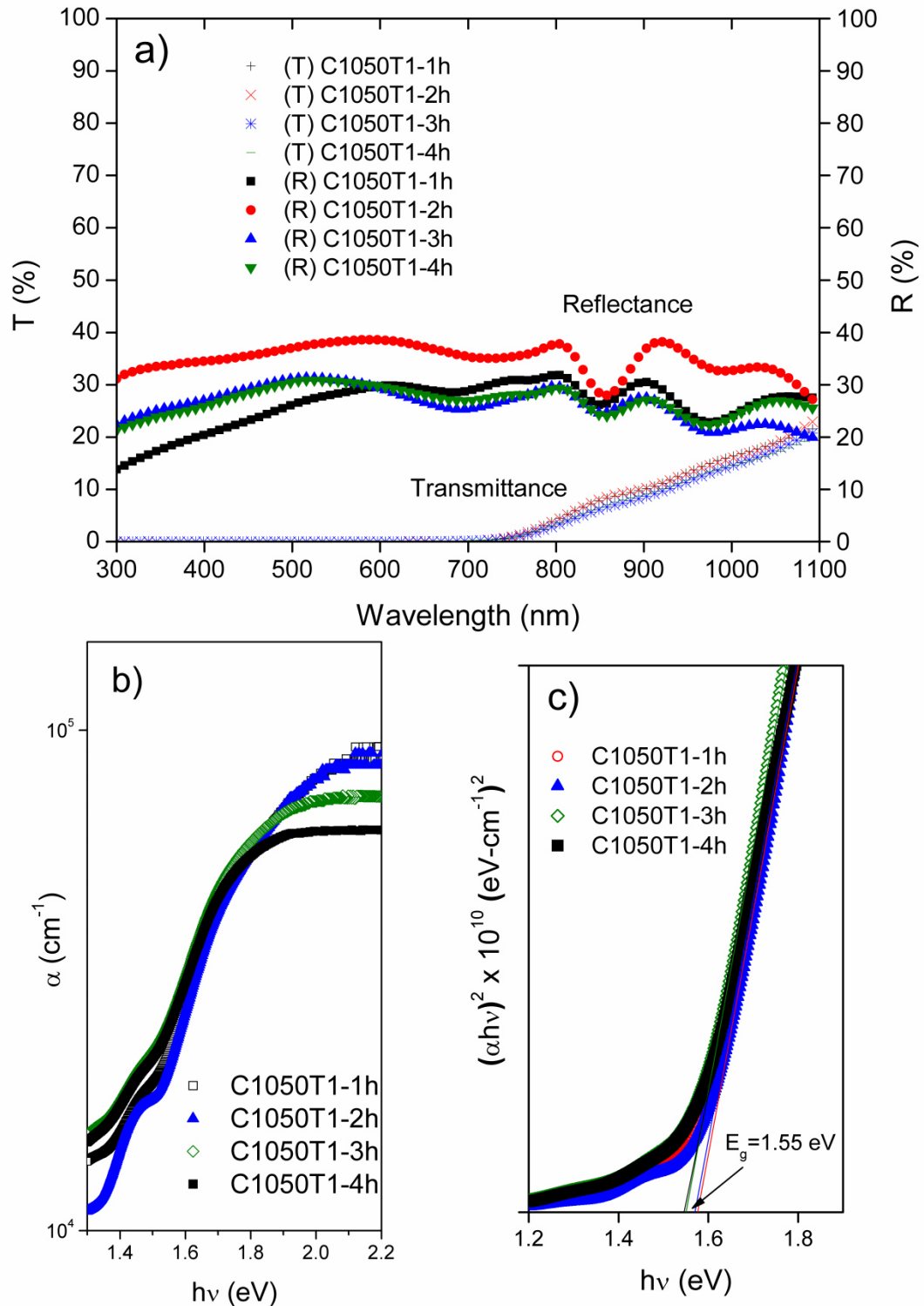
Figure 5.28 (a) Transmittance (T) and Reflectance (R) spectra, (b) absorption coefficient and (c) evaluation of optical band gap for glass/Sb$_2$S$_3$/Cu of 1050 nm annealed at 350 °C for 1h, 2h, 3h and 4h

5.1.5 Electrical properties

5.1.5.1 Photoresponse

Electrical properties of dark conductivity and photoconductivity of the glass/Sb_2S_3/Cu thin films of 650 nm in thickness annealed at 350 °C, 375 °C and 400 °C and glass/Sb_2S_3/Cu of 850 nm and 1050 nm in thickness annealed at 350 °C for 1 h, were determined from the photocurrent response measurements at room temperature by applying a D.C. bias as shown in Figure 5.29, illuminated using a tungsten halogen lamp. In the present experiment a bias of 10 V was applied across a pair of planar carbon paint electrodes, the current through the sample was measured in an interval of 20 s each, first in the dark (I_o), followed by illumination (I) of the sample and then after switching off the light source. The value of dark conductivity was evaluated using the equation:

$$\sigma = \frac{l}{Rwt} \tag{5.3}$$

where σ is the conductivity in $(\Omega \cdot cm)^{-1}$, R is the measured resistance in Ω (voltage/current), w is the width of the electrodes, l is the distance between two electrodes and t is the thickness of the thin film.

The calculations gave values in the order of 10^{-4} $(\Omega\text{-}cm)^{-1}$ for all samples annealed at 350 °C and 10^{-3} $(\Omega\text{-}cm)^{-1}$ for sample annealed at 400 °C. The samples were photoconductive as seen from the figure.

The photosensitivity, defined as $(I\text{-}I_o)/I_o$, was determined in the values of 0.2, 0.4, 0.3, 0.1 and 0.7 for C650T1, C650T2, C650T3, C850T1 and C1050T1 respectively. The photosensitivity increased when the annealing temperature and thickness increased. The high photoconductivity obtained for the C650T3 sample (annealed at higher temperature 400 °C) can be attributed to the reduction in surface roughness according to our AFM results and the increase of Cu vacancies due annealing which produce an increase in hole concentration. The surface roughness caused electron scattering which reduce the mean free

path length decreasing the conductivity. In the case of the sample C1050T1, the value of surface roughness is similar to the sample C650T1, but this is not the main effect which causes the reduction in photoconductivity. In this case, the thickness of Sb_2S_3 increases from 600 nm to 1000 nm, producing a reduction of Cu vacancies as well as a hole concentration giving a decrease of dark conductivity. The measurements of mobility and carrier concentration of the thin films are analyzed in the next section.
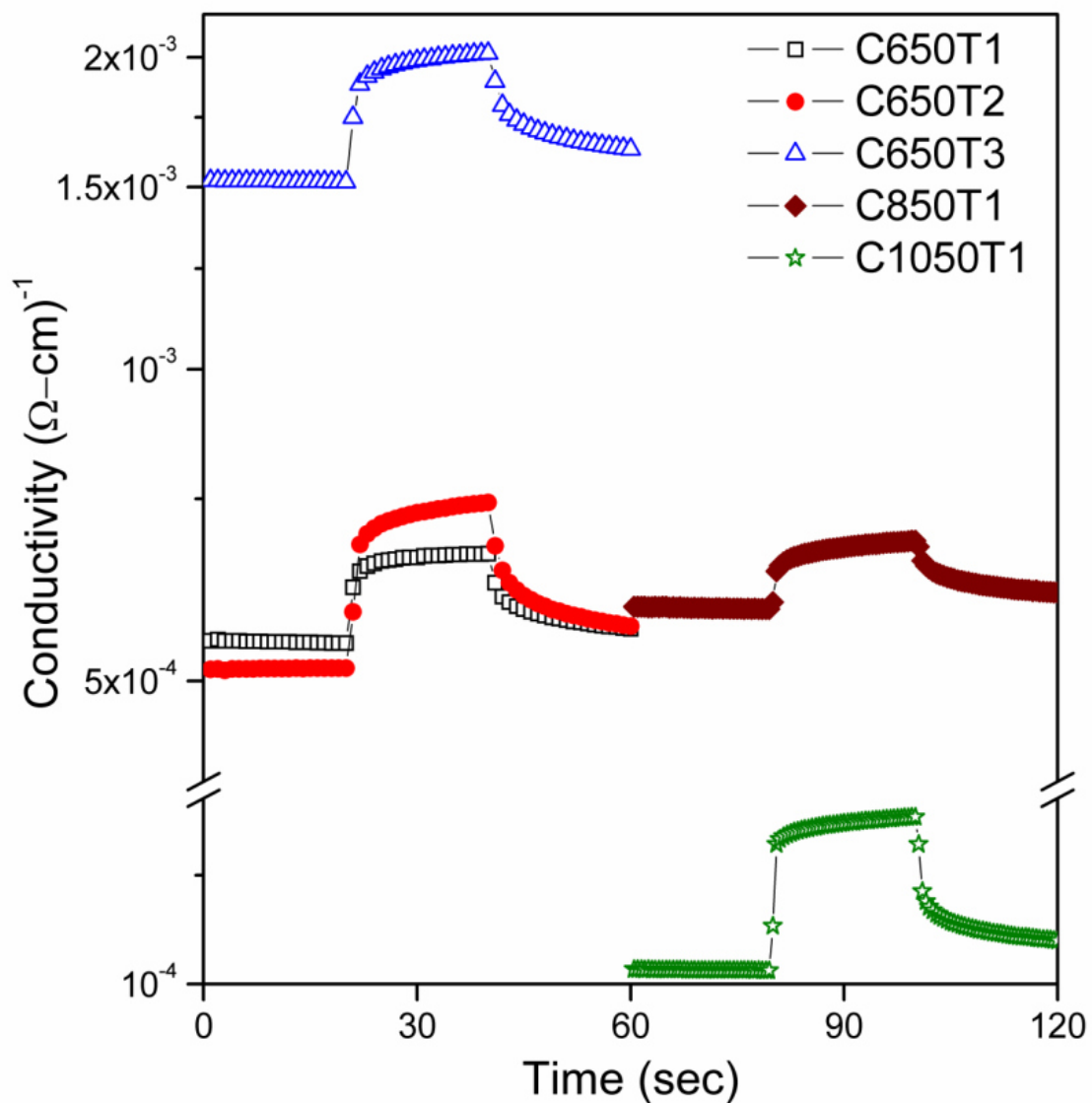
Figure 5.29 Photoconductivity curves for C650T1, C650T2, C650T3, C850T1 and C1050T1 thin films

5.1.5.2 Hall Effect measurements

The Hall effect measurements determine the concentration and type (*n* or *p*) of charge carriers in semiconductors, also give us the mobility and conductivity of these carriers. The analysis of these parameters were performed for the most representative samples, for the glass/Sb_2S_3/Cu of 650 nm annealed at 350 °C, 375 °C and 400 °C for 1 h, glass/Sb_2S_3/Cu of 850 nm and 1050 nm annealed at 350 °C for 1h and glass/Sb_2S_3/Cu of 1050 nm annealed at 350 °C for 2-4 hours.
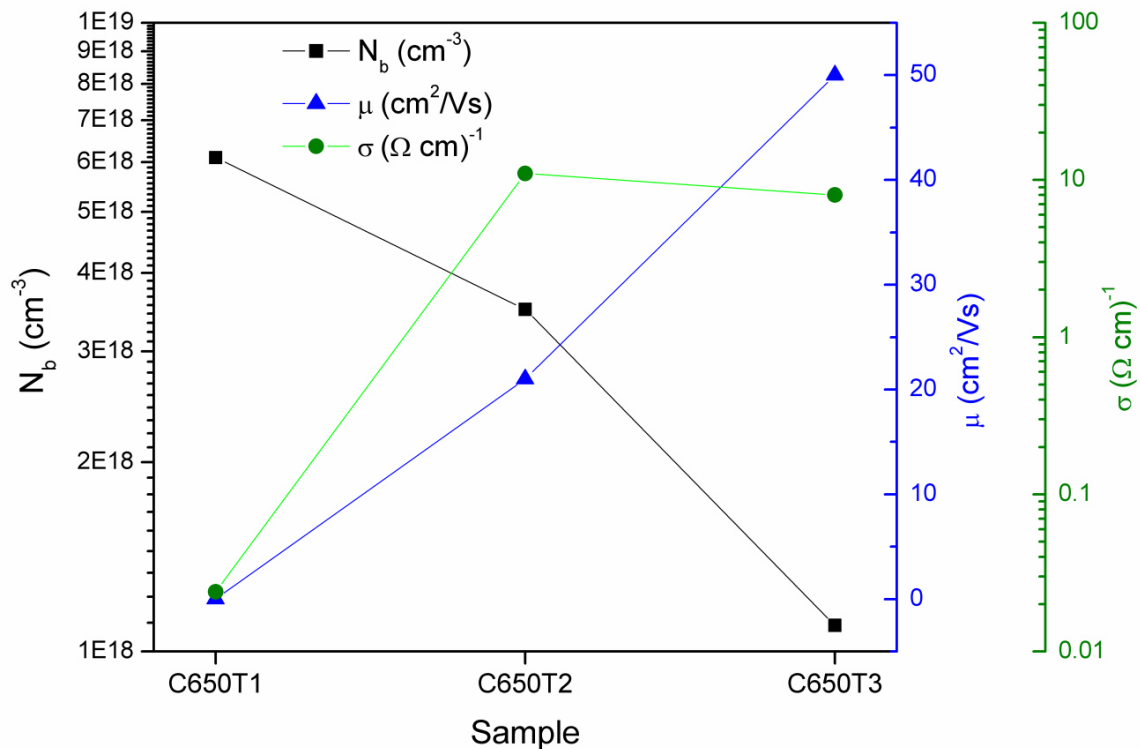
Figure 5.30 Carrier concentration (N_b), carrier mobility (μ) and conductivity (σ) as a function of anneal temperature (T1:350 °C, T2: 375 °C, T3: 400 °C) for $CuSbS_2$ thin films of 650 nm

The dependence of carrier concentration, carrier mobility and conductivity on $CuSbS_2$ thin films of glass/Sb_2S_3/Cu of 650 nm annealed at 350 °C, 375 °C and 400 °C for 1h is shown in Figure 5.30. It can be seen that the carrier mobility and conductivity of the thin films increases from 0.03 cm^2/Vs to 50 cm^2/Vs and from 2.4 x 10^{-2} $(\Omega \cdot cm)^{-1}$ to 11 $(\Omega \cdot cm)^{-1}$, respectively. The carrier concentration decreases from 6.1 x 10^{18} cm^{-3} to 1.1 x 10^{18} cm^{-3} as the anneal temperature

increases. The increase of carrier mobility with anneal temperature is due to reduction of the scattering of the carriers in the films by elimination of defects (Öztas and Bedir, 2008) supported by the lattice strain values calculated from XRD data. The decrease in carrier concentration by annealing the thin films can be attributed to reduction of structural defects in the thin film (Fang et al., 2013) and the reduction of Cu vacancies which cause that $CuSbS_2$ have a p-type conductivity (Yang, 2014). The possible defects that $CuSbS_2$ thin films could have are Cu vacancies (V_{Cu}) and Cu-Sb antisites (Cu_{Sb}) which acts as acceptors, meanwhile Cu interstitials (Cu_i), S vacancies (V_S) and Sb-Cu antisites (Sb_{Cu}) acts as donors. Vacancy defect is when an atom in a lattice site is missing; interstitial defect is when an atom is located between lattice sites and the antisite defect is when an atom (B) is occupying a site that should have had another different atom (A). The most probable defect present in $CuSbS_2$ thin films is Cu vacancies, due to the high Cu diffusion which is easier to left its lattice site with lower energy.

In polycrystalline semiconductors the trapping of charge at the grain boundaries has a decisive influence on the electrical transport properties. Distortion of the crystal lattice creates trapping states localized at the grain boundary. A grain boundary becomes electrically active by trapping an excess charge of majority carriers at the interface. Overall charge neutrality is established by the formation of an electrostatic potential barrier with two depletion layers adjacent to the boundary (Greuter and Blatter, 1990). In this case, when annealing temperature increase, a reduction of lattice strain and carrier concentration lead to a decrease in trapping states created at grain boundaries of the thin film leading to an increase of conductivity.

The carrier concentration, carrier mobility and conductivity on $CuSbS_2$ thin films of glass/Sb_2S_3/Cu of Sb_2S_3 3 layers (600 nm), 4 layers (800 nm) and 5 layers (1000 nm) and Cu layer of 50 nm for each sample annealed at 350 °C for 1h are shown in Figure 5.31. It can be observed that the carrier concentration and conductivity of the thin films decreases from 6.1×10^{18} cm^{-3} to 2.5×10^{13} cm^{-3} and from 2.4×10^{-2} ($\Omega \cdot$cm)$^{-1}$ to 5.1×10^{-5} ($\Omega \cdot$cm)$^{-1}$, respectively. The carrier

mobility increases from 0.03 cm^2/Vs to 13 cm^2/Vs as the film thickness increases. The increase of carrier mobility is attributed to improved crystallinity enhancing photosensitivity and reducing trapping states which are capable to trapping carriers and immobilizing them (Öztas and Bedir, 2008). The decrease of carrier concentration can be due to the reduction of Cu vacancies which implies a reduction of hole concentration by the increasing of Sb_2S_3 precursor layer thickness which might produce other kind of defects such as sulfur or antimony vacancies. The height of the potential barrier formed at the grain boundaries by the creation of trapping states varies with the doping concentration of the semiconductor as follows:

(1) At low doping levels, there are only a few free carriers to be trapped in the grain boundary and the barrier height is low.

(2) At intermediate doping levels, more carriers are available to be trapped and so the barrier height will increase.

(3) At high doping levels, there is an excess of carriers over and above those needed to saturate all the mid-gap grain boundary states, the Fermi level will be freed from these states and will rapidly approach its equilibrium level in the grains, reducing the barrier height.

Figure 5.32 present a model where shows the effect of the variation of doping density in the mobility and resistivity of silicon thin films (Grovenor, 1985). The critical doping concentration at which the mobility is a minimum and the resistivity decreases sharply, N^*_G, is at that point at which the maximum value of barrier height at the grain boundary is reached.

This could explain the decrease of conductivity in this samples, in which the concentration of the $CuSbS_2$ thin films of 1050 nm is below the point N^*_G, giving the reduction in conductivity combined by an increase in mobility.
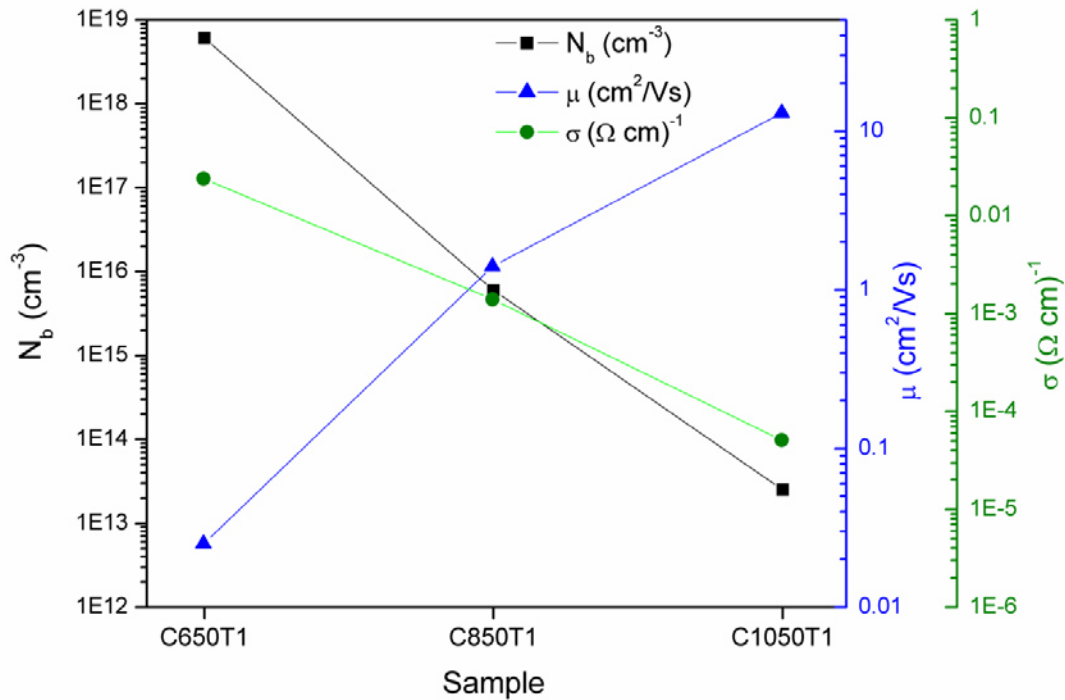
Figure 5.31 Carrier concentration (N_b), carrier mobility (μ) and conductivity (σ) as a function of film thickness for CuSbS$_2$ thin film of 650 nm, 850 nm and 1050 nm annealed at 350 °C 1h (C650T1, C850T1 and C1050T1 respectively)
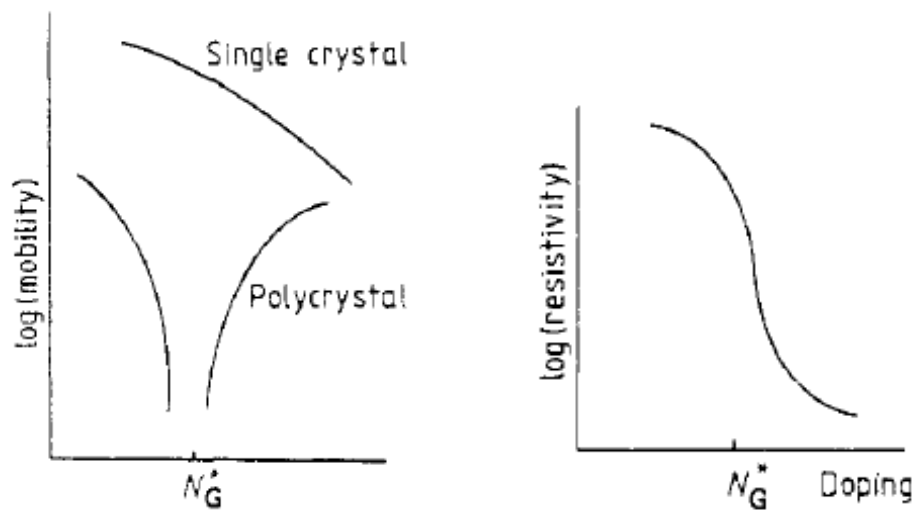
Figure 5.32 Schematic representation of the variation of mobility and resistivity with doping level in polycrystalline silicon films.

The dependence of carrier concentration, carrier mobility and conductivity on annealing time for CuSbS$_2$ thin films of glass/Sb$_2$S$_3$/Cu of 5 layers of Sb$_2$S$_3$ (1000 nm) and 50 nm of Cu (1050 nm) annealed at 350 °C for 1 h, 2 h, 3 h and

4 h is shown in Figure 5.33. It can be seen from the results that this p-type semiconducting sample has changed to n-type semiconducting by annealing at 350 °C above 2 h. This can be attributed to thermally induced defects which causes the conversion from p-type to n-type (Fung et al., 1999). Before conversion, decrease of carrier concentration and conductivity and an increase of carrier mobility are observed at low annealing times (1 h and 2 h). This decrease of carrier concentration with increasing annealing time can be due by the reduction of copper vacancies as acceptor defects. At large annealing times (3 h and 4 h) a complete reduction of acceptor defects and formation of donor defects are reached forming large concentration of sulfur vacancies which acts as donor defect giving the type conversion (Yang et al., 2014). According to the model of the grain boundaries explained above, the increase in carrier concentration after conversion from p-type to n-type lead to an increase in mobility and conductivity, this is due to the concentration is above N^*_G, for that reason the barrier height formed at grain boundaries decreases (Grovenor, 1985).
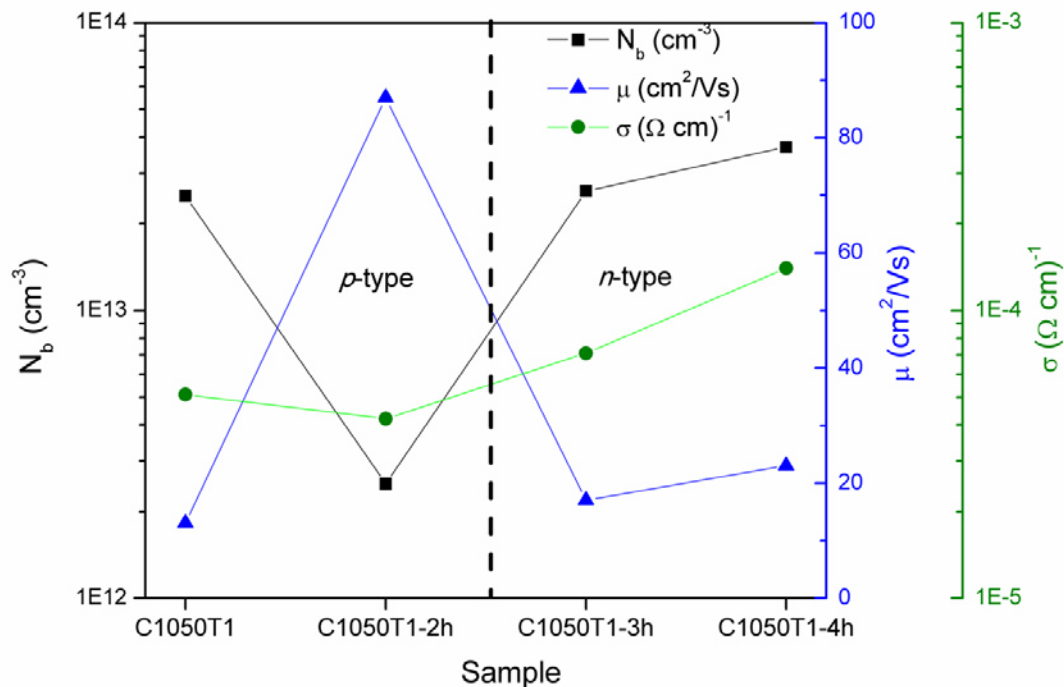
Figure 5.33 Carrier concentration (N_b), carrier mobility (μ) and conductivity (σ) as a function of annealing time for CuSbS$_2$ thin film 1050 nm annealed at 350 °C for 1h, 2h, 3h and 4h (C1050T1, C1050T1-2h, C1050T1-3h and C1050T1-4h respectively)

Table 5.1summarizes the crystallite size, lattice strain, photosensitivity, carrier concentration, carrier mobility and conductivity for samples of 650 nm annealed at 350 °C, 375 °C and 400 °C for 1h (C650T1, C650T2, C650T3), samples of 850 nm and 1050 nm annealed at 350 °C for 1h (C850T1, C1050T1) and samples of 1050 nm annealed at 350 °C for 2h, 3h and 4h (C1050T1-2h, C1050T1-3h, C1050T1-4h).

Table 5.1 Variation of structural and electrical parameters with different film thickness and anneal temperature and times

				XRD		Elec. Prop.	Hall Effect			
Sample	Thickness (nm)	Anneal temperature	Annealing time (h)	Crystallite Size (nm)	Lattice strain (10^{-3})	Photosensitivity	Carrier concentration (cm^{-3})	Mobility (cm^2/Vs)	Conductivity ($\Omega \cdot cm)^{-1}$	Type
C650T1		350 °C		35	4	0.2	6.1×10^{18}	0.03	2.4×10^{-2}	p
C650T2	650	375 °C	1	32	2	0.4	3.5×10^{18}	21	1.1×10^{1}	p
C650T3		400 °C		32	0.98	0.3	1.1×10^{18}	50	8	p

C650T1	650			35	4	0.2	6.1×10^{18}	0.03	2.4×10^{-2}	p
C850T1	850	350 °C	1	27	1.6	0.1	2.2×10^{16}	1.3	4.5×10^{-3}	p
C1050T1	1050			20	0.74	0.7	2.5×10^{13}	13	5.1×10^{-5}	p

C1050T1			1	20	0.74	0.7	2.5×10^{13}	13	5.1×10^{-5}	p
C1050T1-2h	1050	350 °C	2	19	-0.71	1.1	2.5×10^{12}	87	4.2×10^{-5}	p
C1050T1-3h			3	18	-0.78	0.5	2.6×10^{13}	17	7.1×10^{-5}	n
C1050T1-4h			4	21	0.51	0.7	3.7×10^{13}	23	1.4×10^{-4}	n

5.2 CuSb(Se$_x$,S$_{1-x}$)$_2$THIN FILMS

One way to modify optical and electrical properties of ternary CuSbS$_2$ in order to achieve high solar cell efficiencies is alloying this compound with Se in solid solution to form a quaternary CuSb(Se$_x$,S$_{1-x}$)$_2$. As the Se content increases the band gap of the compound shift from 1.5 eV to1.2 eV. In our experiment, we considered only the samples with large thicknesses (above 1000 nm). The reason to select these samples is because the sample with 1050 nm in thickness was the only have single CuSbS$_2$ phase, supported by our XRD and XPS results. CuSb(Se$_x$S$_{1-x}$)$_2$ thin films were prepared by heating layered structures of glass/Sb$_2$S$_3$/Se/Cu of 5 layers of Sb$_2$S$_3$ (1000 nm), Se layer of 100 nm and 300 nm and Cu layer of 50 nm annealed at 350 °C for 1h in low vacuum (10^{-3} Torr), giving a selenization process via chemical bath deposition technique. The final thickness of the thin films was in the order of 1100 nm to 1350 nm. The results and discussion of the thin films characterization will be presented.

5.2.1 Structure (XRD)

Structural characteristics of the thin films of glass/Sb$_2$S$_3$/Se/Cu of 5 Sb$_2$S$_3$ layers (1000 nm) and varying thickness of Se (100 nm and 300 nm) and Cu (10 nm, 30 nm and 50 nm) precursor layers were analyzed from the XRD patterns.

Figure 5.34shows diffraction patterns recorded in grazing incidence at angle of 0.3° for the thin films of Sb$_2$S$_3$ with 1000 nm and Se with 100 nm in thickness and 10 nm and 30 nm of Cu annealed at 350 °C for 1h. Film of 1110 nm in thickness shows peaks of chalcostibite CuSbS$_2$marked by the planes (200), (410), (301), (501), (321), (421) and (521). New peaks are observed at values of 2θ = 15.31°, 17.12°, 24.27°, 31.52°, 32.60° and 34.48°, which were compared with Sb$_2$S$_3$ standard pattern (PDF#42-1393) giving a left shift in 2θ in all these peaks, this might be due to the formation of a solid solution of Sb$_2$(S$_{1-x}$Se$_x$)$_3$.There was detected one peak of Cu$_2$S at 2θ = 27.70° (PDF#83-1462). For

the film of 1130 nm, a decrease in peak intensity of $Sb_2(S_{1-x}Se_x)_3$ is shown accompanied with an increase of those of $CuSbS_2$ and the presence of Cu_2S peak.
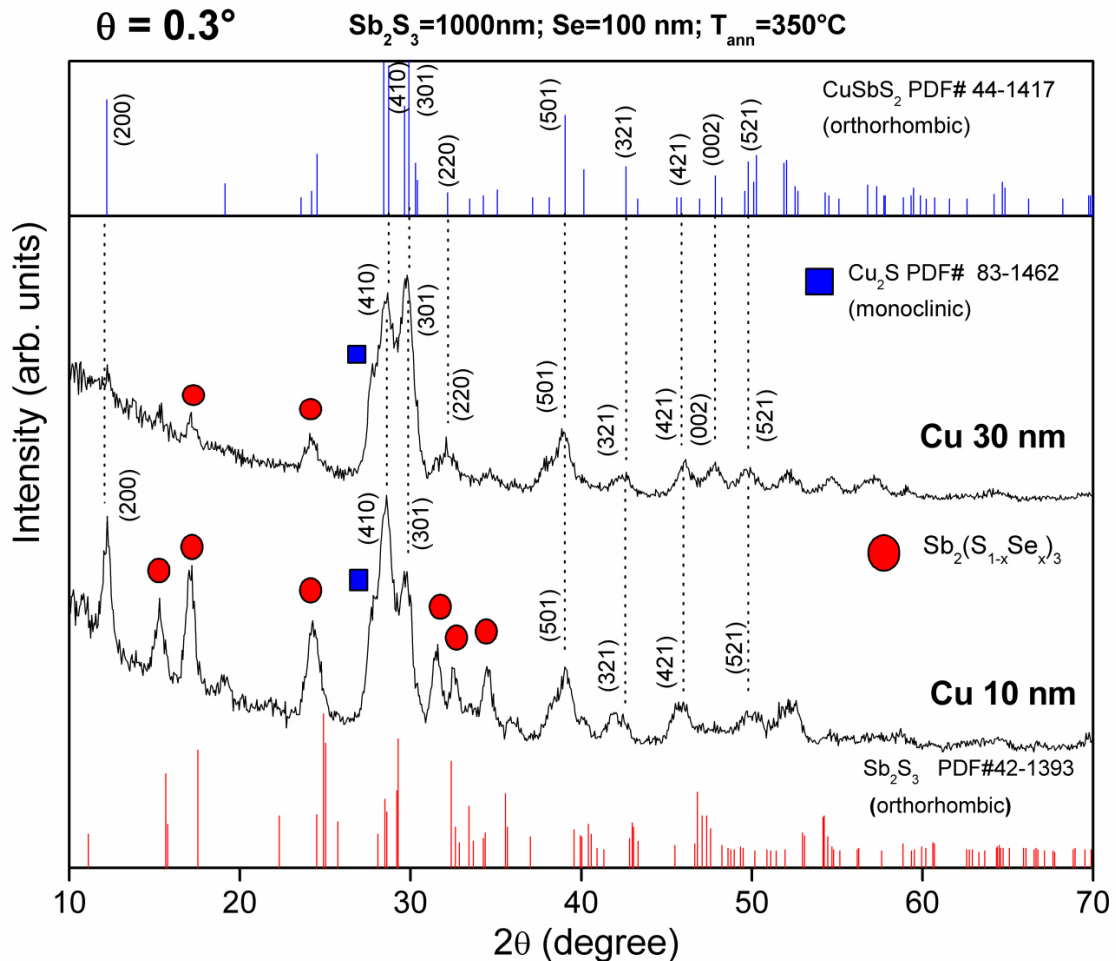
Figure 5.34 GIXRD patterns at θ=0.3° for glass/Sb₂S₃/Se/Cu of 1000 nm Sb₂S₃, 100 nm Se and variation of Cu thickness in 10 nm and 30 nm, annealed at 350 °C for 1h

For thin film of 1150 nm (Figure 5.35), $CuSbS_2$ peak of higher intensity and $Sb_2(S_{1-x}Se_x)_3$ and Cu_2S phases are present. For this sample, no traces of quaternary $CuSb(Se_xS_{1-x})_2$ formation are present. One possible reason for this is that the thickness of selenium layer is low.
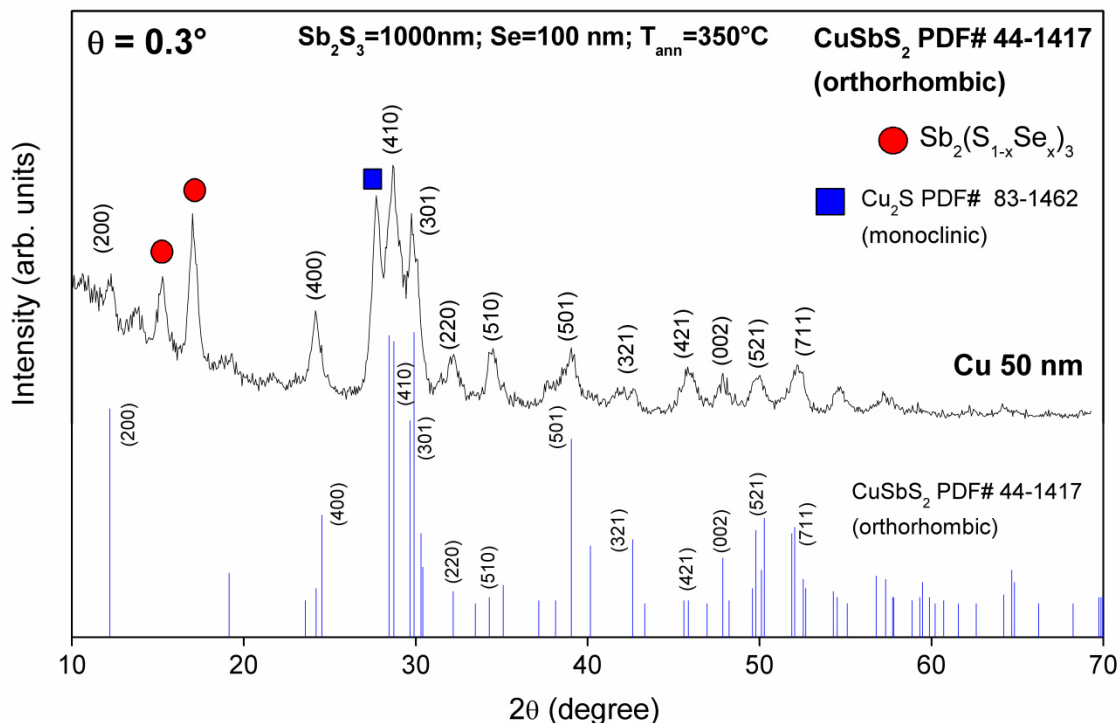
Figure 5.35 GIXRD patterns at θ=0.3° for glass/Sb$_2$S$_3$/Se/Cu of 1000 nm Sb$_2$S$_3$, 100 nm Se and Cu thickness of 50 nm, annealed at 350 °C for 1h

Figure 5.36shows diffraction patterns recorded in grazing incidence at angle of 0.3° for the thin films of glass/Sb$_2$S$_3$/Se/Cu of Sb$_2$S$_3$ with 1000 nm and Se with 300 nm in thickness and 10 nm and 30 nm of Cu annealed at 350 °C for 1h. Thin film of 1310 nm in thickness shows peaks of chalcostibite CuSbS$_2$left shifting in 2θ indicating the formation of a solid solution of CuSb(Se$_x$S$_{1-x}$)$_2$ comparing with orthorhombic CuSbS$_2$ (PDF#44-1417) pattern. Peaks of Sb$_2$(S$_{1-x}$Se$_x$)$_3$ are present. For the thin film of 1330 nm, a decrease in peaks intensity of Sb$_2$(S$_{1-x}$Se$_x$)$_3$and an increase of CuSb(Se$_x$S$_{1-x}$)$_2$ and no presence of Cu$_2$S peaks is observed.
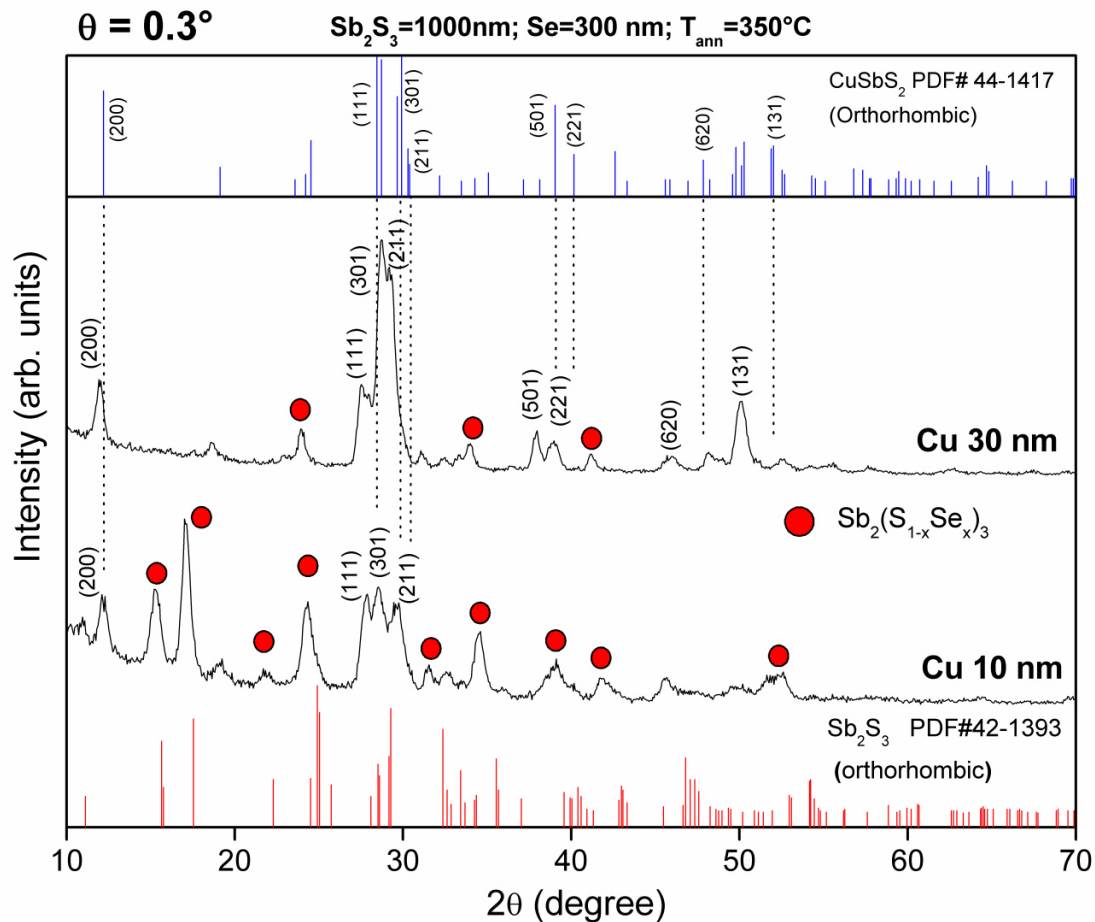
Figure 5.36 GIXRD patterns at θ=0.3° for glass/Sb$_2$S$_3$/Se/Cu of 1000 nm Sb$_2$S$_3$, 300 nm Se and variation of Cu thickness in 10 nm and 30 nm, annealed at 350 °C for 1h

For the thin film of 1350 nm (Figure 5.37) **a complete formation of CuSb(Se$_x$S$_{1-x}$)$_2$** is achieved marked by the planes (200), (400), (111), (301), (501), (221), (620), (131) and (022) without the presence of secondary phases like Sb$_2$(S$_{1-x}$Se$_x$)$_3$ or Cu$_2$S.
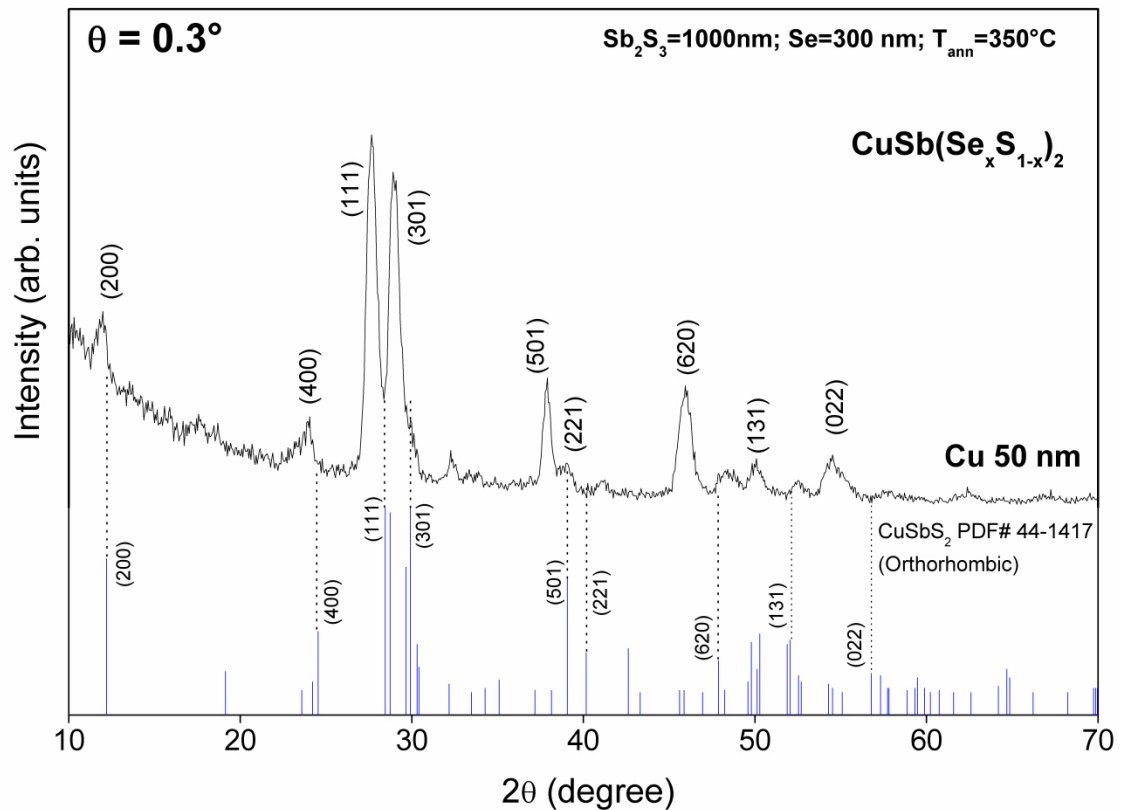
Figure 5.37 GIXRD patterns at θ=0.3° for glass/Sb₂S₃/Se/Cu of 1000 nm Sb₂S₃, 300 nm Se and Cu thickness of 50 nm, annealed at 350 °C for 1h

From Figure 5.38, the comparison of both glass/Sb$_2$S$_3$/Cu and glass/Sb$_2$S$_3$/Se/Cu films of 1050 nm (C1050T1) and 1350 nm (1350T1) annealed at 350 °C for 1h respectively is given. The XRD patterns show clearly the shift of all peaks peaks towards small 2θ angles indicating the formation of a solid solution of CuSb(Se$_x$S$_{1-x}$)$_2$ using a selenization process via chemical bath deposition. This shifting is due that in solid solution, selenium atoms are introduced into CuSbS$_2$ lattice by substitution of sulfur atoms, selenium atoms are bigger than sulfur atoms giving a lattice deformation increasing the lattice parameter and so on the increase of interplanar distance. This effect is shown in Figure 5.39 where CuSb(Se$_x$S$_{1-x}$)$_2$ peaks marked by the planes (200), (111), (301), (501) and (221) show the shift from the CuSbS$_2$ peaks, including the standard lines patterns of CuSbS$_2$ and CuSbSe$_2$.
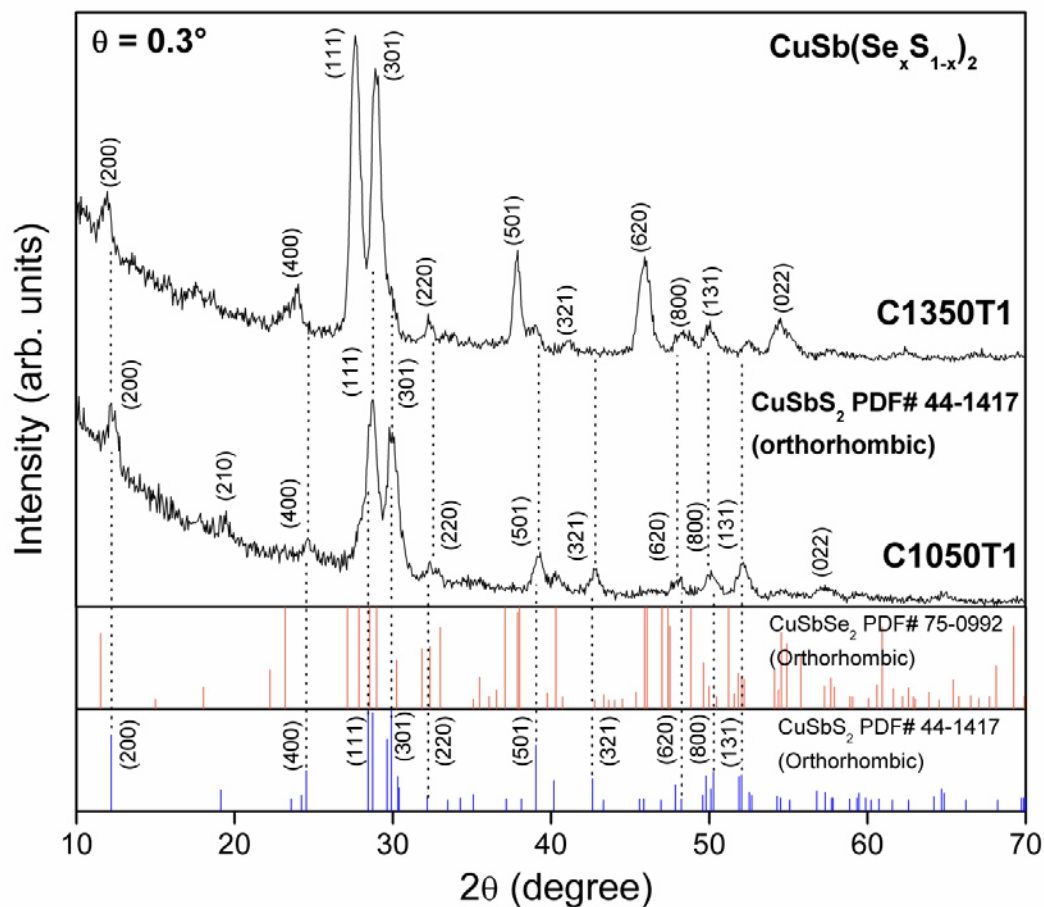
Figure 5.38 GIXRD patterns at θ=0.3° for glass/Sb$_2$S$_3$/Cu and glass/Sb$_2$S$_3$/Se/Cu of 1050 nm (C1050T1) and 1350 nm (C1350T1) respectively annealed at 350 °C for 1h
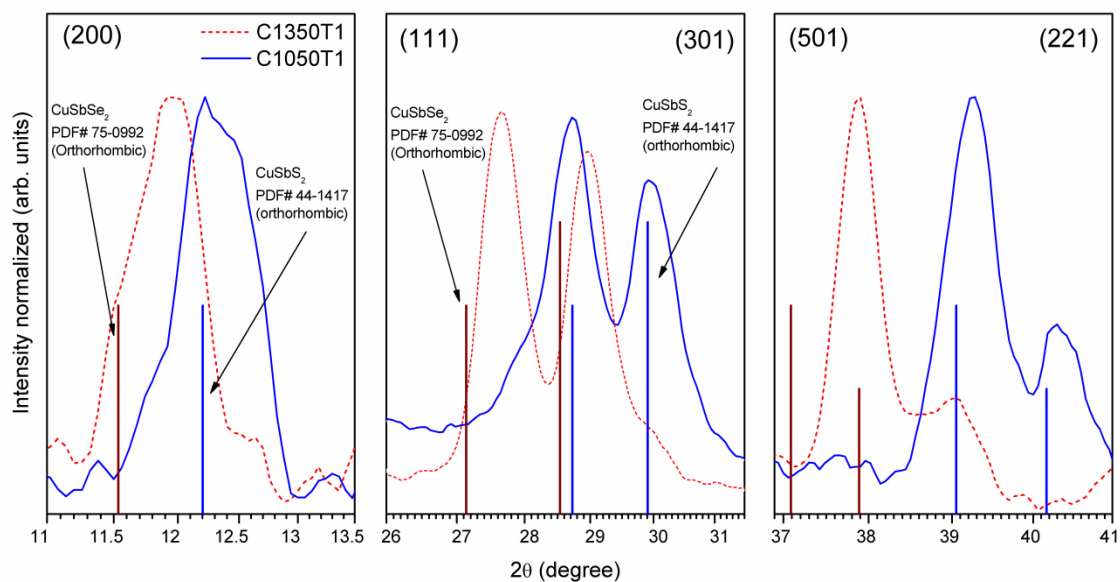
Figure 5.39 Shift of the GIXRD peaks at θ=0.3° of glass/Sb$_2$S$_3$/Cu and glass/Sb$_2$S$_3$/Se/Cu of 1050 nm (C1050T1) and 1350 nm (C1350T1) respectively annealed at 350 °C for 1h

Based on the last results, the diffraction patterns for the thin film of 1350 nm annealed at 350 °C 1h at grazing incident angles of 0.3° and 1.5° are analyzed as shown in Figure 5.40. At 1.5° grazing angle there is no peaks shifting, indicating the presence only of ternary $CuSbS_2$, besides the presence of Cu_2S. This indicates that only in the surface at thickness of approximately 60 nm we have single quaternary $CuSb(Se_xS_{1-x})_2$phase and in the rest of the thickness a mix of $CuSbS_2$ and Cu_2S phases are present.
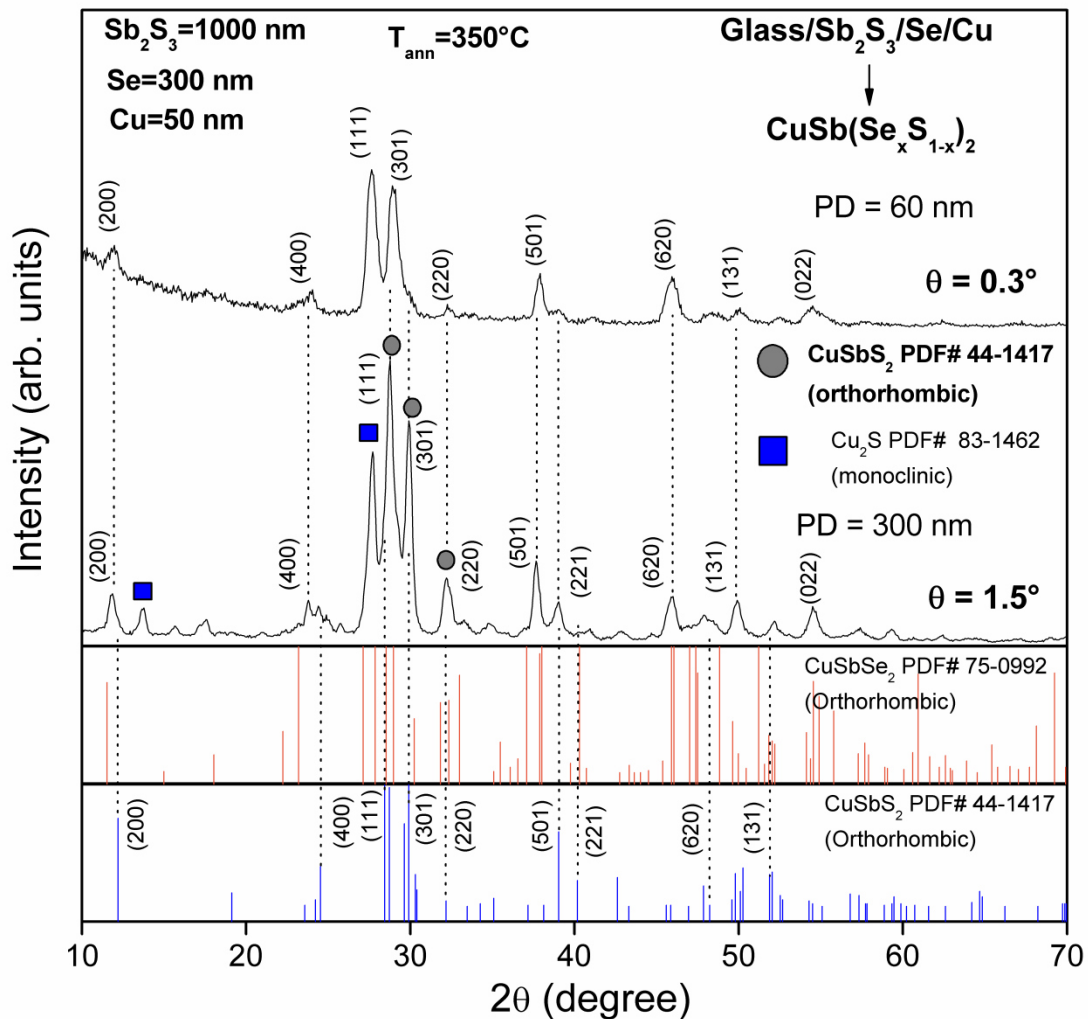
Figure 5.40 GIXRD patterns at θ=0.3° and 1.5°for glass/Sb₂S₃/Se/Cu of 1350 nm annealed at 350 °C for 1h

5.2.2 Morphology (AFM)

Figure 5.41 shows morphological features of glass/Sb_2S_3/Se/Cu thin film of 1350 nm and glass/Sb_2S_3/Cu of 1050 nm annealed at 350 °C for 1h illustrated by 1 μm × 1 μm atomic force micrographs. Figure 5.41a, corresponds to semicontact mode 3D, in which the image reveals spherical grains of diameter in ranges of 50-80 nm. The phase contrast image of the respective topography is illustrated in Figure 5.41b it can be seen densely packed grains with well-defined grain boundaries. In comparison with the thin film of $CuSbS_2$ (Figure 5.41c and d) the diameter of the grains is in the range of 50-100 nm. The RMS roughness analysis measured from 3D images showed a decrease in roughness from 9.5 nm to 4.9 nm for $CuSbS_2$ and $CuSb(Se_xS_{1-x})_2$ thin film respectively.
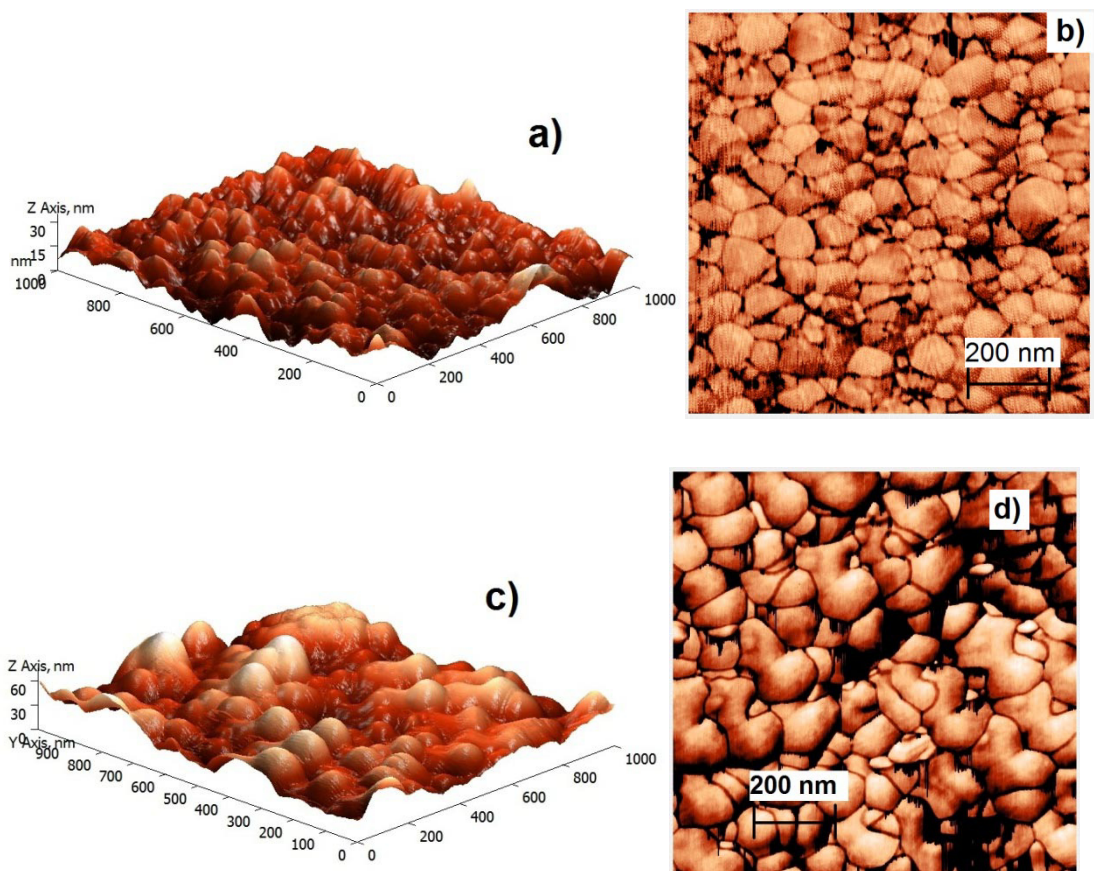
Figure 5.41 Atomic force micrographs for glass/Sb_2S_3/Se/Cu thin film of 1350 nm (a) in semicontact mode 3D, (b) phase contrast mode and for glass/Sb_2S_3/Cu thin film of 1050 nm (c) in semicontact mode 3D and (d) phase contrast mode annealed at 350 °C for 1h

5.2.3 Composition (XPS)

The elemental composition and the oxidation states of each element present in the $CuSb(Se_xS_{1-x})_2$ thin film was analyzed by X-ray photoelectron spectroscopy, in order to confirm the results obtained from the structural characterization by XRD. The analysis was carried out by selecting the sample in which the complete quaternary compound was formed, the sample of glass/Sb_2S_3/Se/Cu of 5 layers of Sb_2S_3 (1000 nm), 300 nm of selenium and 50 nm of copper annealed at 350 °C for 1h in low vacuum. The analysis of high resolution spectra and depth profile was performed.
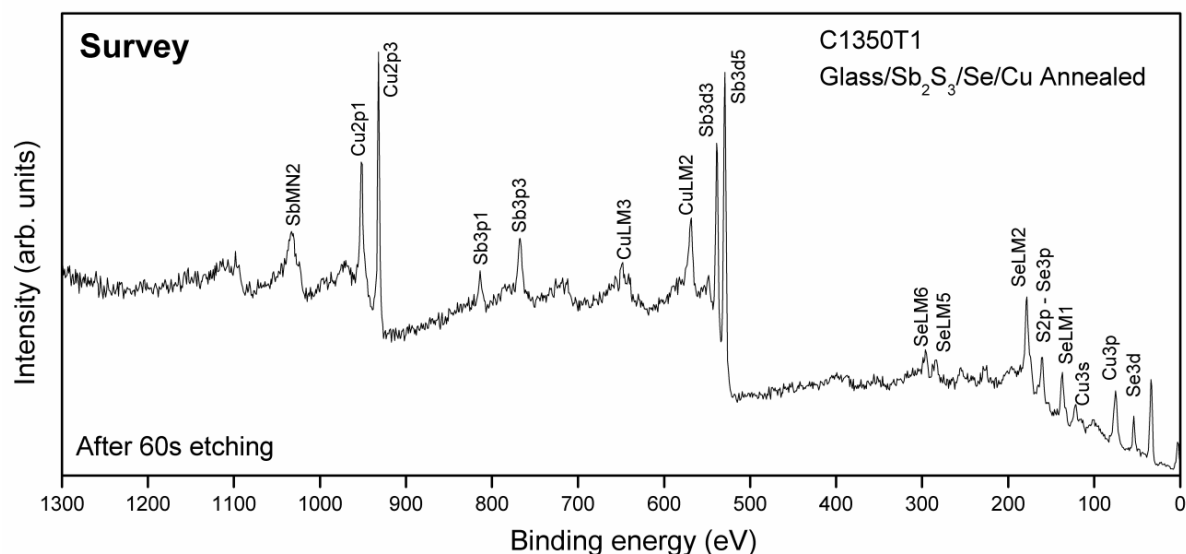
Figure 5.42 Survey spectrum of glass/Sb_2S_3/Se/Cu precursor thin film of 1350 nm annealed at 350 °C for 1 h after 60 s Ar$^+$ ions etching

The analysis of the survey spectrum after 60 s Ar$^+$ ions etching generated at 2 keV is shown in Figure 5.42. From the survey spectrum, the presence of copper, antimony, sulfur and selenium without contaminant elements such as carbon and oxygen which were removed by the Ar$^+$ ion etching is observed.
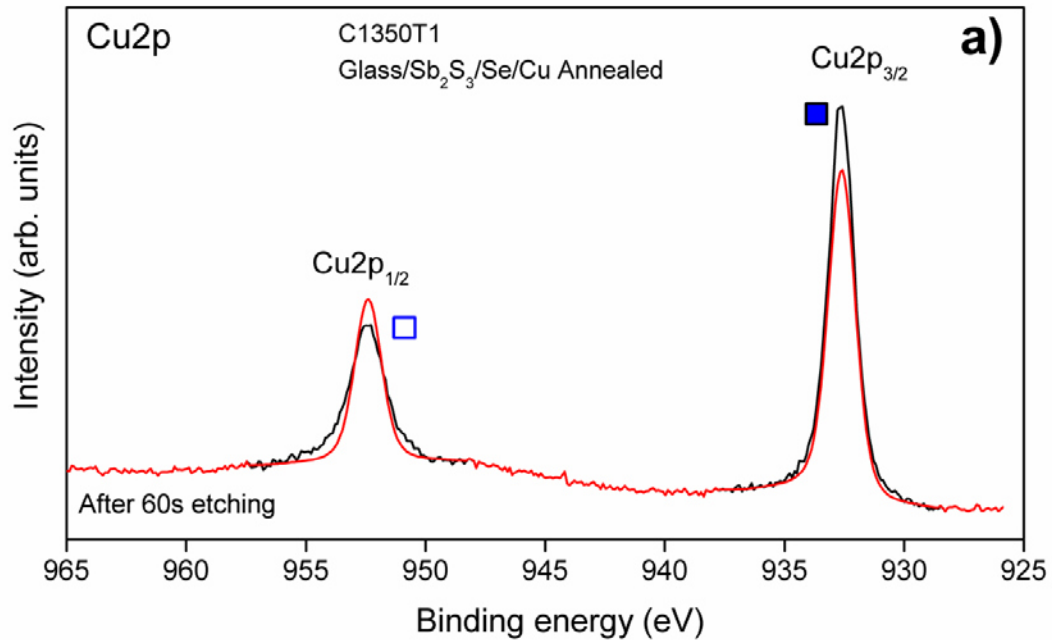
Core Level Peak	Binding energy (eV)	FWHM	Area ratio	Compound
■ Cu2p$_{3/2}$	932.60	1.35	1.00	CuSb(S,Se)$_2$
□ Cu2p$_{1/2}$	952.40	1.35	0.50	CuSb(S,Se)$_2$
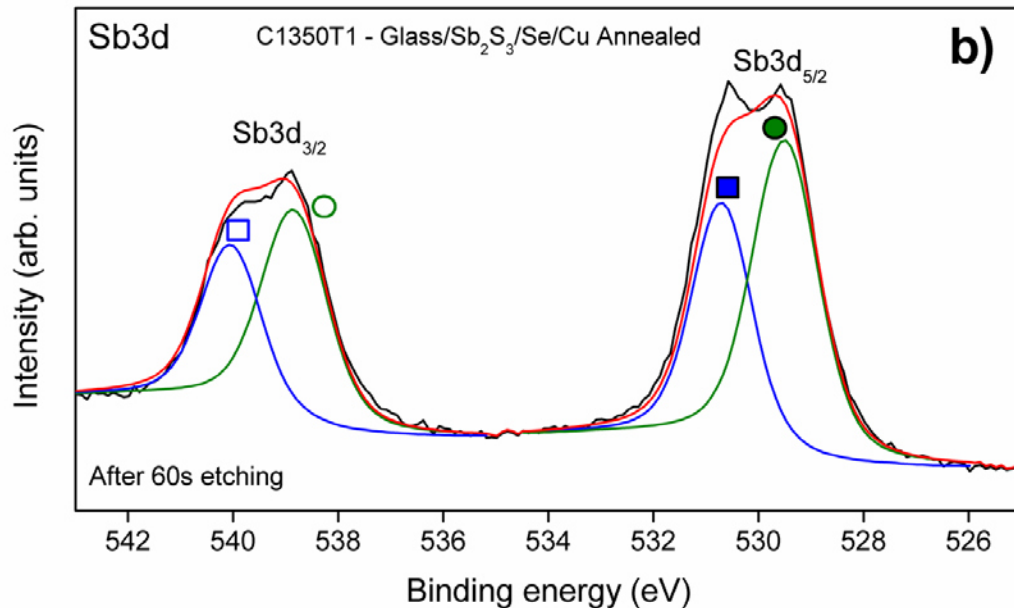
Core Level Peak	Binding energy (eV)	FWHM	Area ratio	Compound
■ Sb3d$_{5/2}$	530.70	1.35	1.00	CuSb(S,Se)$_2$
□ Sb3d$_{3/2}$	540.04	1.35	0.66	CuSb(S,Se)$_2$
● Sb3d$_{5/2}$	529.50	1.50	1.00	Sb$_2$S$_3$
○ Sb3d$_{3/2}$	538.84	1.50	0.67	Sb$_2$S$_3$

Core Level Peak	Binding energy (eV)	FWHM	Area ratio	Compound
■ $S2p_{3/2}$	161.90	0.75	1.00	$CuSb(S,Se)_2$
□ $S2p_{1/2}$	163.06	0.75	0.49	$CuSb(S,Se)_2$
● $S2p_{3/2}$	161.50	0.70	1.00	Sb_2S_3
○ $S2p_{1/2}$	162.66	0.70	0.51	Sb_2S_3
▲ $Se3p_{3/2}$	160.40	2.00	1.00	$CuSb(S,Se)_2$
△ $Se3p_{1/2}$	166.20	2.00	0.50	$CuSb(S,Se)_2$

Core Level Peak	Binding energy (eV)	FWHM	Area ratio	Compound
■ $Se3d_{5/2}$	54.10	1.00	1.00	$CuSb(S,Se)_2$
□ $Se3d_{3/2}$	54.96	1.00	0.66	$CuSb(S,Se)_2$
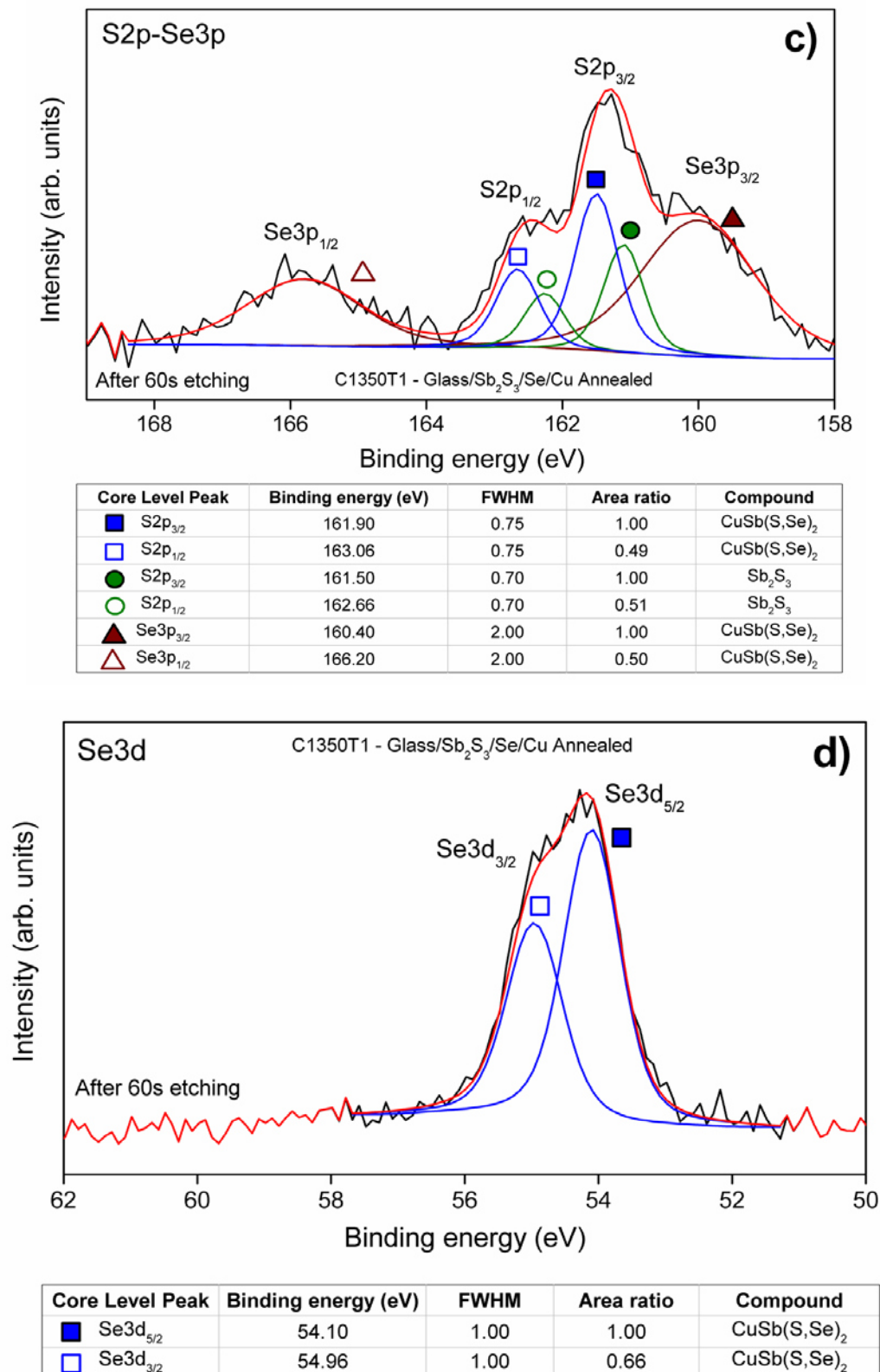
Figure 5.43 High-resolution spectra of (a)Cu2p, (b) Sb3d, (c) S2p-Se3p and (d) Se3d core levels of glass/Sb_2S_3/Se/Cu of 1350 nm thin film annealed at 350 °C for 1 h (C1350T1) after 60 s Ar^+ ions etching

Figure 5.43a, b, c and d shows high resolution experimental spectra (black curve) and theoretical spectra (red curve) for Cu2p, Sb3d, S2p-Se3p and Se3d core levels along with the deconvoluted ones (color curves). From graph in Figure 5.43a, the $Cu2p_{3/2}$ and $Cu2p_{1/2}$ core levels peaks at 932.6 eV and 952.4 eV do not match with the formation of $CuSbS_2$ or elemental Cu, implying the formation of new compound, we assign these peaks at the quaternary $CuSb(Se_xS_{1-x})_2$ since there is not any report available for this compound. Figure 5.43b shows high resolution spectra for $Sb3d_{5/2}$ and $Sb3d_{3/2}$ core levels and the deconvoluted ones. The peaks observed at 529.5 eV and 538.84 eV corresponding to Sb^{3+} due to unreacted Sb_2S_3. The peaks at 530.7 eV and 540.04 eV did not match with the values for ternary compound $CuSbS_2$, assigning these peaks at $CuSb(Se_xS_{1-x})_2$ compound. From the high resolution core level spectra for S2p doublets given Figure 5.43c, the deconvoluted peaks located at 161.5 and 162.66 eV corresponding to S^{-2} in Sb_2S_3. The peaks observed at 161.9 eV and 163.06 eV did not match with $CuSbS_2$ compound. Also, a $Se3p_{3/2}$ and $Se3p_{1/2}$ core levels are present in the analysis region of S2p core levels, these peaks located at 160.4 eV and 166.2 eV respectively do not corresponds to a compound containing selenium. From Figure 5.43d the $Se3d_{5/2}$ and $Se3d_{3/2}$ core levels have peaks located at 54.1 eV and 54.96 eV respectively. The peaks do not match with any selenium compound reported. Combining our results of the B.E values of Cu2p, Sb3d, S2p-Se3p and Se3d core levels and the phases detected in our XRD results, it was assigned the values for the formation of $CuSb(Se_xS_{1-x})_2$.

The depth profile analysis for glass/Sb_2S_3/Se/Cu thin film of 1350 nm annealed at 350 °C for 1his shows in the XPS profile montage given in Figure 5.44, where Cu 2p, Sb 3d, S 2p and Se3d core levels were detected. The peak shift of the Cu2p, Sb3d and S2p core levels towards depth on the sample may be is due to the surface charge effect by the reduction of the surface charge compensation by the flood gun of the XPS, this not indicating the formation of new compound. From this analysis it is observed that the presence of selenium is only in the surface of the thin film. The complete reaction of selenium with all

elements presents occur only approximately at 60 nm from the surface. This result is in good agreement with the results obtained in XRD analysis. This could lead us to find another alternative to increase selenium content on the sample. The presence of a shift towards higher energy in depth is caused by charge effects due to high resistivity in the surface after etching which lead to kinetic energy loss of photoelectrons emitted from the sample, leading to a shift of XPS peak position.
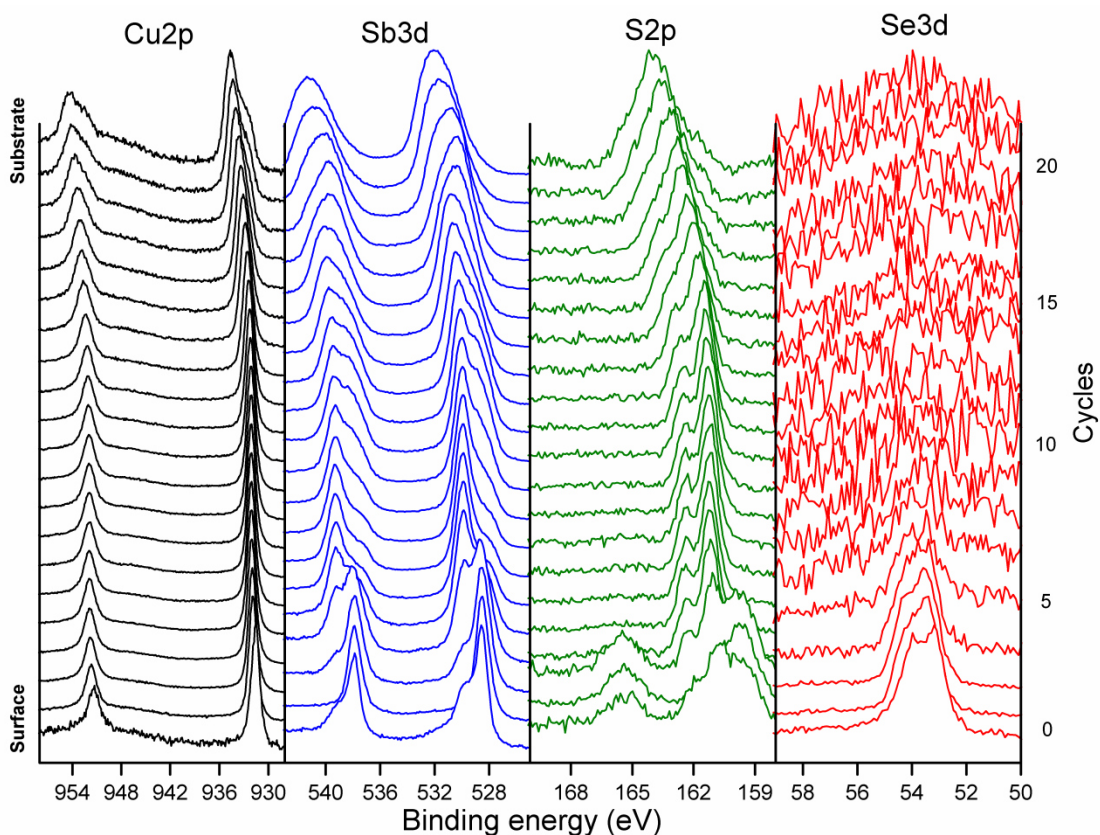
Figure 5.44 Depth profile for glass/Sb$_2$S$_3$/Se/Cu of 1350 nm annealed at 350 °C 1 h for core levels montage of Cu2p, Sb3d, S2p and Se3d

5.2.4 Optical properties (UV-Vis)

The optical transmittance (%T) and reflectance (%R) spectra of glass/Sb$_2$S$_3$/Cu and glass/Sb$_2$S$_3$/Se/Cu thin films of 1050 nm (C1050T1) and 1350 nm (C1350T1) annealed at 350 °C for 1h, respectively, are shown in

Figure 5.45a. In the region above 900 nm an average 20% transmittance and 30% reflectance were observed. Nearly 50% of absorption in the region may be due to the presence of Cu_2S which is a low band gap material (1.2-1.3 eV) in the thin film(Klimov et al., 1995).
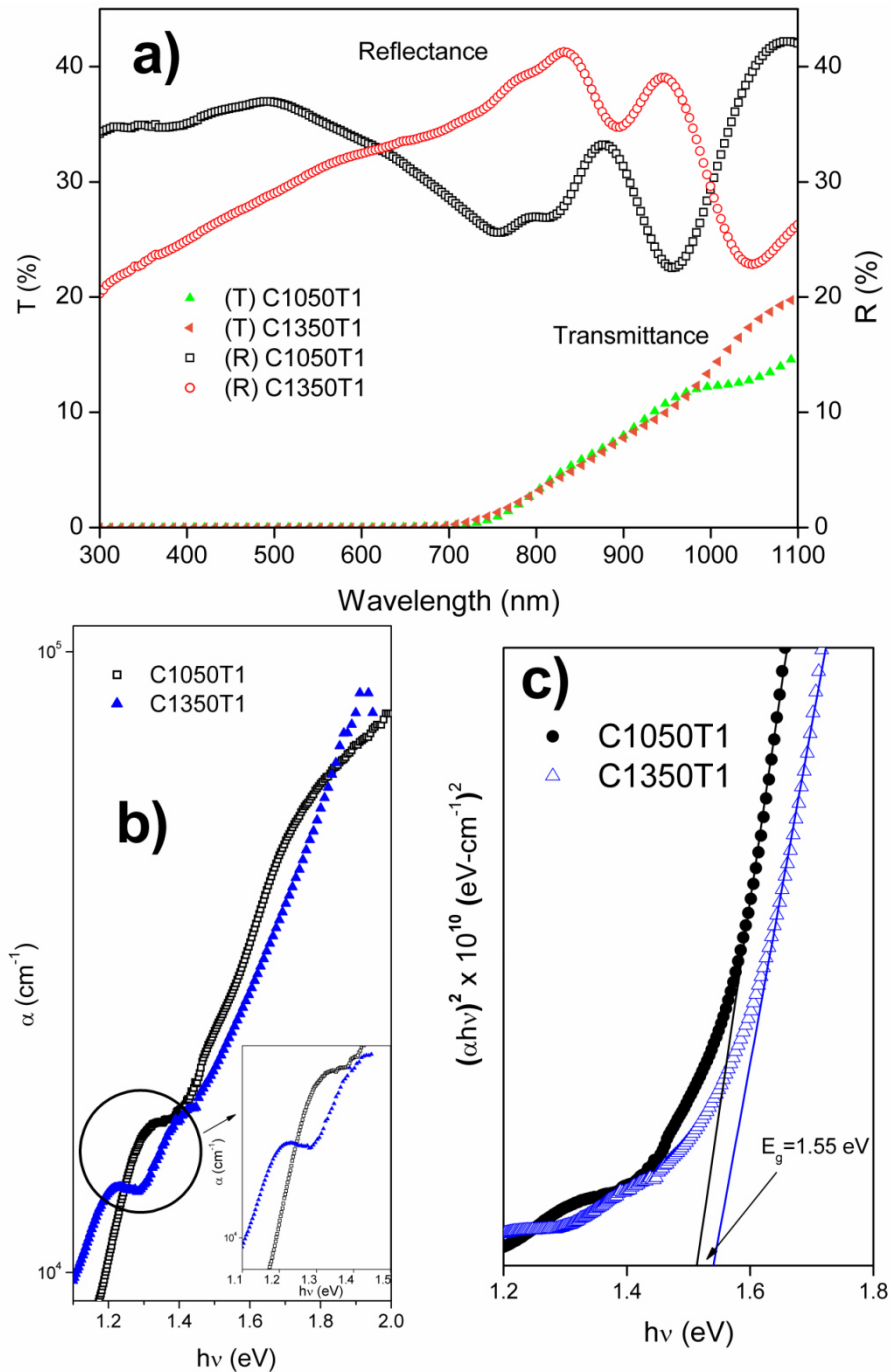
Figure 5.45 (a) Transmittance (T) and Reflectance (R) spectra, (b) absorption coefficient and (c) evaluation of optical band gap for glass/Sb_2S_3/Cu of 1050 nm (C1050T1) and glass/Sb_2S_3/Se/Cu of 1350 nm (C1350T1) annealed at 350 °C for 1h

In the absorbing region, α can be calculated using the equation (2.7). Figure 5.45b shows absorption coefficient of the thin films having values around 10^4-10^5 cm^{-1}. For the sample C1350T1 (blue solid triangle), different transitions approximately at 1.4 eV and 1.2 eV are observed (inset Figure 5.45b), the transition is that when the curve falls abruptly and in this value indicate the value of the band gap of material, the transition that occurs around 1.4 eV correspond to solid solution of CuSb(Se$_x$S$_{1-x}$)$_2$(Colombara et al., 2011) and the transition at 1.2 eV belongs to Cu$_2$S compound (Klimov et al., 1995). These results are in good agreement with the XRD and XPS results obtained where it were identified the formation of pure CuSb(Se$_x$S$_{1-x}$)$_2$ at surface and a mixed of CuSbS$_2$ and Cu$_2$S phases in the rest of the thin film. The optical band gap value of the thin film was determined using the equation (2.8). Figure 5.45c illustrates the plot of $(\alpha h\nu)^2$ vs hν (Tauc plot) for the thin films, corresponding the value of 1.55 eV for ternary CuSbS$_2$.

5.2.5 Electrical properties

Electrical properties of glass/Sb$_2$S$_3$/Cu and glass/Sb$_2$S$_3$/Se/Cu thin films of 1050 nm (C1050T1) and 1350 nm (C1350T1) annealed at 350 °C for 1h, respectively, were determined from the photocurrent response measurements at room temperature by applying a D.C. bias. Dark conductivity and photoconductivity of the thin films C1050T1 and C1350T1 are shown in Figure 5.46 illuminated using a tungsten halogen lamp. In the present experiment a bias of 0.1 V was applied across a pair of planar silver paint electrodes, the current through the sample was measured in an interval of 20 s each, first in the dark (I$_o$), followed by illumination (I) of the sample and then after switching off the light source. The values of dark conductivity and photoconductivity were evaluated as in the order of 10^{-6} (Ω-cm)$^{-1}$ and 10^{-5} (Ω-cm)$^{-1}$ for the samplesC1050T1 and C1350T1 respectively. The samples were photoconductive as seen from the figure. The photosensitivity, defined as (I-I$_o$)/I$_o$, was determined in the values of 1.2 and 0.2 for C1050T1 and C1350T1

respectively, having a decrease in photosensitivity in samples with selenium. The increase in conductivity for thin film with selenium (C1350T1) is due that the surface roughness (measured by AFM) is less than for thin film without selenium (C1050T1), the electron scattering is reduced in the sample in which the roughness is low, for that reason its mean free path length increase giving an increase in conductivity. Other reason for the conductivity increase is the presence of Cu_2S phase, a well-known high conductivity phase. The reason for the increase of photosensitivity is that the drift mobility of the photogenerated carriers in C1350T1 thin film is larger than for C1050T1 due to the reduction of surface scattering by the decrease of roughness from 9.5 nm to 4.9 nm. The conductivity type measured by the hot probe was p-type.
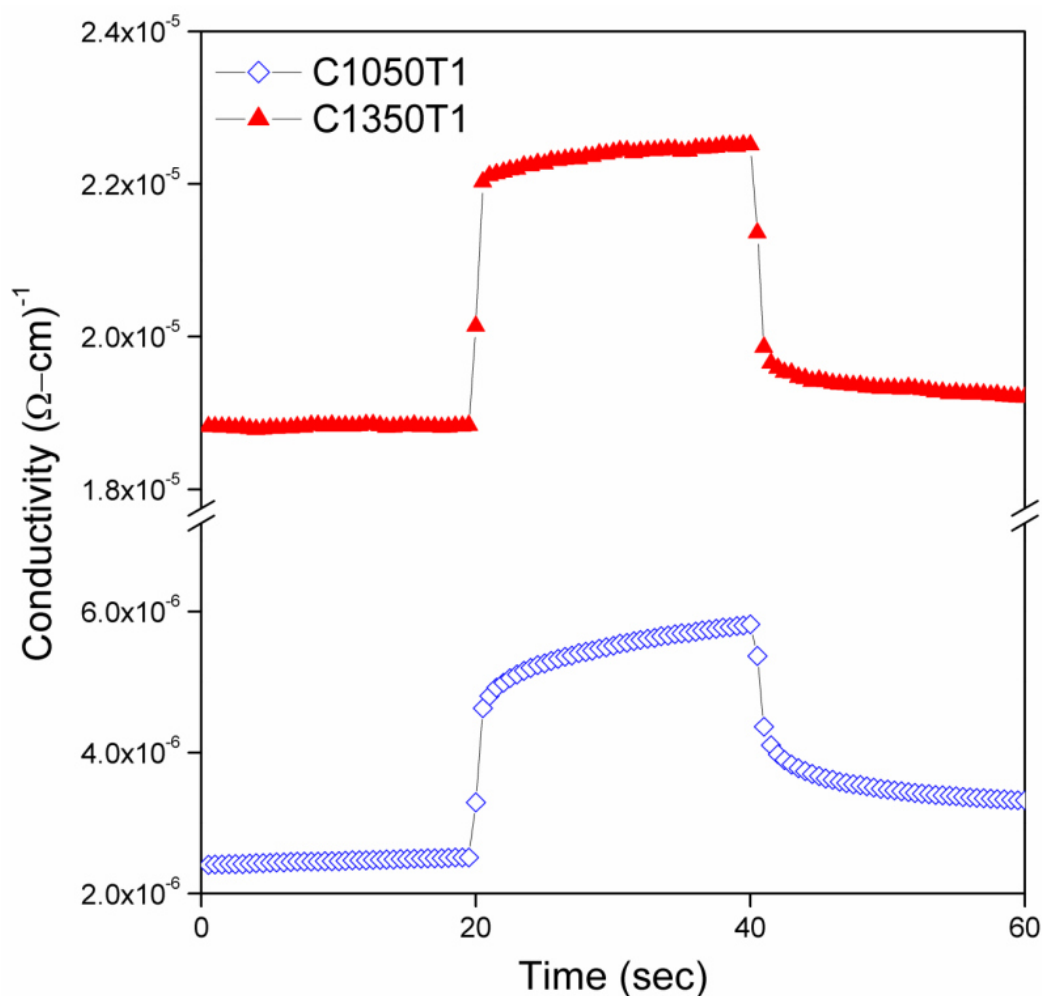
Figure 5.46 Photoconductivity curves for C1050T1 and C1350T1 thin films

5.3 PHOTOVOLTAIC DEVICES

Fabrication of photovoltaic devices at low cost and high efficiency is a great challenge. Based on the above studies, various photovoltaic structures were prepared using $CuSbS_2$ and $CuSb(Se_xS_{1-x})_2$ thin films as absorber and CdS thin films as window layer. Multilayered structures of glass/SnO_2:F/CdS/Sb_2S_3/Cu and glass/SnO_2:F/CdS/Sb_2S_3/Se/Cu were prepared and annealed at different conditions to form photovoltaic p-n junctions of type glass/SnO_2:F/n-CdS/p-$CuSbS_2$ and glass/SnO_2:F/n-CdS/p-$CuSb(Se_xS_{1-x})_2$. Further, PV junctions using layer structures of glass/SnO_2:F/n-CdS/i-Sb_2S_3/p-$CuSbS_2$ with an intrinsic layer of Sb_2S_3 between $CuSbS_2$ and CdS layers were also prepared.

Table 5.2 gives a list of all the experimental conditions that were carried out for the fabrication of photovoltaic devices in this work. The results presented in this section are considering the materials at conditions for the best photovoltaic device performance, which are the glass/Sb_2S_3/Cu thin film of 650 nm annealed at 350 °C, 375 °C, 400 °C for 1 h, thin film of 850 nm and 1050 nm annealed at 350 °C for 1 h and thin film of 1050 nm annealed at 350 °C for 2, 3 and 4 h.

Table 5.2 Experiment conditions for the preparation of photovoltaic devices

Solar Cell	n-CdS	i-Sb_2S_3	Absorber material			Annealing temperature
			Sb_2S_3	Se	Cu	
1	45 min as prepared	N/A	600 nm	N/A	50 nm	350 °C – 1h
2						375 °C – 1h
3						400 °C – 1h
4			800 nm			350 °C – 1h
5	45 min annealed at 400 °C 1h air		600 nm			350 °C – 1h
6						375 °C – 1h
7						400 °C – 1h
8			800 nm			350 °C – 1h
9			1000 nm			
10			1200 nm			

11			1000 nm		70 nm	
12			1200nm			
13	20 min annealed at 400 °C 1h air	50 nm	1000 nm		50 nm	
14		100 nm				
15		200 nm				
16		100 nm			30 nm	
17				100 nm		
18				300 nm		
19	45 min annealed at 400 °C 1h air	50 nm	1000 nm	N/A	50 nm	
20		100 nm				
21		200 nm				
22		50 nm				
23		100 nm			30 nm	
24				100 nm		
25						
26		100 nm				
27				300 nm	50 nm	350 °C – 2h
28						350 °C – 3h
29						350 °C – 4h

5.3.1 Window layer (CdS)

Photovoltaic devices were prepared using CdS annealed at 400 °C 1h in air prior to deposition of the absorber material. It was found that after CdS annealing, band gap decreased from 2.5 eV to 2.4 eV as shown in Figure 5.47a. The photoconductivity was measured as shown in Figure 5.47b, giving an increase in photosensitivity for CdS annealed from 0.2 to 12.7. The thicknesses of the samples were measured using a profilometer giving a thickness of 230 nm and 180 nm for CdS samples before and after annealing respectively.
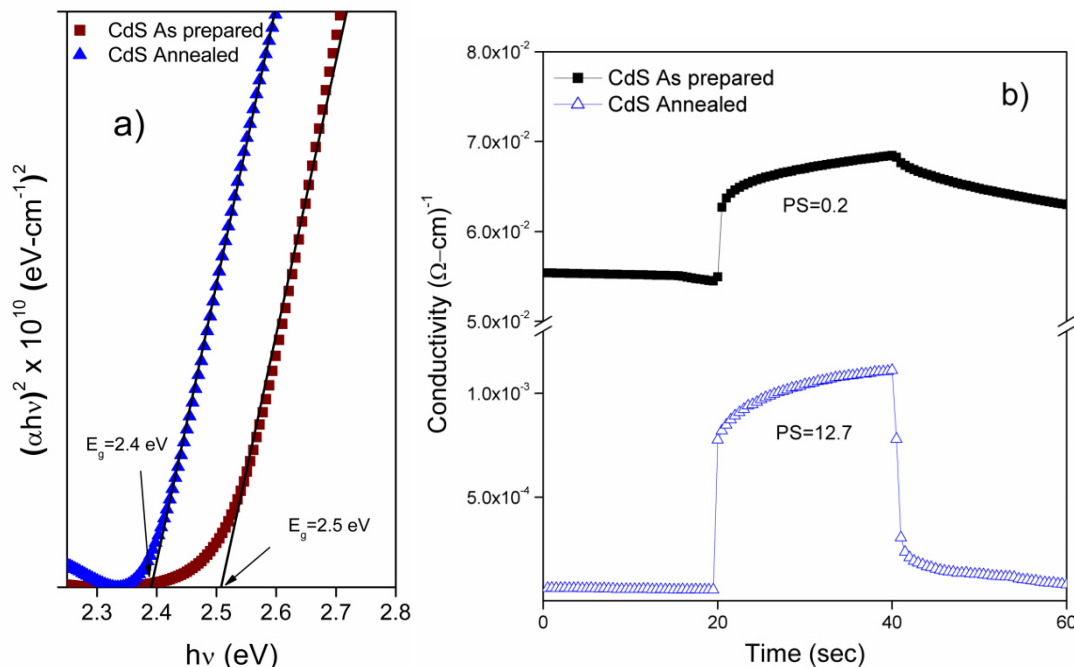
Figure 5.47 (a) optical band gap for CdS before and after annealing at 400 °C for 1h in air and (b) photoconductivity measurements

The oxidation states and the elemental composition of the precursor glass/CdS thin film were analyzed by XPS. For the as prepared and annealed CdS at 400 °C 1h in air, a typical survey spectrum recorded from the surface of the thin film without etching is shown in Figure 5.48a and b respectively, which indicates the presence of Cd, S, Si, C and O. The presence of carbon is due to the adventitious carbon, the oxygen is due to the oxidized surface for the environmental exposure and meanwhile the presence of silicon is attributed to the small pieces of corning glass left on the surface by the process of cutting in the preparation of the sample. In the annealed CdS, an increase in the peak intensity of oxygen is attributed to the incorporation of oxygen due to annealing in air atmosphere. In CdS thin films, the presence of chemisorbed oxygen in the intergrain region improves the photosensitivity (Nair et al., 1993), which is in good agreement with our results obtained.
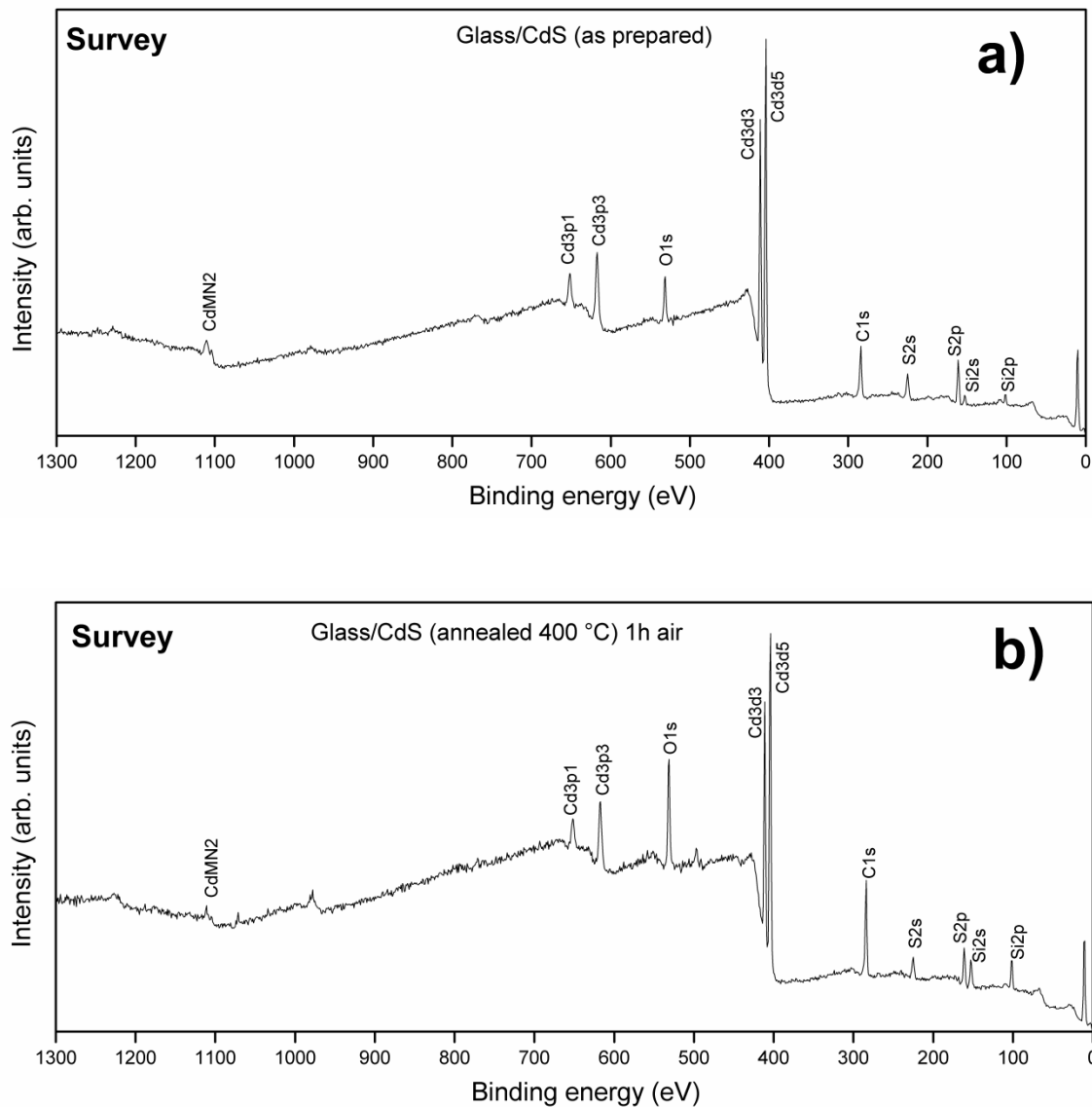
Figure 5.48 Survey spectrum of glass/CdS precursor thin film (a) as prepared and (b) annealed at 400 °C 1h in air

Figure 5.49a,b and Figure 5.50a,b shows Cd3d and S2p core levels for glass/CdS thin film as prepared and annealed at 400 °C 1h in air. From Figure 5.49a and b, the doublet $Cd3d_{5/2}$ and $Cd3d_{3/2}$ core levels constituted one peak located at 404.85 eV and 411.59 eV for the as prepared sample and 405.0 eV and 411.74 eV for the annealed sample, corresponding to Cd^{2+} in CdS (Naumkin et al., 2000). The FWHM for the core level $Cd3d_{5/2}$ and $Cd3d_{3/2}$ peaks for as prepared and annealed sample was 1.1 eV.

Core Level Peak		Binding energy (eV)	FWHM	Area ratio	Compound
■	Cd3d$_{5/2}$	404.85	1.10	1.00	CdS
□	Cd3d$_{3/2}$	411.59	1.10	0.66	CdS

Core Level Peak		Binding energy (eV)	FWHM	Area ratio	Compound
■	Cd3d$_{5/2}$	405.00	1.10	1.00	CdS
□	Cd3d$_{3/2}$	411.74	1.10	0.66	CdS
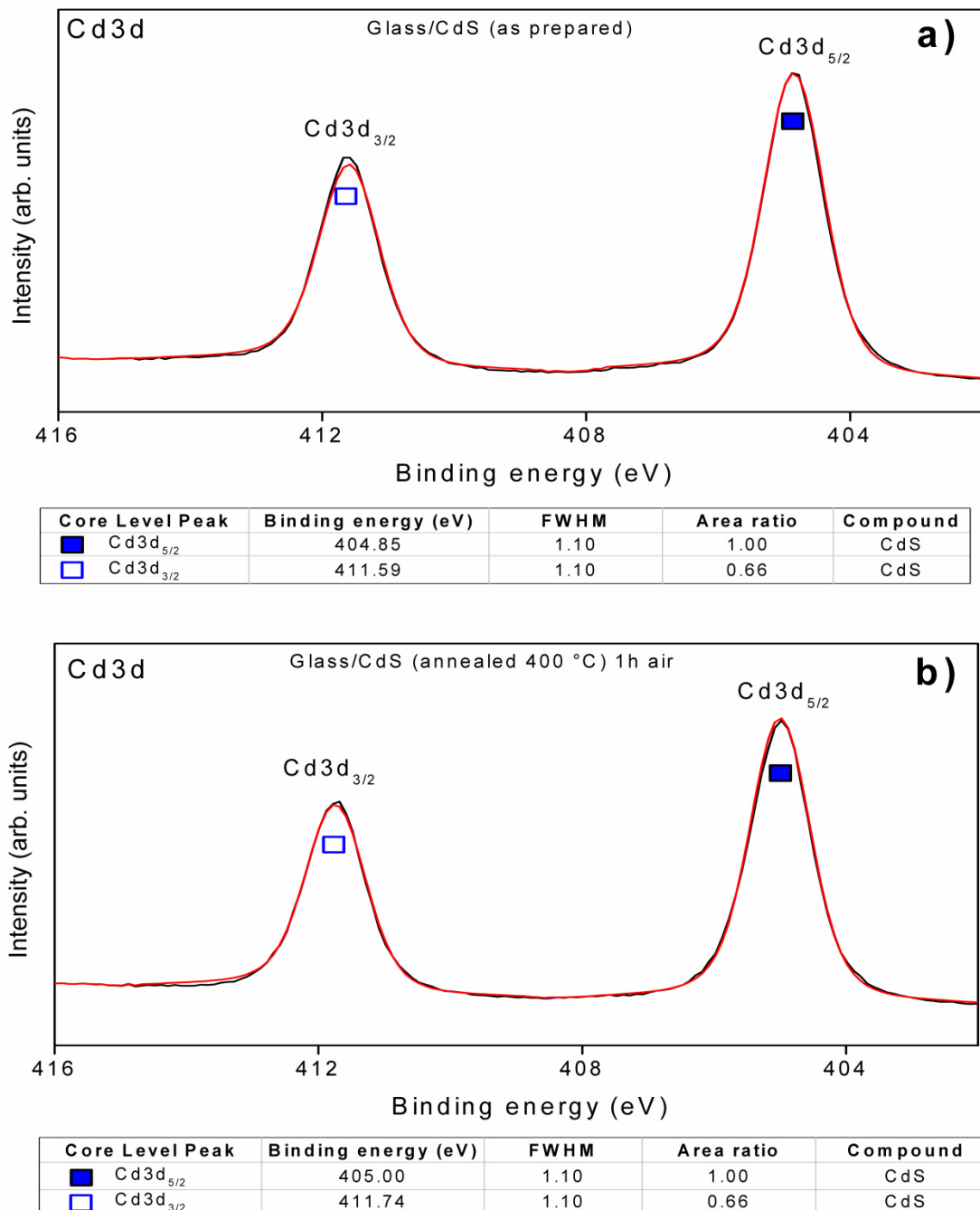
Figure 5.49 High resolution core level Cd3d spectra of Glass/CdS precursor thin film (a) as prepared and (b) annealed at 400 °C 1h in air

Core Level Peak	Binding energy (eV)	FWHM	Area ratio	Compound
■ S2p$_{3/2}$	161.30	1.10	1.00	CdS
□ S2p$_{1/2}$	162.46	1.10	0.50	CdS

Core Level Peak	Binding energy (eV)	FWHM	Area ratio	Compound
■ S2p$_{3/2}$	161.40	1.05	1.00	CdS
□ S2p$_{1/2}$	162.56	1.05	0.50	CdS
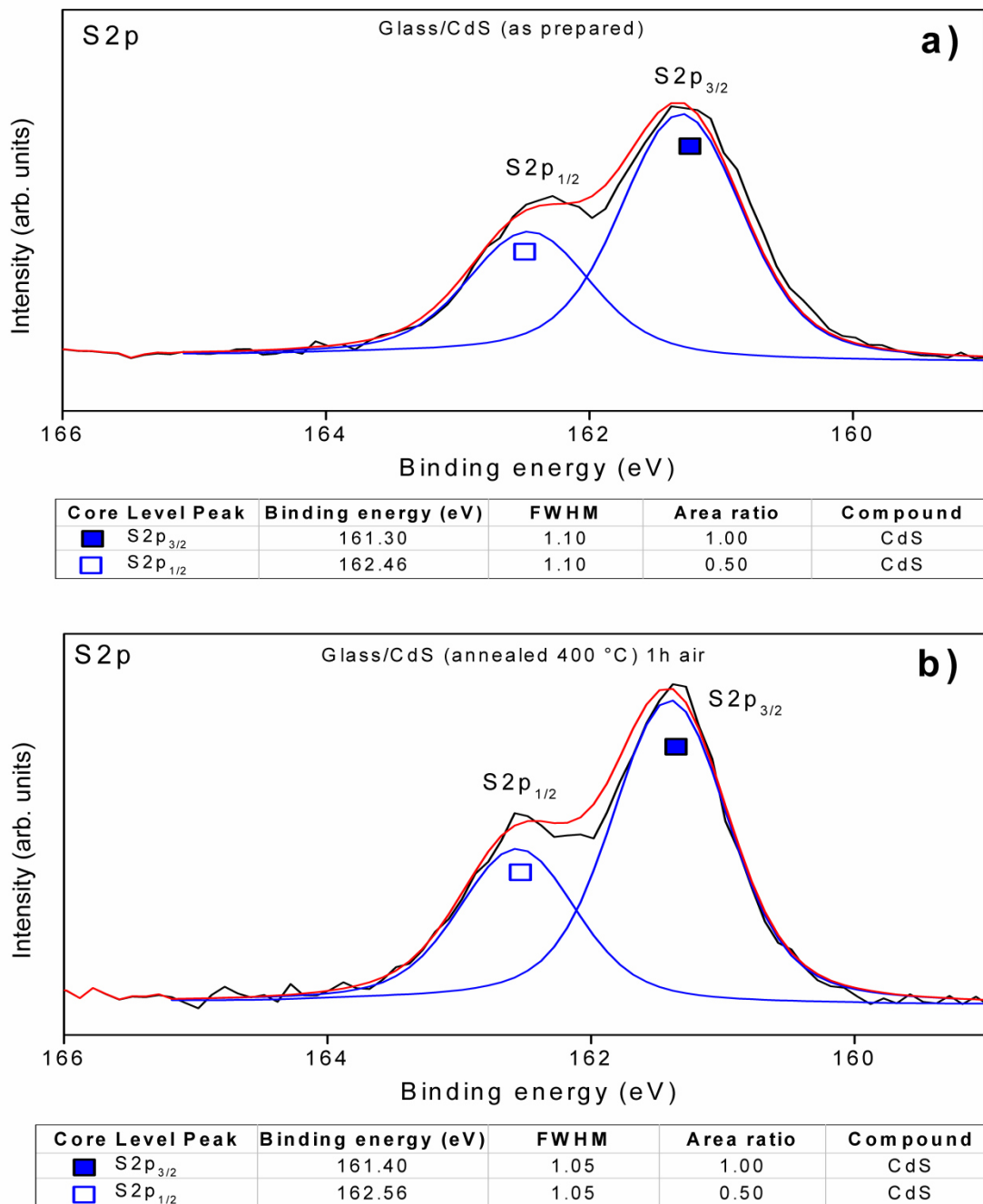
Figure 5.50 High resolution core level S2p spectra of Glass/CdS precursor thin film (a) as prepared and (b) annealed at 400 °C 1h in air

From Figure 5.50a and b, the doublet S2p$_{3/2}$ and S2p$_{1/2}$ core levels constituted one peak located at 161.3 eV and 162.46 eV for the as prepared sample and 161.4 eV and 162.56 eV for the annealed sample, corresponding to S^{2-} in CdS (Naumkin et al., 2000).

The elemental composition of CdS before and after annealing was measured by XPS, giving values of 52.58% Cd, 47.42% S and 55.87% Cd, 44.13% S, before and after annealing, respectively. It was observed that after annealing, there is a loss of sulfur in the thin film, which helps to explain the reduction in thickness measured by profilometer.

The carrier concentration, carrier mobility and conductivity of CdS thin films before and after annealing at 400 °C for 1h in air were measured by Hall Effect technique. It was observed that the carrier concentration and conductivity of the thin films decreased from 1×10^{17} cm^{-3} to 5.5×10^{14} cm^{-3} and from 5.6×10^{-2} ($\Omega \cdot$cm)$^{-1}$ to 1.5×10^{-3} ($\Omega \cdot$cm)$^{-1}$, respectively. The carrier mobility increases from 4 cm^2/Vs to 17 cm^2/Vs after annealing. The decrease in carrier concentration may be due to reduction of structural defects (Fang et al., 2013) such as sulfur vacancies which are the responsible to n-type conductivity. The reduction of sulfur vacancies can be explained by the sulfur loss due to annealing giving a decrease in carrier concentration. The increase in carrier mobility may be due to reduction of the scattering of the carriers and the elimination of defects in the films after annealing (Öztas and Bedir, 2008). The decrease in conductivity is an effect of dependence on carrier concentration and mobility.

5.3.2 PV Layer compositions (XPS depth profiling)

5.3.2.1 *Glass/SnO$_2$:F/n-CdS/p-CuSbS$_2$*

The depth profile analysis of the photovoltaic structures using a p-n junction of glass/SnO$_2$:F/n-CdS/p-CuSbS$_2$ (SC650T1) of 650 nm in thickness of absorber material and annealed at 350 °C 1his shown in the XPS profile montage given in Figure 5.51. From the figure, Cu2p, Sb3d, O1s, S2p, Cd3d and Sn3d core levels were detected throughout the depth of the structure. Sn3d and O1s levels were from the SnO$_2$:F coated glass substrate and Cd3d from window layer. Using the spectral data, corresponding depth profile of relative atomic composition for the device was evaluated, given in Figure 5.53.From Figure 5.53, the distinct layers

showing the formation of $CuSbS_2$ (top layer), CdS and SnO_2:F zones are clearly seen throughout the depth. A uniform atomic composition through absorber material is observed having constant sulfur content, then, an increase in sulfur and cadmium due to CdS window layer is reached. After that a decrease in all elements having an increase in tin is observed, indicating the SnO_2:F coated glass substrate.

5.3.2.2 Glass/SnO$_2$:F/n-CdS/i-Sb$_2$S$_3$/p-CuSbS$_2$

The depth profile analysis of the photovoltaic structures using a p-i-n junction of glass/SnO2:F/n-CdS/i-Sb2S3/p-CuSbS2 (SC1050T1-pin) of 1050 nm in thickness of absorber material and annealed at 350 °C 1h is shown in the XPS profile montage given in Figure 5.52. The Cu2p, Sb3d, O1s, S2p, Cd3d and Sn3d core levels were detected throughout the depth of the structure. Sn3d and O1s levels were from the SnO2:F coated glass substrate

The relative atomic composition for the device from the Figure 5.54 shows the distinct layers indicating the formation of p-$CuSbS_2$ (top layer), i-Sb_2S_3, n-CdS and SnO_2:F zones which are clearly seen throughout the depth.

5.3.2.3 Glass/SnO$_2$:F/n-CdS/i-Sb$_2$S$_3$/p-CuSb(Se$_x$S$_{1-x}$)$_2$

The depth profile analysis of the photovoltaic structure using a p-i-n junction of glass/SnO_2:F/n-CdS/i-Sb_2S_3/p-$CuSb(Se_xS_{1-x})_2$ (SC1350T1-pin) of 1350 nm in thickness of absorber material and annealed at 350 °C 1his shown in the XPS profile montage given in Figure 5.55. In the figure, Cu2p, Sb3d, O1s, S2p, Se3d, Cd3d and Sn3d core levels are detected throughout the depth of the structure. Sn3d and O1s levels are from the SnO_2:F coated glass substrate and Cd3d from window layer, as in the previous cases. Selenium is present only in the first cycles corresponding to a depth of 60-100 nm, implying the formation of $CuSb(Se_xS_{1-x})_2$ only at the surface of the photovoltaic device structure.
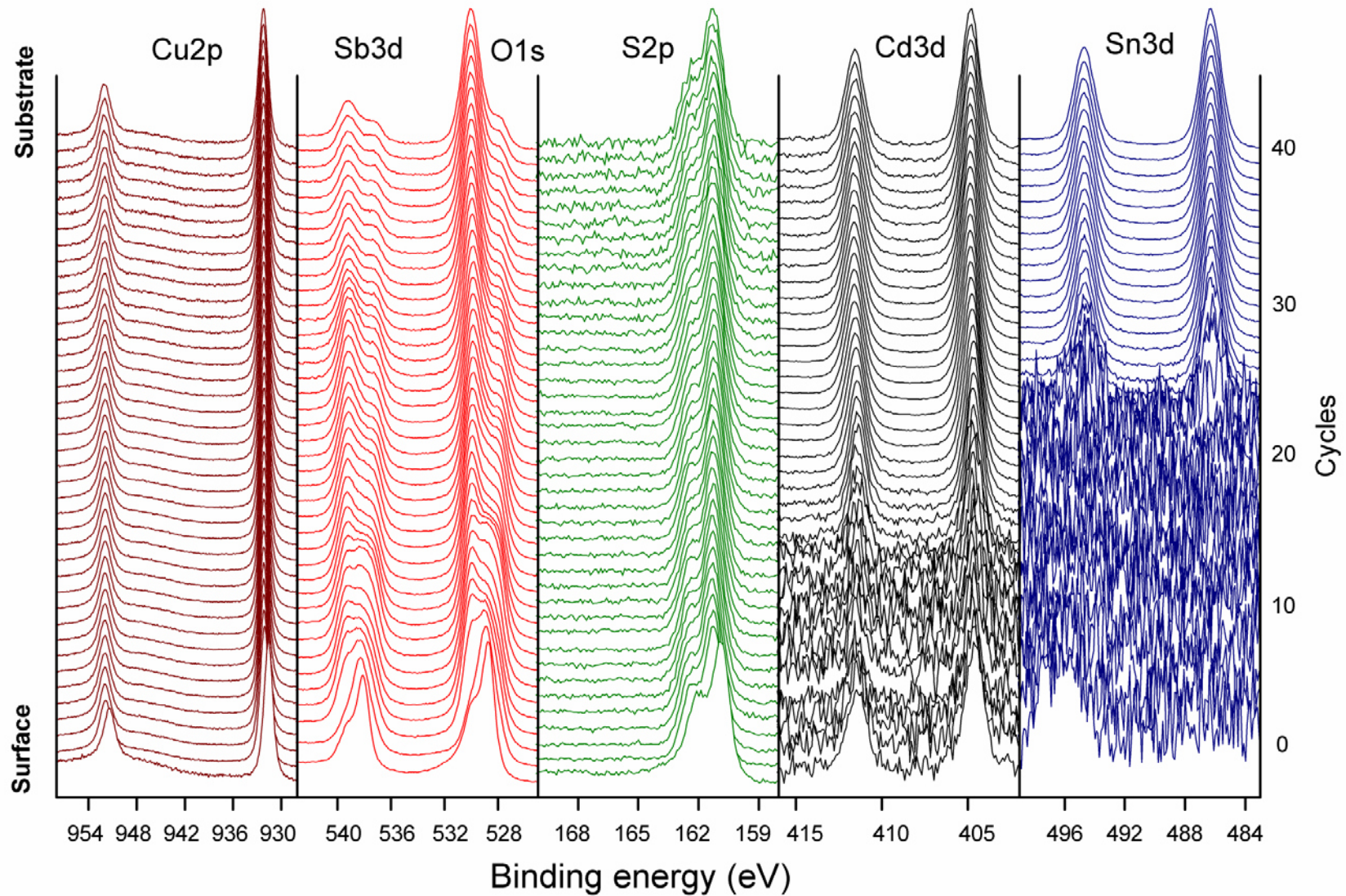
Figure 5.51 XPS profile montage of p-n junction of glass/SnO$_2$:F/n-CdS/p-CuSbS$_2$ of 650 nm in thickness of absorber material annealed at 350 °C 1h (Reproduced with kind permission from Elsevier)
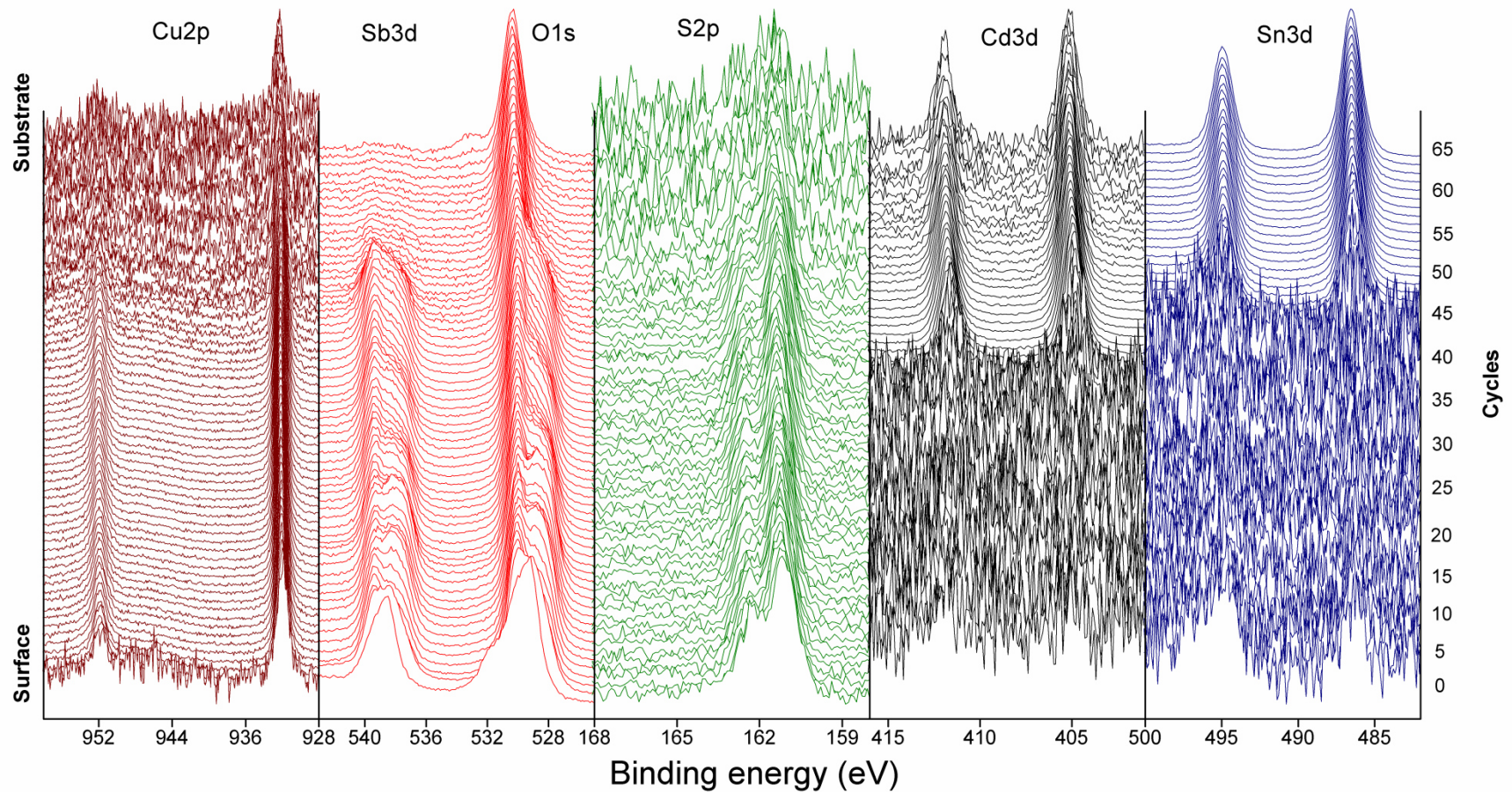
Figure 5.52 XPS profile montage of p-i-n junction of glass/SnO$_2$:F/n-CdS/i-Sb$_2$S$_3$/p-CuSbS$_2$ of 1050 nm in thickness of absorber material annealed at 350 °C 1h
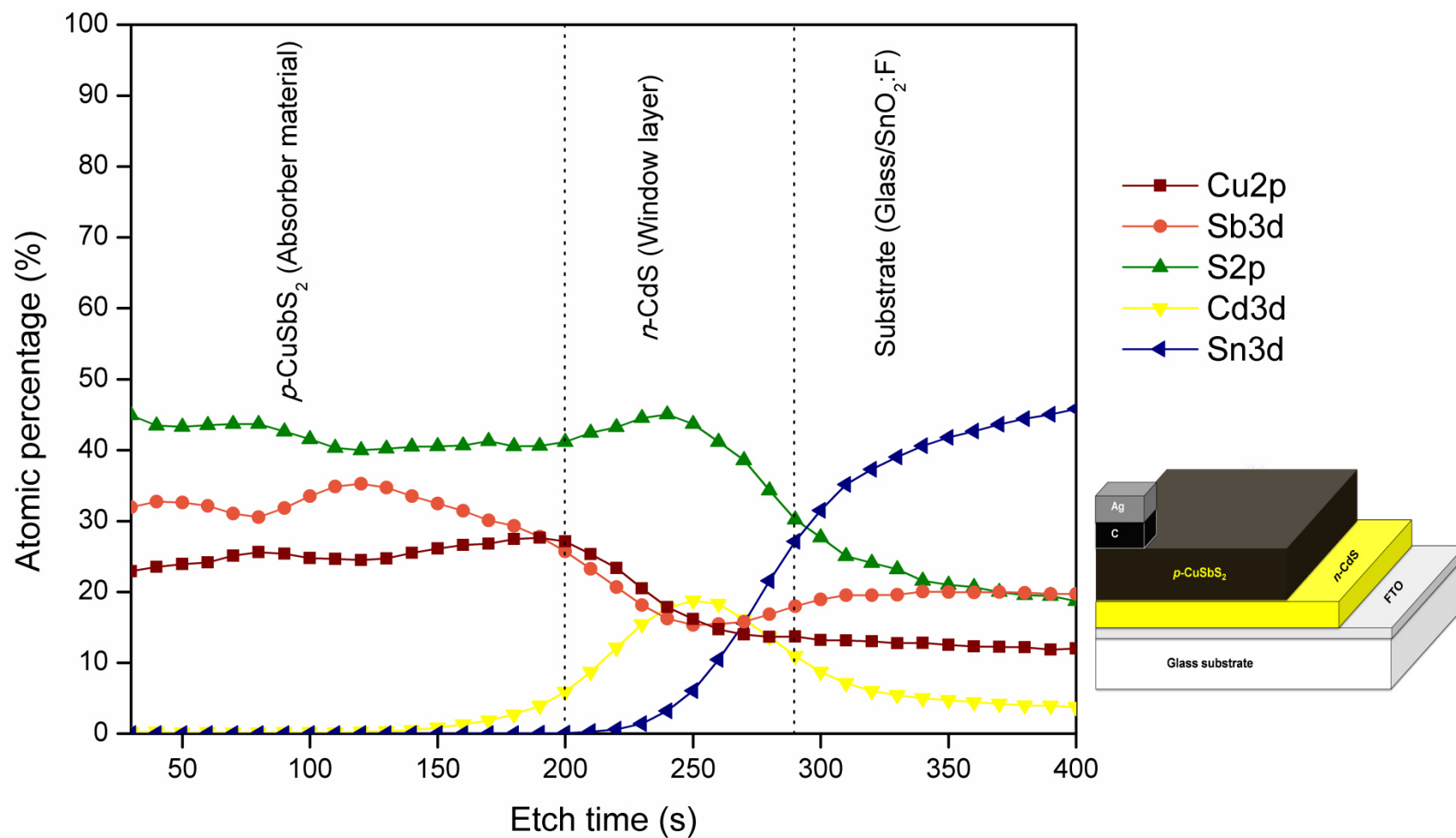
Figure 5.53 Depth profile for compositional analysis of p-n junction of glass/SnO$_2$:F/n-CdS/p-CuSbS$_2$ of 650 nm in thickness of absorber material annealed at 350 °C 1h (Reproduced with kind permission from Elsevier)
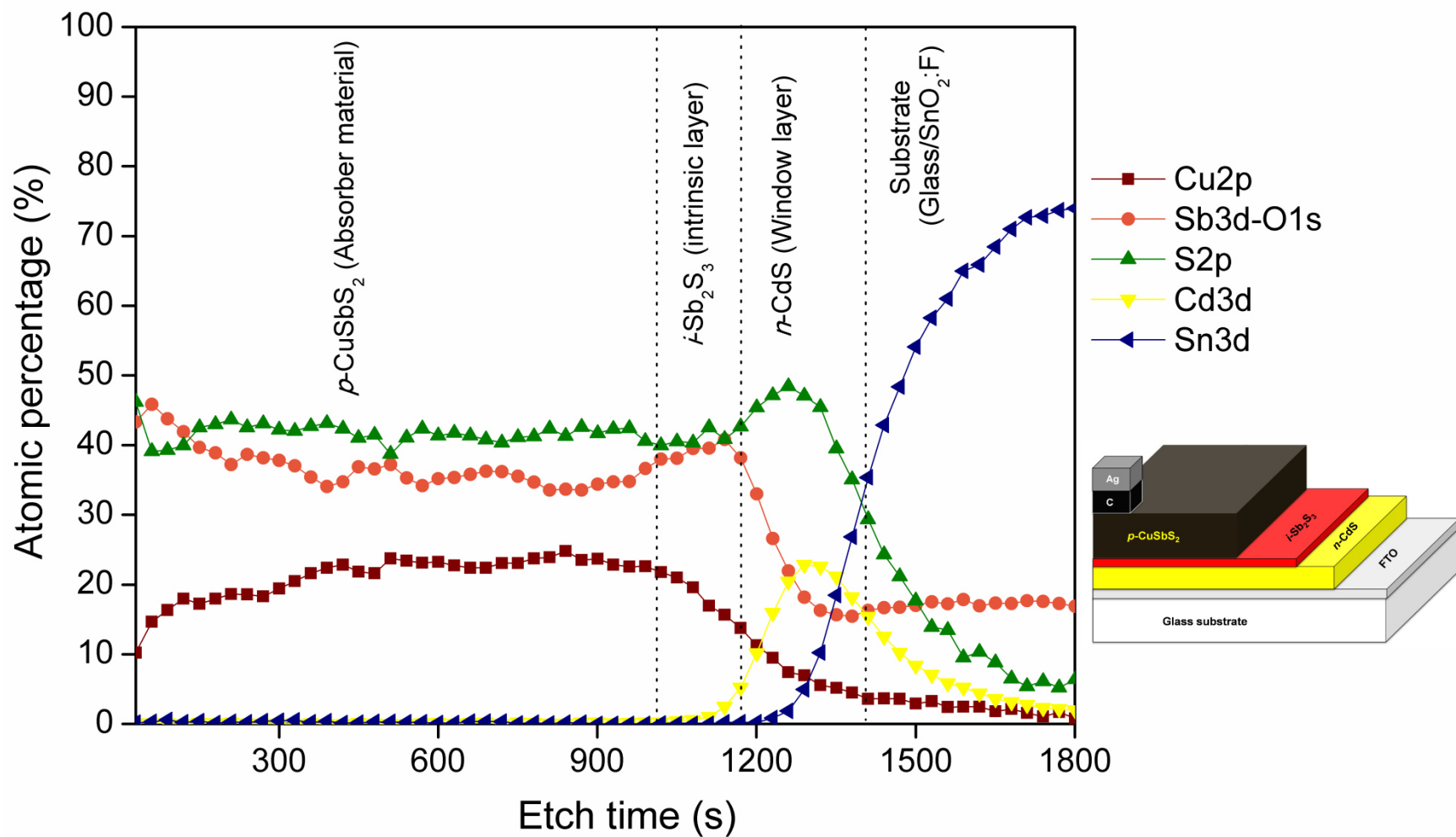
Figure 5.54 Depth profile for compositional analysis of p-i-n junction of glass/SnO$_2$:F/n-CdS/i-Sb$_2$S$_3$/p-CuSbS$_2$ of 1050 nm in thickness of absorber material annealed at 350 °C 1h

From Figure 5.56, the distinct layers showing the formation of p-CuSb(Se$_x$S$_{1-x}$)$_2$ (top layer), i-Sb2S3, n-CdS and SnO$_2$:F zones were clearly seen throughout the depth. The presence of selenium is only at the surface, a uniform atomic composition through absorber material is observed for sulfur and antimony having a copper deficiency through the absorber depth, in the intrinsic zone, a slightly increase in sulfur and antimony indicate the presence of the Sb$_2$S$_3$ as an intrinsic layer formed between absorber and window layer. An increase in sulfur and cadmium due to CdS window layer is reached. After that a decrease in all elements having an increase in tin is observed, indicating the SnO$_2$:F coated glass substrate was achieved.

From the depth profile it was observed that the diffusion of the elements from the p-type to the n-type semiconductors was not achieved due to the intrinsic layer placed between them. Comparing with other reports on p-n junction formed by CdS/CIGSSe and CdS/CdTe have been demonstrated the diffusion and intermixing of the S/Se (Weinhardt et al., 2010) and the formation of a solid solution at interface of CdS$_x$Te$_{1-x}$(Mathew et al., 2012), in which this diffusion affect the electronic properties of the junction and modify the band gap of the absorber materials. In our case, the intrinsic layer band gap may be changed due to the intermixing of elements.
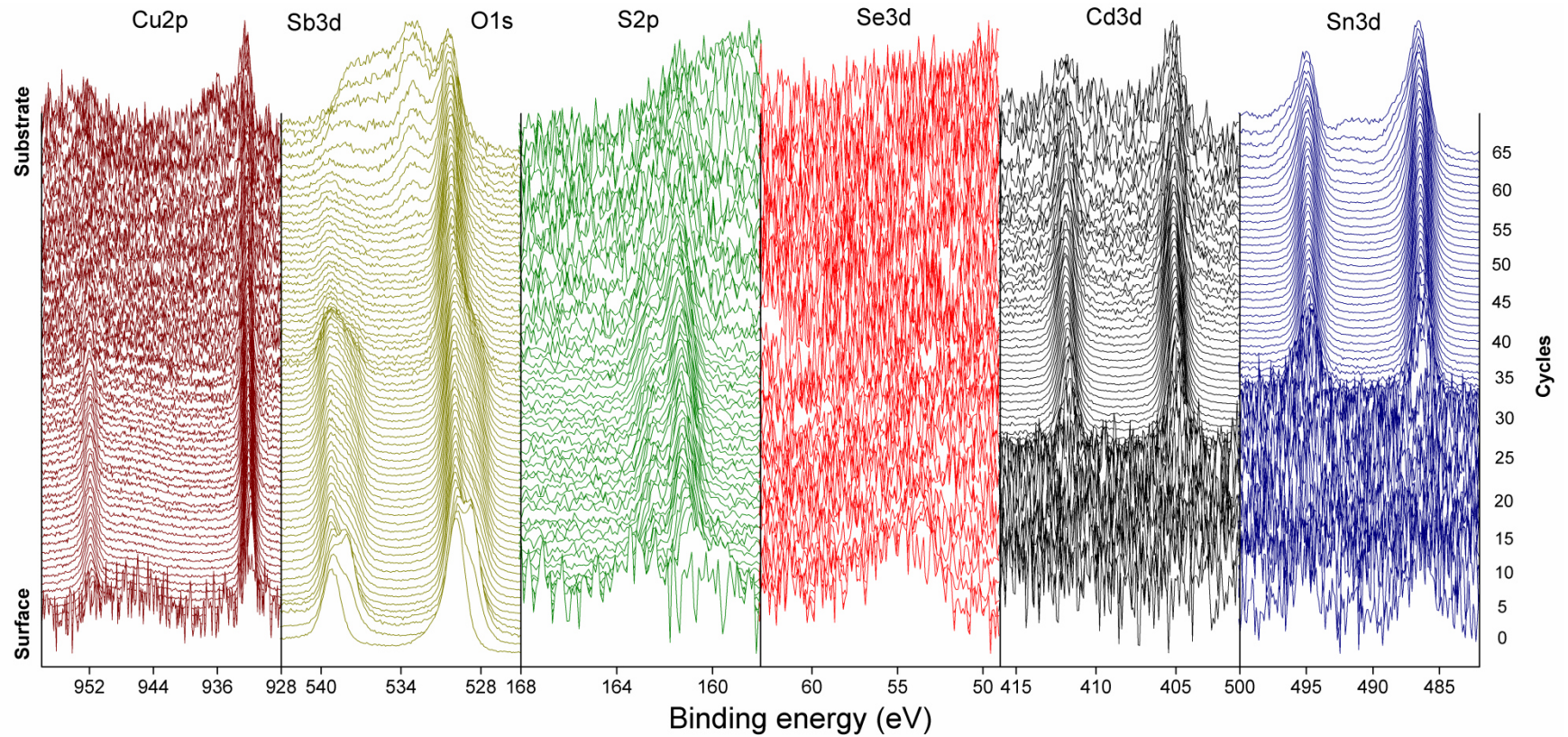
Figure 5.55 XPS profile montage of p-i-n junction of glass/SnO₂:F/*n*-CdS/*i*-Sb₂S₃/*p*-CuSb(SeₓS₁₋ₓ)₂ of 1350 nm in thickness of absorber material annealed at 350 °C 1h
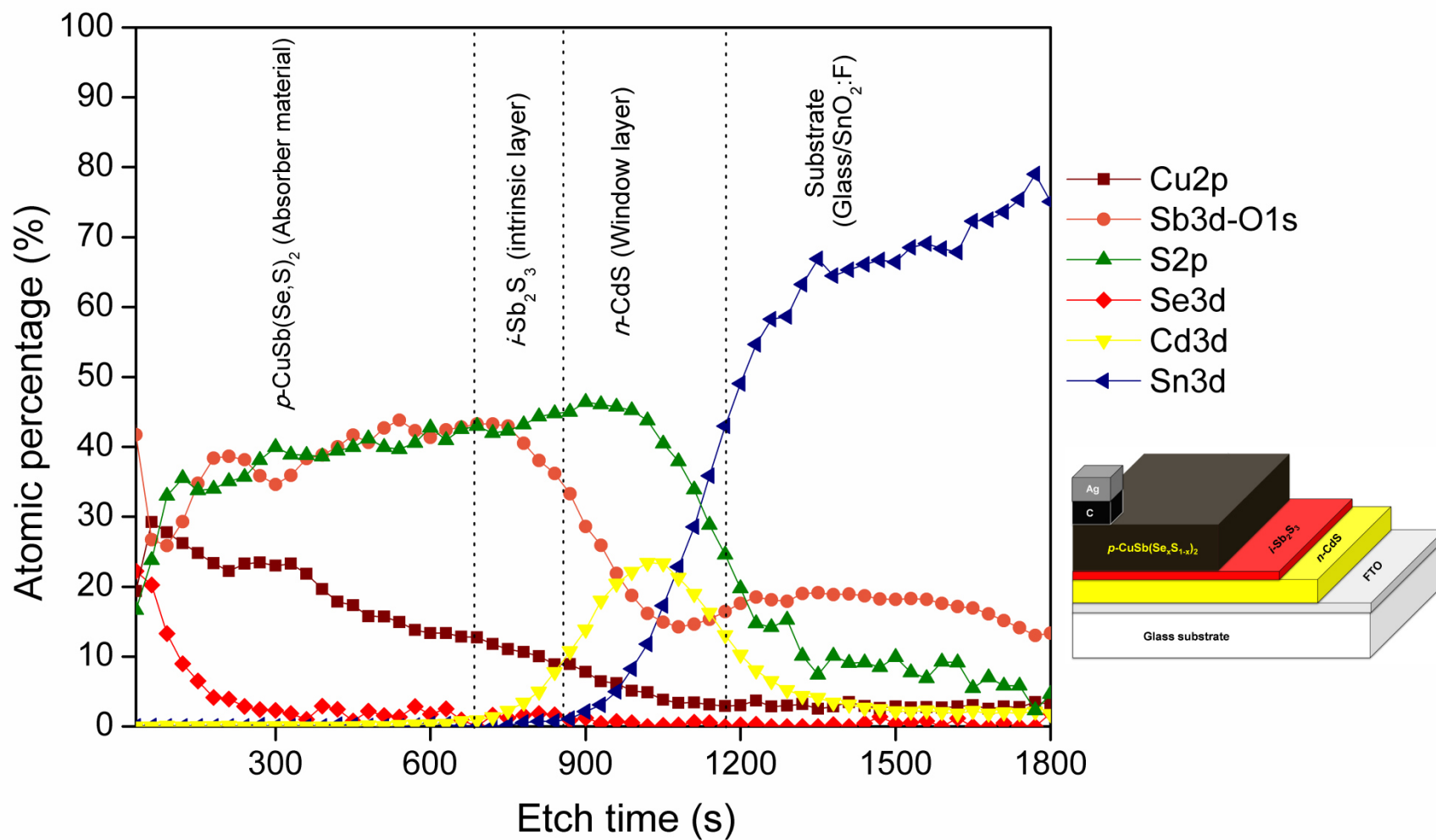
Figure 5.56 Depth profile for compositional analysis of p-i-n junction of glass/SnO₂:F/n-CdS/i-Sb₂S₃/p-CuSb(SeₓS₁₋ₓ)₂ of 1350 nm in thickness of absorber material annealed at 350 °C 1h

5.3.3 Band alignment by XPS measurements

When semiconductors of different band gaps are joined together to form a junction, there will exist discontinuities in the valence band (ΔE_V) and conduction band (ΔE_C). The investigation of these discontinuities is important for device design because these values determine the junction transport and other interface properties.
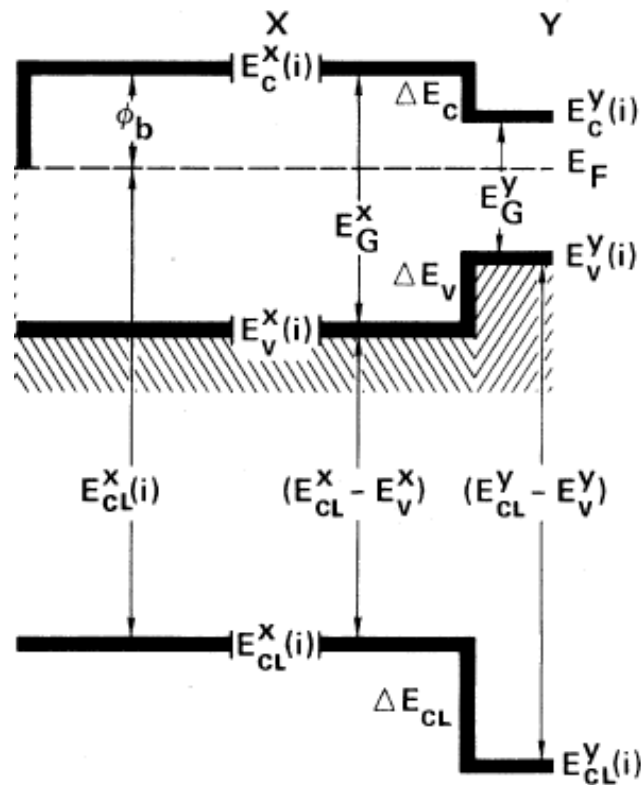
Figure 5.57 Schematic flat band diagram at heterojunction interface

The valence band discontinuity of two semiconductors X and Y as shown in Figure 5.57 can be calculated by XPS measurements using the Kraut's method (Kraut et al., 1980) as follows:

$$\Delta E_V = \left(E_{CL}^Y - E_V^Y \right) - \left(E_{CL}^X - E_V^X \right) - \Delta E_{CL} \qquad (5.4)$$

Where:

$$\Delta E_{CL} = E_{CL}^Y(i) - E_{CL}^X(i) \qquad (5.5)$$

where E_{CL}^X and E_{CL}^Y are the energy core level of the semiconductors X and Y measured from XPS data, E_V^X and E_V^Y are the valence band maximum (VBM) which is calculated by the linear extrapolation of the leading edge of the XPS valence spectra, taking in account that the binding energy value of zero indicates the position of the Fermi level, and ΔE_{CL} is the energy core level difference of the semiconductors X and Y at the interface of the junction between the two semiconductors.

An attempt was done to calculate the valence band discontinuities for the two heterojunctions formed by the p-CuSbS$_2$/i-Sb$_2$S$_3$ and i-Sb$_2$S$_3$/n-CdS on the sample of glass/SnO$_2$:F/n-CdS/i-Sb$_2$S$_3$/p-CuSbS$_2$.

For the heterojunction of p-CuSbS$_2$/i-Sb$_2$S$_3$, the valence band offset is calculated by:

$$\Delta E_{V1} = \left(E_{Sb3d}^{Sb_2S_3} - E_{VBM}^{Sb_2S_3} \right) - \left(E_{Cu2p}^{CuSbS_2} - E_{VBM}^{CuSbS_2} \right) - \Delta E_{CL1}$$

$$\Delta E_{CL1} = E_{Sb3d}^{Sb_2S_3}(i) - E_{Cu2p}^{CuSbS_2}(i)$$

For the heterojunction of i-Sb$_2$S$_3$/n-CdS, the valence band offset is calculated by:

$$\Delta E_{V2} = \left(E_{Cd3d}^{CdS} - E_{VBM}^{CdS} \right) - \left(E_{Sb3d}^{Sb_2S_3} - E_{VBM}^{Sb_2S_3} \right) - \Delta E_{CL2}$$

$$\Delta E_{CL2} = E_{Cd3d}^{CdS}(i) - E_{Sb3d}^{Sb_2S_3}(i)$$

The valence band spectra of CuSbS$_2$, Sb$_2$S$_3$ and CdS are shown in Figure 5.58 and the values of the respectively core level energies are tabulated in Table 5.3.

Table 5.3 XPS core levels energies for valence band offset

Sample	Core level	Peak (eV)	E$_g$ (eV)
CuSbS₂	$E_{Cu2p}^{CuSbS_2}$	932.18	1.55
	$E_{Cu2p}^{CuSbS_2}(i)$	932.14	

	$E_{VBM}^{CuSbS_2}$	0.7	
Sb₂S₃	$E_{Sb3d}^{Sb_2S_3}$	530.01	1.70
	$E_{Sb3d}^{Sb_2S_3}(i)$	530.03	
	$E_{VBM}^{Sb_2S_3}$	0.6	
CdS	E_{Cd3d}^{CdS}	405.00	2.40
	$E_{Cd3d}^{CdS}(i)$	405.01	
	E_{VBM}^{CdS}	1.45	
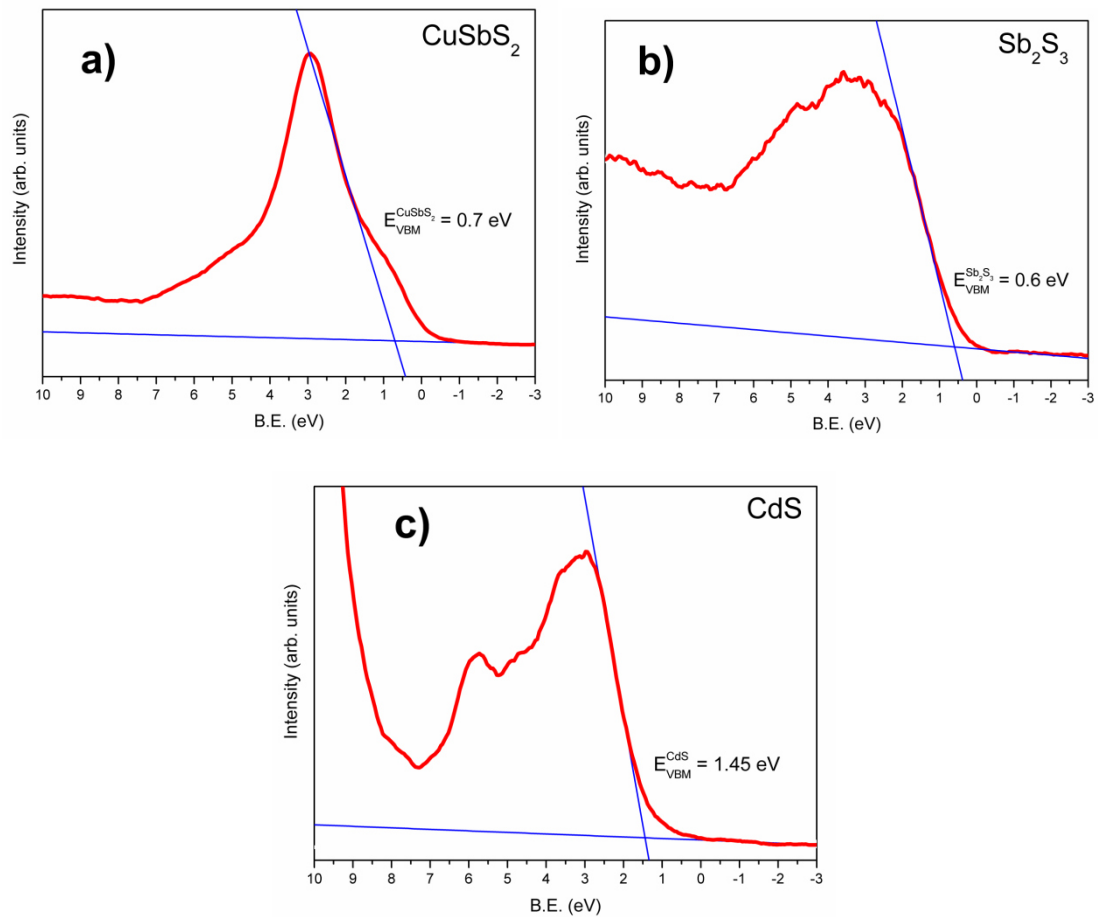
Figure 5.58 Valence band spectra for (a) CuSbS₂, (b) Sb₂S₃ and (c) CdS samples

Figure 5.59 shows the construction of the band alignment for the photovoltaic device glass/SnO_2:F/*n*-CdS/*i*-Sb_2S_3/*p*-$CuSbS_2$. The valence band discontinuities calculated for the $CuSbS_2$/Sb_2S_3 and Sb_2S_3/CdS heterojunction were 0.04 eV and 0.74 eV respectively. This model suggests the formation of a large barrier potential for the flow of electrons from $CuSbS_2$ to CdS. In this case we consider that we have an intrinsic Sb_2S_3 layer between p-type and n-type semiconductors.
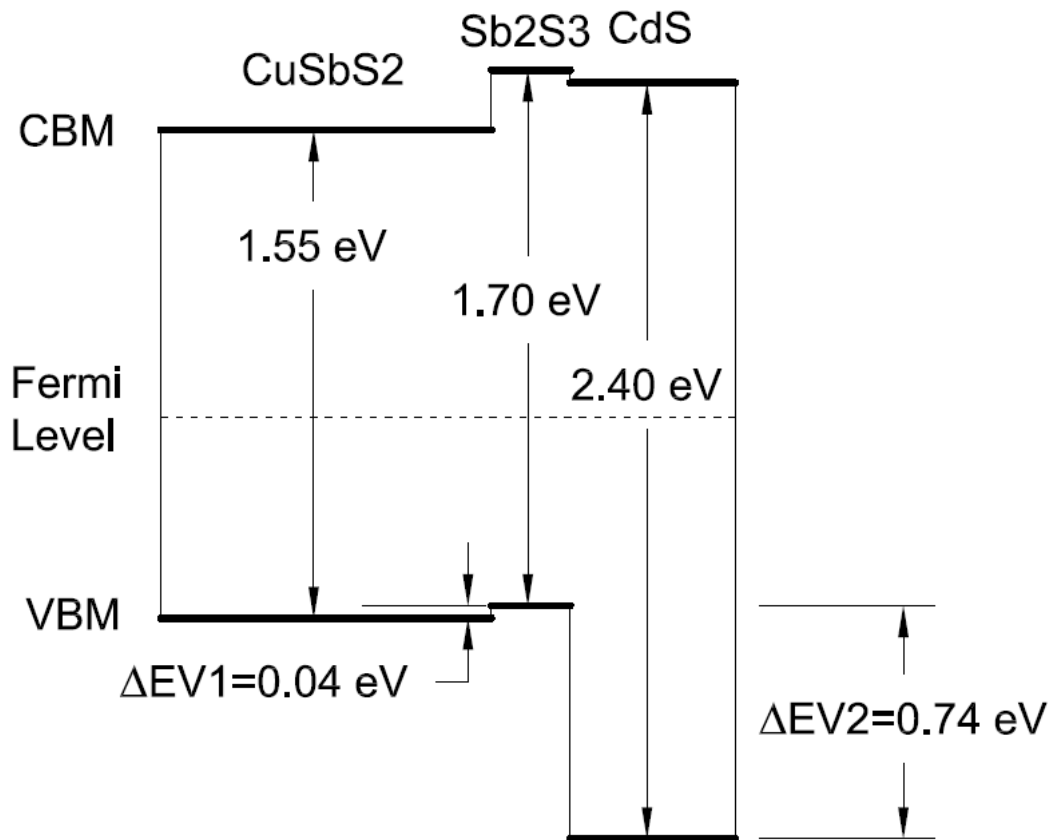
Figure 5.59 Band energy alignment of *p*-CuSbS₂/*i*-Sb₂S₃/*n*-CdS p-i-n heterojunction. Long dash line is the Fermi level (E_F)

Comparing this result with the construction of the band alignment, we propose a band alignment model in which the layer between p-$CuSbS_2$ and n-CdS is composed by a layer of $CuSbS_2$-Sb_2S_3 having a value of band gap similar to p-$CuSbS_2$ (1.55 eV), and the construction of the band alignment considering this conditions is as shown in Figure 5.60, where decrease the

barrier potential for the flow of the electrons from $CuSbS_2$ to CdS suggesting a possible large injection of carriers into electrodes and an increase of the short current density.
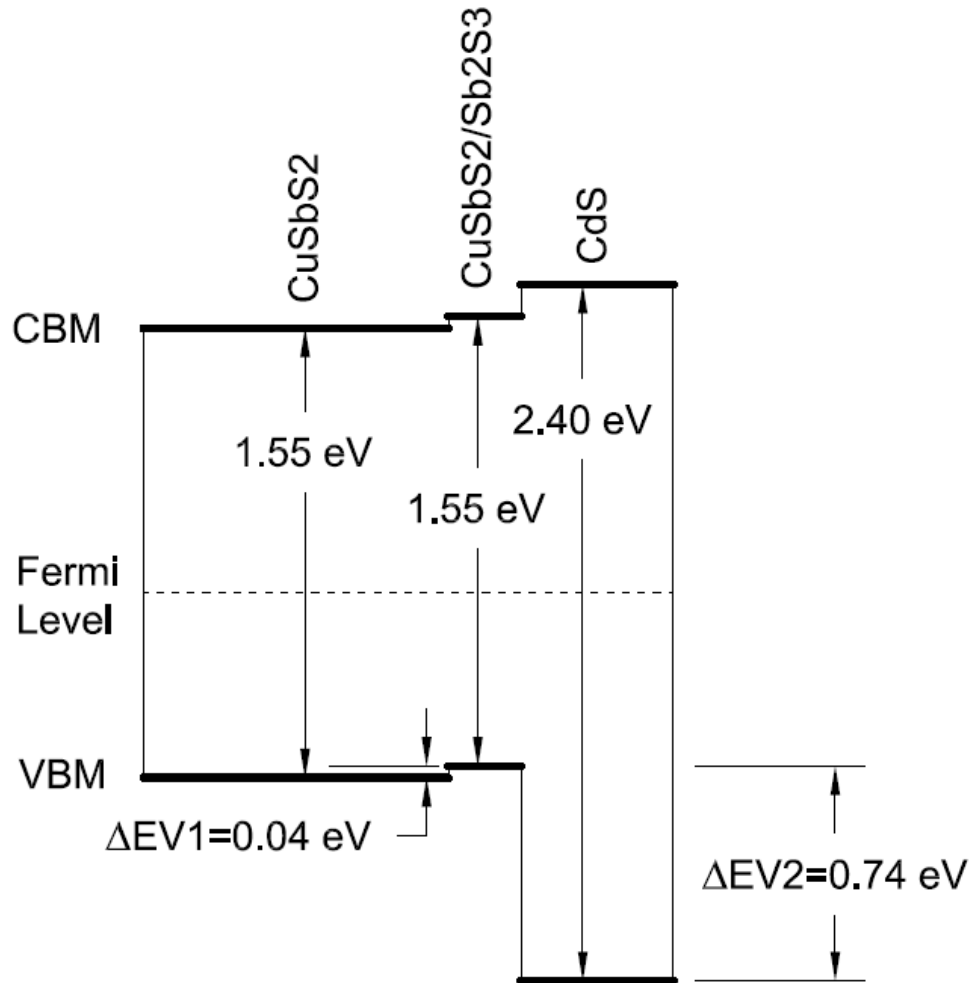
Figure 5.60 Band energy alignment of *p*-CuSbS$_2$/CuSbS$_2$-Sb$_2$S$_3$/*n*-CdS heterojunction. Long dash line is the Fermi level (E$_F$)

5.3.4 J-V Characterization

Many photovoltaic devices at different conditions varying window layer (CdS) and absorber material thickness, annealing temperature and time were fabricated (Table 5.2). The absorber material conditions selected were the glass/Sb$_2$S$_3$/Cu thin film of 650 nm annealed at 350 °C, 375 °C, 400 °C for 1 h,

thin film of 850 nm and 1050 nm annealed at 350 °C for 1 h and thin film of 1050 nm annealed at 350 °C for 2, 3 and 4 h.

The current density-voltage (J-V) curves under dark and illumination(Oriel solar simulator, 100mW/cm^2, AM1.5)measured for p-n junction glass/SnO$_2$:F/n-CdS/p-CuSbS$_2$/C/Ag formed at 350 °C (SC650T1), 375 °C (SC650T2), 400 °C (SC650T3) having CdS layer as prepared, are shown in Figure 5.61.The curve under dark condition presents a diode like behavior. From the curves under illumination, their respective photovoltaic parameters were evaluated as listed in Table 5.4. The values were J$_{sc}$= 1.67-3.21 mA/cm^2, V$_{oc}$ =187-268 mV and FF=0.27-0.39 respectively.
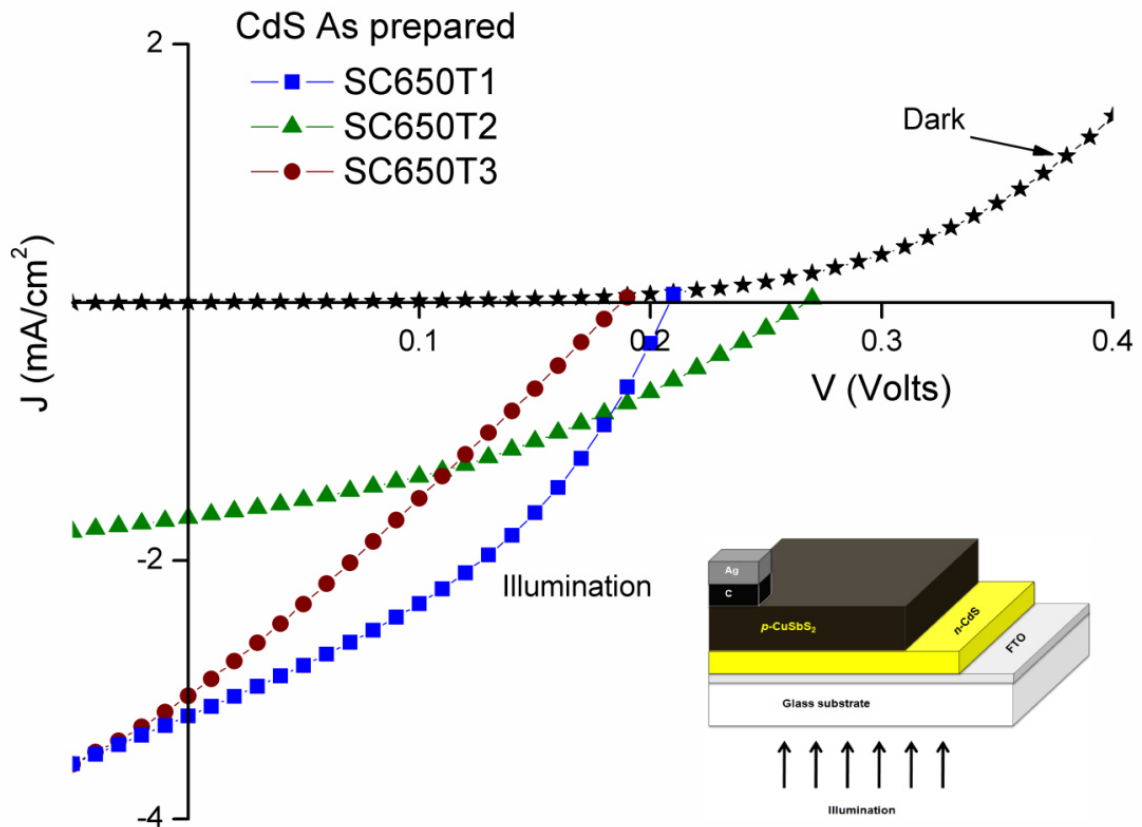
Figure 5.61 Current density (J)-voltage (V) characteristics using as prepared CdS of glass/SnO$_2$:F/n-CdS/p-CuSbS$_2$/C/Ag solar cells formed at 350 °C (SC650T1), 375 °C (SC650T2) and 400 °C (SC650T3)

Table 5.4 Photovoltaic parameters of glass/SnO$_2$:F/n-CdS/p-CuSbS$_2$/C/Ag solar cells using as prepared CdS

Sample	V$_{oc}$ (mV)	J$_{sc}$ (mA/cm^2)	FF (%)	Area (cm^2)	η (%)
SC650T1	214	3.21	39%	0.036	0.27%
SC650T2	268	1.67	36%	0.039	0.16%
SC650T3	187	3.06	27%	0.03	0.15%

The current density-voltage (J-V) curves under dark and illumination using the p-n junction configuration of glass/SnO$_2$:F/n-CdS/p-CuSbS$_2$/C/Ag formed at 350 °C (SC650T1), 375 °C (SC650T2), 400 °C (SC650T3) annealing the CdS layer prior to the deposition of precursor layers of Sb$_2$S$_3$ and Cu, are shown in Figure 5.62.
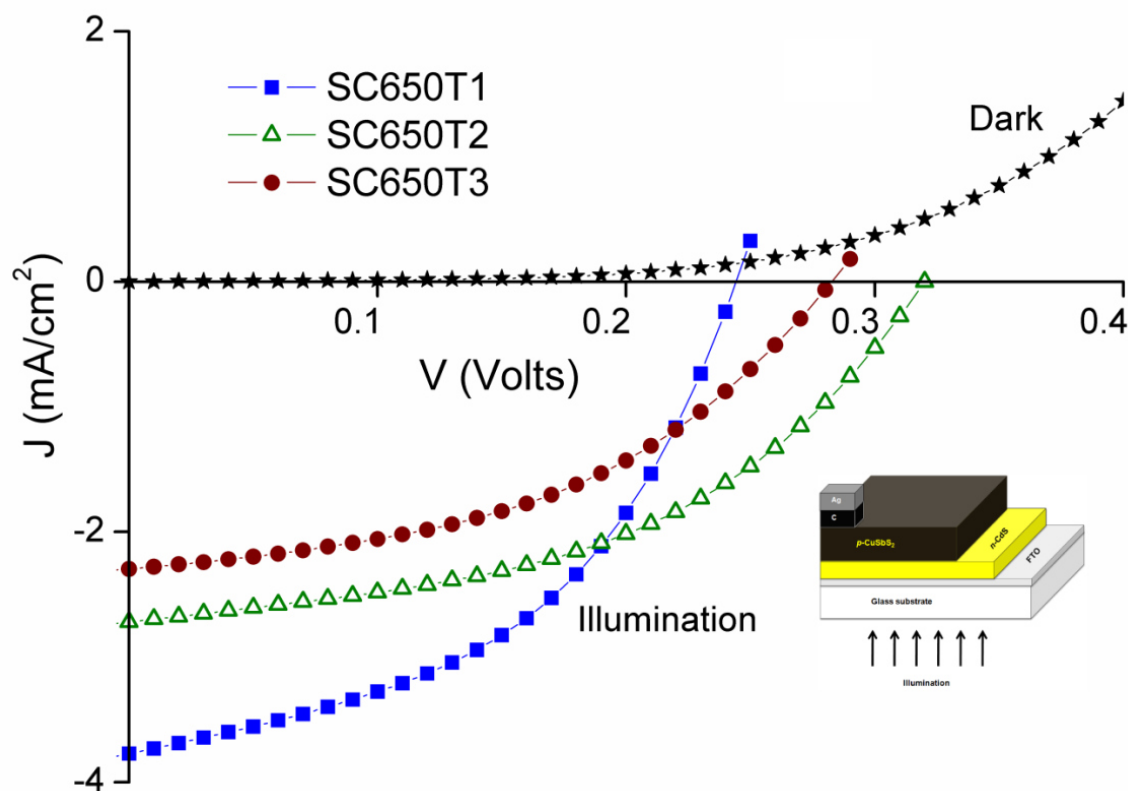
Figure 5.62 Current density (J)-voltage (V) characteristics using CdS pre-annealed at 400 °C 1h in air of glass/SnO$_2$:F/n-CdS/p-CuSbS$_2$/C/Ag solar cells formed at 350 °C (SC650T1), 375 °C (SC650T2) and 400 °C (SC650T3) (Reproduced with kind permission from Springer)

An improvement in the photovoltaic parameters is observed, especially in V_{oc} and fill factor, and thus increasing the efficiency, as shown in Table 5.5, having J_{sc}, V_{oc} and FF values around 2.28-3.77 mA/cm^2, 249-323 mV and 0.46-0.48, respectively. The annealing in air atmosphere of CdS is beneficial for enhancing the device efficiency. Oxygen in CdS plays an important role on its electrical properties and hardening against diffusion. The prominent effect is to make it resistant to in-diffusion of elements from absorber material and out-diffusion of S (Mathew et al., 2012). From XPS analysis we found an increase of oxygen in the surface for the sample annealed in air atmosphere. The photovoltaic parameters were improved using annealed CdS in air enhancing the efficiency of the solar cells.

According to these results, it was selected the condition of CdS pre-annealed at 400 °C 1h in air, prior deposit absorber material for further photovoltaic devices.

Table 5.5 Photovoltaic parameters of glass/SnO$_2$:F/n-CdS/p-CuSbS$_2$/C/Ag solar cells using CdS pre-annnealed at 400 °C 1h in air

Sample	V_{oc} (mV)	J_{sc} (mA/cm^2)	FF (%)	Area (cm^2)	η (%)
SC650T1	249	3.77	47%	0.03	0.45%
SC650T2	323	2.72	48%	0.0273	0.42%
SC650T3	285	2.28	46%	0.039	0.30%

The current density-voltage (J-V) curves under dark and illumination using thep-n junction configuration of glass/SnO$_2$:F/n-CdS/p-CuSbS$_2$/C/Ag of 650 nm, 850 nm and 1050 nm in thickness of CuSbS$_2$annealed at 350 °C for 1 h in low vacuum are shown in Figure 5.63. Under illumination, the devices of 650 nm and 1050 nm shown a J_{sc} and V_{oc} around 3.7 mA/cm^2 and 249-259 mV respectively, having SC1050T1 a fill factor lower than SC650T1 due to SC1050T1 have more multi-layers than SC650T1, increasing series resistance having a decrease in fill factor, also a decrease in efficiency is noted due to reduction of fill factor (Table 5.6). Sample of 850 nm present low photovoltaic performance with J_{sc} and V_{oc} of 1.3 mA/cm^2 and 250 mV respectively.
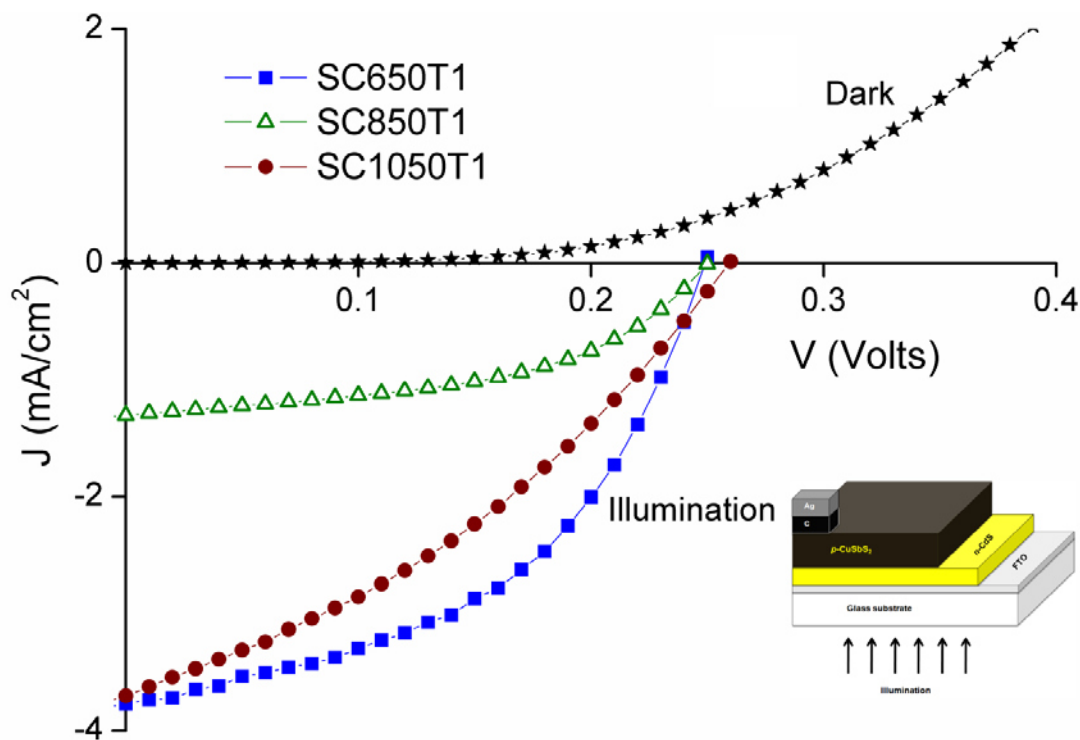
Figure 5.63 Current density (J)-voltage (V) characteristics using CdS pre-annealed at 400 °C 1h in air of glass/SnO$_2$:F/n-CdS/p-CuSbS$_2$/C/Ag solar cells for CuSbS$_2$ of 650 nm (SC650T1), 850 nm (SC850T1) and 1050 nm (SC1050T1) in thickness annealed at 350 °C 1h

The low current density of the sample SC850T1 may be is due to the lower photosensitivity (0.1), low conductivity (4.5x10^{-3} (Ω·cm)$^{-1}$) and low mobility (1.3cm^2/Vs) of the carriers for CuSbS$_2$ of 850 nm, which generate less electron-hole pairs under illumination. The increase in J$_{sc}$ for SC650T1 can be due to its high conductivity of the absorber and in SC1050T1 is due that the high n-doping (10^{14} cm^{-3}) of the CdS compared with the p-doping (10^{13} cm^{-3}) of CuSbS$_2$ of 1050 nm, the depletion width in CuSbS$_2$ layer increasing the photoelectron collection.

Table 5.6 Photovoltaic parameters of glass/SnO$_2$:F/n-CdS/p-CuSbS$_2$/C/Ag solar cells using different thickness of absorber material annealed at 350 °C 1h

Sample	V$_{oc}$ (mV)	J$_{sc}$ (mA/cm^2)	FF (%)	Area (cm^2)	η (%)
SC650T1	249	3.77	47%	0.03	0.45%
SC850T1	250	1.3	49%	0.03	0.16%
SC1050T1	259	3.7	35%	0.032	0.33%

Until now in the present study, photovoltaic devices using p-n configuration have shown relatively low short circuit current density and open circuit voltage, reaching efficiency up to 0.45 %. To maximize these photovoltaic parameters, it was implemented the use of a very thin intrinsic layer of Sb_2S_3 between n-type CdS and p-type $CuSbS_2$. The main reason is that the presence of intrinsic layer essentially stretches out the electrostatic field region and hence allows more photogenerated carriers to be brought to the collection region (Böer, 1992). In a p-i-n junction, holes from the p-type and electron from the n-type materials diffuse leaving behind negatively charged acceptors and positively charged donors, respectively, creating a space charge region near the intrinsic layer when the concentration of the free charge carriers is equilibrated, creating an internal electric field of the size of the built in voltage create at the junction of each materials and the intrinsic layer thickness (Figure 5.64). The use of intrinsic layer is preferable in materials with short minority carrier diffusion lengths because the drift field enhances minority carrier collection, improving J_{sc} and thus the efficiency.
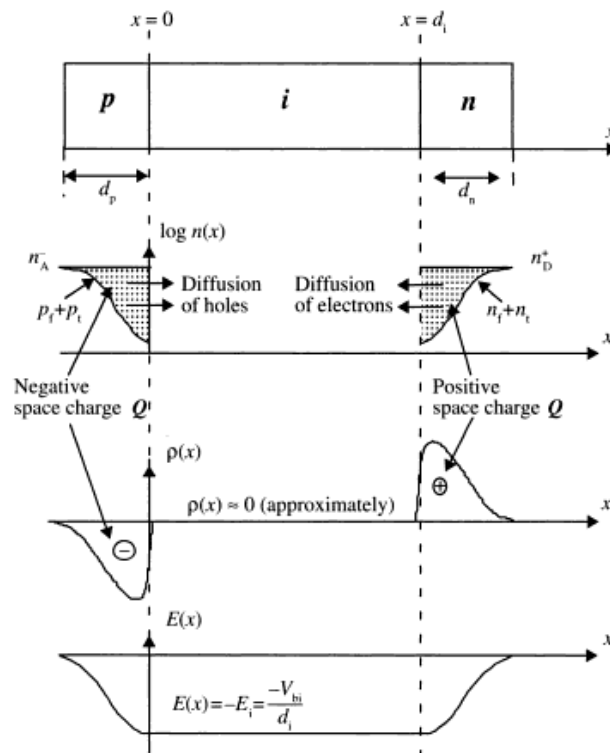
Figure 5.64 Space charge region and internal electric field within a p-i-n type solar cell

For this purpose, the sample SC1050T1 annealed at 350 °C during 1h (SC1050T1-1h), 2h (SC1050T1-2h), 3h (SC1050T1-3h) and 4h (SC1050T1-4h) were selected. The intrinsic layer was formed by annealing 100 nm Sb_2S_3 at 300 °C for 20 min. The window layer CdS was prior deposited to intrinsic layer during 45 min annealing at 400 °C 1 h. The absorber layer was formed after deposited the intrinsic layer by annealing multilayered structure of Sb_2S_3 (1000 nm)/Cu (50 nm) at 350 °C. The current density-voltage (J-V) curves under dark and illumination using the p-i-n junction configuration of glass/SnO_2:F/n-CdS/i-Sb_2S_3/p-$CuSbS_2$/C/Ag annealed at 350 °C during different annealing times are shown in Figure 5.65.
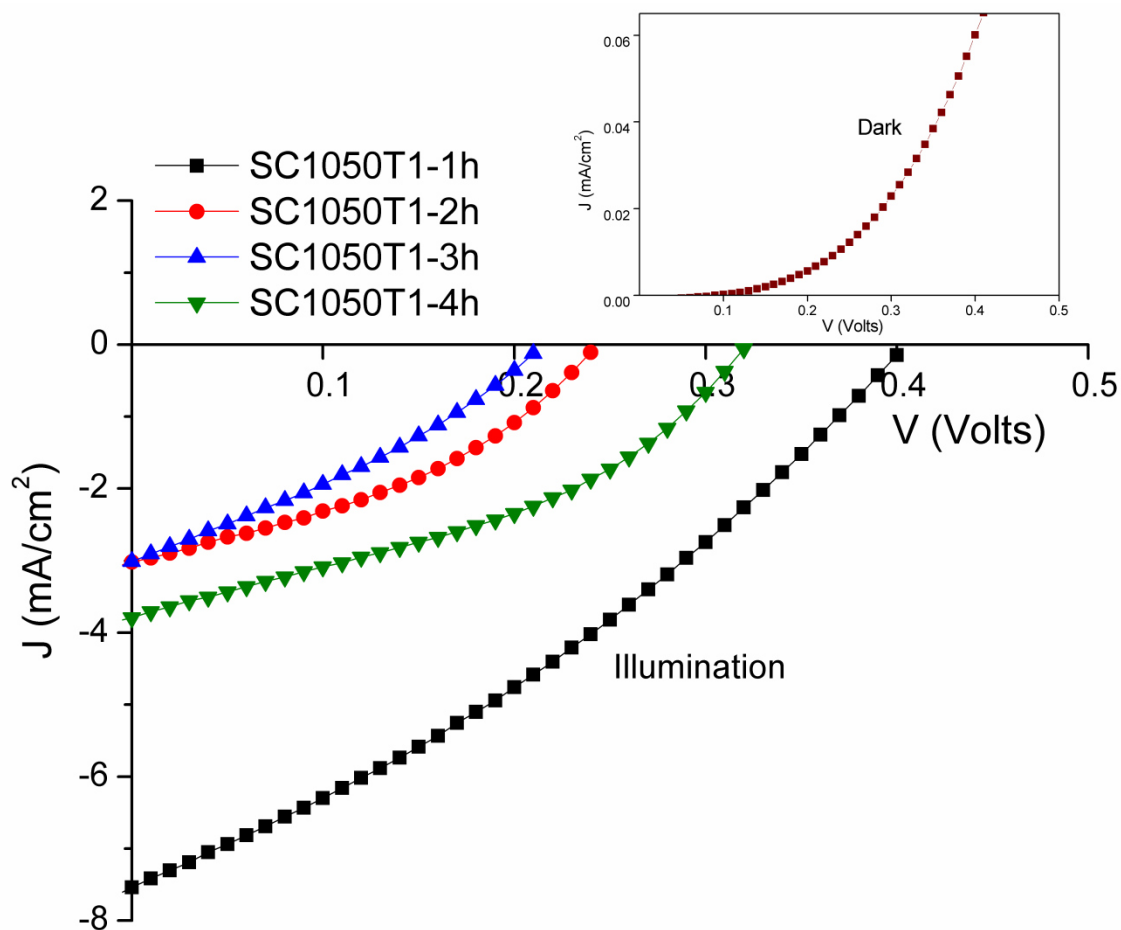
Figure 5.65 Current density (J)-voltage (V) characteristics using p-i-n configuration of glass/SnO_2:F/n-CdS/i-Sb_2S_3/p-$CuSbS_2$/C/Ag solar cells for $CuSbS_2$ of 1050 nm annealed at 350 °C during 1h (SC1050T1-1h), 2h (SC1050T1-2h), 3h (SC1050T1-3h) and 4h (SC1050T1-4h)

Under illumination, the devices annealed at large times (2-4 h) shown a J_{sc} and V_{oc} around 3.01-3.8 mA/cm^2 and 215-322 mV respectively, maintaining a relatively high fill factor around 38-39%. The device annealed for 1 h shows the best performance having photovoltaic parameters of J_{sc}, V_{oc}, FF and efficiency of 7.54 mA/cm^2, 405 mV, 32% and 1.0% respectively (Table 5.7). The increase in J_{sc} and efficiency is attributed to the use of an intrinsic layer in the device, whereas the reduction in fill factor can be due to the high series resistance attributed to the all stacked multilayers, necessary to form the complete device.

Table 5.7 Photovoltaic parameters of glass/SnO$_2$:F/n-CdS/i-Sb$_2$S$_3$/p-CuSbS$_2$/C/Ag solar cells using different annealing times

Sample	V_{oc} (mV)	J_{sc} (mA/cm^2)	FF (%)	Area (cm^2)	η (%)
SC1050T1-1h	**405**	**7.54**	**32%**	**0.028**	**1.00%**
SC1050T1-2h	244	3.02	38%	0.023	0.28%
SC1050T1-3h	215	3.01	31%	0.023	0.20%
SC1050T1-4h	322	3.8	39%	0.023	0.47%

Figure 5.66 shows the comparison for both, p-n and p-i-n configurations of devices for the condition of CuSbS$_2$ of 1050 nm in thickness annealed at 350 °C for 1 h. The remarkable improvement in photovoltaic performance and the parameters J_{sc}, V_{oc} and efficiency, is clearly shown in the Table 5.7.

Figure 5.67 shows the current density-voltage (J-V) curves under illumination using the p-i-n junction configuration of glass/SnO$_2$:F/n-CdS/i-Sb$_2$S$_3$/p-CuSbS$_2$/C/Ag for CuSbS$_2$ of 1050 nm (SC1050T1) and glass/SnO$_2$:F/n-CdS/i-Sb$_2$S$_3$/p-CuSb(Se$_x$S$_{1-x}$)$_2$/C/Ag for CuSb(Se$_x$S$_{1-x}$)$_2$ of 1350 nm (SC1350T1) annealed at 350 °C during 1h. The device with selenium shows good J_{sc} and V_{oc} values of 5.58 mA/cm^2 and 410 mV respectively, having poor fill factor of 28% and efficiency of 0.64 %.
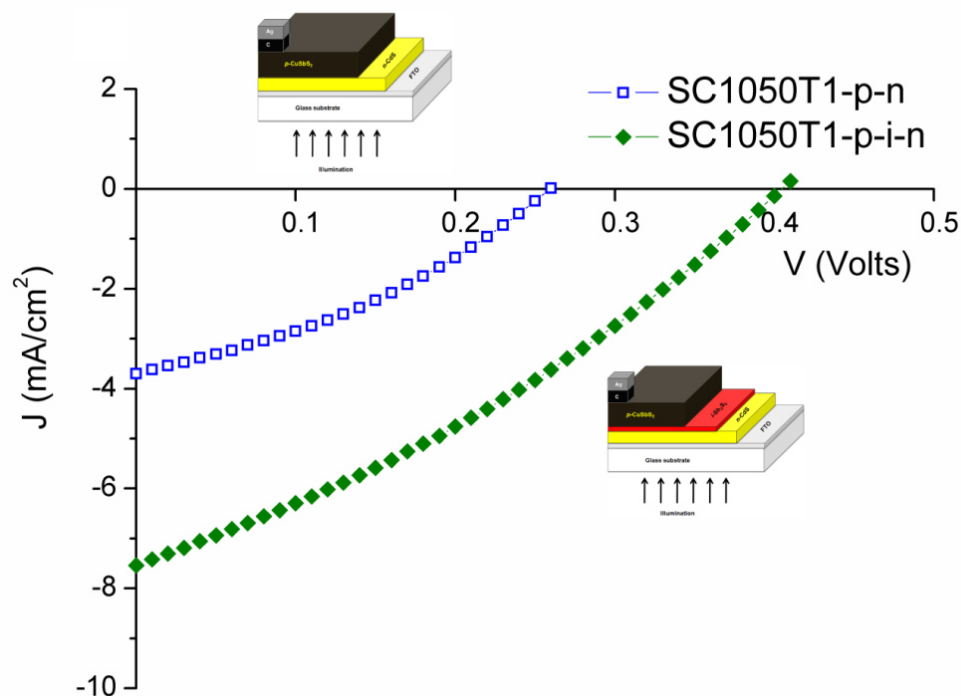
Figure 5.66 Comparison of the current density (J)-voltage (V) curves of p-n and p-i-n configurations of solar cells for CuSbS$_2$ of 1050 nm annealed at 350 °C during 1h (Reproduced with kind permission from Springer)
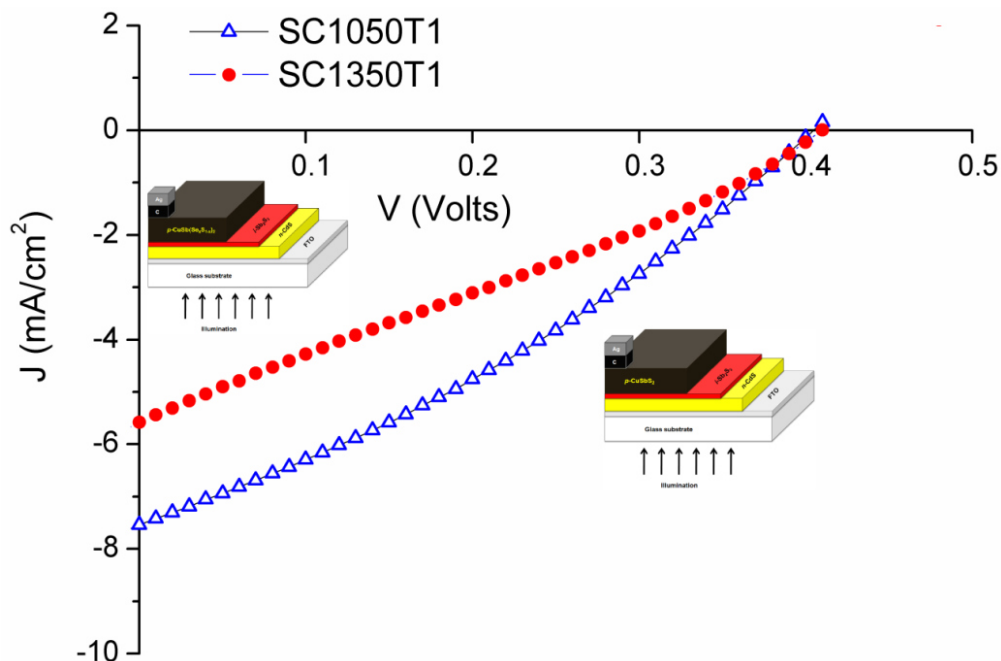
Figure 5.67 Current density (J)-voltage (V) characteristics using p-i-n configuration of glass/SnO$_2$:F/n-CdS/i-Sb$_2$S$_3$/p-CuSbS$_2$/C/Ag solar cell for CuSbS$_2$ of 1050 nm and glass/SnO$_2$:F/n-CdS/i-Sb$_2$S$_3$/p-CuSb(Se$_x$S$_{1-x}$)$_2$/C/Ag solar cell for CuSb(Se$_x$S$_{1-x}$)$_2$ of 1350 nm annealed at 350 °C during 1h

5.3.5 Fabrication of a PV module

To prove that our fabrication process is scalable, we fabricated a first prototype of small area module interconnecting cells of 0.03 cm^2 each in series (7 lines) and parallel (2 rows). The configuration of the module was a p-i-n junction of glass/SnO$_2$:F/n-CdS/i-Sb$_2$S$_3$/p-CuSbS$_2$/C/Ag, of CdS deposited by CBD during 45 min annealed at 400 °C 1 h in air, Sb$_2$S$_3$ deposited by CBD during 30 min annealed at 300 °C for 20 min in air and the precursor of Sb$_2$S$_3$ (1000 nm) and Cu (50 nm) to form CuSbS$_2$ after annealed the entire configuration at 350 °C for 1 h in low vacuum. After annealing, carbon and silver electrodes were painted and the individual cells were isolated as shown in Figure 5.68. The mini-module was measured using a solar simulator obtaining for each cell the photovoltaic parameters of J_{sc} = 2.06 mA/cm2, V_{oc} = 0.44 V and FF = 31%. For the entire mini-module, the parameters were I_{sc} = 0.125 mA, V_{oc} = 2.93 V and FF = 30% (Figure 5.69).
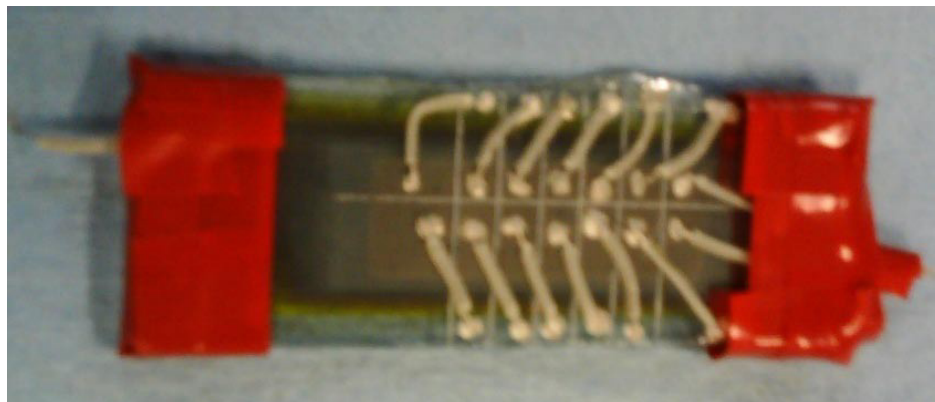
Figure 5.68Small area module of glass/SnO$_2$:F/n-CdS/i-Sb$_2$S$_3$/p-CuSbS$_2$/C/Ag

A second prototype was development with a large area module of 60 cm^2, interconnecting small cells (6.6 mm x 30 mm) in series and parallel to increase the short current density and open circuit voltage. The configuration of the module was a p-i-n junction of glass/SnO$_2$:F/n-CdS/i-Sb$_2$S$_3$/p-CuSbS$_2$/C/Ag, of CdS deposited by CBD during 45 min annealed at 400 °C 1 h in air,

Sb_2S_3deposited by CBD during 30 min annealed at 300 °C for 20 min in air and the precursor of Sb_2S_3 (1000 nm) and Cu (50 nm) to form $CuSbS_2$ after annealed the entire configuration at 350 °C for 1 h in low vacuum. After annealing, carbon and silver electrodes were painted and the individual cells were isolated in two rows of 15 cells. The cells in raw were interconnected in series and the two rows were connected in parallel as shown in Figure 5.70.
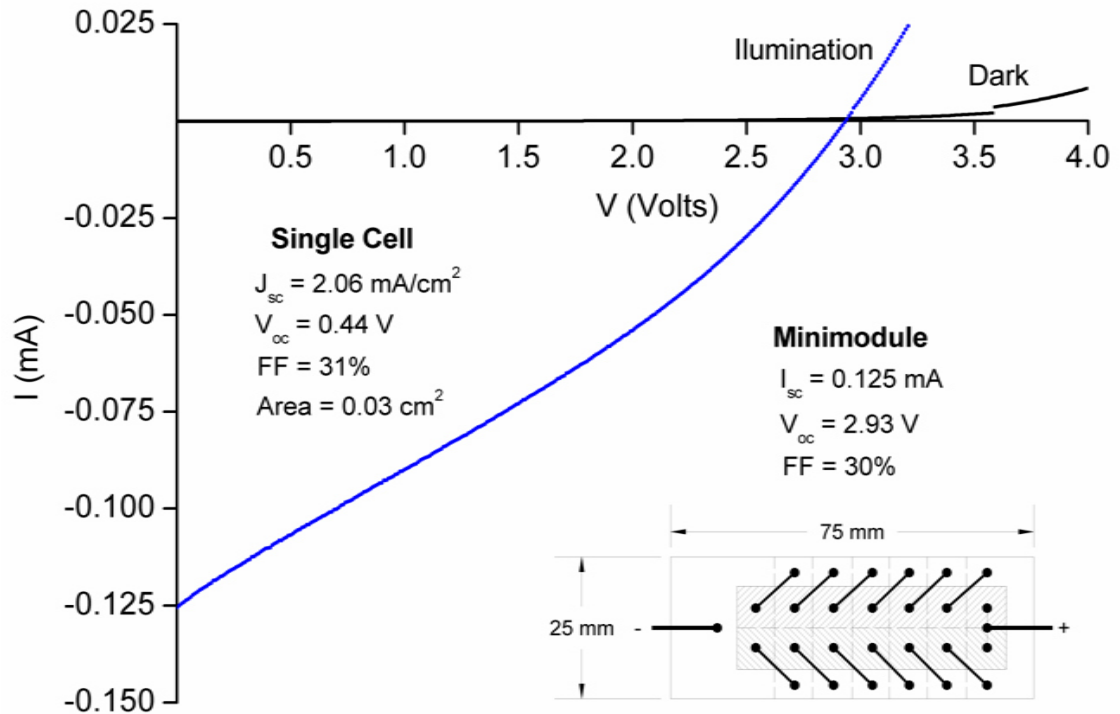
Figure 5.69 I-V curve of the first mini-module prototype

The module was measured using a multimeter under sun illumination on a sunny day around 13:00 pm, time at which the solar height reach its maximum and we have the maximum solar irradiation of the day (close to 1000 W/m^2).

The values obtained in the measurements were a maximum current of 2 mA and a maximum voltage of 2.2 V. We expect more voltage, but the large area contacts painted induced a high series resistance due to the non-uniform carbon/silver paint, reducing the voltage.

Figure 5.70 Large area module of glass/SnO$_2$:F/n-CdS/i-Sb$_2$S$_3$/p-CuSbS$_2$/C/Ag
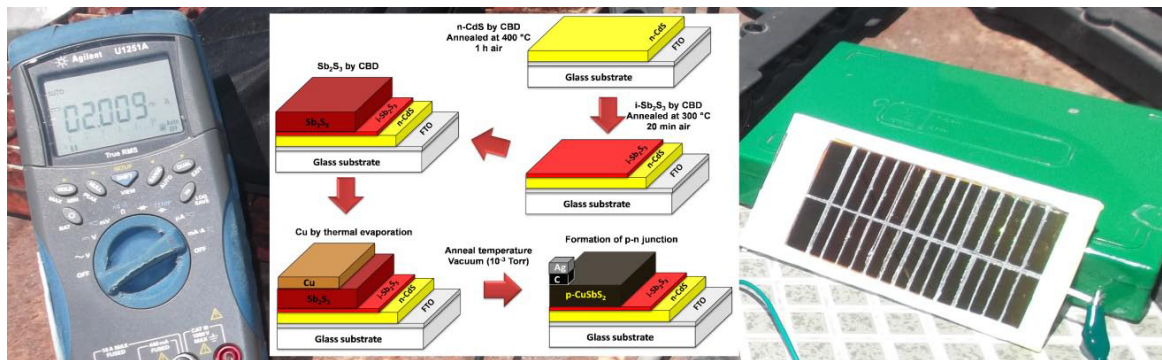
Figure 5.71 Set-up of the module under sun illumination

Using this type of experiment, we proved that our fabrication process can be scalable to produce large area modules using this method and materials.

This chapter explained the properties of the different absorber materials deposited with different thickness and annealed at different temperatures and times, as well as the implementation of this material to fabricate photovoltaic devices using p-n and p-i-n configurations, obtaining our best solar cell performance of 1.0 % of efficiency.

5.4 REFERENCES

BHIDE, V. G., SALKALACHEN, S., RASTOG, A. C., RAO, C. N. R. & HEGDE, M. S. 1981. Depth profile composition studies of thin film CdS:Cu$_2$S solar cells using XPS and AES. *Journal of Physics D: Applied Physics,* 14**,** 1647.

BIRKHOLZ, M. 2006. *Thin Film Analysis by X-Ray Scattering,* Weinheim, Wiley-VCH.

BÖER, K. W. 1992. *Survey of Semiconductor Physics: Barriers, Junctions, Surfaces, and Devices*, Van Nostrand Reinhold.

CALIXTO-RODRIGUEZ, M., MARTINEZ, H., PENA, Y., FLORES, O., ESPARZA-PONCE, H. E., SANCHEZ-JUAREZ, A., CAMPOS-ALVAREZ, J. & REYES, P. 2010. A comparative study of the physical properties of Sb$_2$S$_3$ thin films treated with N-2 AC plasma and thermal annealing in N-2. *Applied Surface Science,* 256**,** 2428-2433.

COLOMBARA, D., PETER, L. M., ROGERS, K. D., PAINTER, J. D. & RONCALLO, S. 2011. Formation of CuSbS$_2$ and CuSbSe$_2$ thin films via chalcogenisation of Sb–Cu metal precursors. *Thin Solid Films,* 519**,** 7438-7443.

CHANDRAMOHAN, R., VIJAYAN, T. A., ARUMUGAM, S., RAMALINGAM, H. B., DHANASEKARAN, V., SUNDARAM, K. & MAHALINGAM, T. 2011. Effect of heat treatment on microstructural and optical properties of CBD grown Al-doped ZnO thin films. *Materials Science and Engineering: B,* 176**,** 152-156.

DUFTON, J. T., WALSH, A., PANCHMATIA, P. M., PETER, L. M., COLOMBARA, D. & ISLAM, M. S. 2012. Structural and electronic properties of CuSbS$_2$ and CuBiS$_2$: potential absorber materials for thin-film solar cells. *Phys Chem Chem Phys,* 14**,** 7229-33.

FANG, B., ZENG, Z., YAN, X. & HU, Z. 2013. Influence of annealing on the structural and electrical transport properties of Bi$_{0.5}$Sb$_{1.5}$Te$_{3.0}$ thin films deposited by co-sputtering. *Journal of Materials Science,* 48**,** 4408-4415.

FUNG, S., ZHAO, Y. W., BELING, C. D., XU, X. L., SUN, N. F., SUN, T. N. & CHEN, X. D. 1999. Thermally induced conduction type conversion in n-type InP. *Journal of Applied Physics,* 86**,** 2361-2363.

GARZA, C., SHAJI, S., ARATO, A., PEREZ TIJERINA, E., ALAN CASTILLO, G., DAS ROY, T. K. & KRISHNAN, B. 2011. p-Type $CuSbS_2$ thin films by thermal diffusion of copper into Sb_2S_3. *Solar Energy Materials and Solar Cells,* 95**,** 2001-2005.

GREUTER, F. & BLATTER, G. 1990. Electrical properties of grain boundaries in polycrystalline compound semiconductors. *Semiconductor Science and Technology,* 5**,** 111-137.

GROVENOR, C. R. M. 1985. Grain boundaries in semiconductors. *Journal of Physics C: Solid State Physics,* 18**,** 4079.

HAN, Q., CHEN, L., ZHU, W., WANG, M., WANG, X., YANG, X. & LU, L. 2009. Synthesis of Sb_2S_3 peanut-shaped superstructures. *Materials Letters,* 63**,** 1030-1032.

HENRICH, V. E. & COX, P. A. 1996. *The Surface Science of Metal Oxides*, Cambridge University Press.

JIASONG, Z., WEIDONG, X., HUAIDONG, J., WEN, C., LIJUN, L., XINYU, Y., XIAOJUAN, L. & HAITAO, L. 2010. A simple L-cystine-assisted solvothermal approach to Cu3SbS3 nanorods. *Materials Letters,* 64**,** 1499-1502.

KıRMıZıGÜL, F., GÜNERI, E. & GÜMÜŞ, C. 2012. Effects of different deposition conditions on the properties of Cu_2S thin films. *Philosophical Magazine,* 93**,** 511-523.

KLIMOV, V., HARING BOLIVAR, P., KURZ, H., KARAVANSKII, V., KRASOVSKII, V. & KORKISHKO, Y. 1995. Linear and nonlinear transmission of Cu_xS quantum dots. *Applied Physics Letters,* 67**,** 653-655.

KRAUT, E., GRANT, R., WALDROP, J. & KOWALCZYK, S. 1980. Precise Determination of the Valence-Band Edge in X-Ray Photoemission

Spectra: Application to Measurement of Semiconductor Interface Potentials. *Physical Review Letters,* 44**,** 1620-1623.

KUMAR, M. & PERSSON, C. 2013. $CuSbS_2$ and $CuBiS_2$ as potential absorber materials for thin-film solar cells. *Journal of Renewable and Sustainable Energy,* 5**,** 031616.

LALITHA, S., SATHYAMOORTHY, R., SENTHILARASU, S., SUBBARAYAN, A. & NATARAJAN, K. 2004. Characterization of CdTe thin film—dependence of structural and optical properties on temperature and thickness. *Solar Energy Materials and Solar Cells,* 82**,** 187-199.

MATHEW, X., CRUZ, J. S., CORONADO, D. R., MILLÁN, A. R., SEGURA, G. C., MORALES, E. R., MARTINEZ, O. S., GARCIA, C. C. & LANDA, E. P. 2012. CdS thin film post-annealing and Te-S interdiffusion in a CdTe/CdS solar cell. *Solar Energy,* 86**,** 1023-1028.

MIELCZARSKI, J. & MINNI, E. 1984. The adsorption of diethyldithiophosphate on cuprous sulphide. *Surface and Interface Analysis,* 6**,** 221-226.

MOULDER, J. F., STICKLE, W. F., SOBOL, P. E. & BOMBEN, K. D. 1992. *Handbook of X-ray Photoelectron Spectroscopy,* Eden Prairie, Minnesota, Perkin-Elmer Corporation.

NAIR, M. T. S. 1998. Chemically Deposited Sb_2S_3 and Sb_2S_3-CuS Thin Films. *Journal of The Electrochemical Society,* 145**,** 2113.

NAIR, M. T. S., NAIR, P. K., ZINGARO, R. A. & MEYERS, E. A. 1993. Enhancement of photosensitivity in chemically deposited CdSe thin films by air annealing. *Journal of Applied Physics,* 74**,** 1879-1884.

NAUMKIN, A. V., KRAUT-VASS, A., GAARENSTROOM, S. W. & POWELL, C. J. 2000. NIST X-ray Photoelectron Spectroscopy Database. NIST Standard Reference Database 20, Version 4.1.

ÖZTAS, M. & BEDIR, M. 2008. Thickness dependence of structural, electrical and optical properties of sprayed ZnO:Cu films. *Thin Solid Films,* 516**,** 1703-1709.

SEPTINA, W., IKEDA, S., IGA, Y., HARADA, T. & MATSUMURA, M. 2014. Thin film solar cell based on $CuSbS_2$ absorber fabricated from an electrochemically deposited metal stack. *Thin Solid Films,* 550**,** 700-704.

TU, K.-N., MAYER, J. W. & FELDMAN, L. C. 1992. *Electronic Thin Film Science: For Electrical Engineers and Materials Scientists*, Macmillan.

VAN EMBDEN, J. & TACHIBANA, Y. 2012. Synthesis and characterisation of famatinite copper antimony sulfide nanocrystals. *Journal of Materials Chemistry,* 22**,** 11466-11469.

WEINHARDT, L., BÄR, M., POOKPANRATANA, S., MORKEL, M., NIESEN, T. P., KARG, F., RAMANATHAN, K., CONTRERAS, M. A., NOUFI, R., UMBACH, E. & HESKE, C. 2010. Sulfur gradient-driven Se diffusion at the $CdS/CuIn(S,Se)_2$ solar cell interface. *Applied Physics Letters,* 96**,** 182102.

WILLIAMSON, G. K. & HALL, W. H. 1953. X-ray line broadening from filed aluminium and wolfram. *Acta Metallurgica,* 1**,** 22-31.

YANG, B., WANG, L., HAN, J., ZHOU, Y., SONG, H., CHEN, S., ZHONG, J., LV, L., NIU, D. & TANG, J. 2014. $CuSbS_2$ as a Promising Earth-Abundant Photovoltaic Absorber Material: A Combined Theoretical and Experimental Study. *Chemistry of Materials*.

YANG, B., WANG, L., HAN, J., ZHOU, Y., SONG, H., CHEN, S., ZHONG, J., LV, L., NIU, D. AND TANG, J. 2014. $CuSbS_2$ as a promising earth-abundant photovoltaic absorber material: a combined theoretical and experimental study. *Chemistry of Materials*.

YU, L., KOKENYESI, R. S., KESZLER, D. A. & ZUNGER, A. 2013. Inverse Design of High Absorption Thin-Film Photovoltaic Materials. *Advanced Energy Materials,* 3**,** 43-48.

6
Conclusions

In the present thesis, the methodology of preparation of In_6Se_7, $CuSbS_2$ and $CuSb(Se_xS_{1-x})_2$ thin films by a two-stage process combining chemical bath deposition and thermal evaporation techniques were explained. Photovoltaic devices using two different configurations: p-n and p-i-n junction types using $CuSbS_2$ and $CuSb(Se_xS_{1-x})_2$ thin films as absorber materials and CdS as window layer were fabricated.

Absorber layer

We can conclude that $CuSbS_2$ thin films were formed by heating stacked layers of glass/Sb_2S_3/Cu deposited Sb_2S_3 by CBD and Cu by thermal evaporation annealed in low vacuum for 1 h at various temperatures for different durations by varying thickness of individual layers. The structural analysis by XRD of the stacked layers of glass/Sb_2S_3/Cu at different anneal temperatures and times, and different Sb_2S_3 and Cu thicknesses showed the formation of orthorhombic $CuSbS_2$ with the presence of Cu_2S as secondary phase with a decrease on microstrain. A single phase $CuSbS_2$ near the surface was obtained for the condition of Sb_2S_3 and Cu thickness of 1000 nm and 50 nm respectively, annealed at 350 °C for 1 h, whereas a mixed phases of $CuSbS_2$ and Cu_2S in the depth. According to the Cu-Sb-S system (Figure 6.1), the progression of the phases from Cu through to Sb_2S_3 (precursor layers) show the formation of mixed phases, which might be ternary $CuSbS_2$ and Cu_2S, having a traces of Sb_2S_3. The probable cause not to form pure $CuSbS_2$ lies into the sulfur deficiency and Sb rich obtained by the use of these precursors as shown in Figure 6.1, which are in good agreement with the results obtained by XPS measurements. The good combination of precursors to assure form pure ternary $CuSbS_2$ is the use of Cu_2S and Sb_2S_3.
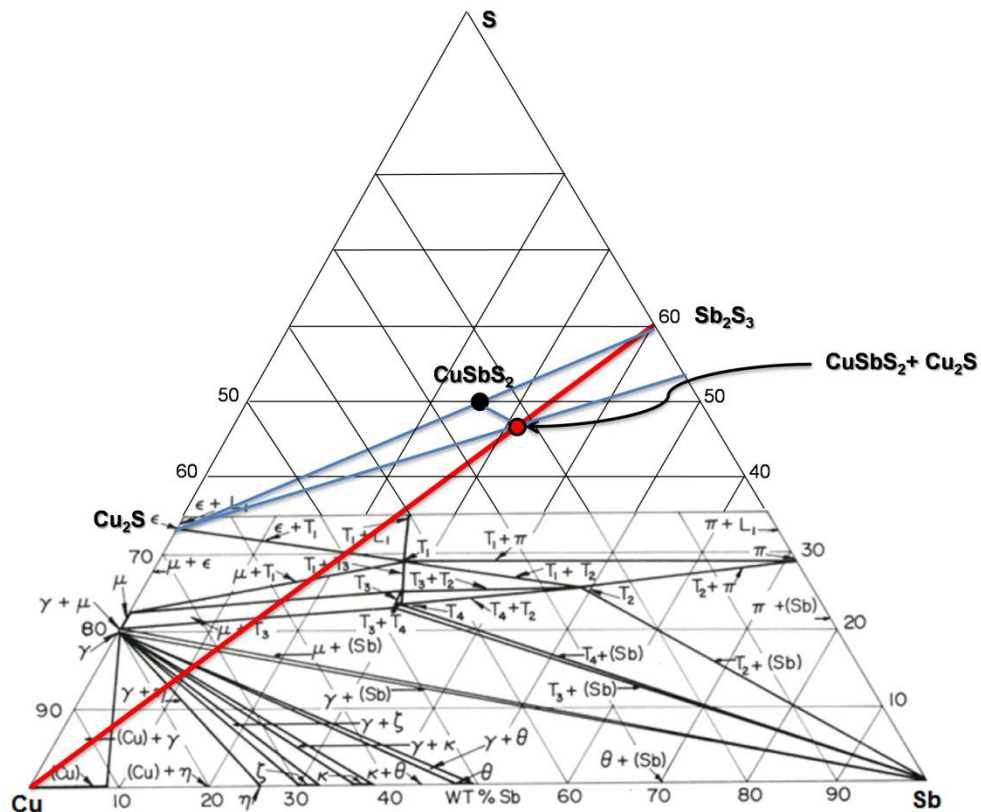
Figure 6.1 Ternary Cu-Sb-S system

Ternary $CuSbS_2$ compound was formed by the combination of two deposition techniques, such as chemical bath deposition and thermal evaporation which are low cost and less toxic techniques. One disadvantage in our thin film deposition process is the formation of Cu_2S as secondary phase which produce electronic defects states that limit the charge transport and promote recombination across the junctions in the photovoltaic device. The diffusion and reaction of Cu through Sb_2S_3 layer was performed by the movement of Cu atoms through Sb_3S_3 lattice activated by the annealing of the thin film, suggesting an interstitial transport mechanism due to the fast diffusion of copper, as presented in XPS depth profile analysis. The optical absorption of the thin films showed direct allowed transitions at 1.55 eV and 1.2 eV, corresponding to $CuSbS_2$ and Cu_2S respectively. As the anneal temperature increase, there was an increase in carrier mobility due to the reduction of

scattering of the charge carriers by the elimination of defects, related to the reduction of lattice microstrain and there was an increase in conductivity due to the sublimation of unreacted Sb_2S_3 phase. As the vapor pressure of Sb_2S_3 is higher for temperatures above 350 °C than pressure of heating chamber (10^{-3} Torr) the sublimation of these Sb and S atoms will occur (Figure 6.2), giving less Sb_2S_3 phase present in the compound (Welch et al., 2015). As the thickness of Sb_2S_3 layer increase, there was a decrease in carrier concentration and conductivity due to the presence of more poorly conductive Sb_2S_3. For this condition of heating at 350 °C the sublimation of Sb_2S_3 phase is not high, because its vapor pressure is close to the pressure of the heating chamber (Figure 6.2) decreasing the sublimation rate of this phase.
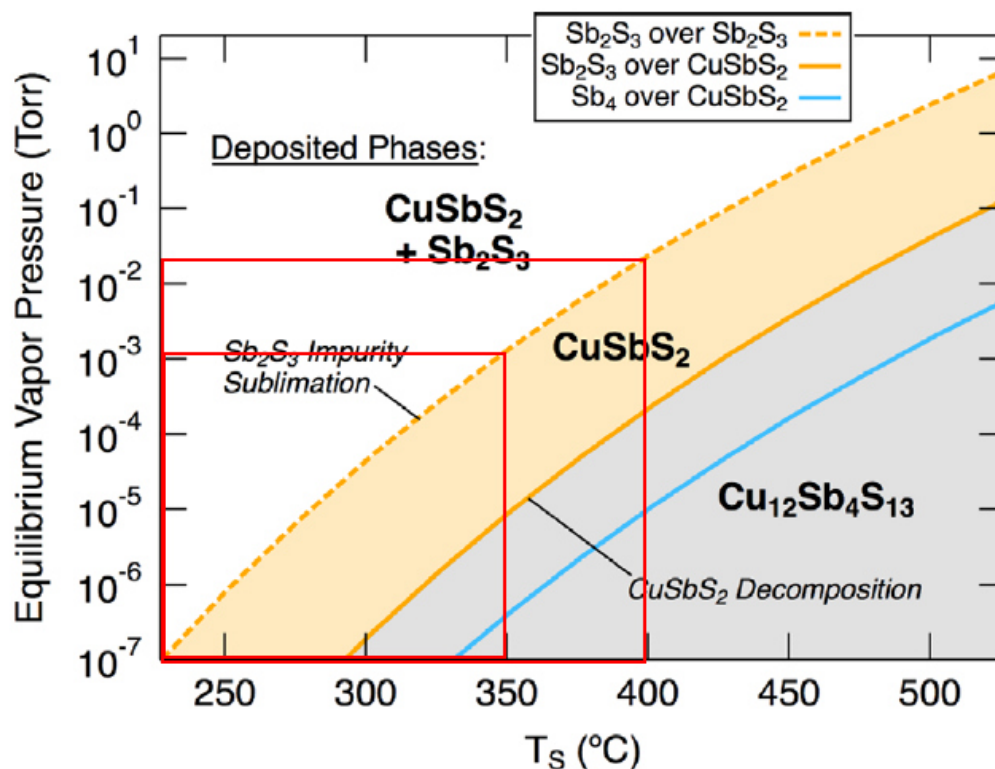
Figure 6.2 Calculated vapor pressures showing the point of Sb_2S_3 sublimation ((Welch et al., 2015)) (Reproduced with kind permission from Elsevier)

Quaternary compound $CuSb(Se_xS_{1-x})_2$was formed by heating layered structures of glass/Sb_2S_3/Se/Cu of 5 layers of Sb_2S_3 (1000 nm), Se layer of 300 nm and Cu layer of 50 nm annealed at 350 °C for 1h in low vacuum (10^{-3} Torr),

giving a selenization process via chemical bath deposition technique. The formation was near the surface giving a mixed of $CuSbS_2$ and Cu_2S phases in depth. The analysis of the absorption coefficient of $CuSb(Se_xS_{1-x})_2$ thin films showed the formation of three different transitions, at 1.55 eV, 1.4 eV and 1.2 eV corresponding to $CuSbS_2$, $CuSb(Se_xS_{1-x})_2$ and Cu_2S respectively. Quaternary compound showed more conductivity than ternary compound due to the surface roughness reduction from 9.5 nm to 4.9 nm, where the electron scattering is reduced, increasing the conductivity.

Photovoltaic devices

Various photovoltaic structures were fabricated using $CuSbS_2$ thin film as absorber and CdS thin films as window layer. Multilayered structure of glass/SnO_2:F/CdS/Sb_2S_3/Cu were prepared and annealed at different conditions to form photovoltaic p-n junctions of type glass/SnO_2:F/*n*-CdS/*p*-$CuSbS_2$. For the p-n junction of glass/SnO_2:F/*n*-CdS/*p*-$CuSbS_2$/C/Ag formed at different annealing temperatures (CdS as prepared) there was a decrease in V_{oc}, J_{sc}, FF and efficiency with values in range of 214-187 mV, 3.21-3.06 mA/cm2, 39-27% and 0.27-0.15% respectively, this is due to the inter-diffusion of the Cu and Sb into CdS layer (according to our XPS depth profile analysis) which degrades the junction. For the p-n junction of glass/SnO_2:F/*n*-CdS/*p*-$CuSbS_2$/C/Ag formed at different annealing temperature using CdS annealed at 400 °C for 1 h in air, showed an improvement of the photovoltaic parameters V_{oc}, J_{sc}, FF and efficiency with values in range of 249-323 mV, 2.28-3.77 mA/cm^2, 46-48% and 0.45-0.30% respectively, with the best efficiency (0.45 %) for the annealing condition at 350 °C for 1 h in low vacuum. For this condition was obtained the maximum J_{sc} (3.77 mA/cm^2), in which the absorber layer promote a large injection of charge carriers due to the large carrier concentration (6.1×10^{18} cm^{-3}) obtained by this sample. For the p-n junction of glass/SnO_2:F/*n*-CdS/*p*-$CuSbS_2$/C/Ag formed with different absorber thickness showed an increase of V_{oc} of 259 mV for the large thickness (1050 nm) due to the reduction in the

structural defects (decreasing lattice strain) causing a reduction on recombination at the junction and a J_{sc} of 3.7 mA/cm^2 by the reduction on surface roughness contributing to the reduction of carrier scattering. The fill factor for this sample was low (35%) due to the increase of precursor layers (Sb_2S_3) in order to increase the total thickness, having a high series resistance which contributes to reduce the fill factor. For the p-n junction solar cells, Cu and Sb diffuses through the heterojunction to CdS layer, reason for the low V_{oc} values obtained by the trap states formed which act as recombination sites for minority carriers.The way to improve the photovoltaic parameters was using a p-i-n junction of glass/SnO_2:F/n-CdS/i-Sb_2S_3/p-$CuSbS_2$/C/Ag for $CuSbS_2$ of 1050 nm and CdS annealed, using an intrinsic layer of Sb_2S_3. This configuration allows collecting more photogenerated carriers due to the stretches out of the electrostatic field in the depletion zone by the intrinsic layer. The photovoltaic parameters of this device were **V_{oc}=405 mV, J_{sc}=7.54 mA/cm^2, FF=32% and $\eta \approx$1.0%**, the best photovoltaic device obtained in this research work.

In order to apply our results in a device with large area, a mini-module of 60 cm^{2}was fabricated interconnecting small cells in series and parallel of glass/SnO_2:F/n-CdS/i-Sb_2S_3/p-$CuSbS_2$/C/Ag obtaining a maximum current of 2 mA and a maximum voltage of 2.2 V measured under sun illumination.

The initial objectives were accomplished by obtaining the absorber materials using low cost and less toxic methods such as chemical bath deposition and thermal evaporation as well as the fabrication of photovoltaic devices using earth abundant materials to obtain devices with efficiencies up to 1.0 %.

This work leaves a door open for research in the solar cell field to explore the full potential of $CuSbS_2$absorber material to obtain high efficiency solar cells.

6.1 REFERENCES

WELCH, A. W., ZAWADZKI, P. P., LANY, S., WOLDEN, C. A. & ZAKUTAYEV, A. 2015. Self-regulated growth and tunable properties of CuSbS2 solar absorbers. *Solar Energy Materials and Solar Cells,* 132, 499-506.

LIST OF TABLES

LIST OF FIGURES